Joana Ribeiro da Cunha Gomes Teixeira

General Relativistic Radiation Transport of massive and massless particles in strong gravity

Thesis submitted for the degree of

Doctor of Philosophy (PhD)

of

University College London

December 2023

I, Joana Ribeiro da Cunha Gomes Teixeira,
confirm that the work presented in my thesis is my own.
Where information has been derived from other sources,
I confirm that this has been indicated in the thesis.

Signed: _____

Dated: _____

Abstract

General relativity is the best theory at present to describe gravitational interactions. One of its predictions is the existence of black holes. Because general relativity is not compatible with Quantum Mechanics, some new Physics must exist to unify them. This makes systems like black holes, where both quantum mechanical and general relativistic phenomena are expected to occur, particularly interesting objects of study. The discovery of astrophysical black holes opened the doors to detailed studies of these objects, both from the point of view of understanding the consequences and limitations of general relativity and of gaining insight into the effects of strong gravity on physical processes that occur in their vicinity.

To study these objects, we must resort to observations performed on Earth (or in space around the Earth). This means that we require radiation or particles to travel between these regions of the universe towards our detectors. In the transport process, radiation or particles may be absorbed, scattered, or added to the original bundle, as well as distorted by the gravitational and relativistic phenomena at play in the extreme regions of their origin. As such, it is essential to have a way of understanding this transport mechanisms and how it may affect the observations performed on Earth. Only in this way are we able to confidently make conclusions about the phenomena happening very close to these black holes.

The main focus of this thesis was the development of a formalism and algorithm able to perform general relativistic transport calculations of both particles with and without mass in a self-consistent manner. This algorithm was built on and generalized another general relativistic radiation transport (GRRT) formalism which focused on massless particles.

This formalism is then applied to two distinct astrophysical scenarios. The first is related to the detection of electromagnetic flares across multiple energy bands from the vicinity of Sagittarius A*, the black hole at the centre of the Milky Way. We performed GRRT calculations for this system, performing a thorough analysis of the effects of general and special relativity in the distortion of flares, considering a time-dependent spectral evolution of the emissivity profile and taking into account the energy bands in which observations take place.

The second scenario is related to the propagation of massive particles accelerated in the vicinity of black hoes and their interactions with the medium around them. We were able to identify and explain interesting trends in their behaviour and see how they were affected by different aspect of special and general relativity. We investigated how the particle's Lorentz factor and its acceleration region influences the location and timing of where interactions would take place and found some unexpected degeneracies which may impact the interpretations made from observations associated to these systems.

Impact Statement

The unifying theme of this thesis is its contribution to better understanding the physical processes happening in massive black hole environments. The impact of the work performed here, however, is more far-reaching, applying to other systems and providing useful insights into fundamental physics. Some of the impact areas of this thesis are highlighted below.

1. **Impact on the field of general relativistic radiation transport (GRRT)**

   A key focus of this work was to develop a general covariant formalism for the transport of massive and massless particles in strong gravity. This formalism surpasses the traditional general relativistic radiative transfer formulations constructed by previous researchers. The ability to calculate the covariant transport of both massless and massive particles, in non-relativistic and highly relativistic regimes, across 3 dimensional media with non-uniform absorption and emission was essential to the calculations presented in this thesis. The formalism can go beyond the specific science questions addressed in this work, and it will be a useful means for us to gain better understanding of the physical processes taking place in strong-gravity systems. The code developed during this PhD is modular in nature, making it easy to add to and adapt to different astrophysical contexts. This will allow further work in the fields described below and others where problems rely on a proper treatment of radiation transport in strong gravity systems.

2. **Impact on the field of general relativity (GR)**

   In the process of developing the formalism and code mentioned above, several interesting facts were found regarding the propagation of particles in general relativity. These findings contribute to a better understanding of certain aspects of this complicated theory. The code developed may provide useful visualizations of unexpected phenomena which, while a direct consequence of GR, might not be intuitively predicted or understood.

3. **Impact on the applications of GRRT to real astrophysical systems**

   The study of flares associated to massive black holes, in particular to Sagittarius A*, has been going on for over 20 years. Despite the multiple observational, theoretical and modelling efforts, the physical processes responsible for them are not yet clear. The research in this thesis shed light into how gravitational, relativistic and bandwidth effects affect the observations of such flares. The intense distortions caused by these effects together with

the fact that narrow band observations may significantly differ from the bolometric light curve profiles demonstrates the importance of being cautious when proposing physical models in light of such observations alone. This has the potential to justify proposals to fund multi-band observational campaigns of both nuclear massive black holes and other black hole systems.

4. **Impact on the understanding of the physics of massive particle transport in black hole environments**

   Processes associated to the production of flares very close to massive black hole systems are also capable of accelerating massive particles to very large energies. These particles, produced or accelerated very close to the black hole, will go on to interact with the medium surrounding them in ways which are affected by the black hole's strong gravitational field. By exploring how particles of different mass and energy accelerated at different distances from the black hole interacted with the medium around them, we were able to identify degeneracies which will affect the interpretation of observations from such systems. We also demonstrated the potentialities of the GRRT formalism developed during this PhD to studying the propagation and interactions of massive particles in black hole systems with their surrounding medium.

5. **Impact on the wider community**

   The ray tracing and covariant transport work produced in this thesis has several applications that go beyond the realm of Astrophysical research. Firstly, it is a great tool for outreach. People are curious about black holes, and having visualization tools such as the ones developed in this work allows them to gain a better understanding about these strange objects. Secondly, it can contribute to the entertainment industries. As an example, several *Pixar* animation movies rely on ray tracing techniques to produce their realistic images. Similarly, movies featuring black holes, such as *Interstellar*, rely on scientifically accurate ray tracing and radiation transport algorithms to produce the realistic black hole images which make them so iconic. It is possible that the algorithms developed in this work may find their way into such industries, impacting a community to whom it would at first sight appear useless. Finally, this work deals above all with transport equations. While here they are used in the very concrete case of radiation and particles transported from the vicinity of black holes, similar transport equations are

widely used in several different fields, from fluid dynamics to the calculation of absorbed dose in radiotherapy. While the algorithm presented in this thesis is not directly applicable to these situations, some of the tools developed in the process may become useful to researchers working with transport equations in their own fields.

Acknowledgements

I start by thanking the people from UCL who accompanied me during my studies. Firstly, I thank my supervisor, Kinwah Wu, for sharing his knowledge with me with guidance and patience throughout my PhD studies. I thank Ziri for his help with coding issues and some mathematical concepts. A special thanks goes to Kaye, my academic sister, who has been so generous in sharing her knowledge and insight with me through very interesting discussions during the last 4 years. She also read my thesis in detail from cover to cover, providing me with comments and suggestions which greatly improved this manuscript. I hope I can do the same for you! I would also like to thank the people from the CPI, who welcomed me so kindly into their department, making my PhD experience so much more enjoyable. A special thanks to my desk neighbours and lunch buddies!

I thank my CLC and Anabel for accompanying me on my journey in the last 4 years. Their support has helped me have a balanced and centered life throughout my PHD and keep developing as a person way beyond academia. I am also very grateful to the English Martyrs community, which became a second home in the last few years. My thanks extend to all the other friends I made since coming to London, whose friendship has been a solid ground for me in all these years.

My school teachers and friends played a big role in encouraging me to be ambitious with my goals and follow them to London. They have been a great support in the 10 years since leaving school. Obrigada Beatriz, Maria e Sofia por estarem sempre presentes!

My time in London was made possible by the generous financial support of Fundação Calouste Gulbenkian and Fundação Rocha dos Santos during my undergraduate and master studies. I particularly acknowledge Eng. Francisco van-Zeller, who saw potential in me from the start.

Finally, I very much want to thank my families. First, a big thank you to my British family, who adopted me as a daughter/sister long before I was so officially. Thank you for being my home away from home all these years, for your huge generosity and kindness towards me and for making me feel part of the family. A special thanks to my husband, who has been part of my life for so many years, accompanying, supporting, encouraging and loving me through so much. Thanks for always believing in me! Por fim, agradeço à minha família Portuguesa, que me nutriu, amou, encorajou e apoiou desde sempre, e que continua a ser uma parte tão importante da minha vida - mesmo depois de 10 anos a viver em Inglaterra. Obrigada aos meus pais e irmãs, que têm acompanhado de perto todas as minhas aventuras. Aos meus avós, meus grandes fãs que sempre me fizeram sentir especial. E aos meus tios e primos, que sempre se alegraram com os meus sucessos e esperaram grandes coisas de mim.

To all of you, a big thank you!

Contents

Nomenclature

Physical Constants

c	Speed of light in a vacuum	$2.997\,924\,58 \times 10^{10}\,\mathrm{cm\,s^{-1}}$
G	Gravitational constant	$6.67430 \times 10^{-8}\,\mathrm{cm^3\,g^{-1}\,s^{-2}}$
h	Planck constant	$6.62607015 \times 10^{-27}\,\mathrm{erg\,s}$

Astrophysical Constants

$M_\odot$	Solar mass	$1.989 \times 10^{33}\,\mathrm{g}$

Acronyms

AGN Active galactic nucleus

ALMA Atacama Large Millimeter/submillimeter Array

BH Black hole

BL Boyer-Lindquist

ESO European Southern Observatory

FRSD Fast rise slow decay

GRMHD General relativistic magneto-hydrodynamics

GRRT General relativistic radiation transport

IR Infrared

ISCO Innermost stable circular orbit

LNFR Locally non-rotating frame

MHD Magneto-hydrodynamics

NIR Near-infrared

SED Spectral energy density

Sgr A* Sagittarius A*

SMBH Super massive black hole

SRFD Slow rise fast decay

VLT Very Large Telescope

XRB X-ray binary

ZAMO Zero angular momentum observer

Other Symbols

a Black hole spin parameters, $a = J/Mc$, where J is the BH's spin angular momentum

M Black hole mass

$(r_{\rm obs}, \theta_{\rm obs}, \phi_{\rm obs})$ Location of the origin of the observer plane in BL coordinates

Δ Shorthand for $r^2 - 2Mr + a^2$

$\dot{z}_0$ Magnitude of the spatial part of the particle's 4-velocity

∂_μ Partial derivative with respect to x^μ, i.e. $\partial_\mu = \frac{\partial}{\partial x^\mu}$

Σ Shorthand for $r^2 + a^2 \cos^2\theta$

$\tau^{(\mathcal{E})}$ Optical depth at energy $\mathcal{E}$

ξ Norm of 4-velocity, $\xi = 0$ for massless particles and $\xi = -1$ for massive particles

$\{\hat{\boldsymbol{\epsilon}}^a\}$ Dual of non-coordinate basis

$\{\hat{\boldsymbol{\epsilon}}_a\}$ Non-coordinate basis

$\{\boldsymbol{e}^\mu\}$ Dual of coordinate basis

$\{\boldsymbol{e}_\mu\}$ Coordinate basis

C_t Conserved quantity due to time translation symmetry of the spacetime metric

C_ϕ Conserved quantity due to axisymmetry of the spacetime metric

D_s Physical extent of emitting body in chapters 3 and 4.

r_em Radial coordinate of the emission/ acceleration of particles in chapter 4.

$\Gamma^\mu{}_{\nu\rho}$ Christoffel symbols

$\hat{\epsilon}_a{}^\mu$ Tetrad that relates coordinate and non-coordinate bases

[...] Depending on context: dimensions of ... ; explicit dependence on ... when ... =1 in the unit system used

α; $\alpha_\mathcal{E}$; $\alpha_{0,\mathcal{E}}$ Absorption coefficient; idem at energy $\mathcal{E}$, idem measured by local co-moving observer

$\dot{x}^\mu$ Derivative of the μ-th spacetime coordinate with respect to the geodesic parameter

η Minkowski metric tensor

$\hat{\mathcal{E}}$ Particle energy as measured by a "hatted" observer, typically: rest mass energy (massive particles); stationary observer at infinity (massless particles)

$\hat{p}$ Particle 4-momentum measured by a "hatted" observer

$\hat{u}$ Particle 4-velocity measured by a "hatted" observer

κ Covariant absorption coefficient

λ Affine parameter (for massless particles) or proper time (for massive particles) along a geodesic

$\mathbf{p}$ Relativistic three-momentum vector

$\mathbf{x}$ Spatial position vector

$\mathcal{E}$; $\mathcal{E}_\nu$; $\mathcal{E}_0$ Particle/photon total energy measured by some specified observer; Energy of a photon with frequency ν; Energy of particle measured by local co-moving observer

$\mathcal{F}$ Covariant distribution function

$\mathcal{I}^{(\mathcal{E})}$ Covariant specific intensity at energy $\mathcal{E}$

$\mathcal{I}^{(\nu)}$ Covariant specific intensity at frequency ν

$\mathcal{J}$ Covariant source function

$\mathcal{L}$ Lagrangian density

$\mathcal{N}; \mathcal{N}_\nu$ Number of particles; number of particles with frequency between ν and $\nu + \mathrm{d}\nu$

$\mathcal{V}$ Phase space volume

ν Frequency

Ω Solid angle

ω_{LNRF} Angular velocity caused by frame dragging

f Phase space density

g Spacetime metric tensor

$g_{\mu\nu}$ Spacetime metric component $\mu\nu$

$I_{\mathcal{E}}$ Specific intensity at energy $\mathcal{E}$

I_ν Specific intensity at frequency ν

j; $j_{\mathcal{E}}$; $j_{0,\mathcal{E}}$ Emission coefficient; idem at energy $\mathcal{E}$, idem measured by local co-moving observer

m Particle mass

n_0 Proper number density of a medium

p; p^μ 4-momentum; μ-th component of 4-momentum

Q Depending on context: Covariant emissivity coefficient (GRRT); or Carter's constant (geodesic integration)

r_{g} Gravitational radius: $r_{\mathrm{g}} = GM/c^2$

$r_{\rm s}$	Schwarzschild radius: $r_{\rm s} = 2GM/c^2$
S	Source function, $S = j/\alpha$
u; u^μ	4-velocity; μ-th component of 4-velocity
x^μ	μ-th spacetime coordinate

List of Figures

Chapter 1

Introduction

1.1 Massive nuclear black holes

Michell (1784) and Laplace (1799) were the first people to predict the existence of objects whose escape velocity would be larger than the speed of light. They predicted that nothing would escape from them and that they would be dark. Although their calculations were performed using Newtonian gravity, the result of the radius below which such objects would become "dark" turned out to coincide with the event horizon radius calculated using general relativity (The Nobel Comittee for Physics, 2020).

Very soon after the publication of Einstein's theory of general relativity (Einstein, 1916), Schwarzschild published a solution to the Einstein field equations corresponding to the space-time due to a spherically symmetric stationary mass (Schwarzschild, 1916). Later, Kerr proposed another solution to Einstein's equations, this time for a spinning body (Kerr, 1963), which generalized the Schwarzschild solution.

In 1939, Oppenheimer and Snyder realized that the collapse of spherically symmetric, pressure-free matter would eventually result in the presence of a horizon from inside which there could be no communication to the outside (Oppenheimer and Snyder, 1939). However, it was not obvious that such collapse into a singularity with the formation of a horizon would occur in real astrophysical situations, where the assumption of perfect spherical symmetry would be unlikely to hold.

It was only in 1965 that Penrose showed that during the collapse of matter, there is a formation of trapped surfaces regardless of the symmetries of the system. These are two-dimensional space-like surfaces with the property that the two null geodesics orthogonal to them at a point[1] will converge. Penrose showed that, when such surfaces form, gravitational collapse inevitably ends in a singularity (Penrose, 1965). This showed that the collapse of matter into a singularity is a consequence of general relativity without the requirement of special symmetries[2].

[1] E.g. if the surface is a 2-sphere with t =constant and r =constant, then there will be an in-going and an out-going radial null geodesic orthogonal to the surface at each point.

[2] Penrose was awarded half of the 2020 Physics Nobel Prize for this work (The Nobel Comittee for Physics,

1.1.1 Massive black hole in the Galactic Centre - Sagittarius A*

The first empirical observations to determine the existence of supermassive black holes consisted of measuring the motion of bodies in the central regions of galaxies, calculating the density of the object responsible for the gravitational field on which they moved and comparing it to that of the densest stable multi-body objects known to exist. A density larger than this would indicate the presence of a single, very dense object which could be a supermassive black hole. Miyoshi et al. (1995) noticed that the kinematics around the centre of a galaxy (NGC 4258) could not be explained by a dense stellar population.

In 1971 it had been suggested that, just as other galaxies, the Milky Way would host a supermassive black hole at its centre (Lynden-Bell and Rees, 1971). Evidence for the presence of a supermassive black hole in the centre of the Mikly Way was obtained by the monitoring of the orbits of stars at the galactic centre. This was performed by two independent teams lead by Ghez (at the Keck Observatory) and Genzel (at the Very Large Telescope), both of whom shared the 2020 Physics Nobel Prize with Penrose for their work (The Nobel Comittee for Physics, 2020). These observations were performed in the near infrared band, as the dust present in the line-of-sight towards the Earth does not significantly obscure radiation with wavelength as long as this. Another advantage of using these wavelengths was that it was possible to obtain a very good angular resolution, which is necessary to distinguish and monitor the motion of individual stars. In particular, the two groups (Schödel et al., 2002; Ghez et al., 2003) looked at the motion of the star S2, with a period of less than 16 years, and established that the elliptical orbit was due to a mass of about $4 \times 10^6\,\mathrm{M}_\odot$ constrained in a region of radius at most equal to the pericentre of the orbit (Ghez et al., 2008; Gillessen et al., 2009). This corresponds to a density consistent with the presence of a supermassive black hole. In these works, the authors also provided consistent estimates of the distance to the galactic centre to be approximately 8 kpc.

The numerical values for the properties of Sgr A* used for the calculations presented in this thesis are summarised below[3]

- **Mass:** $4.297 \times 10^6 \mathrm{M}_\odot = 8.547 \times 10^{36}\mathrm{Kg}$ (GRAVITY Collaboration et al., 2022)
- **Distance to Earth:** $8.277\mathrm{kpc} = 2.56111239 \times 10^{22}\mathrm{cm}$ (GRAVITY Collaboration et al., 2022)
- **Spin and viewing angle:** Currently, there is no consensus as to the spin of Sgr A* nor the viewing angle of the line of sight from the Earth relative to the spinning axis.

2020).

[3]See (GRAVITY Collaboration et al., 2022, table B1) for a summary of the best fits for these parameters in other recent studies.

Different studies using different models and data favour very different values of both spin and inclination (or viewing) angle. For instance, the models tested in Event Horizon Telescope Collaboration et al. (2022) yielded values as diverse as a spin of $a = 0.998$ and inclination of $i = 10°$ through $a = 0.5$ and $i = 30°$ to $a = 0.9$ and $i = 70°$. These are just some examples of how poorly constrained these values are at the moment. In an attempt to make the results as applicable as possible, not only for Sgr A* but for other black hole systems, we perform most calculations for two extreme spins: $a = 0$ for non rotating (Schwarzschild) black holes and $a = 0.998$ for rotating (Kerr) black holes. All calculations can be easily reproduced for any other value of spin. Unless otherwise stated, the spin of the Kerr black holes used in the calculations in this thesis was $a = 0.998$. In terms of inclination, we calculate some results for various inclinations and then focus on mostly edge on views (i.e. inclinations close to $i = 90°$) due to the particularly interesting features that arise at such viewing angles.

1.2 Flares in the Galactic Centre

1.2.1 Multi-waveband observations

Brown and Lo (1982) discovered variability in the emission around Sgr A* using the 35 km radio-link interferometer at the National Radio Astronomy Observatory (NRAO). They found that the flux density of the radio emission changed by 20-40% on timescales ranging from days to years. Later, Miyazaki et al. (1999) found variations of 100% in the emission of millimeter wavelengths on timescales of a week.

Baganoff et al. (2001) provided the first observation of what is now widely referred to as "flares" from Sgr A*. The authors detected a large X-ray flare in the 2-8 keV band in a Chandra observation, with a power increase by a factor of 50 on timescales of $\sim$ 160 minutes. This observation was followed by the detection of other X-ray flares, this time with XMM-Newton. Some were similar to those detected by Baganoff et al. (2001), namely (Goldwurm et al., 2003), and one seemed of a different nature, being much brighter and softer than previously detected flares (Porquet et al., 2003). Later, Bélanger et al. (2005) detected two bright X-ray flares with a luminosity increase by factor of 40, with durations of 4ks and 10ks, both of which were accompanied by smaller flares. Porquet et al. (2008) also detected a nearly symmetrical, bright flare with XMM-Newton, followed by 3 smaller flares. It was later discovered that the X-ray variability extends to the 3-70 keV band, as measured by *NuStar* (Barrière et al., 2014; Zhang et al., 2017). Some bright X-ray flares were found to have nearly symmetrical light curves (Porquet et al., 2003), while others showed an asymmetric profile with a slow-rise-fast decay profile (Nowak et al., 2012).

Flares were also detected on near infra-red (NIR) bands both with the Very Large Telecope (VLT), lasting from 30 to 85 minutes, (Genzel et al., 2003) and with the Keck telescope (Ghez et al., 2004), lasting around 40 minutes. Short term variability on the scale of 90 minutes was also found at 100 GHz and 140 GHz (Miyazaki et al., 2004). At lower frequency, flares at 20 GHz were found to lag flares at 43 GHz by 20-40 minutes (Yusef-Zadeh et al., 2006). Observations on the Very Large Array (VLA) found that the peak of a flare at 8 GHz lagged the peak at 9.9 GHz by 18 minutes (Michail et al., 2021a), while ALMA found no time lags between the 223 GHz and 229 GHz flares (Wielgus et al., 2022).

These joint detections led to an effort to perform coordinated observations across the electromagnetic spectrum in order to better understand the nature of the flares. The first simultaneous detection of an NIR and X-ray flare was reported by Eckart et al. (2004). The authors found an X-ray flare with a duration of ∼40 minutes with Chandra (2-8 keV) and a simultaneous NIR flare with the VLT. A potential time lag between the X-ray and the NIR flares was reported in (Eckart et al., 2006a), though other studies found that the time delay was consistent with zero (Eckart et al., 2006a, 2008; Boyce et al., 2019). A time lag was also found between X-ray and radio flares (Capellupo et al., 2017), although there was a possibility that the observations over the two bands were not correlated.

A systematic lag was found between NIR flares and radio/submm flares (Yusef-Zadeh et al., 2007, 2009; Michail et al., 2021b; Boyce et al., 2022), and between X-ray and submm flares (Yusef-Zadeh et al., 2008; Marrone et al., 2008; Trap et al., 2011; Kunneriath et al., 2010). An exception to this was the multi-band flare reported by Fazio et al. (2018), where the X-ray emission followed the sub-mm flare, both of which preceded were preceded by an NIR counterpart. Based on multiple observations, X-ray flares always seem to be associated with NIR flares, with the NIR flares being longer than their X-ray counterparts (Dodds-Eden et al., 2009), while the reverse isn't always the case (Marrone et al., 2008; Trap et al., 2011). Furthermore, NIR flares were found to have substructure with a quasi-periodicity of ∼15 minutes (Eckart et al., 2006a) or ∼20 minutes (Trippe et al., 2007) and they were found to be highly linearly polarized (Nishiyama et al., 2009).

Finally, by analysing the linear polarization of a bright NIR flare, the GRAVITY collaboration found that its polarization angle rotated during the flare (GRAVITY Collaboration et al., 2020b). This is consistent with the astrometric observations in GRAVITY Collaboration et al. (2018), where the centroid of the emission shows a clockwise motion, and it suggests that the emission source is polarised and orbiting the black hole.

1.2.2 Current understanding and models

To have a full picture of the astrophysics involved in the production of the flares observed, it is necessary to understand: i) the radiation process responsible for the emission; ii) the mechanism responsible for energising the radiating particles; iii) the properties (structure, location and motion) of the emitting region. We noted that over 100 papers have been produced which present results addressing the three points above, both recurring to modelling and analysis of observational data. Some of the main findings are summarised below.

i) Radiation processes

Bremsstrahlung radiation, synchrotron radiation and inverse Compton (IC) scattering are among the most common radiative processes in energetic astrophysical environments. They are believed to responsible for producing the flaring emission from Sgr A*. While the low energy radiation such as radio and NIR is likely due to synchrotron emission, higher energy radiation, such as X-rays, could be due to Bremsstrahlung or direct synchrotron emission, Compton up-scattering of lower energy photons of the ambient radiation field by the same population of electrons that contribute to the synchrotron emission (synchrotron self Compton, or SSC) or Compton up-scattering off a different electron population (IC). Which one of these mechanisms is actually responsible for the flares is still a debated topic.

For example, Baganoff et al. (2001) and Markoff et al. (2001) proposed that X-rays could be due to either pure synchrotron radiation or synchrotron self-Comptonisation (SSC), while Liu and Melia (2002) argued that they are thermal Bremsstrahlung radiation. Ghez et al. (2004) favoured the direct synchrotron scenario; Eckart et al. (2004) favoured SSC without excluding the possibility of pure synchrotron; Yuan et al. (2004) excluded the option of SSC on the basis of the required non-thermal to thermal electron fraction (the requirement would be too high). Goldston et al. (2005) found general agreement between their calculations using synchrotron emission with magneto-hydrodynamic (MHD) simulations and the observations; while Eckart et al. (2006a, 2008, 2012) showed agreement between their SSC calculations and the observations.

Yusef-Zadeh et al. (2006, 2008) argued for IC and against synchrotron emission, but Liu et al. (2006) reopened the hypothesis of pure synchrotron, which was supported by Nishiyama et al. (2009). Marrone et al. (2008) found agreement of observations with calculations of an expanding emission region by SSC. Dodds-Eden et al. (2009) found it difficult to quantitatively explain a particular bright X-ray flare with IC processes, and instead found synchrotron emission more viable; Barrière et al. (2014) also found that a pure synchrotron model was preferred to the SSC alternative. Boyce et al. (2019) supported the SCC process but pointed out that it was not clear whether all X-ray flares were produced by the same mechanism. Fazio et al. (2018)

and Michail et al. (2021a) found that the data was consistent with an expanding synchrotron plasma model. Other relevant studies include e.g. Zhang et al. (2017); Fazio et al. (2018); Boyce et al. (2022).

Despite the different opinions on the radiative process responsible for the flares, it is indisputable that very energetic particles must be present. As such, another large field of research with regards to the flaring activity in the Galactic Centre is the investigation of possible energising mechanisms to accelerate the emitting particles.

ii) Origin of the energetic particles

In order to explain the observed flares, one needs a mechanism capable of accelerating the particles to the required high energies while, simultaneously, doing so on a compact spatial region.

Yuan et al. (2003) performed magneto-hydrodynamic (MHD) simulations of radiatively inefficient accretion flows (RIAFs) and found a highly time-dependent dissipation of magnetic energy. This raised the hypothesis that solar flare-like acceleration events might happen in the vicinity of the black hole, giving rise to the flares. Liu et al. (2004) performed simulations using an acceleration mechanism inspired by the solar flare model (plasma wave turbulence) and saw the creation of IR flares accompanying X-ray bursts, as seen in observations. Chan et al. (2009) found that MHD turbulence by itself was not enough to produces flares of the magnitudes observed and suggested that other physical processed would be necessary to explain them.

With this information, Yuan et al. (2009) proposed that the flares could be energised by magnetic reconnection, in a way similar to the production of solar flares. These could be accompanied by the formation of a blob of plasma (or a *plasmoid*), similar to the process that causes coronal mass ejections (CMEs) in the Sun.

Following this proposal, several groups performed MHD and GRMHD (General relativistic magneto-hydrodynamic) simulations to investigate whether magnetic reconnection would occur in the black hole's accretion environment. Dodds-Eden et al. (2010) found that magnetic reconnection may occur neat the innermost stable circular orbit around the black hole in time scales consistent with those of the observed flares. Masada et al. (2010) and Uzdensky (2011) investigated the role of extreme gravity and magnetic fields to understand the differences between magnetic reconnection in such extreme systems and the Sun.

The scenario proposed by Yuan et al. (2009) was developed into a more concrete MHD model for Sgr A* flares by Li et al. (2017), who were able to reproduce the broad light curve and spectral properties of IR and X-ray flares, despite not being able to reproduce the temporal asymmetries of the light curves. Chael et al. (2018) performed GRMHD simulations with and

without magnetic reconnection and unable to replicate the large flares observed with thermal electrons only, indicating a need to include non-thermal electrons in the models. These were included in simulations by Chatterjee et al. (2021), who indeed found an agreement between the flares resulting from their calculation and the constraints on the flares provided by multi-band observations.

The simulations from Ripperda et al. (2020) and Dexter et al. (2020) indicated that magnetic reconnection events can take place in magnetically arrested disks, with the former showing the formation of hot spots which could be responsible for the energetics of the Sgr A* flares and the latter finding an agreement of the calculated light curves and sky motion of the emitter with the observations of IR flares. Murchikova and Witzel (2021) also reported that magnetic reconnection was likely the cause of large NIR flares.

The GRMHD simulations performed by Nathanail et al. (2022) demonstrated the formation of plasmoids associated with magnetic reconnection events very close to the event horizon. Ripperda et al. (2022) found similar results and noticed that the escaped plasmoids could last a full orbit as hot spots, agreeing with the observations from Sgr A*.

All of these studies indicate that magnetic reconnection is expected to occur in the vicinity of black holes and, similarly to what happens in the sun, it may give rise to the formation of plasmoids.

iii) Emitting region properties

The timing of the flares constrain the emitting region to be small. For instant, the changes in the NIR flux from Sgr A* on timescales $\Delta t \lesssim 45$ s (Eckart et al., 2012) place an upper-bound on the spatial size of the flaring region to be $[c]\Delta t \lesssim 2.2\ r_{\rm g}$ (neglecting the effects gravitational lensing and other relativistic effects). This upper bound is consistent with the more recent constraint of $[c]\Delta t \lesssim 5\ r_{\rm g}$, obtained from the modelling of near-IR flares detected by the GRAVITY instrument (GRAVITY Collaboration et al., 2020a). Similarly, assuming mm-wavelength flares are connected to IR and X-ray flaring events, the observed adiabatic expansion velocities of the radio components (typically $\sim 10^{-2}$ $[c]$) and the observed durations of these multi-wavelength flares ($\sim$20 mins – 1 hr), when combined imply a minimum flaring region size of $[c]\Delta t \gtrsim 0.5\ r_{\rm g}$ (Eckart et al., 2012).

This, together with the shape of the light curves, suggest that the compact region is on an orbit around the black hole. The solar magnetic reconnection and plasmoid model discussed in the previous section, which is supported by the results from MHD simulations which show the potential formation of such plasmoids is consistent with such a small orbiting emitting region. Further details and references regarding the emitting region properties are provided in section 3.1.

1.3 Overview of radiation and particle transport

Astrophysics is, at its core, an observational science. Historically, it has relied mostly on observations of electromagnetic radiation. These consist of the detection of photons from far away sources and in the measurement of their properties, such as intensity, frequency/energy, direction and polarization, in order to understand both their source and the media through which they propagated. Radiative transport (also referred to as radiation transfer/transport) is a tool which allows astrophysicists to calculate how radiation propagates between it's emission and detection sites. It consists of an equation which takes into account the different phenomena that radiation is subject to along it's path, e.g. emission, absorption, polarization changes and scattering.

With the development of new instrumentation technologies, non-photonic *messengers* started to be used to gather information about the universe. These include particles (e.g. neutrinos) and, since more recently, gravitational waves. Given the importance of the role played by these new messengers, in particular non-photonic particles, in modern astrophysics, it became important to have a formulation of radiation transport that could also deal with radiation in the form of particles other than photons. Such a formulation is developed in chapter 2. Below is a summary of the classical ways in which radiation and particle transport are usually dealt with.

1.3.1 Radiative transport

i) Geometrical optics approximation

The classical radiative transfer equation deals with the propagation of electromagnetic radiation in the framework of *geometrical optics*. In this framework, which also referred to as the *eikonal* approximation, the propagation of light is considered to occur as *rays* rather than waves in the electric and magnetic fields. Rays are conceptually constructed "lines" tangent to the direction of propagation of the electromagnetic wave (Rybicki and Lightman, 1979). The propagation laws resulting from this simplification are valid as long at the wave can be locally approximated by a planar and monochromatic wave. As such, geometric optics is always true to plane waves. Other types of wave (and waves propagating in in-homogeneous media) can only be considered approximately planar if the deviations from planarity occur in length and time scales respectively much larger than the wavelength and period of the wave, respectively (see chapter 7 of Thorne and Blandford, 2017, for a rigurous proof of this limit).

The systems of interest to this thesis are massive nuclear black holes. One can take the radius of the event horizon to be the smallest in-homogeneity length scale in the system. For a black hole such as Sgr A*, this radius is approximately 13×10^6 km and the time it takes for light to cross

it is 42s[4], both of which are much larger than the wavelength or period of any electromagnetic radiation that can be realistically detected on earth. As such, this approximation is valid for the systems dealt with in this thesis.

The exposition in this section follows that in Rybicki and Lightman (1979).

Consider a bundle of photons with frequency within $d\nu$ of ν moving along nearly the same trajectory (a *ray*) and reaching some detector of area $\mathrm{d}A$ from some a direction within a solid angle $d\Omega$. The specific intensity I_ν is defined as the energy crossing that area from that solid angle by photons of that frequency per unit time, i.e.:

$$I_\nu \coloneqq \frac{\mathrm{d}E}{\mathrm{d}A\ \mathrm{d}t\ \mathrm{d}\Omega\ \mathrm{d}\nu}. \tag{1.1}$$

In vacuum, the specific intensity of a bundle of photons is conserved along a ray. This is a result of energy conservation, as can be seen by the following simple argument presented in (Rybicki and Lightman, 1979, section 1.4):

Considers two areas normal to the propagation of a ray at different locations, $\mathrm{d}A_1$ and $\mathrm{d}A_2$, stationary with respect to each other at a distance R from one another. The solid angle from which the radiation through $\mathrm{d}A_1$ originated is given by Rybicki and Lightman (1979) $\mathrm{d}\Omega_1 = \mathrm{d}A_2/R^2$, and similarly $\mathrm{d}\Omega_2 = \mathrm{d}A_1/R^2$.

The energy going through them in a time interval t is given by $\mathrm{d}E_1 = I_{\nu,1}\mathrm{d}A_1\ \mathrm{d}t\ \mathrm{d}\Omega_1\ \mathrm{d}\nu_1$ and $\mathrm{d}E_2 = I_{\nu,2}\mathrm{d}A_2\ \mathrm{d}t\ \mathrm{d}\Omega_2\ \mathrm{d}\nu_2$, respectively, where $I_{\nu,i}$ is the specific intensity through the area $\mathrm{d}A_i$. By energy conservation, the energy carried by rays going through both surfaces must be the same at both surfaces, i.e. $\mathrm{d}E_1 = \mathrm{d}E_2$. For the same frequency interval $\mathrm{d}\nu$ around ν, we must have $I_{\nu,1}\mathrm{d}A_1\ \mathrm{d}t\ \mathrm{d}A_2/R^2\ \mathrm{d}\nu = I_{\nu,2}\mathrm{d}A_2\ \mathrm{d}t\ \mathrm{d}A_1/R^2\ \mathrm{d}\nu \Rightarrow I_{\nu,1} = I_{\nu,2}$ along the ray. In other words, if s denotes distance travelled along the ray, one must have that

$$\frac{\mathrm{d}I_\nu}{\mathrm{d}s} = 0. \tag{1.2}$$

If the ray goes through some medium, however, energy can be added to (by emission or scattering into the ray) or removed from (by absorption or scattering out of the ray) the ray, changing its specific intensity. For the purpose of this thesis, no scattering is considered. Emission can be split into two different types: spontaneous and stimulated emission. Since stimulated emission depends on the incident radiation, it is treated together with absorption. The spontaneous emissivity coefficient j_ν is defined as the energy emitted spontaneously per unit volume $\mathrm{d}V$ per

[4] Assuming a black hole mass of $4.297 \times 10^6 M_\odot$.

unit time $\mathrm{d}t$ per solid angle $\mathrm{d}\Omega$ per frequency range $\mathrm{d}\nu$, i.e. $j_\nu = \mathrm{d}E^{\mathrm{em}}/(\mathrm{d}V\mathrm{d}\Omega\mathrm{d}\nu\mathrm{d}t)$. So the intensity added to a bundle of cross section $\mathrm{d}A$ travelling a distance $\mathrm{d}s$ through an emitting medium (i.e. travelling through a volume $\mathrm{d}V = \mathrm{d}A\mathrm{d}s$) is given by

$$\mathrm{d}I_\nu{}^{\mathrm{em}} = \frac{\mathrm{d}E^{\mathrm{em}}}{\mathrm{d}A\ \mathrm{d}t\ \mathrm{d}\Omega\ \mathrm{d}\nu} = j_\nu \mathrm{d}s. \tag{1.3}$$

The absorption coefficient α_ν is defined as the fraction of intensity lost when traveling a certain distance through a medium, i.e.

$$\mathrm{d}I_\nu{}^{\mathrm{abs}} = -\alpha_\nu I_\nu \mathrm{d}s \tag{1.4}$$

As mentioned above, one can include stimulated emission in this term by splitting α_ν into two terms: one positive, corresponding to the true absorption which removes intensity from the bundle, $\alpha_\nu^{\mathrm{abs}}$; and one negative, which incorporates the role of stimulated emission, adding intensity to the bundle, α_ν^{em}. Hence $\alpha_\nu = \alpha_\nu^{\mathrm{abs}} + \alpha_\nu^{\mathrm{em}}$ can be positive or negative, depending on the relative strength of the true absorption and stimulated emission processes.

ii) The radiative transfer equation

Since, by equation (1.2), the intensity in vacuum remains constant along a ray, the only changes in intensity (in the absence of scattering) are those due to emissivity and absorption of the medium through which the ray propagates, i.e. $\mathrm{d}I_\nu = \mathrm{d}I_\nu{}^{\mathrm{em}} + \mathrm{d}I_\nu{}^{\mathrm{abs}}$. So, the change in intensity along a ray is given by the *classical transfer equation*:

$$\frac{\mathrm{d}I_\nu}{\mathrm{d}s} = -\alpha_\nu I_\nu + j_\nu \tag{1.5}$$

$$\Leftrightarrow \frac{\mathrm{d}I_\nu}{\mathrm{d}\tau_\nu} = -I_\nu + S_\nu \tag{1.6}$$

where the *optical depth*

$$\tau_\nu(s) \coloneqq \int_0^s \mathrm{d}s' \alpha_\nu(s') \tag{1.7}$$

and the *source function*

$$S_\nu \coloneqq \frac{j_\nu}{\alpha_\nu} \tag{1.8}$$

were introduced. Using an integrating factor, the solution to this equation can be readily found to be (Rybicki and Lightman, 1979):

$$I_\nu(s) = I_\nu(0)\mathrm{e}^{-\tau_\nu(s)} + \int_0^s \mathrm{d}s'\, j_\nu(s')\mathrm{e}^{-(\tau_\nu(s)-\tau_\nu(s'))} \Leftrightarrow \tag{1.9}$$

$$I_\nu(\tau_\nu) = I_\nu(0)\mathrm{e}^{-\tau_\nu} + \int_0^{\tau_\nu} \mathrm{d}\tau'_\nu \; S_\nu(\tau'_\nu)\mathrm{e}^{-(\tau_\nu - \tau'_\nu)}. \tag{1.10}$$

Equation (1.10) is known as the *formal solution of the transfer equation*. This equation is not covariant[5] , as some of its terms depend on frequencies, times and areas, all of which are frame dependent. This is the basic equation which is generalized, in a covariant manner, to massive particles in section 2.

1.3.2 Boltzmann equation for particle transport

The exposition in this subsection follows that in Thorne and Blandford (2017).

Of one the simplest ways of studying the behaviour of large numbers of particles, including the energy carried by them, is provided by *kinetic theory*. The main object of kinetic theory is that of *distribution function* or *phase-space density*, i.e. the density of particles in a certain phase-space volume.

The Boltzmann transport equation, which forms the basis of the covariant formalism for radiation transport, describes the conservation laws associated with this distribution function.

i) Phase-space density and conservation laws

Relativistic phase-space is a 7-dimensional space comprised of 4-dimensional spacetime together with the 4-dimensional relativistic momentum space, constrained to the 3-dimensional mass hyperboloid[6]. An inertial observer can, at any time t, consider a spacetime volume $\mathrm{d}\mathcal{V} = \mathrm{d}\mathcal{V}_x \mathrm{d}\mathcal{V}_{\boldsymbol{p}}$, where $\mathrm{d}\mathcal{V}_x = \mathrm{d}x\,\mathrm{d}y\,\mathrm{d}z$ is a small spatial 3-volume element at time t around some event and $\mathrm{d}\mathcal{V}_{\boldsymbol{p}} = \mathrm{d}p_x\,\mathrm{d}p_y\,\mathrm{d}p_z$ is a small 3-volume element in momentum space centered at relativistic momentum $\boldsymbol{p}$. Then, if $\mathrm{d}\mathcal{N}$ is the number of particles lying in that, the *phase-space density* of particles is defined as

$$\mathcal{F} := \frac{\mathrm{d}\mathcal{N}}{\mathrm{d}\mathcal{V}}. \tag{1.11}$$

[5]Throughout this thesis, *covariant* is used to refer to quantities which are Lorentz scalars, i.e. which are the same in any observer frame, and to equations whose form remains unchanged in any frame (also known as tensor equations). *Invariant*, on the other hand, is used to refer to quantities which remain constant. Quantities may be covariant and not invariant (i.e. all observer agree with their value, but that value is changing), invariant and not covariant (i.e. observer disagree on its value but agree that it is unchanging), covariant and invariant or neither.

[6]Recall that, in special and general relativity, the 4-momentum of a particle of mass m is constrained by the fact that $p \cdot p = -m^2$. This constraint corresponds to constraining the particle's momentum to lie on a 3-dimensional hyper-surface of momentum space where $p \cdot p = -m^2$. This is known as the mass hyperboloid. This is true for both massive and massless particles.

Although the definition above uses a particular inertial observer, it is a standard result that both $\mathrm{d}\mathcal{N}$ and $\mathrm{d}\mathcal{V}$ are covariant (see e.g. Misner et al. (1973) pages 585-587 or Thorne and Blandford (2017) chapter 3). This means that $\mathcal{F}$ also is covariant, i.e. it has the same value regardless of the frame in which it is measured.

The key conservation law with respect to phase-space density is given by *Liouville's theorem*. Consider a phase-space volume $\mathrm{d}\mathcal{V}$ around a fiducial particle, small enough that the world lines of those particles remain very close to the of the fiducial particle. Liouville's theorem states that, given some parameter l along the fiducial particle's world line[7], the phase-space volume occupied by these particles remains constant. I.e.

$$\frac{\mathrm{d}\mathcal{V}}{\mathrm{d}l} = 0. \tag{1.12}$$

In the absence of non-gravitational interactions, the number of particles in $\mathrm{d}\mathcal{V}$ does not change. As such, Liouville's theorem implies that the phase-space density $\mathcal{F}$ also remains constant along that world line. This is known as the *collisionless Boltzmann equation*:

$$\frac{\mathrm{d}\mathcal{F}}{\mathrm{d}l} = 0. \tag{1.13}$$

The collisionless Boltzmann equation implies that, in the presence of collisions, any changes in phase-space density must be due to those collisions, i.e.

$$\frac{\mathrm{d}\mathcal{F}}{\mathrm{d}l} = \left(\frac{\mathrm{d}\mathcal{F}}{\mathrm{d}l}\right)_{\mathrm{col}}. \tag{1.14}$$

This is known as the *Boltzmann transport equation*. In this thesis, we do not consider general collisions (e.g. no scattering, energy re-distribution or polarization changing phenomena are considered). The types of collision considered here are effectively interactions in which radiation is emitted or absorbed. So we restrict $\left(\frac{\mathrm{d}\mathcal{F}}{\mathrm{d}l}\right)_{\mathrm{col}}$ to $\left(\frac{\mathrm{d}\mathcal{F}}{\mathrm{d}l}\right)_{\mathrm{int}}$, where "int" refers to interactions where line-of-sight absorption or emission takes place.

ii) Phase-space density and covariant intensity for photons

The covariance of phase-space density makes it a very useful object to study when transporting radiation. The whole covariant radiative transport formulation described in chapter 2 is in fact based on a quantity very closely related to it: the *covariant intensity*.

Consider a system of photons with phase-space density $\mathcal{F}$. In spherical coordinates, the momentum-space volume $\mathrm{d}\mathcal{V}_{\boldsymbol{p}}$ can be written as $\mathrm{d}^3\boldsymbol{p} = |\boldsymbol{p}|^2\ \mathrm{d}|\boldsymbol{p}|\ \mathrm{d}\Omega$, where $\mathrm{d}\Omega = \mathrm{d}\theta + \sin^2(\theta)\mathrm{d}\phi$ is the solid angle element spanned by $\mathrm{d}\mathcal{V}_{\boldsymbol{p}}$.

[7] The world line is the particle's trajectory in four-dimensional spacetime.

Now consider the spatial volume occupied by all photons which can go through a surface of area $\mathrm{d}A$ orthogonal to the direction of propagation. These photons must be within a distance $c\,\mathrm{d}t$ of the surface, so the spatial volume occupied by them is[8] $\mathrm{d}\mathcal{V}_x = ([c]\,\mathrm{d}t)\,\mathrm{d}A$.

In this system, the number of photons with momentum within $\mathrm{d}|\boldsymbol{p}|$ of $|\boldsymbol{p}|$ going through this surface of area $\mathrm{d}A$ in time $\mathrm{d}t$ is then given by

$$\mathrm{d}\mathcal{N}_{|\boldsymbol{p}|} = \mathcal{F}\,([c]\,\mathrm{d}t)\,\mathrm{d}A\,|\boldsymbol{p}|^2\,\mathrm{d}|\boldsymbol{p}|\,\mathrm{d}\Omega \tag{1.15}$$

where the subscript $|\boldsymbol{p}|$ was added to emphasise the dependency of $\mathrm{d}\mathcal{N}$ on the photon's momentum. The photon's momentum is given by $\boldsymbol{p} = \hat{\boldsymbol{n}}\,h\nu/[c]$, where $\hat{\boldsymbol{n}}$ is the unit vector pointing in the direction of propagation. This, in turn, can be related to the its energy $\mathcal{E}_\nu = h\nu$, where the subscript ν was added to emphasise the dependency of $\mathcal{E}$ on ν. So the number of photons in the phase-space volume $\mathrm{d}\mathcal{V}$ can be written as a function of photon frequency as

$$\mathrm{d}\mathcal{N}_\nu = \mathcal{F}\left(\frac{h\nu}{[c]}\right)^2([c]\,\mathrm{d}t)\,\mathrm{d}A\,\frac{h\mathrm{d}\nu}{[c]}\,\mathrm{d}\Omega \tag{1.16}$$

The total energy going through the surface due to photons with energy $\mathcal{E}_\nu = h\nu$ is the photon energy times the number of photons with that energy, i.e.

$$\begin{aligned}\mathrm{d}E &= \mathcal{E}_\nu\,\mathrm{d}\mathcal{N}_\nu \\ &= (h\nu)\,\mathcal{F}\left(\frac{h\nu}{[c]}\right)^2([c]\,\mathrm{d}t)\,\mathrm{d}A\,\frac{h\mathrm{d}\nu}{[c]}\,\mathrm{d}\Omega \\ &= \frac{h^4}{[c^2]}\,\nu^3\,\mathcal{F}\,\mathrm{d}A\,\mathrm{d}t\,\mathrm{d}\nu\,\mathrm{d}\Omega\end{aligned} \tag{1.17}$$

By comparing this to the definition of I_ν (equation (1.1)), the relationship between intensity and phase-space density becomes clear:

$$I_\nu = \left(\frac{h^4}{[c^2]}\right)\nu^3\,\mathcal{F}. \tag{1.18}$$

Since $\mathcal{F}$ is covariant and $h^4/[c^2]$ is a constant, we can define a covariant quantity, $\mathcal{I}_\nu$, known as the *covariant intensity*, as:

$$\mathcal{I}_\nu := \frac{I_\nu}{\nu^3} = \left(\frac{h^4}{[c^2]}\right)\mathcal{F}. \tag{1.19}$$

This is the quantity that is transported in the general relativistic radiation transport formulation

[8] Throughout this thesis, geometrical units will be used, where $G = c = 1$. However, in order to make the physical meaning of the expressions clearer, factors of c and G are printed in most equations inside square brackets. To perform calculations in geometrical units one must simply set the terms in square brackets to 1.

described in chapter 2. Bolzmann's equation can then be written in terms of the covariant intensity as

$$\frac{\mathrm{d}\mathcal{I}_\nu}{\mathrm{d}l} = \left(\frac{\mathrm{d}\mathcal{I}_\nu}{\mathrm{d}l}\right)_{\mathrm{int}} . \tag{1.20}$$

1.3.3 Classical radiative transfer and Boltzmann's transport equation

The classical radiative transfer equation (1.5) can be seen as a particular case of Boltzmann's transport equation valid only in a specific frame. A frame-dependent version of equation (1.20) can be written as

$$\frac{\mathrm{d}I_\nu}{\mathrm{d}l} = \left(\frac{\mathrm{d}I_\nu}{\mathrm{d}l}\right)_{\mathrm{int}} . \tag{1.21}$$

In that particular frame, the collisions (or interactions) that the bundle of rays is subject to are, in the absence of scattering, those which cause emission or absorption of radiation. Then, the right hand side of equation (1.5) corresponds to the collision term, where the collisions are measured in that particular frame, i.e. $(\mathrm{d}I_\nu/\mathrm{d}l)_{\mathrm{col}} = -\alpha_\nu I_\nu + j_\nu$. As such, equation (1.5) can be viewed as a frame-specific version of the Boltzmann transport equation (1.20) in the absence of scattering, where the collision terms are represented by the phenomenological quantities α_ν and j_ν.

1.4 Thesis outline

This thesis is organised as follows. In chapter 2 we derive the general relativistic radiation transport (GRRT) formalism developed during this PhD for both massive and massless particles. We also introduce the algorithm written to use the given formalism in astrophysical contexts in the presence of Schwarzschild or Kerr black holes (the largest portion of this PhD), as well as some of the code validation exercises that were performed.

In chapter 3 we apply the GRRT formalism to the concrete scenario of flares in the vicinity of black holes. In this chapter we make use of the massless GRRT formalism, reproduce some results from literature which validate the correct working of the code and explore the novel idea of how a time-dependent emissivity affects the observations of flares at different energy bands.

Finally, in chapter 4 we showcase the potentialities of the GRRT formalism for massive particles by performing some calculations for a simplified emission and absorption model inspired by potential astrophysical situations. We conclude our work in chapter 5.

Chapter 2

General relativistic radiation transport formalism

The fundamental tool used in this thesis for studying astrophysical systems is radiation transport. In section 1.3 the classic radiation transport formalism was introduced. In this section, a fully covariant formulation of the same equations is presented. Such a formulation is particularly useful when transporting radiation to and from systems which are highly relativistic or live in strong gravitational fields. In general, as a photon propagates through a certain medium, in order to calculate the absorption and emission at each point, one must constantly transform all these observer dependent quantities into a new frame. This is tricky and prone to errors. Instead, the idea presented in this chapter is to perform the transport using solely covariant quantities, i.e. quantities which are not observer dependent. At the end, these are transformed into observer-dependent quantities. This formalism has another advantage: it is valid for both massless particles (such as photons), and massive particles (such as protons). We treat the motion of both massive and massless particles as following geodesics. For realistic massive particles, which have spin, this is a simplification which neglects the spin-orbit coupling interaction, which results in a non-geodesic motion. Assessing the degree to which this impacts the particle trajectory for the particle energies and the particle to black hole mass ratios presented in this thesis is beyond the scope of this work. Since the spacetimes considered here are not charged, magnetic fields are neglected and the particles are treated classically, their charge will not impact their trajectories.

The formalism, therefore, consists of solving the covariant form of the radiation transport equations along geodesics. As such, the algorithm has two key steps, which are described in detail in this chapter. First, one needs to solve the geodesic equations to find the trajectories followed by the individual particles. When we talk about the intensity of a ray/ intensity along a geodesic, we are referring to the collection of all particles travelling along the same geodesic. This step will be referred to as *ray tracing* and it is explained in detail in section 2.1. Then, the covariant radiation transport equations are integrated along the particle geodesics. The equations relate to a generalized notion of covariant intensity applicable to both massless and

massive particles, defined in section 2.2. The formalism derivation and algorithm are both presented in section 2.3.

2.1 Geodesics

2.1.1 Tangent vectors and connections

The exposition in this subsection follows that in Hull (2020).

Throughout this thesis, *spacetime* $(\mathcal{M}, g)$ refers to a 4-dimensional, time-oriented smooth manifold $\mathcal{M}$ equipped with a smooth metric g, which is a solution to Einstein's equations.

Tangent vectors can be viewed as *directional derivatives*[1] of functions: given a curve $\mathcal{C} : \lambda \in \mathbb{R} \to \mathcal{C}(\lambda) = p \in \mathcal{M}$, a set of coordinates $\{x^\mu\}$ in the neighbourhood[2] of p and a function $f : p \in \mathcal{M} \to \iota \in \mathbb{R}$, the *tangent vector* V_p to the curve $\mathcal{C}(\lambda)$ at $p = \mathcal{C}(\lambda_0)$ measures the directional change of the function f along the curve:

$$V_p[f] = \frac{\mathrm{d}}{\mathrm{d}\lambda}\left(f \cdot \mathcal{C}(\lambda)\right)\Big|_{p=\mathcal{C}(\lambda_0)} = \frac{\mathrm{d}}{\mathrm{d}\lambda}\, x^\mu(\mathcal{C}(\lambda))\Big|_{\lambda_0} \frac{\partial}{\partial x^\mu} f(x)\Big|_{x(p)} \tag{2.1}$$

The set of all tangents vectors at p form the *tangent space* $\mathcal{T}_p(\mathcal{M})$, and is it isomorphic to the vector space $\mathbb{R}^4$. As such, any vector $V_p \in \mathcal{T}_p(\mathcal{M})$ can be written as linear combination of basis vectors at p, $\boldsymbol{e}_{(p)}$, as $V_p = v^\mu \boldsymbol{e}_{(p)\mu}$. $V_p[f]$ can be re-written as

$$V_p[f] = v^\mu \boldsymbol{e}_{(p)\mu}[f] \tag{2.2}$$

Although the definition of V_p is coordinate independent, the calculations in these thesis are all performed in particular coordinate systems. As such, it is useful to refer to vectors in a coordinate way. By comparing equations (2.1) and (2.2), one can consider $\partial/\partial x^\mu$ as a basis for the vector space $\mathcal{T}_p(\mathcal{M})$. Such a basis, where basis vectors are given by

$$\boldsymbol{e}_{(p)\mu} = \partial/\partial x^\mu|_p \tag{2.3}$$

[1] Tangent vectors are originally defined as equivalent classes of tangent curves. Two curves $\mathcal{C}$ and $\mathcal{C}'$ at p are considered equivalent if they are *tangent* to each other. I.e. if $\frac{\mathrm{d}}{\mathrm{d}\lambda}\mathcal{C}(\lambda)\big|_{p=\mathcal{C}(\lambda_0)} = \frac{\mathrm{d}}{\mathrm{d}\sigma}\mathcal{C}'(\sigma)\big|_{p=\mathcal{C}'(\sigma_0)}$. The equivalence class of all curves tangent to each other at a point p is a tangent vector at p. The space of all tangent vectors at p, i.e. all equivalence classes of tangent curves, forms the tangent space at p, $\mathcal{T}_p(\mathcal{M})$. The term directional derivative comes from the fact that the derivative depends only on the rate of change of a function in some direction at a particular point, without the need to recur to other points in the manifold.

[2] One can always define coordinates in *coordinate charts*, i.e. portions of the manifold where the same set coordinates make sense, such that in the intersection between charts the coordinate transformations are smooth. Hence defining coordinates in the neighbourhood of a point is sensible.

is called the *coordinate basis*. The components of the tangent vector are then given by (see equation (2.1)):

$$v^\mu = \frac{\mathrm{d}}{\mathrm{d}\lambda}\, x^\mu(\mathcal{C}(\lambda))\bigg|_{\lambda_0}. \tag{2.4}$$

v^μ are components of a vector in $\mathbb{R}^4$ and only depend on the equivalence class of curves, not on the particular choice of curve. It is important to keep in mind that each tangent vector (including the basis vectors) lives in the tangent space at a particular point in spacetime.

The vector space dual to the tangent space is called the co-tangent space $\mathcal{T}_p^*\mathcal{M}$, and elements of this space, co-tangent vectors (or co-vectors), can be thought of as linear maps $\omega_p : v_p \in \mathcal{T}_p\mathcal{M} \to \omega_p(v_p) \in \mathbb{R}$. Given a basis $\{\boldsymbol{e}_\mu\}$ for $\mathcal{T}_p\mathcal{M}$ and a dual basis $\{\boldsymbol{e}^\mu\}$ for $\mathcal{T}_p^*\mathcal{M}$, we write $\omega_p(v_p) = \omega_\mu v^\mu$, where $\omega_p = \omega_\mu \boldsymbol{e}_{(p)}{}^\mu$ and $v_p = v^\mu \boldsymbol{e}_{(p)\mu}$.

Tensors are generalizations of these concepts, with an (r, s) tensor being a linear function on r vectors and s co-vectors, i.e $A_p : \mathcal{T}_s{}^r(\mathcal{M}) = \mathcal{T}_p\mathcal{M} \times ... \times \mathcal{T}_p^*\mathcal{M} \times ... \to \mathbb{R}$. The components of the tensor A_p in a certain basis $\{e_\mu\}$ and dual basis $\{e^\mu\}$ are given by $A_p(e_{\mu_1}, ..., e_{\mu_s}, e^{\nu_1}, ..., e^{\nu_r})$

We defined vectors as directional derivatives of functions. It is also useful to define some sort of directional derivative of vectors and tensors. This requires the notion of an *affine connection* (or just *connection*). A connection is a bi-linear map $\nabla : (X, Y) \in \mathcal{T}_0{}^1(\mathcal{M}) \times \mathcal{T}_0{}^1(\mathcal{M}) \to \nabla_X Y \in \mathcal{T}_0{}^1(\mathcal{M})$ defined by its action on basis vectors:

$$\nabla_\mu \boldsymbol{e}_\nu \coloneqq \nabla_{\boldsymbol{e}_\mu} \boldsymbol{e}_\nu = \Gamma_{\mu\nu}{}^\alpha \boldsymbol{e}_\alpha, \tag{2.5}$$

and $\Gamma_{\mu\nu}{}^\alpha$ are the connection components. This connection is chosen so that it has certain properties, namely:

$$\begin{aligned} \nabla_X(Y + Z) &= \nabla_X Y + \nabla_X Z \\ \nabla_{(X+Y)} X &= \nabla_X Z + \nabla_Y Z \\ \nabla_{(fX)} Y &= f \nabla_X Y \\ \nabla_X(fY) &= X[f]Y + f\nabla_X Y. \end{aligned} \tag{2.6}$$

Given these properties, one can work out the form of the connection for two general vectors in a coordinate chart, $X = X^\mu \boldsymbol{e}_\mu$, $Y = Y^\mu \boldsymbol{e}_\mu$:

$$\nabla_X Y = \nabla_{X^\mu \boldsymbol{e}_\mu}(Y^\nu \boldsymbol{e}_\nu) = X^\mu \left(\partial_\mu Y^\nu + \Gamma_{\mu\alpha}{}^\nu Y^\alpha\right) \boldsymbol{e}_\nu \tag{2.7}$$

Given a vector field $X \in \mathcal{T}_0^1$ and a tensor field $T \in \mathcal{T}_s^r$, one can define a covariant derivative $\nabla_X : T \in \mathcal{T}_s^r \to \nabla_X T \in \mathcal{T}_s^r$, whose explicit form is worked out by using the properties 2.6.

Given a manifold with a metric tensor g, one can define a particular type of connection called a *metric connection*. A metric connection is a connection for which $\nabla_X g = 0$, $\forall\, X \in \mathcal{T}(\mathcal{M})$, where $\mathcal{T}(\mathcal{M})$ space of all vector fields in $\mathcal{M}$ (i.e. all maps that smoothly assign a vector to each point in $\mathcal{M}$) .

2.1.2 Geodesics in Kerr spacetime

A curve parameterized by λ is a geodesic if its tangent vector u is parallel-transported along the curve, i.e.

$$\nabla_u u = 0 \tag{2.8}$$

where ∇ is an affine connection. In a coordinate basis, the components of the tangent vector can be written as $u = u^\mu \boldsymbol{e}_\mu = (\mathrm{d}x^\mu/\mathrm{d}\lambda)\boldsymbol{e}_\mu$. So, in coordinates, equation (2.8) becomes

$$\ddot{x}^\mu + \Gamma^\mu{}_{\nu\rho}\dot{x}^\nu \dot{x}^\rho = 0 \ , \tag{2.9}$$

where $\Gamma^\mu{}_{\nu\rho}$ are the connection components and the dot represents the derivative with respect to λ. It corresponds to four second order differential equations, one for each coordinate. The components of a metric connection can be decomposed into a symmetric part, the Christoffel connection (2.10), and an anti-symmetric part, formed by the components of a tensor called the *torsion tensor*. A torsion-free connection is therefore one for which all components of the torsion tensor vanish, and which is therefore symmetric. In general relativity we use the Levi-Civita connection, which is the unique torsion-free metric connection. This fixes it to be given precisely by the Christoffel connection:

$$C^\mu{}_{\nu\rho} = \frac{1}{2} g^{\mu\sigma} \left(\partial_\rho g_{\sigma\nu} + \partial_\nu g_{\sigma\rho} - \partial_\sigma g_{\nu\rho}\right) \ . \tag{2.10}$$

Here, ∂_ρ is the partial derivative with respect to x^ρ, i.e. $\partial_\rho \equiv \partial/\partial x^\rho$.

As such we will always take $\Gamma^\mu{}_{\nu\rho}$ in equation (2.9) to be given by equation (2.10). We will refer to them as "Christoffel symbols", as they are usually referred to in literature.

According to the stationary-action principle, in the absence of external forces, particles move through spacetime along curves of extremal length. The length of a curve in a spacetime with

a metric g is given by (Hull, 2020)[3]:

$$s = \int \mathrm{d}\lambda \sqrt{g_{\mu\nu} \frac{\mathrm{d}x^\mu}{\mathrm{d}\lambda} \frac{\mathrm{d}x^\nu}{\mathrm{d}\lambda}} \tag{2.11}$$

By treating the length s as an action with Lagrangian density $\mathcal{L}' = \sqrt{g_{\mu\nu}\dot{x^\mu}\dot{x^\nu}}$, it is easy to see that, for the Levi-Civita connection, geodesics are length maximizing curves which obey the Euler-Lagrange equations.

We next consider a Lagrangian $\mathcal{L} = (1/2) g_{\mu\nu}\dot{x^\mu}\dot{x^\nu}$, which leads to the same equations of motion as $\mathcal{L}'$. This Lagrangian is half of what is called the *line element*, since its square root is precisely the infinitesimal length which, once integrated, provides the length of the curve. If a spacetime is stationary, it is possible to find coordinates such that all the metric components are independent of the time coordinate. Similarly, if a spacetime is axisymetric, it is possible to find coordinates such that all the metric components are independent of ϕ. In such a coordinate system with $x^\mu = ([c]\, t, r, \theta, \phi)$, the Euler-Lagrange equations yield

$$\begin{aligned} \frac{\partial \mathcal{L}}{\partial([c]\,\dot{t})} &= C_t \ ; \\ \frac{\partial \mathcal{L}}{\partial \dot{\phi}} &= C_\phi \ , \end{aligned} \tag{2.12}$$

where C_t and C_ϕ are constants. Having two conserved quantities means that the four second order differential equations (2.9) may be simplified into two second order and two first order differential equations.

There is a third quantity which is a constant of motion along a geodesic. Since the geodesic equations are curves of extremal length, by definition we have that, for a geodesic, $\mathrm{d}/\mathrm{d}\lambda(g_{\mu\nu}\dot{x}^\mu\dot{x}^\nu) = 0$. Not only is this conserved along the geodesic, but it is also a covariant quantity, i.e. it is the same in any frame. By definition, the tangent vector of a null geodesic is null, so that $g_{\mu\nu}\dot{x}^\mu\dot{x}^\nu = 0$. For timelike geodesics, we consider a local Minkowski frame where the particle is at rest. In this frame, $\dot{x}^\mu = [c]\,(1, \mathbf{0})$, so that $g_{\mu\nu}\dot{x}^\mu\dot{x}^\nu = [c]\, g_{tt} = -[c]$. We can summarize this as

$$g_{\mu\nu}\dot{x}^\mu\dot{x}^\nu = \xi \ , \tag{2.13}$$

where $\xi = 0$ for massless particles (null geodesics) and $\xi = -1$ for massive particles (timelike geodesics) in geometrical units ($[c] = 1$).

[3]The length of a curve $\mathcal{C} : \lambda \in \mathbb{R} \to \mathcal{C}(\lambda) \in \mathcal{M}$ is found by considering the curve as an embedded 1D submanifold $\mathcal{N}$ of spacetime $\mathcal{M}$ with coordinate given by λ. The induced metric on this submanifold, $g_\mathcal{N}$, is the pull back on the spacetime metric i.e. $g_\mathcal{N} = g_{\mu\nu}(\mathrm{d}x^\mu/\mathrm{d}\lambda)(\mathrm{d}x^\nu/\mathrm{d}\lambda)$. The length of the curve is then the integral of the volume form on $\mathcal{N}$, $\Omega_\mathcal{N} = \sqrt{g_\mathcal{N}}$ over $\mathcal{N}$, i.e. $s = \int_\mathcal{N} \Omega_\mathcal{N}$.

In this thesis we consider Kerr spacetimes, which are stationary and axisymetric. In Boyer-Lindquist (BL) coordinates, where $x^\mu = ([c]t, r, \theta, \phi)$, the line element of a Kerr metric is given by

$$\begin{aligned} \mathrm{d}s^2 = g_{\mu\nu}\dot{x^\mu}\dot{x^\mu} = -\left(1 - \frac{r_\mathrm{s} r}{\Sigma}\right)[c^2]\,\mathrm{d}t^2 - \frac{2ar_\mathrm{s} r\sin^2\theta}{\Sigma}[c]\,\mathrm{d}t\,\mathrm{d}\phi + \frac{\Sigma}{\Delta}\mathrm{d}r^2 \\ + \Sigma\,\mathrm{d}\theta^2 + \left(r^2 + a^2 + \frac{r_\mathrm{s} r\, a^2}{\Sigma}\sin^2\theta\right)\sin^2\theta\,\mathrm{d}\phi^2\ , \end{aligned} \tag{2.14}$$

where the following quantities were introduced for convenience:

$$\begin{aligned} r_\mathrm{s} &= 2M\left[\frac{G}{c^2}\right] \text{ (the Schwarzschild radius)} \\ a &= \frac{J}{M[c]} \\ \Sigma &= r^2 + a^2\cos^2\theta \\ \Delta &= r^2 - r_\mathrm{s} r + a^2. \end{aligned} \tag{2.15}$$

Here, M is the mass of the black hole and J is its spin angular momentum. Since in practical calculations we use units such that $c = G = 1$, the explicit c and G metric dependencies is shown by leaving c and G in square brackets. The Schwarzschild line element is recovered by setting $J = 0$ in (2.14) and (2.15) above.

Later it will be convenient to think of the metric tensor as a matrix, which in BL coordinates is given by:

$$g = \begin{pmatrix} -\alpha^2 + {\beta_\phi}^2\gamma_{\phi\phi} & 0 & 0 & \beta_\phi\gamma_{\phi\phi} \\ 0 & \gamma_{rr} & 0 & 0 \\ 0 & 0 & \gamma_{\theta\theta} & 0 \\ \beta_\phi\gamma_{\phi\phi} & 0 & 0 & \gamma_{\phi\phi} \end{pmatrix} \tag{2.16}$$

with

$$\begin{aligned} \alpha &= \sqrt{\frac{\Sigma\Delta}{A}} \\ A &= (r^2 + a^2)^2 - a^2\Delta\sin^2\theta \\ \beta_\phi &= -\frac{r_\mathrm{s} r a}{A} \\ \gamma_{rr} &= \frac{\Sigma}{\Delta} \\ \gamma_{\theta\theta} &= \Sigma \\ \gamma_{\phi\phi} &= \frac{A\sin^2\theta}{\Sigma}. \end{aligned} \tag{2.17}$$

In Kerr spacetimes, the constants of motion along a geodesic - equations (2.12) - are given by:

$$C_t = g_{tt}([c]\,\dot{t}) + g_{t\phi}\dot{\phi} \tag{2.18}$$

$$C_\phi = g_{\phi\phi}\dot{\phi} + g_{\phi t}([c]\,\dot{t}). \tag{2.19}$$

One can find an explicit expression for C_ϕ in terms of C_t and $\dot{\phi}$ by eliminating $\dot{t}$ between equations (2.18) and (2.19). After some algebra, one finds that

$$C_\phi = \frac{(\Sigma\Delta\dot{\phi} - 2aMrC_t)\sin^2\theta}{\Sigma - 2Mr}\ . \tag{2.20}$$

Away from the event horizon, equation (2.18) can be rewritten as

$$[c]\dot{t} = \frac{g_{t\phi}\dot{\phi} - C_t}{g_{tt}}. \tag{2.21}$$

$\dot{t}$ can be substituted by this expression in equation (2.13), and hence one may solve for C_t:

$${C_t}^2 = \left(\frac{\Sigma - 2Mr}{\Sigma\Delta}\right)\left(\Sigma\dot{r}^2 + (\Sigma\Delta)\dot{\theta}^2 - \xi\Delta\right) + \Delta\sin^2\theta\dot{\phi}^2\ . \tag{2.22}$$

One can also substitute for $\dot{\phi}$ in equation (2.21) using (2.20) or for $\dot{t}$ using (2.22), to find the first order differential equations describing $\dot{t}$ and $\dot{\phi}$. The equations of motion are now described by two first order and two second order differential equations:

$$\dot{t} = C_t + \frac{2Mr}{\Sigma\Delta}\left[\left(r^2 + a^2\right)C_t - aC_\phi\right]\ ; \tag{2.23}$$

$$\begin{aligned}\ddot{r} = \frac{\Delta}{\Sigma}\Bigg\{ & \frac{M\left(\Sigma - 2r^2\right)}{\Sigma^2}\dot{t}^2 + \frac{(r-M)\Sigma - r\Delta}{\Delta^2}\dot{r}^2 \\ & + r\dot{\theta}^2 + \left[r + \left(\frac{\Sigma - 2r^2}{\Sigma^2}\right)a^2M\sin^2\theta\right]\sin^2\theta\dot{\phi}^2 \\ & - 2aM\sin^2\theta\left(\frac{\Sigma - 2r^2}{\Sigma^2}\right)\dot{t}\dot{\phi} + \frac{a^2\sin 2\theta}{\Delta}\dot{r}\dot{\theta}\Bigg\};\end{aligned} \tag{2.24}$$

$$\begin{aligned}\ddot{\theta} = \frac{1}{2\Sigma}\Bigg(\sin(2\theta)\Bigg\{ & \frac{2a^2Mr}{\Sigma^2}\dot{t}^2 - \frac{4aMr\left(r^2 + a^2\right)}{\Sigma^2}\dot{t}\dot{\phi} - \frac{a^2}{\Delta}\dot{r}^2 \\ & + a^2\dot{\theta}^2 + \left[\Delta + \frac{2Mr\left(r^2 + a^2\right)^2}{\Sigma^2}\right]\dot{\phi}^2\Bigg\} - 4r\dot{r}\dot{\theta}\Bigg)\ ;\end{aligned} \tag{2.25}$$

$$\dot{\phi} = \frac{2aMrC_t + (\Sigma - 2Mr)\,C_\phi\mathrm{cosec}^2\theta}{\Sigma\Delta}\ . \tag{2.26}$$

These can be split into 6 first order differential equations, which is how our code performs the

numerical integration.

Kerr spacetime admits a fourth constant of motion along geodesics. This is the Carter constant, $\mathcal{Q}$, given by:

$$\mathcal{Q} = \Sigma^2\dot{\theta}^2 + \left[{C_\phi}^2\mathrm{cosec}^2\theta - a^2\left({C_t}^2 + \xi\right)\right]\cos^2\theta \tag{2.27}$$

The meaning of Carter's constant has been discussed in several papers (e.g. de Felice and Preti, 1999; Rosquist et al., 2009) since it was discovered in Carter (1968). In the limit of $a \to 0$, it corresponds to the total angular momentum of the particle minus its component in the z direction; in the weak field limit ($G \to 0$) it is a combination of the total angular momentum excluding it's component in the z direction and a term quadratic in the linear momentum in the same direction. This constant is a result of the existence of a $(2,0)$ Killing tensor field in Kerr spacetime (see section 2.1.2.i).

C_t and C_ϕ are calculated using the initial conditions of each geodesic. It is those values, as calculated from the initial conditions, which are used in the integration of the geodesic equations (2.23)-(2.26). In order to evaluate the error in the integration, C_t and C_ϕ are also calculated independently at each integration step using equations (2.18) and (2.19), and their value is compared to the initial value. Since only the initial value is used in the integration, this provides an independent error estimation of the geodesic integration.

i) Killing tensor fields and Carter's constant

A Killing tensor field is a generalization of a Killing vector field. A vector field X is a Killing vector field if the Lie derivative $\mathcal{L}$ of the metric with respect to X is zero, i.e.

$$\mathcal{L}_X g = 0, \tag{2.28}$$

where the lie derivative of a tensor field A with respect to a vector field X with flow $\sigma_X(\lambda)$ for some parameter λ is defined as

$$\mathcal{L}_X A|_p \coloneqq \lim_{\epsilon\to\infty}\left(\frac{\sigma(\epsilon)^* A|_{p'} - A|_p}{\epsilon}\right). \tag{2.29}$$

Here $p' = \sigma(\epsilon)$, and $\sigma(\epsilon)^*A$ is the pullback of the tensor A at p to p'. This means that the metric does not change along the flow defined by X which indicates some symmetry of the metric. This definition implies that Killing vectors satisfy Killing's equation:

$$\nabla_\mu X_\nu + \nabla_\nu X_\mu = 0 \tag{2.30}$$

The quantities given by $X_\mu u^\mu$ are conserved along geodesics tangent to u (for a proof see e.g. Wald, 1984, appendix C). Kerr spacetimes have two Killing vectors: ∂_t and ∂_ϕ, in BL coordinates. C_t and C_ϕ can be found from these killing vectors as $C_t = \partial_t \cdot u = g_{\mu\nu}(\partial_t)^\mu u^\nu = g_{tt}u^t + g_{t\phi}u^\phi$ and $C_\phi = \partial_\phi \cdot u = g_{\mu\nu}(\partial_\phi)^\mu u^\nu = g_{\phi t}u^t + g_{\phi\phi}u^\phi$, recovering equations (2.18)-(2.19). This notion can be generalized to tensor fields: a Killing tensor field A is a tensor field that satisfies

$$\nabla_{(\mu}A_{\nu_1\nu_2,\ldots)} = 0 \tag{2.31}$$

where the brackets indicate the symmetrical part of the tensor (e.g. $B_{(\mu\nu)} = (B_{\mu\nu} + B_{\nu\mu})/2$). In particular, the following tensor :

$$K_{\mu\nu} = 2\Sigma l_{(\mu}n_{\nu)} + r^2 g_{\mu\nu} \tag{2.32}$$

with

$$l^\mu = \left(\frac{r^2+a^2}{\Delta}, 1, 0, \frac{a}{\Delta}\right) \tag{2.33}$$

$$n^\nu = \left(\frac{r^2+a^2}{2\Sigma}, -\frac{\Delta}{2\Sigma}, 0, \frac{a}{2\Sigma}\right) \tag{2.34}$$

is a Killing tensor of Kerr spacetime (Wald, 1984, chapter 12). $K_{\mu\nu}u^\mu u^\nu = \mathcal{Q} + (C_\phi + aC_t)^2$ is its corresponding conserved quantity (Misner et al., 1973, sec 33.5), where $\mathcal{Q}$ is the Carter constant as given in 2.27, which is also conserved.

ii) Physical interpretation of C_t

In Newtonian mechanics, a time translation symmetry corresponds to the conservation of energy. However, given the difficulty in defining energy in general relativity, the physical meaning of the conserved quantity C_t is not obvious. To gain some insight into its physical meaning, we start be rewriting equation (2.18) by re-scaling C_t into a new quantity $C_t{}^*$, and writing it in terms of the particle's momentum p^μ instead of its 4-velocity u^μ. For massive particles the particle's 4-momentum p and its four velocity u are related by $p = mu$. For massless particles, one can define

$$p \coloneqq (\hat{\mathcal{E}}/[c^2])u \tag{2.35}$$

where $\hat{\mathcal{E}}$ is the energy of the particle measured by some particular observer (e.g. the energy measured by a stationary observer at infinity). Note that, although the choice of $\hat{\mathcal{E}}$ is arbitrary, given a particular choice of observer, $\hat{\mathcal{E}}$ is a Lorentz scalar, i.e. everyone will agree on the energy measured by that observer[4].

[4]This energy it is given by $\hat{\mathcal{E}} = -p_\alpha \hat{u}^\alpha$ where $\hat{u}$ is the 4-velocity of such observer, in whatever coordinates one chooses to work on.

Then we have:

$$C_t{}^* = g_{tt}p^t + g_{t\phi}p^\phi. \tag{2.36}$$

For particles of mass m, $C_t{}^* = mC_t$. For photons, $C_t{}^* = (\hat{\mathcal{E}}/[c^2])\, C_t$, where $\hat{\mathcal{E}}$ is the energy measured by the reference frame on which the 4-momentum p is defined[5]. For convenience, let the photon's 4-momentum p be defined with respect to a stationary observer far from the black hole, so that $\hat{\mathcal{E}}$ is the photon's energy measured by this observer.

Now consider some emitter/absorber moving with 4-velocity u' relative to the stationary observer at infinity. In the rest frame of the emitter/absorber, $u' = [c]\,(1,0,0,0)$. So, we can write:

$$\begin{aligned} C_t{}^* &= g_{tt}p^t + g_{t\phi}p^\phi = \frac{1}{[c]}g_{tt}p^t u'^t + \frac{1}{[c]}g_{t\phi}p^\phi u'^t = \frac{1}{[c]}g_{t\mu}u'^t p^\mu \\ &= \frac{1}{[c]}g_{t\mu}u'^t p^\mu + g_{i\mu}u'^i p^\mu = \frac{1}{[c]}u'_\mu p^\mu = -\frac{\mathcal{E}'}{[c]} \end{aligned} \tag{2.37}$$

where $\mathcal{E}'$ is the particle's energy measured by the primed observer. Here we used the fact that the Kerr metric in Boyer-Lindquist coordinates has $g_{tr} = g_{t\theta} = 0$ and that all components of u' other than u'^t are zero. Above, i was used to represent the 3 spatial indices and μ the 4 spacetime indices.

A different emitter/absorber, say one with 4-velocity $u^\dagger$, would measure a different value of $C_t{}^*$, namely $C_t{}^* = -\mathcal{E}^\dagger/[c]$, where $\mathcal{E}^\dagger$ is the particle's energy as measured in the dagger frame. Hence, the value of the constant of motion $C_t{}^*$ will be different in different reference frames. Since the choice of primed (or dagger) frame is arbitrary, we see that $C_t{}^*$ is in fact the energy of the particle measured by any observer/emitter/absorber in its own rest frame.

Returning to the original constant of motion, C_t, we see that

$$C_t = \frac{[c^2]}{\hat{\mathcal{E}}}C_t{}^* = -\frac{\mathcal{E}'}{\hat{\mathcal{E}}}[c]. \tag{2.38}$$

This is actually an energy shift (up to a factor of c and a minus sign): a ratio between the energy of the particle measured by some emitter/absorber (the primed frame) and that measured by the stationary observer far from the black hole (the hatted frame)[6].

[5] For massive particles we can also write $C_t{}^* = (\hat{\mathcal{E}}/[c^2])\, C_t$, where $\hat{\mathcal{E}}$ is the particle's rest mass energy.

[6] For clarity of argument, we called the hatted observer a "stationary observer at infinity" and the prime and dagger observers "emitters/absorbers". This language is intuitive when talking about astrophysical observations, where typically one is interested in comparing the photon energy at emission vs at detection. However, as mentioned previously, the choice of the hatted reference frame used to define the photon momentum is arbitrary.

For massive particles, where $\hat{\mathcal{E}}$ is the particle's rest mass energy, then $C_t = -[c]\mathcal{E}'/\hat{\mathcal{E}} = -[c]\mathcal{E}'/(m[c^2]) = -\gamma'\,[c]$, where γ' is the Lorentz factor of the particle measured in the prime frame. This implies that the Lorentz factor is, in a way, the massive particle analogue of redshift in massless particles.

The meaning of C_t for massive particles can also be interpreted in terms of observers and emitters. Considering the same stationary observer far from the black hole and naming its frame a tilde frame, so that the energy of the particle measured by the observer is $\tilde{\mathcal{E}}$, one can write C_t

$$C_t = -\frac{\mathcal{E}'}{\tilde{\mathcal{E}}}\frac{\tilde{\mathcal{E}}}{m[c^2]}[c] = -\frac{\mathcal{E}'}{\tilde{\mathcal{E}}}\tilde{\gamma}[c]. \tag{2.39}$$

As such, one can interpret C_t for both massive and massless particles as the energy shift between some emitter (prime) and observer (tilde) which, for massive particles, requires a correction term corresponding to the particle's Lorentz factor in the observer's rest frame.

iii) Physical interpretation of C_ϕ

Just time translation symmetry is associated with conservation of energy, in Newtonian mechanics rotational symmetries are related to the conservation of angular momentum. However, just as in the case of energy, one needs to check the physical meaning of C_ϕ in the context of general relativity. In Newtonian mechanics, angular momentum is defined as $\boldsymbol{L} = \boldsymbol{r} \times \boldsymbol{p}$, where $\boldsymbol{r}$ is the particle's position vector and $\boldsymbol{p}$ its linear momentum. As explained in Grant (2020), there is no equivalent of a position vector in GR, so it is not obvious how to define an angular momentum in GR.

In section 2.1.2.i, we saw that C_ϕ is conserved as a result of the existence of killing vector $\partial_\phi = \partial/\partial\phi$. In order to gain some insight into the physical interpretation of C_ϕ, let us consider this vector in Cartesian coordinates. Cartesian coordinates are related to BL coordinates via

$$x = \sqrt{r^2 + a^2}\sin\theta\cos\phi \tag{2.40}$$
$$y = \sqrt{r^2 + a^2}\sin\theta\sin\phi \tag{2.41}$$
$$z = r\cos\theta. \tag{2.42}$$

So we can rewrite the vector ∂_ϕ as

$$\begin{aligned}\partial_\phi &= (\partial x/\partial\phi)\partial_x + (\partial y/\partial\phi)\partial_y \\ &= -\sqrt{r^2 + a^2}\sin\theta\sin\phi\partial_x + \sqrt{r^2 + a^2}\sin\theta\cos\phi\partial_y \\ &= -y\partial_x + x\partial_y.\end{aligned} \tag{2.43}$$

If one think as a quantum physicist, this already looks like the operator of angular momentum in the z-direction. As a general relativist, we go further and consider the conserved quantity $C_\phi = \partial_\phi \cdot u$ (see section 2.1.2.i):

$$\begin{aligned} C_\phi &= \partial_\phi \cdot u \\ &= g_{xx}(\partial_\phi)^x u^x + g_{yy}(\partial_\phi)^y u^y \\ &= g_{xx}(-y\, u^x) + g_{yy}(x\, u^y) \\ &= \frac{g_{xx}(-y\, p^x) + g_{yy}(x\, p^y)}{(\hat{\mathcal{E}}/[c^2])} \end{aligned} \tag{2.44}$$

where g_{xx} and g_{yy} are components of the metric in Cartesian coordinates. Far away from the black hole, the metric (2.16) becomes the Minkowski metric in spherical coordinates. In Cartesian coordinates, it is simply $\mathrm{diag}(-1, 1, 1, 1)$. So, far from the black hole (e.g. for an observer "at infinity"), $C_\phi = (-y\, p^x + x\, p^y)([c^2]/\hat{\mathcal{E}})$. For a massive particle, by analogy with the Newtonian angular momentum, this is precisely the angular momentum in the z-direction per unit rest mass. For massless particles it is instead the angular momentum per unit $(\hat{\mathcal{E}}/[c^2])$.

As such C_ϕ can be interpreted as the value that a far away observer would obtain when measuring the usual angular momentum of the particle in its rest frame, agreeing with the intuition from Noether's theorem in Newtonian mechanics.

2.1.3 Initial conditions for backward geodesic integration

In this section all expressions are written in geometrical units ($G = c = 1$), unless clearly stated otherwise.

In order to integrating the geodesic equations one must choose an initial position and 4-velocity as initial conditions to the differential equations. Given that different initial conditions will result in different geodesics, it is important that the choices made are physically motivated. For the purpose of the calculations performed in the rest of these thesis, two different types of initial conditions were considered. These are described below.

When performing radiative transfer calculations, one is often interested in the radiation from a particular astrophysical event that will reach a distant observer. This is the setup for the scenario considered in chapter 3. In particular, we consider radiation produced by events happening in the vicinity of a black hole and reaching an observer very far from it. The observer is represented by a screen which the particles (massless or massive) hit. Because of the distance from the black hole, this screen can be considered to be approximately flat and the particles are assumed to hit it perpendicularly. This is the same setup used in (Younsi, 2013), which we will replicate here for completeness - see figure 2.1.

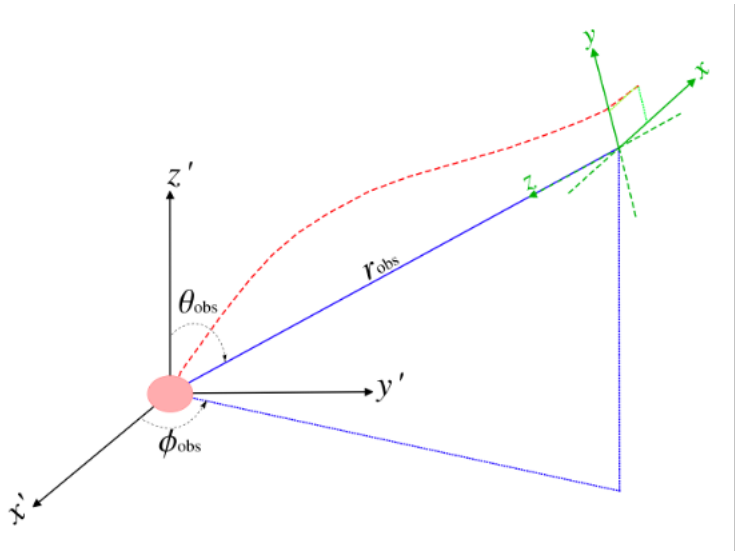

Figure 2.1: Backward ray tracing initialization setup. Diagram from Figure 3.4 of Younsi (2013), used with permission. The particle trajectories (red dashed line) are initialized at thee observer plane (green axes), which is oriented so that the z-axis points in the negative r direction, towards the black hole. The black (x', y', z') axis correspond to Cartesian coordinates centered at the black hole. The observer plane is centered at Boyer-Lindquist coordinates $(r_{\rm obs}, \theta_{\rm obs}, \phi_{\rm obs})$. The initial position of each ray is given in terms of $(x, y, z) = (\alpha, \beta, 0)$ coordinates in the observer plane and the coordinates of the observer plane origin.

The plane is oriented so that its normal, which we will call $\hat{\mathbf{z}}$, points towards the black hole. In this way, we define the initial conditions of the geodesic's coordinates by picking Cartesian coordinates (α, β) in the observer plane, and defining the location of the observer plane by choosing $(r_{obs}, \theta_{obs}, \phi_{obs})$ in BL coordinates. The initial condition for t at the observer plane are set by choosing the time at the moment of detection to be $t = 0$. The observer coordinates are transformed into BL coordinates in a manner similar to Younsi (2013). First, they are transformed into "black hole coordinates" and refer to as (x', y', z'), Cartesian coordinates centered at the black hole. Given coordinates (x_0, y_0, z_0) in the observer frame, the initial conditions (x'_0, y'_0, z'_0) are given by:

$$x'_0 = \mathcal{D}(y_0, z_0) \cos\phi_{\rm obs} - x_0 \sin\phi_{\rm obs} \tag{2.45}$$

$$y'_0 = \mathcal{D}(y_0, z_0) \sin\phi_{\rm obs} + x_0 \cos\phi_{\rm obs} \tag{2.46}$$

$$z'_0 = (r_{\rm obs} - z_0) \cos\theta_{\rm obs} + y_0 \sin\theta_{\rm obs} \tag{2.47}$$

where $\mathcal{D}(y, z) = \left(\sqrt{{r_{\rm obs}}^2 + a^2} - z\right) \sin\theta_{\rm obs} - y \cos\theta_{\rm obs}$. Then, they are transformed into BL coordinates as:

$$r_0 = \sqrt{\frac{\sigma + \sqrt{\sigma^2 + 4a^2 (z'_0)^2}}{2}} \tag{2.48}$$

$$\theta_0 = \arccos\left(\frac{z'_0}{r_0}\right) \tag{2.49}$$

$$\phi_0 = \operatorname{atan2}\left(y'_0, x'_0\right) \tag{2.50}$$

with $\sigma \equiv (x'_0)^2 + (y'_0)^2 + (z'_0)^2 - a^2$.

These relations can be easily derived by setting $M = 0$ in the Kerr metric (2.14), which corresponds to Minkowski spacetime, and comparing the metrics for this spacetime written in Cartesian and BL coordinates. For the calculations performed in this thesis, the initial position condition are always set as $(x_0, y_0, z_0) = (\alpha, \beta, 0)$.

The initial conditions for the derivatives $\dot{t}$, $\dot{r}$, $\dot{\theta}$, and $\dot{\phi}$ must also be determined. For this, it is assumed that geodesics intersect the observer plane perpendicularly. This means that $v_{x,0} = v_{y,0} = 0$, since the only non-zero component of the velocity is in the $\hat{z}$ direction. This implies that $\dot{x}_0 = \dot{t}\, v_{x,0} = 0 = \dot{y}_0$. $\dot{z}_0$, on the other hand, remains to be determined.

By differentiating equations (2.48)-(2.50) and (2.45)-(2.47) with respect to proper time or affine parameter, they can be written as a function of $\dot{x}_0, \dot{y}_0, \dot{z}_0$. In particular, the following expressions for $\dot{r}_0, \dot{\theta}_0, \dot{\phi}_0$ are obtained after setting $\dot{x}_0 = \dot{y}_0 = 0$:

$$\dot{r}_0 = \dot{z}_0 \frac{r_0 \mathcal{R} \sin\theta_0 \sin\theta_{\rm obs} \cos\Phi + \mathcal{R}^2 \cos\theta_0 \cos\theta_{\rm obs}}{\Sigma} := \dot{z}_0\, \tilde{\dot{r}}_0 \tag{2.51}$$

$$\dot{\theta}_0 = -\dot{z}_0 \frac{r_0 \sin\theta_0 \cos\theta_{\rm obs} - \mathcal{R} \cos\theta_0 \sin\theta_{\rm obs} \cos\Phi}{\Sigma} := \dot{z}_0\, \tilde{\dot{\theta}}_0 \tag{2.52}$$

$$\dot{\phi}_0 = \dot{z}_0 \frac{\sin\theta_{\rm obs} \sin\Phi}{\mathcal{R} \sin\theta_0} := \dot{z}_0\, \tilde{\dot{\phi}}_0 \tag{2.53}$$

where $\mathcal{R} \equiv \sqrt{r_0^2 + a^2}$ and the tilde quantities are the factors of the derivatives which are independent of $\dot{z}_0$. The sign in front of the equations was set so that, for $\dot{z}_0 > 0$ - see equation (2.58) - the 4-velocity points *away from* the black hole, as it would in a real detection (i.e., since we will chose $\dot{z}_0 > 0$, the sign of the initial conditions is reversed with respect to what it would be by differentiating the coordinates)[7].

The initial condition for $\dot{t}$ or not free, since the 4-velocity must obey equation (2.13). Its required value can be found either from equation (2.13) or from equations (2.21) and (2.22), yielding the exact same result. The algorithm written for this thesis uses the first option,

[7]Note that these expressions differs slightly from those in Younsi (2013), who do not have an explicit $\dot{z}_0$ dependence. Since in Younsi (2013) the author deals only with massless particles, there is no need to show this explicit dependency. This is for the reasons explained later in the main text: for massive particles any value of $\dot{z}_0$ can be chosen, including $\dot{z}_0 = 1$. Secondly, the signs are reversed. This is because the author wrote the equations pointing backwards in time, while we chose to calculate them first forward, to be consistent with observations, and flip them when performing backward ray tracing.

finding that $\dot{t}_0$ for the Kerr metric is given by:

$$\dot{t}_0 = \frac{-(2g_{t\phi}\dot{\phi}_0) + \sqrt{(2g_{t\phi}\dot{\phi}_0)^2 - 4g_{tt}(g_{rr}\dot{r}_0^2 + g_{\theta\theta}\dot{\theta}_0^2 + g_{\phi\phi}\dot{\phi}_0^2 - \xi)}}{2g_{tt}} \tag{2.54}$$

where we picked the positive root. This has an implicit dependence on the choice of $\dot{z}_0$, which becomes clear by rewriting $\dot{t}_0$ as:

$$\dot{t}_0 = \dot{z}_0 \frac{-(2g_{t\phi}\tilde{\dot{\phi}}_0) + \sqrt{(2g_{t\phi}\tilde{\dot{\phi}}_0)^2 - 4g_{tt}(g_{rr}(\tilde{\dot{r}}_0)^2 + g_{\theta\theta}(\tilde{\dot{\theta}}_0)^2 + g_{\phi\phi}(\tilde{\dot{\phi}}_0)^2 - \xi/\dot{z}_0^2)}}{2\,g_{tt}}. \tag{2.55}$$

For null geodesics $\xi = 0$ and $\dot{t}_0 \propto \dot{z}_0$. So the initial conditions for the derivatives are $\dot{x}^\mu = \dot{z}_0\,(\tilde{\dot{t}}_0, \tilde{\dot{r}}_0, \tilde{\dot{\theta}}_0, \tilde{\dot{\phi}}_0)$, where $\tilde{\dot{t}}_0$ is also defined as the component of $\dot{t}_0$ with $\dot{z}_0$ factored out. As such, the choice of $\dot{z}_0$ is not significant for massless particles. In particular, one may set it to $\dot{z}_0 = 1$ and find the initial conditions for $(\dot{t}_0, \dot{r}_0, \dot{\theta}_0, \dot{\phi}_0) = (\tilde{\dot{t}}_0, \tilde{\dot{r}}_0, \tilde{\dot{\theta}}_0, \tilde{\dot{\phi}}_0)$. Any other choice of $\dot{z}_0$ would yield the same geodesic: since null geodesics must lie on the light cone of the point where they hit the observer plane, there is only one possible null geodesic which reaches that same point perpendicularly[8]. Choosing a different value of $\dot{z}_0$ simply corresponds to re-scaling the affine parameter linearly.

For massive particles, on the other hand, the $\xi/\dot{z}_0^2$ term breaks the linearity between $\dot{t}_0$ and $\dot{z}_0$. Since the particle's 4-velocity $\dot{x}^\mu$ is not linearly proportional to $\dot{z}_0$, one is not free to arbitrarily choose a value of $\dot{z}_0$. In particularly, one cannot simply normalize it to 1. As will be seen later, this would correspond to choosing a particular timelike geodesic from a particular location in the observer plane, which in practice corresponds to only allowing particles with a certain velocity to reach the observer plane at that location.

When detecting a particle, the observer usually has information about the particle's energy and mass. With this knowledge, in an orthonormal frame[9], one can find the particle's momentum using (with the factors of c added explicitly for clarity):

$$p_\mu p^\mu = -m^2[c^2] = -\mathcal{E}^2/[c^2] + |\boldsymbol{p}|^2 \tag{2.56}$$

where $|\boldsymbol{p}|^2 = m^2\,|\dot{\boldsymbol{x}}|$ (since this now related to dealing with massive particles) is the norm of the spatial part of its 4-momentum and $\mathcal{E}$ its total energy measured in that frame (all quantities are measured in the same frame). For the setup presented above, the initial conditions for the spatial part of the 4-velocity in the observer frame are $\dot{\boldsymbol{x}} = (\dot{x}, \dot{y}, \dot{z}) = (0, 0, \dot{z}_0)$. So, equation

[8] In fact there are two: one future and one past directed. This will be relevant for section 2.1.3.i. But there is a single future directed null geodesic with a certain spatial direction through a point.

[9] An orthonormal frame is a frame in which the metric has the form $g_{\mu\nu} = \eta_{\mu\nu}$. See section 2.1.4 for details.

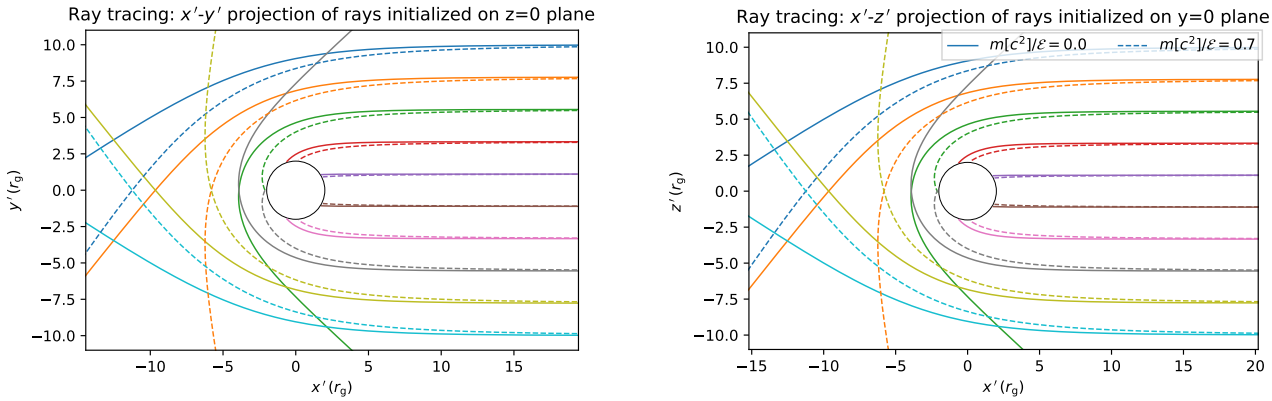

Figure 2.2: Comparison of the spatial trajectories of backward integrated null (filled lines, $m[c^2]/\mathcal{E} = 0.0$) and timelike (dashed lines, $m[c^2]/\mathcal{E} = 0.7$) geodesics around a Schwarzschild black hole. Left: all geodesics were initialized and remain on the equatorial plane; the plot shows the projection of their spatial trajectory into the x'-y' plane. Right: all geodesics were initialized and remain on the $y' = 0$ plane; the plot shows the projection of their spatial trajectory into the x'-z' plane. Due to the spherical symmetry of the spacetime, there is no distinction between the two cases.

(2.56) can be re-arranged as

$$-m^2[c^2] = -\mathcal{E}^2/[c^2] + m^2\,\dot{z}_0^{\,2} \tag{2.57}$$

$$\Leftrightarrow \dot{z}_0 = [c]\sqrt{\left(\frac{\mathcal{E}}{m[c^2]}\right)^2 - 1} \tag{2.58}$$

where the positive root for $\dot{z}_0$ was chosen. For a particle of mass m, the value of $\dot{z}_0$ depends only on the ratio of its total energy to rest mass energy and not on its energy nor its mass alone. Note that this $\dot{z}_0$ is not the particle's speed, $v = |\mathrm{d}\boldsymbol{x}/\mathrm{d}t| \leq [c]$. Instead, it is $\dot{z}_0 = \dot{t}\,v/[c]$ and, for highly relativistic particles one has $\dot{z}_0 \gg 1$.

In the limit of ultra-relativistic particles, where $\mathcal{E} \gg m[c^2]$, $\dot{z}_0$ becomes very large, so that $\xi/\dot{z}_0^2 \to 0$ in equation (2.55) and the linear dependency of the initial conditions on $\dot{z}_0$ is approximately recovered. This means that in the ultra-relativistic limit, trajectories of massive particles approach null geodesics. In practice, this implies that, above a certain $\mathcal{E}/m[c^2]$ threshold, massive particles can be treated effectively as massless in the geodesic calculation. Figures 2.2 and 2.3 show the spatial trajectories of geodesics with different $m[c^2]/\mathcal{E}$ ratio: some null ($m[c^2]/\mathcal{E} = 0$) and some timelike ($m[c^2]/\mathcal{E} = 0.7$). Different values of $m[c^2]/\mathcal{E}$ yield different geodesics, with their trajectories quickly approaching null trajectories as $m[c^2]/\mathcal{E}$ increases (see chapter 4 for details). An interesting feature to notice is how the spatial trajectories of particles with different masses only start to deviate from each other once they get very close to the black hole.

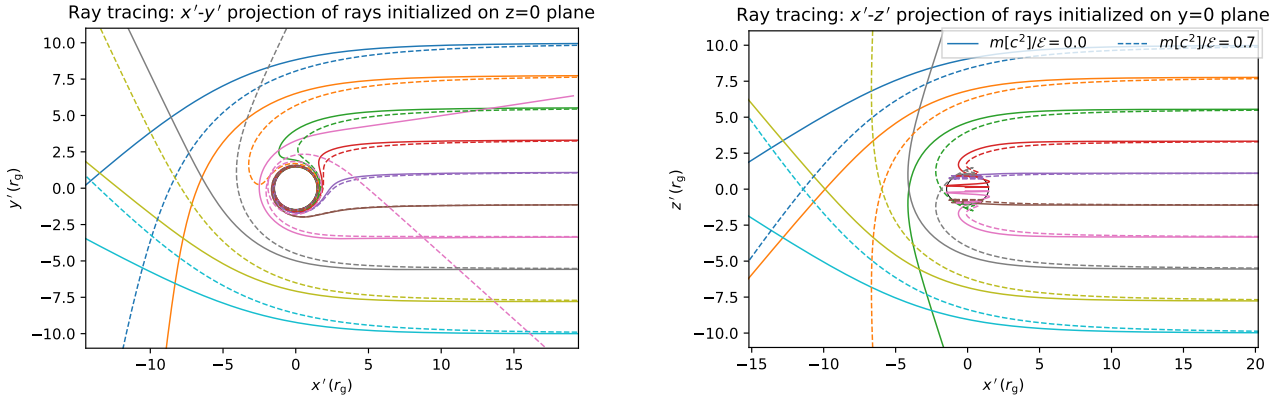

Figure 2.3: Comparison of the spatial trajectories of backward integrated null (filled lines, $m[c^2]/\mathcal{E} = 0.0$) and timelike (dashed lines $m[c^2]/\mathcal{E} = 0.7$) geodesics around a Kerr black hole with spin parameter $a = 0.998$. Left: all geodesics were initialized and remain in the equatorial plane; the plot shows the projection of their spatial trajectory into the x'-y' plane; the asymmetry around the x-axis is due to the frame dragging caused by the spin of the black hole. Right: all geodesics were initialized in the $y' = 0$ plane, but do not remain in that plane due to frame dragging. Note that, in Cartesian coordinates, the event horizon is no longer a sphere but rather an ellipsoid with the x' and y'-axes elongated with respect to the z'-axis due to the black hole spin.

i) Backward initial conditions algorithm

In real astrophysical situations, the photons or massive particles originate from far away and travel along geodesics towards the observer. However, it is more efficient to perform the geodesic calculation backwards, starting from the observer and moving backwards in time along the geodesic. By doing this, one avoids integrating many rays which never reach the observer. Equations (2.51)-(2.53) point away from the black hole and (2.54) is positive, as expected. However, we want to solve the geodesic backward in time, from the observer plane towards its origin. So after calculating $(\dot{t}_0, \dot{r}_0, \dot{\theta}_0, \dot{\phi}_0)$ using the equations above, we flip the sign of the initial conditions: $(\dot{t}_0, \dot{r}_0, \dot{\theta}_0, \dot{\phi}_0) \rightarrow -(\dot{t}_0, \dot{r}_0, \dot{\theta}_0, \dot{\phi}_0)$. We then use equations (2.18)-(2.19) to calculate the values of C_t and C_ϕ required to solve the geodesic equations (2.23)-(2.26) for the new initial conditions . Using these values, we are able to perform the geodesic integration backwards in time.

2.1.4 Initial conditions for forward geodesic integration

In some situations, one might be interested in performing ray tracing and radiative transfer calculations in order to understand local physical processes rather than to compute observables. In these cases, the backward ray tracing approach described in section 2.1.3 is not as useful and one must resort to forward ray tracing. This involves determining physically motivated initial conditions for the geodesic integration at the emission site.

The scenario described in chapter 4 addresses the interaction of radiation emitted by a source

close to the black hole with its surroundings. As such, a forward ray tracing algorithm is more appropriate in this case. In order to choose the initial conditions for the integration, one must make some assumptions about the emission on a local level and define them in the co-moving frame of the emitter, i.e. the local inertial frame[10] in which the emitter is at rest. Then, an appropriate tetrad is used to transform the vector components between this co-moving frame and the Boyer-Lindquist frame, i.e. the frame in which the metric has the form in equation (2.16). In this section, the tetrad formalism is introduced and its application to the algorithm described.

i) Tetrads

In a region of spacetime with a particular set of coordinates $\{x^\mu\}$, there is a natural way to define a basis for vectors in the tangent space of the spacetime manifold in that region. This is called the *coordinate basis*[11] $\{\boldsymbol{e}_\mu\} \coloneqq \{\partial/\partial x^\mu\}$, and its dual $\{\boldsymbol{e}^\mu\} \coloneqq \{\mathrm{d}x^\mu\}$ is the basis for the cotangent space. Tensors can then be written in terms of components in this basis ($u = u^\mu \boldsymbol{e}_\mu$; $g = g_{\mu\nu}\boldsymbol{e}^\mu\boldsymbol{e}^\nu$; etc). The metric components in (2.14) or (2.16) are written in the coordinate basis corresponding to the Boyer-Lindquist coordinates (t, r, θ, ϕ), whose basis vectors are

$$\begin{aligned} \boldsymbol{e}_t &= (1,0,0,0) \\ \boldsymbol{e}_r &= (0,1,0,0) \\ \boldsymbol{e}_\theta &= (0,0,1,0) \\ \boldsymbol{e}_\phi &= (0,0,0,1). \end{aligned} \tag{2.59}$$

In this section, we will refer to the metric components in this basis as $g_{[BL]\mu\nu} = g(\boldsymbol{e}_\mu, \boldsymbol{e}_\nu)$[12] and we will refer to the frame formed by the basis vectors as the BL frame.

In some situations, it is useful to work on a *non-coordinate basis*. This is a basis where each basis vector is a linear combination of coordinate basis vectors. Usually, roman indices are used to label such bases. I.e. given a certain coordinate basis $\boldsymbol{e}_\mu$, one can create a non-coordinate basis $\hat{\boldsymbol{\epsilon}}_a = \hat{\epsilon}_a{}^\mu \boldsymbol{e}_\mu$. The matrices $\hat{\epsilon}$ with components $\hat{\epsilon}_a{}^\mu$ are usually called *vierbeins* or *tetrads* for 4-dimensional manifolds such as the spacetimes considered in this thesis. A general 4-vector V can be written in either basis: $V = V^a \boldsymbol{\epsilon}_a = V^a(\hat{\epsilon}_a{}^\mu \boldsymbol{e}_\mu) = V^\mu \boldsymbol{e}_\mu$. So, the components of a vector transform as $V^\mu = V^a \hat{\epsilon}_a{}^\mu$, or $V^a = V^\mu (\hat{\epsilon}^{-1})_\mu{}^a$, where we define $\hat{\epsilon}^{-1}$ to be the inverse of $\hat{\epsilon}$, so that $(\hat{\epsilon}^{-1})_\mu{}^a \hat{\epsilon}_a{}^\nu = \delta_\mu{}^\nu$ and $\hat{\epsilon}_b{}^\mu (\hat{\epsilon}^{-1})_\mu{}^a = \delta_b{}^a$. Similarly, the components of a general co-vector $W = W_a \boldsymbol{e}^a = W_a((\hat{\epsilon}^{-1})_\mu{}^a \boldsymbol{e}^\mu) = W_\mu \boldsymbol{e}^\mu$ transform as $W_a = \hat{\epsilon}_a{}^\mu W_\mu$.

[10] A local inertial frame at a point p is a frame in which the metric at p is Minkowskian, i.e. $g_{\mu,\nu}|_p = diag(-1,1,1,1)$ and $\partial_\alpha g_{\mu\nu}|_p = 0$.

[11] This is the basis used in section 2.1.1.

[12] Recall that the components of any tensor in a particular basis are found by acting with that tensor on the basis vectors, e.g. $g_{[BL]\mu\nu} = g(e_\mu, e_\nu)$

It is always possible to transform a non-coordinate bases into another one which is *orthonormal* (Hull, 2020) and so we will only consider non-coordinate bases which are orthonormal. For a Lorentzian manifold, a bases is said to be orthonormal if

$$g(\hat{\boldsymbol{\epsilon}}_a, \hat{\boldsymbol{\epsilon}}_b) = g(\hat{\epsilon}_a{}^{\mu}\boldsymbol{e}_{\mu}, \hat{\epsilon}_b{}^{\nu}\boldsymbol{e}_{\nu}) = \hat{\epsilon}_a{}^{\mu}\hat{\epsilon}_b{}^{\nu} g(\boldsymbol{e}_{\mu}, \boldsymbol{e}_{\nu}) = \hat{\epsilon}_a{}^{\mu}\hat{\epsilon}_b{}^{\nu} g_{\mu\nu} = \eta_{ab} \tag{2.60}$$

where η is the Minkowski metric and the last equality above is the condition for orthonormality.

It is easy to see that the BL coordinate basis is not orthonormal: it has off-diagonal elements (hence it is not orthogonal, since $\boldsymbol{e}_t \cdot \boldsymbol{e}_\phi = g(\boldsymbol{e}_t, \boldsymbol{e}_\phi) \neq 0$) and its eigenvalues are not ± 1 (hence it is not normalized, since e.g. $\boldsymbol{e}_t \cdot \boldsymbol{e}_t = g(\boldsymbol{e}_t, \boldsymbol{e}_t) \neq \pm 1$).

Consider an observer at point p with BL coordinates (t, r, θ, ϕ) moving with a 4-velocity with coordinate basis components given by

$$u = (u^t, u^r, u^\theta, u^\phi) = u^t \boldsymbol{e}_t + u^r \boldsymbol{e}_r + u^\theta \boldsymbol{e}_\theta + u^\phi \boldsymbol{e}_\phi. \tag{2.61}$$

In order to define the initial conditions locally to this observer, one needs to find a set of basis vectors $\{\boldsymbol{\epsilon}_0, \boldsymbol{\epsilon}_1, \boldsymbol{\epsilon}_2, \boldsymbol{\epsilon}_3\}$ corresponding to a locally Minkowski frame at p, co-moving with the observer.

ii) The locally non-rotating frame (LNRF)

Such a frame can be found in two steps. First, we find a *locally non-rotating frame* (LNRF), the frame "carried" by an observer which is *co-rotating* with the black hole. Such an observer, moving at constant r and constant θ and whose angular velocity is exactly that caused by frame dragging, i.e. $\omega_{\text{LNRF}} = -g_{t\phi}/g_{\phi\phi}$ is called a *zero angular momentum observer*, or (ZAMO). Because they co-rotate with the spacetime, such observers see an unchanging geometry in their neighbourhood (Semerák, 1993).

Consider a particular observer with 4-velocity given by

$$u = (u^t, 0, 0, u^\phi) \tag{2.62}$$

One can build a set of orthonormal non-coordinate basis vectors co-moving with this observer. For the frame to be co-moving with the observer, the timelike basis vector, $\boldsymbol{\epsilon}_0$, is chosen to point in the direction of the observer's 4-velocity, i.e.

$$\boldsymbol{\epsilon}_0 = n_0(1, 0, 0, \omega) \propto u \tag{2.63}$$

where $n_0 > 0$ is a normalization constant to ensure that the frame is normalized and $\omega = u^\phi/u^t$. In this new basis, the observer's 4-velocity at p is given by $u \propto 1\boldsymbol{\epsilon}_0 + 0\boldsymbol{\epsilon}_1 + 0\boldsymbol{\epsilon}_2 + 0\boldsymbol{\epsilon}_3$. This

demonstrates that, in this frame, the observer is at rest as desired.

As to the spatial components of the local Minkowski metric, they are chosen so that $\boldsymbol{\epsilon}_1$ points in the Boyer-Lindquist r direction, $\boldsymbol{\epsilon}_2$ points in the θ direction and $\boldsymbol{\epsilon}_3$ points in the ϕ direction.

In order to guarantee the orthogonality of the frame, one must, in general, add a time component to the new basis vectors. However, since $\boldsymbol{\epsilon}_0$ has no $\boldsymbol{e}_r$ nor $\boldsymbol{e}_\theta$ components, $\boldsymbol{\epsilon}_1$ and $\boldsymbol{\epsilon}_2$ do not need an $\boldsymbol{e}_t$ component. As such, in terms of the coordinate basis, the new frame basis vectors have components:

$$\begin{aligned}
\boldsymbol{\epsilon}_1 &= n_1\, \boldsymbol{e}_r = (0, n_1, 0, 0) \\
\boldsymbol{\epsilon}_2 &= n_2\, \boldsymbol{e}_\theta = (0, 0, n_2, 0) \\
\boldsymbol{\epsilon}_3 &= n_{3t}\, \boldsymbol{e}_t + n_{3\phi}\, \boldsymbol{e}_\phi = (n_{3t}, 0, 0, n_{3\phi})
\end{aligned} \tag{2.64}$$

for some components $n_1, n_2, n_{3t}, n_{3\phi}$. The components are found by requiring that $\boldsymbol{\epsilon}_a \cdot \boldsymbol{\epsilon}_a = g_{[BL]\mu\nu}(\boldsymbol{\epsilon}_a)^\mu(\boldsymbol{\epsilon}_b)^\nu = \eta_{ab}$, with the result:

$$\begin{aligned}
n_0 &= \frac{1}{\sqrt{\alpha^2 - \gamma_{\phi\phi}(\beta_\phi + \omega)^2}} \\
n_1 &= \frac{1}{\sqrt{\gamma_{rr}}} \\
n_2 &= \frac{1}{\sqrt{\gamma_{\theta\theta}}} \\
n_{3t} &= \frac{n_0}{\sqrt{\Delta}\sin\theta}\gamma_{\phi\phi}(\beta_\phi + \omega) \\
n_{3\phi} &= \frac{n_0}{\sqrt{\Delta}\sin\theta}\left(\alpha^2 - \beta_\phi\gamma_{\phi\phi}(\beta_\phi + \omega)\right)
\end{aligned} \tag{2.65}$$

where the signs of the roots were chosen to be aligned with the definitions (2.64), and the symbols are those defined in (2.15) and (2.17).

The basis vectors $\{\boldsymbol{\epsilon}_1, \boldsymbol{\epsilon}_2, \boldsymbol{\epsilon}_3\}$ form a spatial Cartesian basis. For the particular case of a ZAMO, where $\omega = \omega_{\text{LNRF}} = -g_{t\phi}/g_{\phi\phi} = -\beta_\phi$, the non-coordinate basis vectors become

$$\begin{aligned}
\boldsymbol{\epsilon}_0 &= \frac{1}{\alpha}\,(1, 0, 0, -\beta_\phi) \\
\boldsymbol{\epsilon}_1 &= \left(0, \frac{1}{\sqrt{\gamma_{rr}}}, 0, 0\right) \\
\boldsymbol{\epsilon}_2 &= \left(0, 0, \frac{1}{\sqrt{\gamma_{\theta\theta}}}, 0\right) \\
\boldsymbol{\epsilon}_3 &= \left(0, 0, 0, \frac{\alpha}{\sqrt{\Delta}\sin\theta}\right)
\end{aligned} \tag{2.66}$$

The new basis $\{\boldsymbol{\epsilon}_a\}$ can be written in terms of the coordinate basis $\{\boldsymbol{e}_\mu\}$ as a linear combination $\boldsymbol{\epsilon}_a = \hat{\epsilon}_a{}^\mu \boldsymbol{e}_\mu$. $\hat{\epsilon}_a{}^\mu$ can be thought of as the components of a matrix formed by stacking the components of the new frame basis vectors, written in the coordinate basis as:

$$\hat{\epsilon} = \begin{pmatrix} \frac{1}{\alpha} & 0 & 0 & 0 \\ 0 & \frac{1}{\sqrt{\gamma_{rr}}} & 0 & 0 \\ 0 & 0 & \frac{1}{\sqrt{\gamma_{\theta\theta}}} & 0 \\ -\frac{\beta_\phi}{\alpha} & 0 & 0 & \frac{\alpha}{\sqrt{\Delta}\sin\theta} \end{pmatrix} \tag{2.67}$$

$$\hat{\epsilon}^{-1} = \begin{pmatrix} \alpha & 0 & 0 & 0 \\ 0 & \sqrt{\gamma_{rr}} & 0 & 0 \\ 0 & 0 & \gamma_{\theta\theta} & 0 \\ \frac{\beta_\phi \sqrt{\Delta}\sin\theta}{\alpha} & 0 & 0 & \frac{\sqrt{\Delta}\sin\theta}{\alpha} \end{pmatrix} \tag{2.68}$$

These provide the correct transformations between a coordinate frame and the LNRF (see e.g. Takahashi, 2007).

The Kerr metric can be written in this new LNFR basis[13] either by calculating $(g_{[\mathrm{LNRF}]})_{ab} = g(\boldsymbol{\epsilon}_a, \boldsymbol{\epsilon}_b) = (g_{[BL]})_{\mu\nu}(\boldsymbol{\epsilon}_a)^\mu(\boldsymbol{\epsilon}_b)^\nu$ or using the tetrad directly as $(g_{[\mathrm{LNRF}]})_{ab} = \hat{\epsilon}_a{}^\mu \, g_{\mu\nu} \, \hat{\epsilon}^\nu{}_b$, which yields (in matrix form):

$$g = \begin{pmatrix} -1 & 0 & 0 & 0 \\ 0 & 1 & 0 & 0 \\ 0 & 0 & 1 & 0 \\ 0 & 0 & 0 & 1 \end{pmatrix} \tag{2.69}$$

Since $g(\boldsymbol{\epsilon}_a, \boldsymbol{\epsilon}_b) = \eta_{ab}$, this frame is indeed orthonormal, as desired.

iii) The co-moving frame

As mentioned above, a particularly interesting frame is one co-moving with an observer. Given the orthonormal LNRF basis, it is possible to use Lorentz transformations to transform to another orthonormal frame. Let the observer have a general 4-velocity given by $u = u^t \boldsymbol{e}_t + u^r \boldsymbol{e}_r + u^\theta \boldsymbol{e}_\theta + u^\phi \boldsymbol{e}_\phi$ in the BL basis, which corresponds to

$$u = u^0 \boldsymbol{\epsilon}_0 + u^1 \boldsymbol{\epsilon}_1 + u^2 \boldsymbol{\epsilon}_2 + u^3 \boldsymbol{\epsilon}_3 \tag{2.70}$$

$$= \alpha u^t \boldsymbol{\epsilon}_0 + \sqrt{\gamma_{rr}} u^r \boldsymbol{\epsilon}_1 + \sqrt{\gamma_{\theta\theta}} u^\theta \boldsymbol{\epsilon}_2 + \frac{(u^\phi + \beta_\phi u^t)\sqrt{\Delta}\sin\theta}{\alpha} \boldsymbol{\epsilon}_3 \tag{2.71}$$

[13] Note that the metric tensor is always the same, independently of the basis in which it is written. As such, it can always be referred to as g. When writing the metric components, the indices used should make it clear which basis one is in: Greek indices and (t, r, θ, ϕ) refer to the BL basis while Latin indices and $(0, 1, 2, 3)$ refer to the co-moving orthonormal basis. For clarity, in some situations the components are written as $(g_{[BL]})_{\mu\nu}$ or $(g_{[\mathrm{com}]})_{ab}$, respectively, though this is not strictly necessary.

in the LNRF basis. In this basis, the observer has spatial 3-velocity given by $v^i = u^i/u^0$, where $i = 1, 2, 3$ represents spatial indices. One can define the absolute 3-velocity as $v^2 \coloneqq \sum_{i=1}^{3}(v^i)^2$ and hence define a Lorentz factor

$$\begin{aligned}\gamma &\coloneqq \frac{1}{\sqrt{1-v^2}} \\ &= \frac{(u^t\alpha)}{\sqrt{-\left((u^r)^2\gamma_{rr} + (u^\theta)^2\gamma_{\theta\theta} + (u^\phi)^2\gamma_{\phi\phi} + 2u^tu^\phi\beta_\phi\gamma_{\phi\phi} + (u^t)^2(-\alpha^2 + {\beta_\phi}^2\gamma_{\phi\phi})\right)}} \\ &= u^t\alpha\end{aligned} \tag{2.72}$$

where in the last line we used the fact that the term in brackets in the denominator is simply the norm of the 4-velocity, which is always equal to -1. A generic Lorentz boost can be used to transform between orthonormal frames moving at a constant velocity with respect to each other. As such, we can use the Lorentz boost transformation as the tetrad for transforming between the LNRF and an orthonormal frame co-moving with some observer/emitter or other object. A generic Lorentz boost is given by (Takahashi, 2007):

$$\Lambda = \begin{pmatrix} \gamma & \mathrm{v}_1\gamma & \mathrm{v}_2\gamma & \mathrm{v}_3\gamma \\ \mathrm{v}_1\gamma & 1 + \frac{\mathrm{v}_1^2\gamma^2}{1+\gamma} & \frac{\mathrm{v}_1\mathrm{v}_2\gamma^2}{1+\gamma} & \frac{\mathrm{v}_1\mathrm{v}_3\gamma^2}{1+\gamma} \\ \mathrm{v}_2\gamma & \frac{\mathrm{v}_1\mathrm{v}_2\gamma^2}{1+\gamma} & 1 + \frac{\mathrm{v}_2^2\gamma^2}{1+\gamma} & \frac{\mathrm{v}_2\mathrm{v}_3\gamma^2}{1+\gamma} \\ \mathrm{v}_3\gamma & \frac{\mathrm{v}_1\mathrm{v}3\gamma^2}{1+\gamma} & \frac{\mathrm{v}_2\mathrm{v}_3\gamma^2}{1+\gamma} & 1 + \frac{\mathrm{v}_3^2\gamma^2}{1+\gamma} \end{pmatrix}. \tag{2.73}$$

The basis vectors transform between the LNRF and the co-moving frame as $\boldsymbol{\epsilon}_{[\mathrm{com}]\,a} = \Lambda_a{}^b\boldsymbol{\epsilon}_{[\mathrm{LNRF}]\,b}$ and the components of vectors transform as $V_{[\mathrm{com}]}{}^a = V_{[\mathrm{LNRF}]}{}^b(\Lambda^{-1})_b{}^a$. The inverse Lorentz transformation Λ^{-1} is obtained by replacing $v^i \to -v^i$ in equation (2.73).

To transform directly from the BL to the co-moving frame, it is only necessary to combine the tetrad which transforms between the BL and the LNFR bases with the Lorentz transformation between the LNRF and the co-moving bases, i.e.

$$\hat{\epsilon}_{[\mathrm{BL\,to\,com}]} = \Lambda \cdot \hat{\epsilon} \tag{2.74}$$

so that the basis vectors transform as

$$\boldsymbol{\epsilon}_{[\mathrm{com}]\,a} = (\hat{\epsilon}_{[\mathrm{BL\,to\,com}]})_a{}^\mu\boldsymbol{e}_{[\mathrm{BL}]\,\mu} = \Lambda_a{}^b\hat{\epsilon}_b{}^\mu\boldsymbol{e}_{[\mathrm{BL}]\,\mu} \tag{2.75}$$

and the components of a generic vector V transform as

$$V_{[\mathrm{com}]}{}^a = V_{[\mathrm{BL}]}{}^\mu(\hat{\epsilon}^{-1}_{[\mathrm{BL\,to\,com}]})_\mu{}^a = V_{[\mathrm{BL}]}{}^\mu(\hat{\epsilon}^{-1})_\mu{}^b(\Lambda^{-1})_b{}^a \tag{2.76}$$

and

$$V_{[\mathrm{BL}]}{}^{\mu} = V_{[\mathrm{com}]}{}^{a}(\hat{\epsilon}_{[\mathrm{BL\,to\,com}]})_{a}{}^{\mu} = V_{[\mathrm{com}]}{}^{a}\Lambda_{a}{}^{b}\hat{\epsilon}_{b}{}^{\mu}. \tag{2.77}$$

iv) Initial Conditions in the co-moving frame

The problem addressed in chapter 4 requires the determination of physically meaningful initial conditions in an orthonormal co-moving frame of an emitter with a generic 4-velocity $u = (u^t, u^r, u^\theta, u^\phi)$ in the BL frame. In particular, the initial conditions are chosen so that all rays are emitted isotropically from a point (the emitter's location), in the frame co-moving with the emitter, as defined above. The spatial orientations of the rays, $\hat{\boldsymbol{n}}$ (with $\hat{\boldsymbol{n}}\cdot\hat{\boldsymbol{n}} = 1$), in this frame are defined by two angles (θ', ϕ') using a Fibonacci grid[14].

Note that θ', ϕ' are not the BL coordinates, but rather some polar coordinates with respect to the centre of the co-moving frame. By using the standard polar to Cartesian coordinate transformation, the initial spatial directions of the rays/particles are written in Cartesian coordinates. Let the spatial part of the relativistic 4-velocity k of the emitted photons or particles be[15] $\boldsymbol{k} = |\boldsymbol{k}|\hat{\boldsymbol{n}}$, where $|\boldsymbol{k}|$ is found using the same expression as for $\dot{z}_0$ in 2.58, hence defining k^1, k^2 and k^3. The timelike component k^0 is found by requiring that $g(k,k) = \xi$, where $\xi = 0$ for massless particles (as photons) and $\xi = -1$ for massive particles. Since the co-moving frame is locally Minkowski, this condition reduces to $(k^0)^2 = \boldsymbol{k}\cdot\boldsymbol{k} - \xi$.

Given these initial 4-velocities in the co-moving frame, the components of k in the BL coordinate basis can be found as $k_{[\mathrm{BL}]}{}^{\mu} = k_{[\mathrm{com}]}{}^{a}(\hat{\epsilon}_{[\mathrm{BL\,to\,com}]})_{a}{}^{\mu}$, using the tetrad 2.74.

In this way, the components of the initial 4-velocity of each ray are found in the BL where all calculations are performed. Figure 2.4 shows an example of the effect of transforming isotropic vectors in the co-moving frame into the BL frame.

An important point is that the co-moving frame defined by the tetrad above is only Minkowski at the point p where the tetrad is defined. Away from p, it starts to deviate from Minkowski. As such, when performing forward ray tracing calculations using these initial conditions, all rays are considered to be emitted from a single point source. In this way, the vector component transformations are ensured to be valid for all rays.

[14] A Fibonacci grid is a particular grid where points are distributed roughly isotropically on a sphere. We used the algorithm described in Roberts (2020): For a grid of N rays, the i-th ray points radially outward from the emission point, in a direction given by $\theta'_i = \arccos(1 - 2(i+0.5)/N)$ and $\phi'_i = 2\pi i/\delta$, where $\delta = (1+\sqrt{5})/2$ is the golden ratio.

[15] Here the particle's 4-velocity is referred to as k rather than u to distinguish it from the emitter's velocity u.

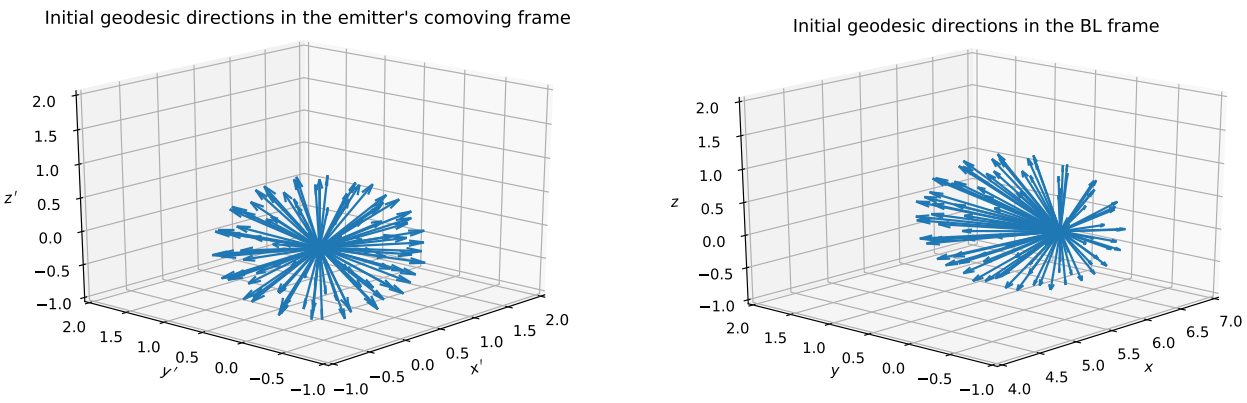

Figure 2.4: Left: Spatial directions of emitted geodesics in the emitter's co-moving frame. The emitter is on a prograde Keplerian orbit (see A.1) around a Kerr black hole at $r = 6r_{\rm g}$. The origin of the vectors is at the emitter's location. The axes centered at the emitter are primed (x', y', z') (left) to distinguish them from the BL Cartesian axes (x, y, z) (right). Right: initial conditions of the same rays transformed into the BL frame for an emitter momentarily at $(r, \theta, \phi) = (6r_{\rm g}, 90°, 0°)$, orbiting in the equatorial plane at constant r and in the direction of increasing ϕ, i.e. momentarily in the $+y$ direction. The relativistic beaming effect is very clearly visible, with rays concentrating towards the direction of motion. The scale of the vector lengths is arbitrary. Only their direction and the ratio of the lengths is relevant. These transformations were calculated for 100 null geodesic initial conditions for illustration purposes. The effect is similar for timelike geodesics.

2.1.5 Ray tracing algorithm

The ray tracing part of the code consists of the integration of the geodesic equations (2.23)-(2.26) with the initial conditions described in sections 2.1.3 and 2.1.4. The code was written in Fortran 90, using a Runge-Kutta-Felhborg algorithm of order 4/5 for the geodesic integration. The integration terminates when one of the following conditions are met:

1. The geodesic reaches an area within some small distance from the event horizon. These geodesics are considered to be absorbed by the black hole. The margin is set in order to avoid the coordinate singularity at the horizon. Given a certain observer grid, the collection of pixels whose geodesics fall into the black hole form what is often referred to as the *black hole shadow*. This is the lensed image of the event horizon: background radiation does not hit those particular pixels as it would have had to originate at the event horizon. See figures 2.5 and 2.6 for illustrations of this effect.

2. The geodesic is moving away from the black hole and goes beyond a certain distance from it. These geodesics are considered to escape. For the case of backward ray tracing, these would be geodesics that reach the observer from distant regions beyond the BH. Since in most cases one is interested in geodesics coming from the vicinity of the black hole, these are not particularly relevant. For the forward ray tracing cases, one is mostly interested in investigating the trajectories of geodesics close to the black hole, without reference to a distant observer. As such, once a geodesic goes beyond a certain distance, it is no longer

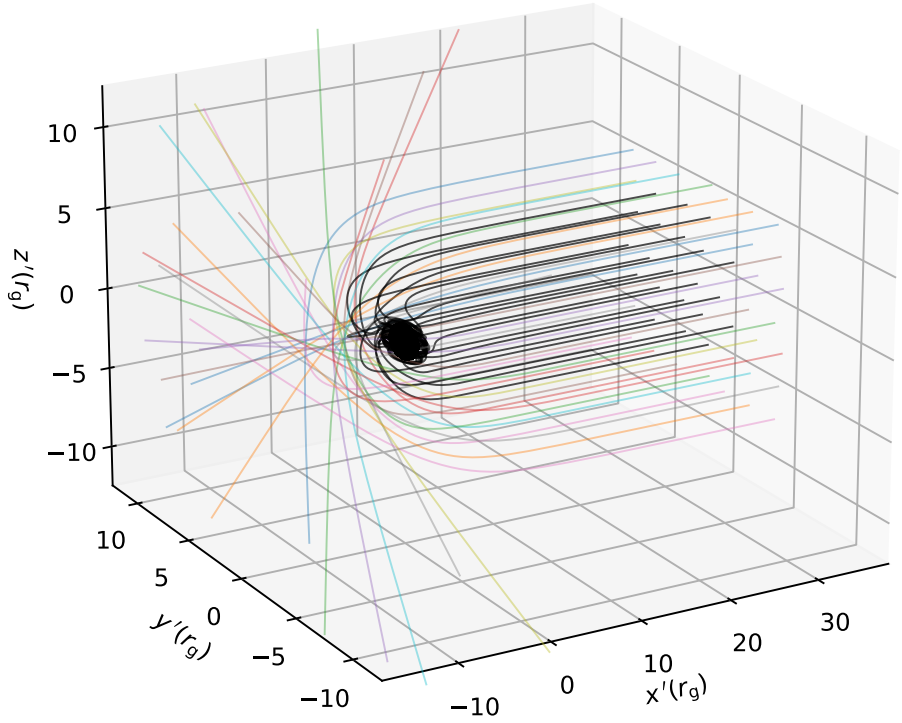

Figure 2.5: Spatial trajectories of backward ray traced null geodesics around a Kerr black hole. Black lines correspond to geodesics which would have had to come from within the event horizon to reach the observer (since in the backward integration they enter the event horizon). The pixels in the observer plane corresponding to these geodesics form the black hole shadow. The observer plane is far away from the black hole and centered on the equatorial plane ($\theta_{\rm obs} = 90°$).

relevant for the processes being considered and the integration can be interrupted.

3. The geodesic reaches an optically thick surface (see notes on surface funding algorithm below).

4. The optical depth along the geodesic exceeds a certain value (see section 2.2).

The radiation transport algorithm (see section 2.2) was also coded in Fortran 90. The code is written in a modular manner, with shorter, more individualized routines being combined into more complex ones to produce the final completed programme. This means that it is relatively straightforward to change small parts of the code (e.g. the equations of motion or the the emission and absorption coefficients), simply by creating new basic routines and using them as the building blocks of the final programme.

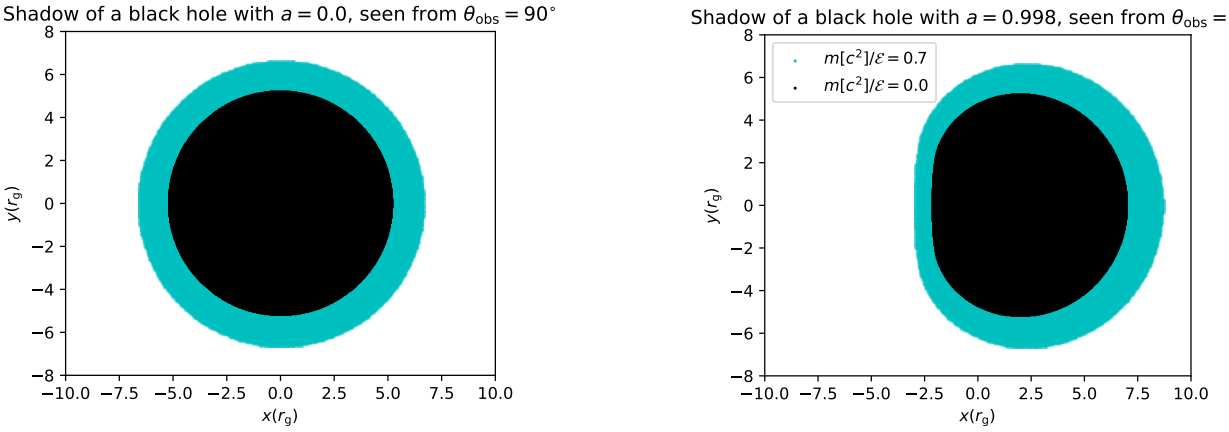

Figure 2.6: Shadow of a Schwarzschild (left) and Kerr (right) black hole viewed from $\theta_{\text{obs}} = 90°$ (edge on). Black: photon shadow; this is the usual black hole shadow, produced by the capture of background photons by the black hole. Cyan: shadow of particles with $m[c^2]/\mathcal{E} = 0.7$. As seen in figures 2.2 and 2.3, particles with different $m[c^2]/\mathcal{E}$ ratio follow different geodesics. The higher this ratio, the more they will feel the gravitational pull of the black hole. As such, particles with a larger mass (for the same energy) which were originally further from the black hole end up falling into it, resulting in a wider "particle shadow". Other than the size, the general features of the shadow are the similar. Note that while the Schwarzschild black hole shadow is circular, the frame dragging in Kerr spacetime shifts and deforms the shadow. (resolution: $122,500$ pixels).

The geodesic integration is the most computationally expensive part of the code. Given that the propagation of particles along different geodesics is independent of each other, the code is parallelized so that multiple geodesics can be calculated simultaneously. As such, the time taken to calculate images of a given resolution depends on the number of CPUs available in the computer being used. As will be explained in section 2.2, the radiative transfer calculations are performed along each of these geodesics simultaneously for all energies in the case of massless particles (the code uses a vectorized covariant intensity, with a vector entry for each particle energy, to be able to perform the GRRT calculation for all energies at the same time). This means that the computational time does not depend on the energy resolution of the calculations. This resolution does, however, impact the computers that the code can run in: due to the presence of very large vectors, computers without large enough RAM available will not be able to run the code, and segmentation fault errors will result from trying to do so. For very large resolutions, therefore, the code should only be run in computers with large enough RAM. For massive particles this vectorization is not possible, since each energy will correspond to a different geodesic. As such, only one particle energy can be calculated at one time. Finally, in cases where one requires the calculation of images at several time steps (e.g. for the calculation of the light curves described in chapter 3) the calculations are performed sequentially for each time snapshot. This means that the computational time taken for the calculations increases linearly with the temporal resolution. In addition to this, as explained in section 3.2.0.iii), there is some additional time taken by the time sorting algorithm which also increases with the

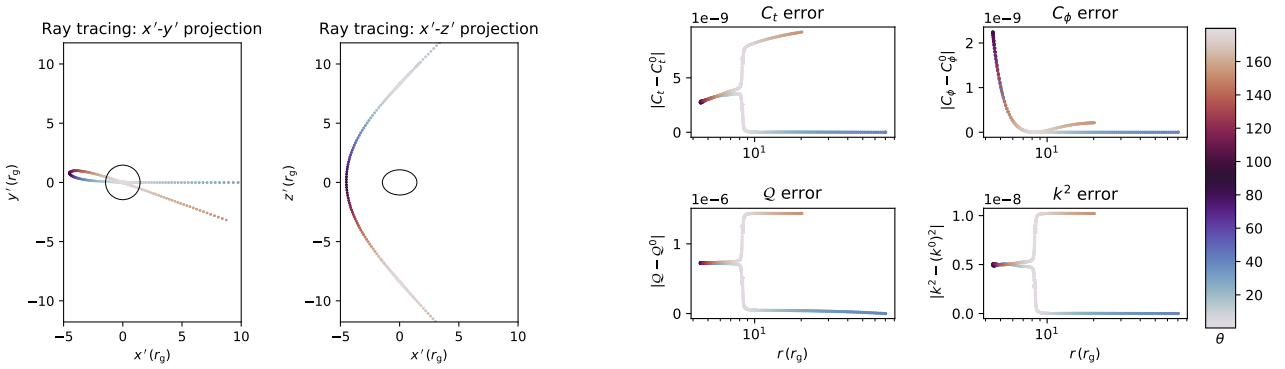

Figure 2.7: Error in the integration of a backward traced null geodesic reaching the observer at $\theta_{\rm obs} = 45°$. Left: projection of the geodesic trajectory in the (x', y') and (x', z') planes; the black circle represents the event horizon of the black hole. Right: difference between the value of all four conserved quantities measured at each integration step vs their initial value, as a function of coordinate r; this difference provides an estimate for the integration error. The colour code corresponds to the value of the θ coordinate at each point. Note how the most abrupt error increases happen when the geodesic passes close to the poles, where the ϕ coordinate is not well defined. This explains the relatively large errors.

temporal (and spatial) resolution. This step uses a Quicksort algorithm and as such it scales, on average as $N \log N$, and, in the worst case scenario, as N^2 (JaJa, 2000), where N is the total number of pixels to be ordered (which depends both on temporal and spatial resolution).

i) Validation of the geodesic integration with conserved quantities

The error associated with the integration of the geodesics is quantified by calculating the four conserved quantities, namely C_t, C_ϕ, Q and k^2, at each integration step and evaluating how much they change compared to their initial values. Figures 2.7 and 2.8 show examples of these tests for two potentially problematic null geodesics: one that goes through the coordinate poles and one that experiences an abrupt change in its ϕ direction.

ii) Surface finding algorithm

Many astrophysical radiative transport problems involve calculating the transport of radiation from a particular emitting region. This can be optically thin or thick. If the emitting region has some boundary, it becomes essential to be able to find that boundary as part of the ray tracing calculation. Two examples of widely used emitting regions are geometrically thin and optically thick accretion disks around the black hole and hotspots, usually represented by a small spherical region in the vicinity of the black hole.

In order to find a surface, at each point of the integration one much check i) the time at which the particle was at a certain point; ii) the location/shape of the surface at that time; iii) whether the particle crossed the surface between the previous step and the current step. Step ii may

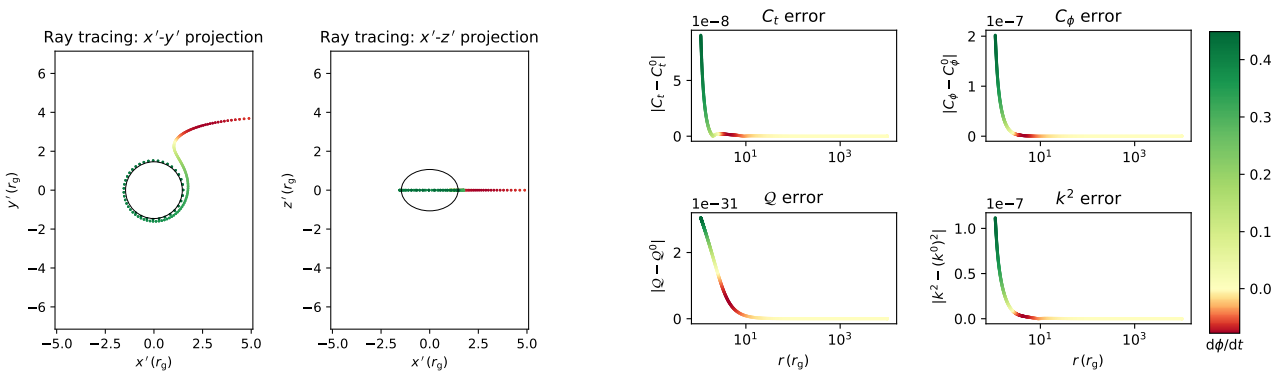

Figure 2.8: Error in the integration of a backward traced null geodesic reaching the observer at $\theta_{\rm obs} = 90°$. Left and right plots as in figure 2.7. The colour code corresponds to the value of $\mathrm{d}\phi/\mathrm{d}t = \dot{\phi}/\dot{t}$ at each point. The geodesic remains in the equatorial plane, so $\theta = 0$ throughout the integration. In this case, the problematic part of the integration is the point where $\mathrm{d}\phi/\mathrm{d}t$ changes sign. It is clear that this point of the integration, in yellow, is when the errors in all four quantities start to increase. Still, they remain within reasonable bounds for the purpose of the GRRT calculations performed in this thesis.

be skipped if the surface is stationary (e.g. a disk or torus) but needs to be considered if the surface changes shape (e.g. expanding hotspot) or location (e.g. orbiting hotspot). In practice, in order to optimize the code, the surface finding is not actually performed at each step. For example, if one knows that the disk is in the equatorial plane and has inner radius $r_{\rm i}$ and outer radius $r_{\rm o}$, then the detailed surface finding is only performed when the particle is close enough to a vertical cylinder of radius $r_{\rm o}$. In this thesis, three types of surfaces were used: a thin equatorial disk, a thick torus and orbiting spherical hotspot with constant radius. The detailed surface finding algorithm is as follows[16].

1. Integrate step using RK4/5 algorithm;

2. If the surface to be found is a thin equatorial disk of inner radius $r_{\rm i}$ and outer radius $r_{\rm o}$:

   (a) Check the θ coordinate at the current and previous iteration. Check whether $z = 0$ plane was crossed between iterations by checking whether $\theta > \pi/2$ in one iteration and $\theta < \pi/2$ in the other.

   (b) **If false**: continue integration. **If true**: check radial coordinate in cylindrical polar coordinates ($\rho = \sqrt{r^2 - z^2}$, where z is the Cartesian z-coordinate of the current integration point) to see whether the crossing of the $z = 0$ plane occurred within the disk region, by investigating whether $r_{\rm i} \leq \rho \leq r_{\rm o}$.

   (c) **If false**: continue integration. **If true**: check whether z coordinate of the current iteration is within the error tolerance ϵ from $z = 0$, i.e. whether $|z| \leq \epsilon$.

[16] Below we refer to the black hole coordinate z' as z for simplicity.

(d) **If true**: the current iteration point is considered to be on the surface. **If false**: check whether the number of surface finding iterations is less than the specified maximum.

(e) **If true**: Go back to the previous iteration and re-integrate with a reduced step size and repeat the process. **If false**: Check whether error in z is less than twice the error tolerance.

(f) **If true**: accept point as being in surface. **If false**: output an error saying that desired surface accuracy could not be reached. Move on to the next ray.

3. If the surface to be found is an equatorial torus (i.e. a torus centered in the equatorial plane):

(a) Define the angle spanned by the torus from the origin, $\alpha_{\text{torus}} = \arctan(r_{\text{min}}/r_{\text{maj}})$, where r_{maj} is the major radius of the torus (from the origin to the centre of the torus) and r_{min} the minor radius, defining the torus' width (see figure 2.9). Look at the θ coordinate of the current iteration and check whether it is within α_{torus} from the equatorial plane.

(b) **If false**: continue integration. **If true:** check whether the radial coordinate in cylindrical polar coordinates ($\rho = \sqrt{r^2 - z^2}$) is within the torus region, i.e. whether $r_{\text{maj}} - r_{\text{min}} - \epsilon \leq \rho \leq r_{\text{maj}} + r_{\text{min}} + \epsilon$, where ϵ is the error tolerance.

(c) **If false**: continue integration. **If true**: check whether the current point is within the error tolerance from the torus cross-section circle, i.e. whether $|\sqrt{(\rho - r_{\text{maj}})^2 + z^2} - r_{\text{min}}| \leq \epsilon$.

(d) **If true**: the point is considered to be on the surface. **If false**: check whether the number of surface finding iterations is less than the specified maximum.

(e) **If true**: Go back to the previous iteration and re-integrate with a reduced step size. **If false**: Check whether $|\sqrt{(\rho - r_{\text{maj}})^2 + z^2} - r_{\text{min}}| \leq 2\epsilon$.

(f) **If true**: accept the point as being on the surface. **If false**: output an error saying that desired surface accuracy could not be reached. Move on to the next ray.

4. If the surface to be found is a spherical orbiting hotspot, find the location of the plasmoid centre at the time of emission in the following way:

(a) Pick the initial location of the hotspot $(r^*(0), \theta^*(0), \phi^*(0))$. Then, the location of

the hotspot at a given time t is given by

$$\begin{aligned} r^*(t) &= r^*(0) \\ \theta^*(t) &= \theta^*(0) \\ \phi^*(t) &= \phi^*(0) + \frac{2\pi t}{T_{\rm orb}} \end{aligned} \tag{2.78}$$

where $T_{\rm orb}$ is the orbital period found by assuming a Keplerian orbit (see A.1 for details). In chapter 3 of this thesis, a backward-forward surface finding algorithm is used. This involves fixing the position of the hotspot at certain emission times, $t_{\rm em}$, performing a full geodesic integration and surface funding for that location, increasing $t_{\rm em}$, fixing the new position, integrating again and so on (as described below). So equations (2.78) above are solved for $t = t_{\rm em}$.

Once the plasmoid location is defined:

(a) Find the spatial distance between the current iteration point and the centre of the hotspot and check whether it is less than than the hotspot radius $r_{\rm hs}$ plus some error tolerance ϵ, i.e. $\sqrt{(x-x^*)^2+(y-y^*)^2+(z-z^*)^2} \leq r_{\rm hs}+\epsilon$, where x^*, y^*, z^* are the Cartesian coordinates of the hotspot's centre and $r_{\rm hs}$ is the radius of the hotspot.

(b) **If false**: continue integration. **If true**: check whether the distance between the previous iteration coordinates and the centre of the hotspot is within the error tolerance of the hotspot radius (since we want to find a point on the surface and not merely inside it).

(c) **If true**: point is considered to be on the surface. **If false**: check if the number of surface finding iterations is less than the specified maximum.

(d) **If true**: Go back to previous iteration and re-integrate with a reduced step size. **If false**: Check whether the distance from the surface is less than twice the error tolerance.

(e) **If true**: accept the point as being in surface. **If false**: output an error saying that the desired surface accuracy could not be reached.

Thin disks are good approximations of certain astrophysical systems such as certain types of accretion flow. More general and more realistic scenarios would be thick tori supported by physical mechanisms (e.g. rotation or pressure supported, see e.g. (Younsi et al., 2012)). However, depending on what one is interested in studying, simplified models of these accreting regions may be good enough. Our code allows for the ad-hoc selection of the disk/ torus parameters - although these are not entirely self-consistent, they speed up the calculations by

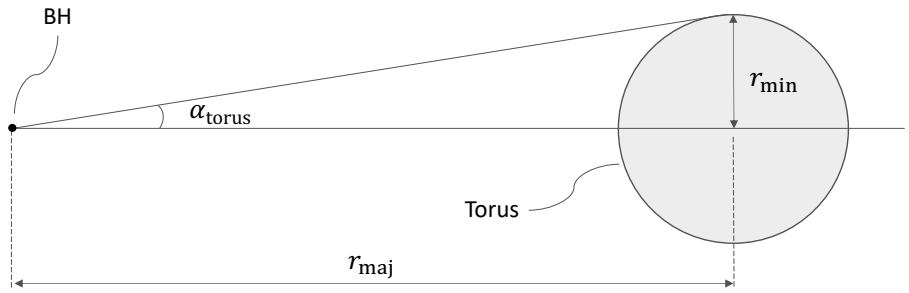

Figure 2.9: Illustration of torus surface finding algorithm, with the definitions of the relevant quantities α_{torus},r_{min} and r_{maj}. The horizontal line is the x' axis and the figure shows a cross sectional cut of the torus, only showing one of its sides with respect to the black hole.

not having to solve for the disk structure and still provide useful insight into the GR effects close to the black hole.

Figure 2.10 shows the image of a photon-emitting thin disk around a Schwarzschild and a Kerr black hole for different viewing angles, colour coded with the photon arrival time. By knowing the velocity profile of the emitters, it is possible to calculate the energy shift of the photons in the emitter's local rest frame vs that measured by a far away observer. Figure 2.11 shows the same disk images, this time colour coded with the energy shift $\mathcal{E}_{\text{obs}}/\mathcal{E}_{\text{em}}$, assuming that the material in the disk is on Keplerian orbits around the black hole, as described in section A.1.

Only photon disk images are shown in this section. However, note that, just as for the black hole shadow (figure 2.6), the image of any other surface will also be different for particles with different $m[c^2]/\mathcal{E}$ ratios.

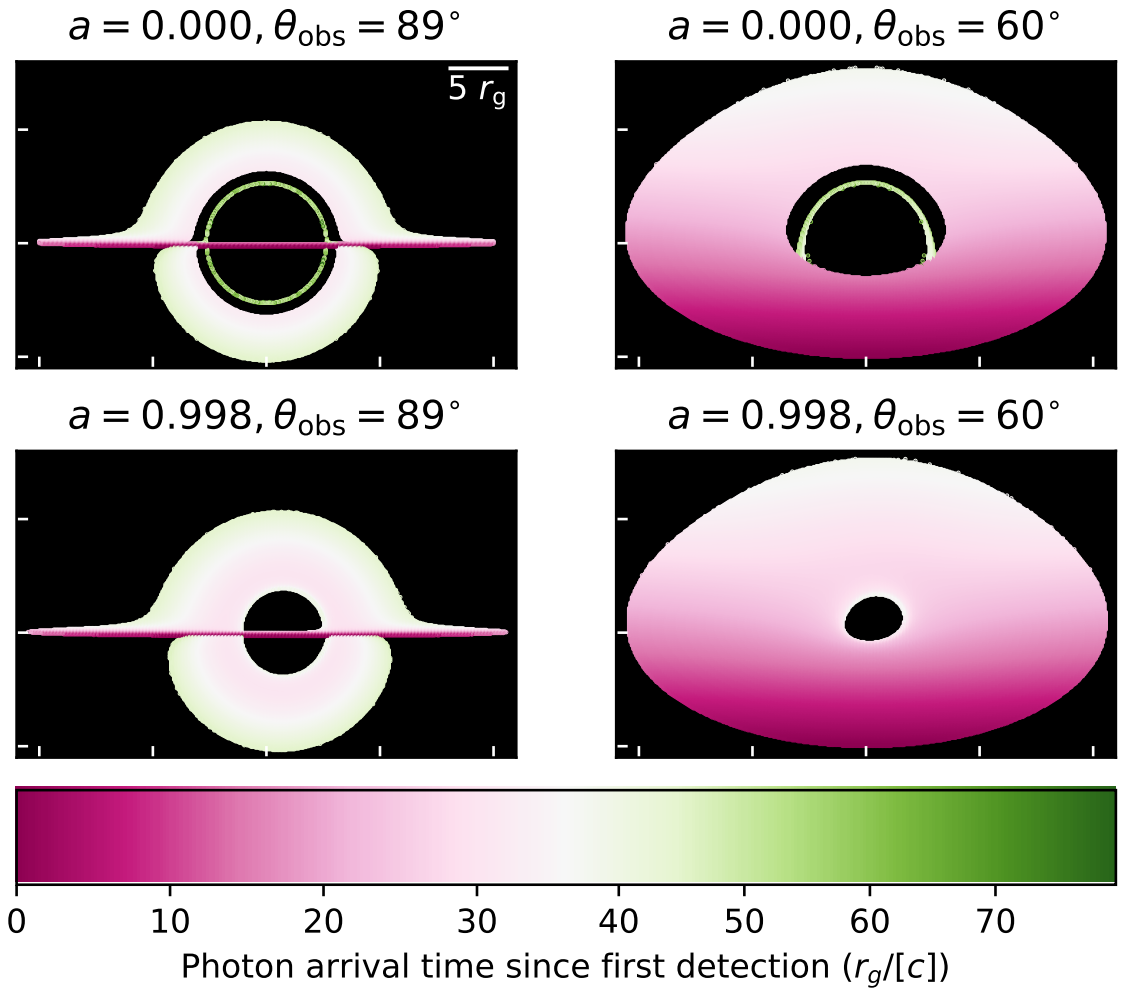

Figure 2.10: Image of a thin disk around a Schwarzschild (top) and Kerr (bottom) black hole seen by a distant observer at a viewing angle of 89° (left) and 60° (right). The colour coding corresponds to the arrival time of each photon calibrated against the arrival of the first photon, in geometrical units. The disk extends from the innermost stable circular orbit ($r_{\rm isco} = 6r_{\rm g}$ for Schwarzschild black holes and $r_{\rm isco} = 1.23r_{\rm g}$ for Kerr black holes with $a = 0.998$) up to an outer radius of $20r_{\rm g}$. In the Schwarzschild case, one can see a secondary image inside the main image (thin green circle). It corresponds to an image of the bottom of the disk. The photons that produce it are emitted downward from the disk and are lensed by the black hole towards the observer (see figure 2.12 for an illustration). This is not visible in the Kerr case because the optically thick disk extends closer to the black hole, preventing such rays from reaching the observer. In fact, the image of a disk in Kerr spacetime with inner radius at $r = 6r_{\rm g}$ also has a secondary inner ring, so the absence of it in the present figure is not due to spin directly, but rather due to the fact that a higher spin allows the disk to extend closer to the black hole. A few interesting points to note are that i) when a secondary image is present (top row), it arrives at the observer plane significantly later than the primary image; ii) when the disk is viewed from 89°, the top and bottom edges of the disk, which are images of its edge furthest from the observer, also reach the detector later, indicating the longer distance that the corresponding rays must travel; iii) similarly, the further half of the disk when viewed from 60° (top half) also experiences a longer travel time than the bottom half, which is closer to the observer. Image resolution: 122500 pixels.

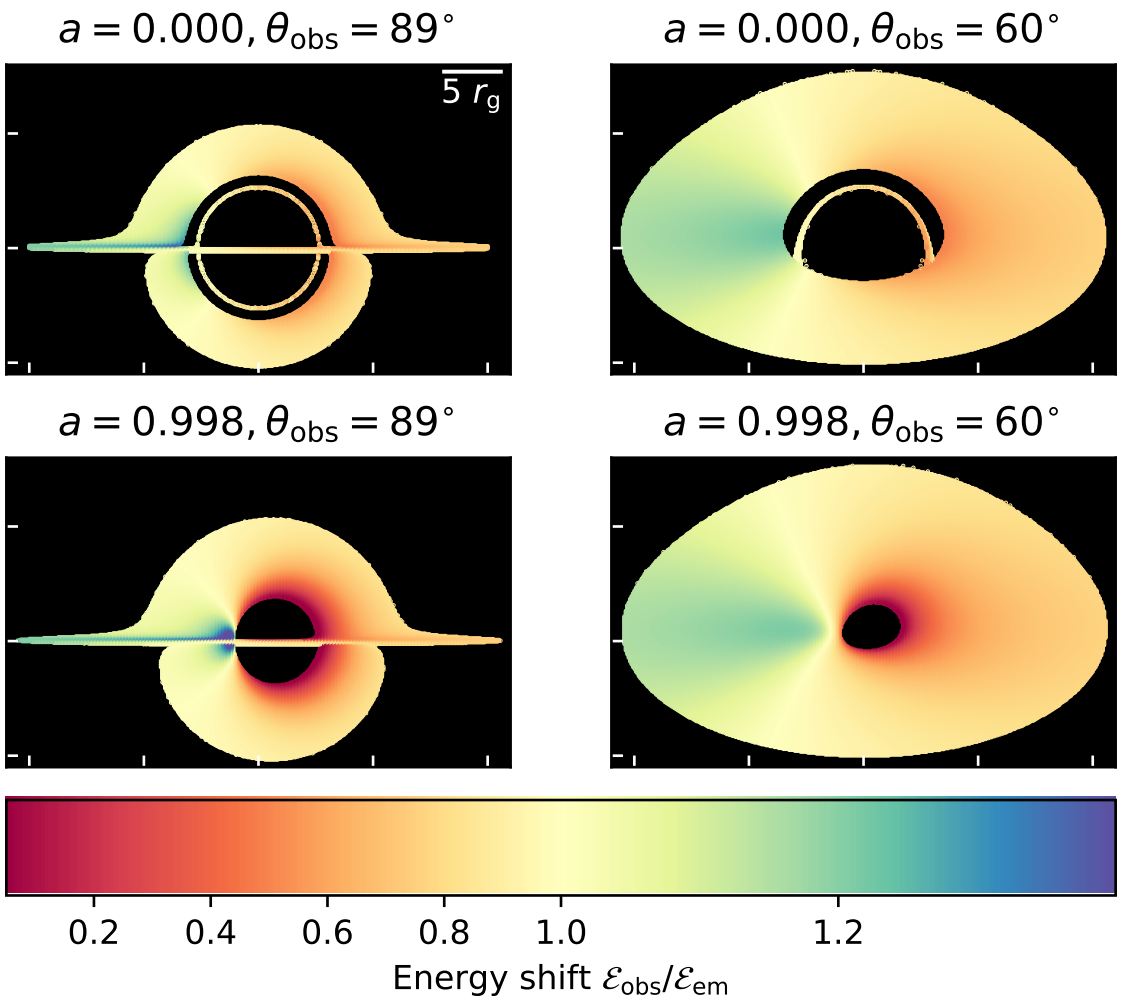

Figure 2.11: Same as in figure 2.10, but colour coded with photon detected energy shift (observed energy relative to the emitted energy), assuming that the emitting material in the disk is moving on Keplerian orbits (section A.1) around the black hole. Being close to the black hole, the radiation emitted from the disk experiences gravitational redshift which, on the left hand side of the disk, competes with the Doppler blue shift. The right hand side of the disk, where the emitters are moving away from the observer, experiences Doppler redshift as well as gravitational redshift. The gravitational redshift, which affects the emission from the whole disk, is responsible for the asymmetry in the fraction of the disk which is blue vs red shifted. Note that the disk in Kerr spacetime experiences a stronger redshift due to its inner boundary being closer to the black hole. The similarity of the images to those in Wu et al. (2006) supports the validity of our code. Resolution: 122500 pixels.

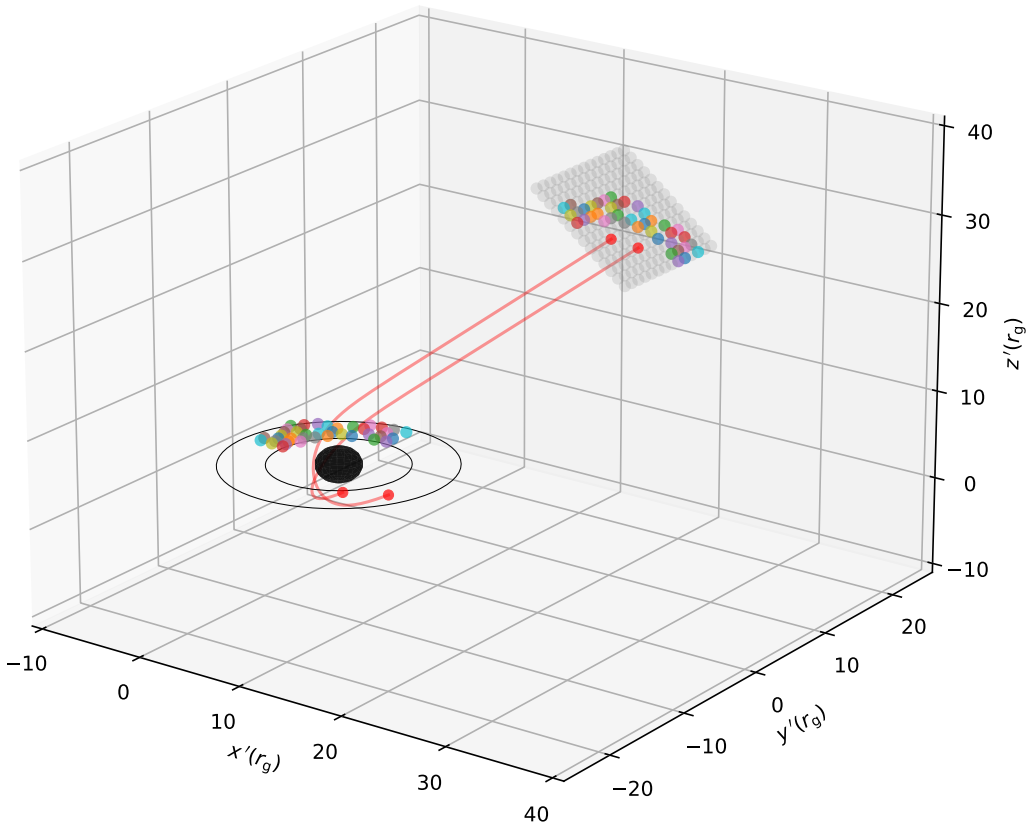

Figure 2.12: Illustration of the formation of the secondary image of a thin disk. The figure shows a Schwarzschild black hole (black sphere) surrounded by a thin disk (black circles). The observer is represented by a grid at a viewing angle of 45°, which here is placed artificially close to the black hole for illustration purposes (in all calculations the observer was at a distance of $10^4 r_g$ from the black hole). Dots of the same color on the disk and observer plane are connected by a geodesic. The image shows the trajectories of two geodesics (red lines) which originate from the bottom of the disk but are lensed into the observer's view by orbiting the black hole. These two geodesics hit the observer plane in a different location, being part of the inner disk which is visible in the Schwarzschild images in figures 2.10 and 2.11. These two geodesics are examples of how the secondary images form. A similar process is responsible for the secondary images of orbiting spheres shown in chapter 3.

2.2 Generalized Covariant Intensity

In section 1.3 the traditional formulations for photon transport using the classical radiative transport equation (section 1.3.1) and particle transport using the Boltzmann transport equation (section 1.3.2) were introduced. The present section defines a generalization of covariant intensity which is also valid for massive particles. In section 2.3 a unified radiation transport formulation is presented which is valid for both massless and massive particles and is completely covariant.

2.2.1 Massive particles (e.g. protons and neutrinos)

One of the key objectives of this thesis was to generalize the current radiation transport formalism to enable it to handle the transport of massive particles. In order to do so, it was first important to define an analogue of specific intensity (1.1) for massive particles. Consider a specific intensity analogue to (1.1) but in terms of the total particle energy $\mathcal{E}$ instead of frequency ν:

$$I_{\mathcal{E}} \coloneqq \frac{\mathrm{d}E}{\mathrm{d}A\,\mathrm{d}t\,\mathrm{d}\Omega\,\mathrm{d}\mathcal{E}}, \tag{2.79}$$

where E is the total energy through the surface of area dA and $\mathcal{E}$ denotes the energy of the individual particles contributing to $I_{\mathcal{E}}$, just as ν was the frequency of the individual particles contributing to I_ν.

By replacing $\mathcal{E} = h\nu$ in the expression above, which is valid in the case of photons, one sees that $I_{\mathcal{E}} = I_\nu/h$. This is expected, since $\mathcal{E} = h\nu$ and so (2.79) has an extra factor of h in the denominator. As such, a definition of specific intensity in terms of particle energy is sensible and can be used for the transport of both massive and massless particles, being easily converted into the usual specific intensity for the case of photons, I_ν, by a factor of h.

Following the same procedure as in section 1.3.2.ii), it is possible to construct a covariant quantity related to this energy-based intensity for massive particles. Consider the number all particles within the same phase space volume, $\mathrm{d}\mathcal{N}_{|\boldsymbol{p}|} = \mathcal{F}\,([c]\,\mathrm{d}t)\,\mathrm{d}A\,|\boldsymbol{p}|^2\,\mathrm{d}|\boldsymbol{p}|\,\mathrm{d}\Omega$ (equation (1.15)). In section 1.3.2.ii) it was useful to rewrite this quantity in term of the particle's frequency instead of momentum ($\mathrm{d}\mathcal{N}_\nu = \mathcal{F}\,(h\nu/[c])^2\,([c]\,\mathrm{d}t)\,\mathrm{d}A\,(hd\nu/[c])\,\mathrm{d}\Omega$). In the present section we want to write it in terms of the particle's energy, $\mathcal{E}$.

For massive particles, in a local orthonormal frame, the 4-momentum is related to the particle's total energy $\mathcal{E}$ and mass m via $p_\mu p^\mu = -(\mathcal{E}/[c])^2 + |\boldsymbol{p}|^2 = -m^2[c^2]$. So we have

$$\mathcal{E} = \sqrt{m^2[c^4] + |\boldsymbol{p}|^2[c^2]}, \tag{2.80}$$

$$\frac{\mathrm{d}\mathcal{E}}{\mathrm{d}|\boldsymbol{p}|} = [c]\frac{|\boldsymbol{p}|}{\mathcal{E}} \Leftrightarrow \mathrm{d}|\boldsymbol{p}| = \frac{\mathcal{E}}{[c]|\boldsymbol{p}|}d\mathcal{E}, \tag{2.81}$$

$$|\boldsymbol{p}| = \frac{1}{[c]}\sqrt{\mathcal{E}^2 - m^2[c^4]}, \tag{2.82}$$

where the positive roots were chosen so that the definition of the particle's energy and the magnitude of its 3-momentum are positive. From the equations above, $\mathrm{d}|\boldsymbol{p}|$ may be written in terms of $\mathrm{d}\mathcal{E}$ as:

$$\mathrm{d}|\boldsymbol{p}| = \frac{\mathcal{E}}{[c]|\boldsymbol{p}|}d\mathcal{E} = \frac{\mathcal{E}}{[c]\sqrt{\mathcal{E}^2 - m^2[c^4]}}\mathrm{d}\mathcal{E}. \tag{2.83}$$

Then, by replacing $|\boldsymbol{p}|$ and $\mathrm{d}|\boldsymbol{p}|$ in equation (1.15), one can define $\mathrm{d}\mathcal{N}_\mathcal{E}$ written in terms of the particle's energy:

$$\begin{aligned} d\mathcal{N}_\mathcal{E} &= \mathcal{F}\,[c]\,|\boldsymbol{p}|^2\,\mathrm{d}|\boldsymbol{p}|\,\mathrm{d}t\,\mathrm{d}A\,\mathrm{d}\Omega\big|_\mathcal{E} \\ &= \mathcal{F}\,[c]\,\left(\frac{1}{[c^2]}(\mathcal{E}^2 - m^2[c^4])\right)\left(\frac{\mathcal{E}}{[c^2]\sqrt{\mathcal{E}^2 - m^2[c^4]}}\mathrm{d}\mathcal{E}\right)\,\mathrm{d}t\,\mathrm{d}A\,\mathrm{d}\Omega \\ &= \mathcal{E}\sqrt{\mathcal{E}^2 - m^2[c^4]}\frac{\mathcal{F}}{[c^2]}\,\mathrm{d}t\,\mathrm{d}A\,\mathrm{d}\Omega \end{aligned} \tag{2.84}$$

The total energy going through a surface of area dA in time dt due to particles with momentum in $d|\boldsymbol{p}|$ and total energy $\mathcal{E}$ is then given by

$$\begin{aligned} \mathrm{d}E &= \mathcal{E}\,d\mathcal{N}_\mathcal{E} \\ &= \mathcal{E}^2\,\sqrt{\mathcal{E}^2 - m^2[c^4]}\frac{\mathcal{F}}{[c^2]}\,\mathrm{d}\mathcal{E}\,\mathrm{d}t\,\mathrm{d}A\,\mathrm{d}\Omega. \end{aligned} \tag{2.85}$$

By comparing this to the definition of $I_\mathcal{E}$ it is easy to see that[17]

$$I_\mathcal{E} = \mathcal{E}^2\sqrt{\mathcal{E}^2 - m^2[c^4]}\,\left(\frac{\mathcal{F}}{[c^2]}\right). \tag{2.86}$$

One can also define a new covariant quantity $\mathcal{I}_\mathcal{E}$, analogous to $\mathcal{I}_\nu$ as

$$\mathcal{I}_\mathcal{E} \coloneqq \frac{I_\mathcal{E}}{\mathcal{E}^2\sqrt{\mathcal{E}^2 - m^2[c^4]}} = \frac{\mathcal{F}}{[c^2]} \tag{2.87}$$

where $\mathcal{F}$ is again the phase space density of the particles.

By taking $m \to 0$ and replacing $\mathcal{E} = h\nu$ and $I_\mathcal{E} = I_\nu/h$ in (2.87), one can check that, in the massless limit:

$$\mathcal{I}_\mathcal{E}\,|_{m\to 0} = \frac{I_\nu}{\nu^3 h^4} = \frac{\mathcal{I}_\nu}{h^4}. \tag{2.88}$$

The fact that the two covariant intensity quantities defined above, $\mathcal{I}_\nu$ and $\mathcal{I}_\mathcal{E}$, differ only by a

[17] c.f. Lindquist (1966) eq. 2.7.

constant factor of h^4 indicates that both are valid for transporting massless particle radiation, while the later is more useful for the transport of massive particles. As such, in the remainder of this thesis $\mathcal{I}_\mathcal{E}$ will be used for both massive and massless particles, and for simplicity we will refer to this quantity as the covariant intensity.

i) Observables

The GRRT formulation described in this thesis can be used to accurately calculate observables corresponding to astrophysical events and processes. The fundamental output of the code is the covariant intensity $\mathcal{I}_\mathcal{E}^{(i)}$ along each geodesic i as a function of observed (or emitted, depending on the context) particle energy, $\mathcal{E}$. Given this information, it is easy to calculate observables such as specific intensities, fluxes, luminosities etc.

In this thesis, factors such as distance to the source or solid angle spanned by it are not relevant, since the focus is mainly on the morphology of images, spectra and light curves and not so much on their numerical values. As such, the results are mainly presented in terms of intensities and fluxes. In particular, the following quantities are calculated:

- **Observer images:** These show the total intensity detected by each pixel i in the observer frame at time t in the observer plane, $I^{(i)}(t)$. I.e. the sum of the specific intensity over all observed particle energies: $I^{(i)}(t) = \sum_\mathcal{E} {I_\mathcal{E}}^{(i)}(t) = \sum_\mathcal{E} \left(\mathcal{E}^2\sqrt{\mathcal{E}^2 - m^2[c^4]}\right) {\mathcal{I}_\mathcal{E}}^{(i)}(t)$. This has dimensions of specific intensity integrated over particle energy, which in cgs units is $\mathrm{erg}/(\mathrm{t\,cm^2\,sr})$. In order to convert this into a luminosity, one would only need to multiply the result by a factor of $A\Omega$, where A is the area of each detector pixel and Ω the solid angle spanned by the source in the observer's sky.

- **Spectra, light curves and spectrograms:** These show the detected intensity across all pixels as a function of particle energy (in spectra), time (in light curves) or both (in spectrograms). This quantity is denoted by $I_\mathcal{E}(t) = \sum_i {I_\mathcal{E}}^{(i)}(t) = \sum_i \left(\mathcal{E}^2\sqrt{\mathcal{E}^2 - m^2[c^4]}\right) {\mathcal{I}_\mathcal{E}}^{(i)}(t)$. Spectra are generally plotted at a specific time snapshot or a time interval. In the latter case, $I_\mathcal{E}(t)$ is summed over all snapshots in that time interval and the plot shows $(\mathcal{E}, I_\mathcal{E})$, where we defined $I_\mathcal{E} = \sum_t I_\mathcal{E}(t)$. In some cases, a spectral energy density (SED) plot is presented instead of a spectrum, for ease of comparison with previous results from literature. In SED plots, the quantity shown is $\mathcal{E}I_\mathcal{E} = \sum_t \mathcal{E}\, I_\mathcal{E}(t)$. Whether a spectrum ($I_\mathcal{E}$) or SED ($\mathcal{E}I_\mathcal{E}$) are plotted is clearly stated in the labels and captions of the relevant figures. For light curves, $I_\mathcal{E}(t)$ is summed over all observed energies before being plotted, i.e. the plot shows $I(t) = \sum_\mathcal{E} I_\mathcal{E}(t)$ as a function of observation time, i.e. $(t, I(t))$. For spectrograms, $I_\mathcal{E}(t)$ is plotted for each time for each detected energy, hence providing a visualization of the time dependent spectral evolution of the detections. It is a stacking of spectra across all observation times into the same plot.

In order to make quantitative astrophysical predictions, these results can be easily scaled by knowing the detector area, the distance between the detector and the source and the solid angle spanned by the source in the observer's sky plane. These are case specific and only change the results by a scaling factor. In this thesis such factors are neglected.

2.3 Generalized covariant GRRT equations

In Lindquist (1966), the author derived a covariant form of the transport equations using the tools of Principal Bundles for particles with arbitrary mass (i.e. massive or massless). The starting point of the formalism developed there is the relativistic generalization of Boltzmann's transport equation (equation (1.14)), given by (Lindquist, 1966):

$$p^\mu \frac{\mathrm{D}}{\mathrm{d}x^\mu}\mathcal{F} = \left(\frac{\mathrm{d}\mathcal{F}}{\mathrm{d}\lambda}\right)_{col}, \tag{2.89}$$

where λ is either the geodesic parameter (for null geodesics) or the proper time (for timelike geodesics) along the geodesic of a fiducial particle; $\mathcal{F}$ is the covariant distribution function (or phase-space density) as defined in section 1.3.2; p^μ is the 4-momentum of the fiducial particle; and $\mathrm{D}/\mathrm{d}x^\mu$ is an operator defined for convenience in Lindquist (1966) as $\mathrm{D}/\mathrm{d}x^\mu := \partial/\partial x^\mu - \Gamma_\mu{}^\alpha{}_\beta\, p^\beta \partial/\partial p^\alpha$. As explained by the author, the term $p^\mu \frac{\mathrm{D}\mathcal{F}}{\mathrm{d}x^\mu}$ is the directional derivative of $\mathcal{F}$ along the geodesic parameterized by λ.

The transport equation in this fully covariant form is derived in Lindquist (1966) (c.f. equation (1.6)):

$$p^\mu \frac{\mathrm{D}}{\mathrm{d}x^\mu}\mathcal{F} = n_0 \kappa \left(-\mathcal{F} + \mathcal{J}\right) \tag{2.90}$$

where $\mathcal{J}$ is the covariant source function, n_0 is the proper number density of the medium (i.e. the number density of the medium in its own rest frame, which is a Lorentz scalar and hence covariant), and κ is the covariant absorption coefficient[18].

While equation (2.90) is extremely elegant, when performing practical calculations it is useful to write in terms of quantities which can be determined from micro-physics. In particular, it is useful to write this equation in terms of quantities such as the usual absorption and emission coefficients in the proper rest frame of the medium[19], α_0 and j_0 respectively. In order to do this, one must first understand how the covariant quantities in equation (2.90) relate to α_0 and j_0.

[18] See section 2.3.2 for a discussion on these quantities.
[19] By proper rest frame, we mean the same as the medium's local co-moving frame.

2.3.1 Total derivative

The operator $\mathrm{D}/\mathrm{d}x^\mu \coloneqq \partial/\partial x^\mu - \Gamma_\mu{}^\alpha{}_\beta\, p^\beta \partial/\partial p^\alpha$ was introduced in Lindquist (1966) for convenience. One can re-write this in a form more useful for practical GRRT calculations by looking at the geodesic equation in terms of the particle's momentum instead of its 4-velocity.

In a Cartesian coordinate system, the particle's 4-velocity is given by $u = (c\dot{t}, \dot{x}, \dot{y}, \dot{z})$. As discussed in section 2.1.2.ii), for massive particles the particle's 4-momentum p and its four velocity u are related by $p = mu$ and for massless particles, one can define $p \coloneqq (\hat{\mathcal{E}}/[c^2])u$ (see equation (2.35)). Using this, the geodesic equation $\ddot{x}^\alpha + \Gamma_\mu{}^\alpha{}_\beta\, \dot{x}^\beta \dot{x}^\mu = 0$ can be written as

$$(\hat{\mathcal{E}}/[c^2])\mathrm{d}p^\alpha/\mathrm{d}\lambda = -\Gamma_\mu{}^\alpha{}_\beta\, p^\beta p^\mu \tag{2.91}$$

for massless particles and

$$m\,\mathrm{d}p^\alpha/\mathrm{d}\lambda = -\Gamma_\mu{}^\alpha{}_\beta\, p^\beta p^\mu \tag{2.92}$$

for massive particles. Given that $\mathcal{F} = \mathcal{F}(x, p)$ and considering its total derivative, the left hand side of equation (2.90) can be written as[20]:

$$\begin{aligned} p^\mu \frac{\mathrm{D}}{\mathrm{d}x^\mu}\mathcal{F} &= \left[p^\mu \frac{\partial}{\partial x^\mu} - \Gamma_\mu{}^\alpha{}_\beta\, p^\beta p^\mu \frac{\partial}{\partial p^\alpha}\right]\mathcal{F} \\ &= \left[p^\mu \frac{\partial}{\partial x^\mu} + m\frac{\mathrm{d}p^\alpha}{\mathrm{d}\lambda}\frac{\partial}{\partial p^\alpha}\right]\mathcal{F} \\ &= m\left[\frac{\mathrm{d}x^\alpha}{\mathrm{d}\lambda}\frac{\partial}{\partial x^\alpha} + \frac{\mathrm{d}p^\alpha}{\mathrm{d}\lambda}\frac{\partial}{\partial p^\alpha}\right]\mathcal{F} \\ &= m\frac{\mathrm{d}\mathcal{F}}{\mathrm{d}\lambda} \end{aligned} \tag{2.94}$$

[20] **A note on dimensions**
One can get some insight into the parameters used in the timeline and null geodesics above by doing some dimensional analysis. Below, square brackets are used to represent the dimension of whatever physical quantity is inside them. The left-hand-side of both equations (2.94) and (2.95) has dimensions of

$$[p][x]^{-1}[\mathcal{F}] = MLT^{-1}L^{-1}[\mathcal{F}] = MT^{-1}[\mathcal{F}] \tag{2.93}$$

The right hand side of equation (2.94) has dimensions $[m][\lambda]^{-1}[\mathcal{F}] = M[\lambda]^{-1}[\mathcal{F}]$. Equating this to (2.93), for the dimensions to be correct, it is required that $[\lambda] = T$, i.e. the parameter used in the geodesics has dimensions of time. This makes sense, since one typically parameterizes timelike geodesics with a parameter proportional to proper time, which has dimensions of time.

For the case on null geodesics, the right hand side of equation (2.95) has dimensions $[\mathcal{E}_0/c^2][\lambda]^{-1}[\mathcal{F}] = ML^2T^{-2}T^2L^{-2}[\lambda]^{-1}[\mathcal{F}] = M[\lambda]^{-1}[\mathcal{F}]$, the same as for timelike geodesics. In order to equate this to (2.93), it is again required that $[\lambda] = T$. Note that, although the affine parameter used to parameterize null geodesics is not proportional to proper time (since there is no passage of proper time in null geodesics), it still has dimensions of time. (In unit systems where $c = 1$ this is the same as the dimension of length.)

for massive particles along timelike geodesics and

$$\begin{aligned} p^\mu \frac{\mathrm{D}}{\mathrm{d}x^\mu}\mathcal{F} &= \left[p^\mu \frac{\partial}{\partial x^\mu} - \Gamma_\mu{}^\alpha{}_\beta\, p^\beta p^\mu \frac{\partial}{\partial p^\alpha}\right]\mathcal{F} \\ &= \left[p^\mu \frac{\partial}{\partial x^\mu} + \frac{\hat{\mathcal{E}}}{[c^2]}\frac{\mathrm{d}p^\alpha}{\mathrm{d}\lambda}\frac{\partial}{\partial p^\alpha}\right]\mathcal{F} \\ &= \frac{\hat{\mathcal{E}}}{[c^2]}\left[\frac{\mathrm{d}x^\alpha}{\mathrm{d}\lambda}\frac{\partial}{\partial x^\alpha} + \frac{\mathrm{d}p^\alpha}{\mathrm{d}\lambda}\frac{\partial}{\partial p^\alpha}\right]\mathcal{F} \\ &= \frac{\hat{\mathcal{E}}}{[c^2]}\frac{\mathrm{d}\mathcal{F}}{\mathrm{d}\lambda} \end{aligned} \tag{2.95}$$

for massless particles along null geodesics.

i) The classical 4-momentum of photons

In this section the 4-momentum for photons was constructed in terms of their 4-velocity as

$$p = \frac{\hat{\mathcal{E}}}{[c^2]}u = \frac{\hat{\mathcal{E}}}{[c^2]}\left([c]\dot{t}, \dot{\boldsymbol{x}}\right) = \frac{\dot{t}\hat{\mathcal{E}}}{[c^2]}([c], \boldsymbol{v}) = \frac{\dot{t}\hat{\mathcal{E}}}{[c]}(1, \hat{\boldsymbol{n}}), \tag{2.96}$$

where $\boldsymbol{v} = [c]\hat{\boldsymbol{n}}$ is the 3-velocity of the photon and $\hat{\boldsymbol{n}}$ the unit vector in the direction of propagation. From a dimensional analysis perspective, this definition is reasonable. One can understand the physical significance of this proportionality factor by comparing it to the equivalent relationship for massive particles.

For massive particles, there is a meaningful concept of intrinsic energy - the rest mass energy in the particle's rest frame $\hat{\mathcal{E}} = m[c^2]$. This $m = \hat{\mathcal{E}}/[c^2]$ is precisely the proportionality factor between p and u. Such a concept of intrinsic energy does not exist for massless particles. However, by picking a particular observer, one can formulate a concept analogue to this intrinsic energy: the energy measured by some agreed upon observer. Then $\hat{\mathcal{E}}/[c^2]$ in equation (2.35) is the massless equivalent to the rest mass $m = \hat{\mathcal{E}}/[c^2]$ for massive particles. Of course for photons $\hat{\mathcal{E}}$ is arbitrary, unlike for massive particles. But once an observer is agreed upon, then $\hat{\mathcal{E}}$ for photons is the same in any frame. It is usual to chose this reference observer to be a stationary observer at infinity, although any other observer would be equally valid.

A final note goes to the relationship between the classical momentum of a photon as defined in this way and the usual quantum mechanical momentum of photons, $p = \hbar k$, where k is its relativistic 4-wavevector. In vacuum, the dispersion of light is given by $|\boldsymbol{k}| = \omega/[c]$, where $\omega = 2\pi/\nu$ is the angular frequency of the wave. So the 4-momentum of photons in a non-dispersing medium can be written as $p = \hbar(\omega/[c], \boldsymbol{k}) = \hbar(\omega/[c], |\boldsymbol{k}|\hat{\boldsymbol{n}}) = (\hbar\omega/[c])(1, \hat{\boldsymbol{n}})$. By comparison with equation (2.96), one may identify $\hbar\omega = \dot{t}\hat{\mathcal{E}}$. The right-hand side is the photon energy measured by a particular observer, which is related to that measured by an observer

at infinity (or whatever observer is chosen to define p) via an energy shift factor $\dot{t}$. The left hand side is also the energy of the photon measured by the particular observer, according to the Plank-Einstein relation. So the definition of the "classical" momentum of a photon as used in this chapter is indeed reasonable.

2.3.2 Covariant absorption and emission coefficients

As discussed at the end of section 1.3.2, it is useful to think of the distribution function of photons in terms of a photon intensity. In Lindquist (1966) the author shows that $I_\nu = (h^4/[c^2])\mathcal{F}\nu^3$, so that $\mathcal{F} = ([c^2]/h^4)\mathcal{I}_\nu$ (cf. equation (1.19)). Using the energy-related quantities defined in this chapter instead of the usual frequency-related quantities, one can show that, for both massless and massive particles, the relationship $\mathcal{F} = [c^2]\mathcal{I}_\mathcal{E}$ holds (as expected from equation (2.87)).

The absorption and emission coefficients are usually functions of the photon frequency. Analogously, for massive particles the absorption and emission coefficients are functions of the particle's total energy, $\mathcal{E}$. Following Lindquist (1966) (eq. 2.1), the covariant absorption coefficient κ is related to the usual absorption coefficient by

$$n_0\kappa = \alpha_0\sqrt{\mathcal{E}_0^2 - m^2[c^4]} = \alpha'_{(\mathcal{E}')}\sqrt{\mathcal{E}'^2 - m^2[c^4]} \tag{2.97}$$

where n_0 is the proper number density of the medium, which is a Lorentz scalar and hence covariant, α_0 is the absorption coefficient as measured in the local rest frame of the medium and $\mathcal{E}_0$ is the energy of the particles as measured in the medium's local rest frame. Since $n_0\kappa$ is covariant, its value is the same when measured in another frame, say a primed frame, where the measured absorption coefficient and particle energy are, respectively α' and $\mathcal{E}'$. Note than this definition of α is not *specific*, i.e. it implicitly includes information about the proper number density of the medium. The same is be true about the emissivity coefficient j as defined below.

Again, following the notation in Lindquist (1966), one can define a covariant emissivity coefficient[21] $Q = \kappa\mathcal{J}$. This can be related to the usual source function $S = j/\alpha$, where j is the usual emissivity coefficient, by first noting that, by the covariance of equation (2.90), the covariant source function $\mathcal{J}$ must relate to the usual source function S in the same way as $\mathcal{F}$ relates to the specific intensity $I_\mathcal{E}$, namely

$$\mathcal{J} = \frac{S[c^2]}{\mathcal{E}^2\sqrt{\mathcal{E}^2 - m^2[c^4]}} \tag{2.98}$$

In particular, in order to to relate Q to the usual emissivity in the medium's proper rest frame,

[21] In Lindquist (1966), scattering terms are also included in the definition of J, but in this thesis we restrict ourselves to scenarios without scattering, so that the definition becomes $\mathcal{J} = Q/\kappa$.

one may write (2.98) this frame, which will be labeled "$_0$". Then, Q and j are related as:

$$\begin{aligned} Q = \kappa\mathcal{J} &= \kappa\frac{S_0[c^2]}{\mathcal{E}_0^2\sqrt{{\mathcal{E}_0}^2 - m^2[c^4]}} \\ &= \left(\frac{\alpha_0}{n_0}\sqrt{\mathcal{E}_0^2 - m^2[c^4]}\right)\frac{[c^2]j_0/\alpha_0}{\mathcal{E}_0^2\sqrt{{\mathcal{E}_0}^2 - m^2[c^4]}} \\ &= \frac{[c^2]j_0}{n_0\mathcal{E}_0^2}. \end{aligned} \tag{2.99}$$

Then,

$$n_0\kappa\mathcal{J} = \frac{[c^2]j_0}{\mathcal{E}_0^2} = \sqrt{{\mathcal{E}_0}^2 - m^2[c^4]}\,\frac{[c^2]j_0}{\mathcal{E}_0^2\sqrt{{\mathcal{E}_0}^2 - m^2[c^4]}}. \tag{2.100}$$

Noting that $\mathcal{E}_0$ is simply the particle's energy in the proper rest frame of the medium, i.e. the particle's energy as measured by an observer co-moving with the medium, it can be re-written as ${\mathcal{E}_0}^2 = (p_\mu u^\mu)^2$, where u is the 4-velocity of the medium. In this way, the expression inside the square root can be rewritten in a manner very easy to compute along a particle's geodesic:

$$\sqrt{{\mathcal{E}_0}^2 - m^2[c^4]} = \sqrt{(p_\mu u^\mu)^2 - m^2[c^4]} = -p_\mu u^\mu\sqrt{1 - \frac{m^2[c^4]}{p_\mu u^\mu}}, \tag{2.101}$$

where the minus sign is due to the fact that $p_\mu u^\mu \leq 0$ for timelike or null geodesics but $\sqrt{(p_\mu u^\mu)^2} \geq 0$. The right hand side of equation (2.90) can now be written in terms of covariant intensity as

$$\begin{aligned} n_0\kappa\left(-\mathcal{F} + \mathcal{J}\right) &= \sqrt{{\mathcal{E}_0}^2 - m^2[c^4]}\left(-\alpha_0[c^2]\mathcal{I}_\mathcal{E} + \frac{[c^2]j_0}{{\mathcal{E}_0}^2\sqrt{{\mathcal{E}_0}^2 - m^2[c^4]}}\right) \\ &= -p_\mu u^\mu[c^2]\sqrt{1 - \left(\frac{m[c^2]}{p_\mu u^\mu}\right)^2}\left(-\alpha_0\mathcal{I}_\mathcal{E} + \frac{j_0}{{\mathcal{E}_0}^2\sqrt{{\mathcal{E}_0}^2 - m^2[c^4]}}\right) \end{aligned} \tag{2.102}$$

2.3.3 GRRT formulation - putting it all together

Finally, putting (2.94) or (2.95) and (2.102) together an expression of the covariant transport equation emerges where local absorption and emission coefficients, which can be obtained from micro-physical considerations, may be used without losing the covariance of the formulation:

$$\frac{\mathrm{d}\mathcal{I}_\mathcal{E}}{\mathrm{d}\lambda} = -\frac{p_\mu u^\mu}{(\hat{\mathcal{E}}/[c^2])}\sqrt{1 - \left(\frac{m[c^2]}{p_\mu u^\mu}\right)^2}\left(-\alpha_{0,\mathcal{E}_0}\mathcal{I}_\mathcal{E} + \frac{j_{0,\mathcal{E}_0}}{{\mathcal{E}_0}^2\sqrt{{\mathcal{E}_0}^2 - m^2[c^4]}}\right) \tag{2.103}$$

where $\hat{\mathcal{E}}$ is the rest mass energy for massive particles and the energy measured by a particular agreed upon observer used to define p (e.g. a stationary observer at infinity) for massless particles[22], while $\mathcal{E}_0$ is the total energy of the particle as measured by the medium at λ; all other quantities on the right hand side are evaluated at λ, with the subscript "$_0$" again referring to quantities measured in the local rest frame of the medium. The subscript $\mathcal{E}_0$ was added to the absorption and emission coefficients to make it explicit that they depend on the total energy as measured by a local observer co-moving with the medium. The "-" sign in the equation comes from the signature chosen $(-+++)$.

The physics of equation (2.103)

Equation (2.103) can be split into two terms: the term in brackets on the right, which describes the changes in intensity due to absorption and emission from the medium. The second term, given by

$$-\frac{p_\mu u^\mu}{(\hat{\mathcal{E}}/[c^2])}\sqrt{1-\left(\frac{m[c^2]}{p_\mu u^\mu}\right)^2} \tag{2.104}$$

where p refers to the particle's 4-momentum and u to the observer's (or medium's) 4-velocity, is a correction factor which appears due to the covariant treatment of the transport equations.

For massless particles, the correction factor is simply $p_\mu u^\mu/(\hat{\mathcal{E}}/[c^2])$, where $\hat{\mathcal{E}}$ is the energy of the photon measured by a chosen observer with 4-velocity $\hat{u}$. By definition, $\hat{\mathcal{E}}$ is such that the photon's 4-momentum is rrelated to its 4-velocity, u_p, via $p_p = (\hat{\mathcal{E}}/[c^2])u_p$. Let $\hat{u}_p = ([c]\dot{\hat{t}}, \dot{\hat{x}}, \dot{\hat{y}}, \dot{\hat{z}})$ be the photon's velocity in Cartesian coordinates as measured in the hatted observer's rest frame, i.e. the frame where $\hat{u} = [c](1,0,0,0)$. Then the photon's momentum in this frame can be written as $\hat{p}_p = (\hat{\mathcal{E}}/[c^2])([c]\dot{\hat{t}}, \dot{\hat{x}}, \dot{\hat{y}}, \dot{\hat{z}})$.

Then, in this frame, it is clear that $(\hat{p}_p)_\alpha \hat{u}^\alpha = -\hat{\mathcal{E}}\dot{\hat{t}}$, where $\dot{t}$ is the rate of change of the photon's time coordinate as viewed by the hatted observer. Of course this is true in any other frame, i.e. regardless of what frame we use to calculate $(\hat{p}_p)_\alpha \hat{u}^\alpha$, it will always correspond to the photon's energy as measured by the hatted observer multiplied by the rate of change of the photon's time coordinate as measured by that same observer.

But since by definition $\hat{\mathcal{E}}$ is the energy measured by the hatted observer, one must have $\dot{\hat{t}} = 1$. This means that the observer chosen as a reference for the definition of 4-momentum is also the

[22] In e.g (Younsi et al., 2012; Younsi and Wu, 2015) and other papers by the same authors, a similar GRRT formulation is used for the massless particles, albeit in terms of frequency rather than energy. However, one might notice that the factor of $\hat{\mathcal{E}}/[c^2]$ does not appear for massless particles. This is the case because the authors use the photon's 4-velocity instead of its 4-momentum. As such, they do not need this extra factor, which in our formulation appears as a conversion between 4-velocity and 4-momentum. Since we are mostly interested in massive particles, however, where formulating the equations in terms of 4-momentum makes the calculations easier, we keep this factor for massless particles too.

reference for the ticking of a clock. It also implies that the affine parameter for the geodesic has been chosen such that it is equivalent to the time measured by this observer.

Now suppose that at some point in the photon's trajectory, say at $x^\mu(\lambda)$ the photon encounters some medium with 4-velocity u', in whose local rest frame, the photon's 4-velocity is measured to be $u'_p = ([c]\dot{t}', \dot{x}', \dot{y}', \dot{z}')$ and the 4-momentum $p'_p = (\hat{\mathcal{E}}/[c^2])([c]\dot{t}', \dot{x}', \dot{y}', \dot{z}')$. The photon's energy measured in this frame is then given by $\mathcal{E}' = -p'_{p,\alpha}u'^\alpha = \hat{\mathcal{E}}\dot{t}'$ where $\dot{t}' = \dot{t}'(\lambda)$, i.e. it varies along the photon's geodesic.

Comparing this with the results for the hatted frame, one can see that $\dot{t}'(\lambda) = \mathcal{E}'/\hat{\mathcal{E}}$. This means that, at each point along the geodesic, $\dot{t}'(\lambda)$ is the energy shift factor, the ratio of the energy measured by the chosen arbitrary observer used in the definition of p and the particular observer encountered by the photon at that point in its trajectory. In other words, $\dot{t}'$ encompasses the information about the Doppler shift and gravitational redshift between that point in the geodesic and the point chosen to be the "standard observer". In this perspective, it becomes clear that gravitational and Doppler energy shifts are simply a result of clocks ticking differently in different frames, rather than of the photon gaining or losing "intrinsic energy" (c.f. the discussion in section 2.1.2.ii)).

If the hatted observer is chosen to be a stationary observer at infinity, then $\dot{t}'(\lambda)$ is the ratio between the energy measured by the observer with 4-velocity $u'(\lambda)$ at λ and the energy measured by the stationary observer at infinity. This is in fact the interpretation of the factor presented in e.g. (Younsi et al., 2012), though here we show its more general physical meaning, regardless of the choice of reference observer.

With this in mind, the correction factor $p_\mu u^\mu/(\hat{\mathcal{E}}/[c^2])$ is, up to a factor of $[c^2]$, simply the energy shift factor between the chosen observer and the observer with velocity u at that point in the geodesic.

For massive particles, the $p_\mu u^\mu/(\hat{\mathcal{E}}/[c^2])$ factor has the same interpretation, except now the chosen observer is always the particle itself, since the energy $\hat{\mathcal{E}}$ is now the particle's rest mass energy. So, this part of the correction factor is just the difference in energy measured by the observer at each point of the geodesic and the particle's intrinsic rest mass energy.

The term inside the square root is maximum for massless particles, for which $m = 0$. In this case, the whole term reduces to 1. For massive particles the effect of the term is to decrease the changes in covariant intensity depending on how relativistic a particle is. For highly relativistic particles (with respect to the medium with velocity u), $m[c^2]/(p_\mu u^\mu) \to 0$ and so this term approaches 1, as for photons. For less relativistic particles, this term will reduce the effect of absorption and emission along the particle's geodesic. In the extreme case of a medium comoving with the particle, $m[c^2]/(p_\mu u^\mu) = 1$ so that $\sqrt{1 - \left(\frac{m[c^2]}{p_\mu u^\mu}\right)^2} = 0$. This means that

there will be effectively no emission nor absorption along the geodesic. This makes sense since this case represents a particle effectively "frozen into" the medium, so that no interactions take place. For massless particles this can never occur, as it is not possible for the medium to co-move with them.

i) Relativistic beaming

Using covariant intensity in the radiative transport formulation deals not only with gravitational and relativistic energy shifts, but also with relativistic beaming. This is the phenomenon by which isotropic emission by a body in its own rest frame appears, in a frame with respect to which it is moving relativistically, to be beamed into the direction of motion of the body. In order to see how this is taken care of in the covariant formulation described in this chapter, consider the following.

The specific intensity is defined as $I_{\mathcal{E}} = \mathrm{d}E\mathrm{d}A\,\mathrm{d}t\,\mathrm{d}\Omega\,\mathrm{d}\mathcal{E}$ (see equation (2.79)). While this specific intensity will be different in frames moving with respect to each other, the covariant intensity $\mathcal{I}_{\mathcal{E}}$ is same in all frames.

Consider a case similar to what will be discussed in detail in chapter 3: a body on an orbit around a black hole, emitting radiation isotropically and mono-chromatically with energy $\mathcal{E}_0$ in its own rest frame, which is seen by a stationary observer far away, edge-on (i.e. at $\theta_{\mathrm{obs}} = 90°$ in figure 2.1). When the object is moving away from the observer, the energy of rays emitted towards the observer will be redshifted to $\mathcal{E}_r < \mathcal{E}_0$. The redshift, $\mathcal{E}_r/\mathcal{E}_0 < 1$ will be further from 1 the faster the object is moving away from the observer. Since the covariant intensity is the same in both frames, then the detected intensity $I_{\mathcal{E}_r,\mathrm{obs}} < I_{\mathcal{E}_0,0}$.

Conversely, consider a portion of the rays emitted in the direction of motion. The observer will measure their energy to be blueshifted, say $\mathcal{E}_b > \mathcal{E}_0$. Then the detected intensity from that direction will be $I_{\mathcal{E},\mathrm{obs}} > I_{\mathcal{E},0}$.

The specific intensity can be thought of as the sum over all photons of the photon energy. So, in a way, it measures the number of photons in a bundle. The increase in the observed intensity when the emitter is moving towards the observer and, conversely, the decrease when it moves away from it, encompasses the beaming effect, by which more radiation is seen to be emitted in the direction of motion and less in the opposite direction.

2.3.4 Solving the GRRT equations

In practice, the GRRT equation are solved along the geodesics of the particles at the same time as the geodesic equations are integrated. Following a similar procedure to that in Younsi (2013), the code integrates the geodesic using an adaptive step size Runge–Kutta–Fehlberg-4/5

integrator[23]. Then, at each point of the integration, it integrates the GRRT equation using a simple Euler method with the same step size as that used for the geodesic integration. The actual integration is performed for a set of two coupled differential equations obtained from equation (2.103). First, one may use an integrating factor to find the analytical expression for the solution, obtaining the following result:

$$\begin{aligned}\mathcal{I}_{\mathcal{E}}(\lambda) = {} & \mathcal{I}_{\mathcal{E}}(\lambda_0)\mathrm{e}^{-\tau_{\mathcal{E}}(\lambda)} \\ & - \int_{\lambda_0}^{\lambda} \mathrm{d}\lambda'' \left(\left(\frac{p_\alpha u^\alpha}{(\hat{\mathcal{E}}/[c^2])} \sqrt{1 - \left(\frac{m[c^2]}{p_\mu u^\mu} \right)^2} \right) \right|_{\lambda''} \\ & \times \frac{j_{0,\mathcal{E}_0}}{{\mathcal{E}_0}^2 \sqrt{{\mathcal{E}_0}^2 - m^2[c^4]}} \exp \left[- \int_{\lambda''}^{\lambda} \mathrm{d}\lambda' \left(\left(\frac{p_\alpha u^\alpha}{(\hat{\mathcal{E}}/[c^2])} \sqrt{1 - \left(\frac{m[c^2]}{p_\mu u^\mu} \right)^2} \right) \right|_{\lambda'} \alpha_{0,\mathcal{E}_0}(\lambda') \right) \right] \Bigg)\end{aligned} \tag{2.105}$$

where the *optical depth* is defined as

$$\tau_{\mathcal{E}}(\lambda) = \int_{\lambda_0}^{\lambda} \mathrm{d}\lambda' \left(- \left(\frac{p_\alpha u^\alpha}{(\hat{\mathcal{E}}/[c^2])} \sqrt{1 - \left(\frac{m[c^2]}{p_\mu u^\mu} \right)^2} \right) \right|_{\lambda'} \alpha_{0,\mathcal{E}_0}(\lambda') \Bigg) . \tag{2.106}$$

Then, equations (2.105) and (2.106) are differentiated with respect to the affine parameter λ. In most cases to which GRRT is applied, the background radiation is negligible, i.e. $\mathcal{I}_{\mathcal{E}}(\lambda_0) = 0$ (this is the case in scenarios such as those considered in chapter 3). As such, for these cases we can write:

$$\frac{\mathrm{d}\tau_{\mathcal{E}}}{\mathrm{d}\lambda} = - \left(\frac{p_\alpha u^\alpha}{(\hat{\mathcal{E}}/[c^2])} \sqrt{1 - \left(\frac{m[c^2]}{p_\mu u^\mu} \right)^2} \right) \alpha_{0,\mathcal{E}_0} \tag{2.107}$$

$$\frac{\mathrm{d}\mathcal{I}_{\mathcal{E}}}{\mathrm{d}\lambda} = - \left(\frac{p_\alpha u^\alpha}{(\hat{\mathcal{E}}/[c^2])} \sqrt{1 - \left(\frac{m[c^2]}{p_\mu u^\mu} \right)^2} \right) \left(\frac{j_{0,\mathcal{E}_0}}{{\mathcal{E}_0}^2 \sqrt{{\mathcal{E}_0}^2 - m^2[c^4]}} \right) \mathrm{e}^{-\tau_{\mathcal{E}}} . \tag{2.108}$$

Equations (2.107) and (2.108) are straightforward to solve along a geodesic: m, the particle's

[23] A few other higher order integrators were tested, especially for massive particles with different mass to energy ratios. However, it was found that no single one of these was better for all particles and that, depending on the fine tuned error parameters, some integrators were better for some mass to energy ratios and others for other. Different integrators are built into the code, so for a specific problem a different integrator can be used. However, the results presented in this thesis were all calculated with the Runge–Kutta–Fehlberg-4/5 integrator. The other available Runge-Kutta integrators are: Dormand-Prince-4/5, Dormand-Price-4/5; Sharp-Smart-4/5, Dormand-Prince-4/5; Dormand-Prince-5/6; Dormand-Prince-7/8, Enrught-Verner-7/8; Feagin-8/10; Legendre-9/10; Feagin-10/12; Peter-11/12; Feagin-12/14.

mass, is known; $\alpha_{0,\mathcal{E}_0}$ and $j_{0,\mathcal{E}_0}$ are the absorption and emission coefficients of the medium that the particles go through in its own rest frame and are found from the relevant micro-physics; p is the particle's momentum at λ and it is related to its 4-velocity, which calculated in the geodesic integration; finally, u is the medium's 4-velocity at that same point in the geodesic. Given that the absorption and emission coefficients are generally energy dependent, these equations are calculated for each individual energy $\mathcal{E}$, so that the final result is an optical depth and a covariant intensity for each individual detected energy. An important detail is that the energy used for the absorption and emission coefficients must be the energy of the particle measured by a local observer co-moving with the medium: it is not the energy that the standard observer (e.g. the observer at infinity) measures.

By letting $m \to 0$ and $E = h\nu$ in equations (2.103),(2.107) and (2.108) the expressions given in Younsi et al. (2012) and Younsi (2013) for photons are recovered, noting that the authors use units where $G = c = h = 1$.

An important note is that these equations were not derived for a specific spacetime. The spacetime information is hidden in the metric used to calculate the dot products $p_\alpha u^\alpha$ and in the geodesic along which the equations are solved. In practice, however, all calculations presented in this thesis were performed in Schwarzschild or Kerr spacetimes.

2.4 Computational algorithm for the GRRT formalism

Equations (2.107) and (2.108) are solved along the particle geodesics using a simple Euler method with the same step size as in the the geodesic integration, $\Delta\lambda$. I.e., the optical depth and covariant intensity at integration step i are calculated as

$$\tau_{\mathcal{E}}{}^{(i)} = \tau_{\mathcal{E}}{}^{(i-1)} + \Delta\lambda \left[\left(\frac{-p^*_\alpha u^\alpha}{(\hat{\mathcal{E}}/[c^2])} \sqrt{1 - \left(\frac{m[c^2]}{p^*_\mu u^\mu} \right)^2} \right) \alpha_{0,\mathcal{E}_0} \right]^{(i-1)} \tag{2.109}$$

$$\mathcal{I}_{\mathcal{E}}{}^{(i)} = \mathcal{I}_{\mathcal{E}}{}^{(i-1)} + \Delta\lambda \left[\left(\frac{-p^*_\alpha u^\alpha}{(\hat{\mathcal{E}}/[c^2])} \sqrt{1 - \left(\frac{m[c^2]}{p^*_\mu u^\mu} \right)^2} \right) \left(\frac{j_{0,\mathcal{E}_0}}{{\mathcal{E}_0}^2 \sqrt{{\mathcal{E}_0}^2 - m^2[c^4]}} \right) \mathrm{e}^{-\tau_\mathcal{E}} \right]^{(i-1)} . \tag{2.110}$$

When performing forward ray tracing, $p^* = p$ is the particle's 4-momentum. However, when performing backward ray tracing, the particle's momentum which comes out of the geodesic integration is pointing in the wrong direction (spatially and in time). As such, it is first necessary to reverse the particle's momentum so that it is pointing in the correct direction when moving forward in time, i.e. $p^* = -p$. This step is necessary because all other quantities, namely the fluid's four velocity u, are defined in the positive time direction.

At each point in the geodesic integration, the following algorithm is used to update the covariant

intensity and optical depth[24]:

1. Find $p^* = -p$. For massive particles, calculate the energy shift factor $-p^*_\alpha u^\alpha/(\hat{\mathcal{E}}/[c^2])$. Calculate also the massive particle correction factor (the square root term in (2.104)). For massless particles, simply calculate $-p^*_\alpha u^\alpha/(\hat{\mathcal{E}}/[c^2]) = -u_{(p)\alpha}u^\alpha$, where $u_{(p)}$ is the photon's four velocity. All of this is calculated using the coordinates of the particle's location at the previous integration step.

2. Using this energy shift factor, calculate the energy of the particles as measured by local observers $\mathcal{E}_0$.

3. Find the local absorption, $\alpha_{0,\mathcal{E}_0}$, and emissivity, $j_{0,\mathcal{E}_0}$ for those energies at the particle's coordinates in the previous integration step.

4. Find the medium's four velocity u at the coordinates occupied by the particle in the previous integration step.

5. Finally, calculate ${\tau_\mathcal{E}}^{(i)}$ and ${\mathcal{I}_\mathcal{E}}^{(i)}$ using equations (2.109)-(2.110).

Since this calculation requires knowledge of the previous integration step, the algorithm always stores both the current and the previous integration steps. Since the trajectory of massless particles is independent of their energy, the process above is performed for all observed energies simultaneously, in a vectorized manner. For massive particles, on the other hand, different energies will result in different initial conditions and, therefore, different trajectories. As such, the algorithm can only be performed for one energy at a time, with each new energy requiring the calculation of new geodesics.

The scenario covered in chapter 4 is different: there one considers a source of background radiation and no further emission along the line of sight, i.e. $\mathcal{I}_\mathcal{E}(\lambda_0) \neq 0$ and $j_{0,\mathcal{E}_0} = 0$. In this case, equation (2.107) remains the same but equation (2.108) no longer captures the correct behaviour of the system. In this case, the covariant intensity can be calculated directly from equation (2.105) as

$$\mathcal{I}_\mathcal{E}(\lambda) = \mathcal{I}_\mathcal{E}(\lambda_0)\mathrm{e}^{-\tau_\mathcal{E}(\lambda)} \tag{2.111}$$

[24]Other codes are available which perform either ray tracing or ray tracing with radiative transport, some analytically/semi-analytically and others fully numerically. Some are specific for particular spacetimes (mostly Kerr), while others are adaptable to different spacetimes, analytical or numerical. The most commonly used ones are the following:

- **Ray tracing only:** Dexter and Agol (2009), and GRay (Chan et al., 2013)
- **Ray tracing with radiative transport:** GRTRANS (Dexter, 2016), which also calculates transport of polarization; Odyssey (Pu et al., 2016b); RAPTOR (Bronzwaer et al., 2018); Elysium Koutsantoniou (2022)

where the optical depth at each step is calculated as per equation (2.109).

2.4.1 Tests and demonstrations

The first test performed on the GRRT code was to calculate the observed spectrum produced by an emitting disk around a black hole. In order to facilitate the validation, the parameters used are the same as in Fuerst and Wu (2004). Figure 2.13 shows the results of this calculation including the spectral energy density for the direct image only[25] and the full image of the disk.

In order to test the absorption part of the code, the image of an optically thick and geometrical thin equatorial disk was calculated, but this time considering the presence of a lump of absorbing material between the disk and the observer. In astrophysical situations, this scenario is very plausible: a cloud of dust or another object can easily obstruct the path of light (or other particles) between their emission and detection sites. For the purpose of this test, the absorbing body was modeled as sphere of radius $2\,r_{\rm g}$ with centre at $r = 8\,r_{\rm g}$ on a circular orbit around the black hole in the equatorial plane. This means that the absorbing body is both above and below the emitting disk, being able to absorb radiation emitted upward or downward from the disk. The results are presented in figure 2.14.

For the purpose of making the image clearer, figure 2.14 is an instantaneous snapshot of the disk's absorption by the absorbing body (i.e. it assumes that all photons emitted simultaneously cross the absorber and reach the observer simultaneously). This allows us to focus on the effects of absorption alone, rather than on the effects of the motion of the absorbing body as the integration progresses. Note, however, that all physically relevant calculations in this thesis in chapters 3 and 4 do account for the photon travel time correctly.

[25] Just as in Fuerst and Wu (2004), the figure includes the image and SED considering direct images only. This is to facilitate the comparison of the results from the numerical calculations with theoretical spectral calculations, which can only be calculated for the direct image.

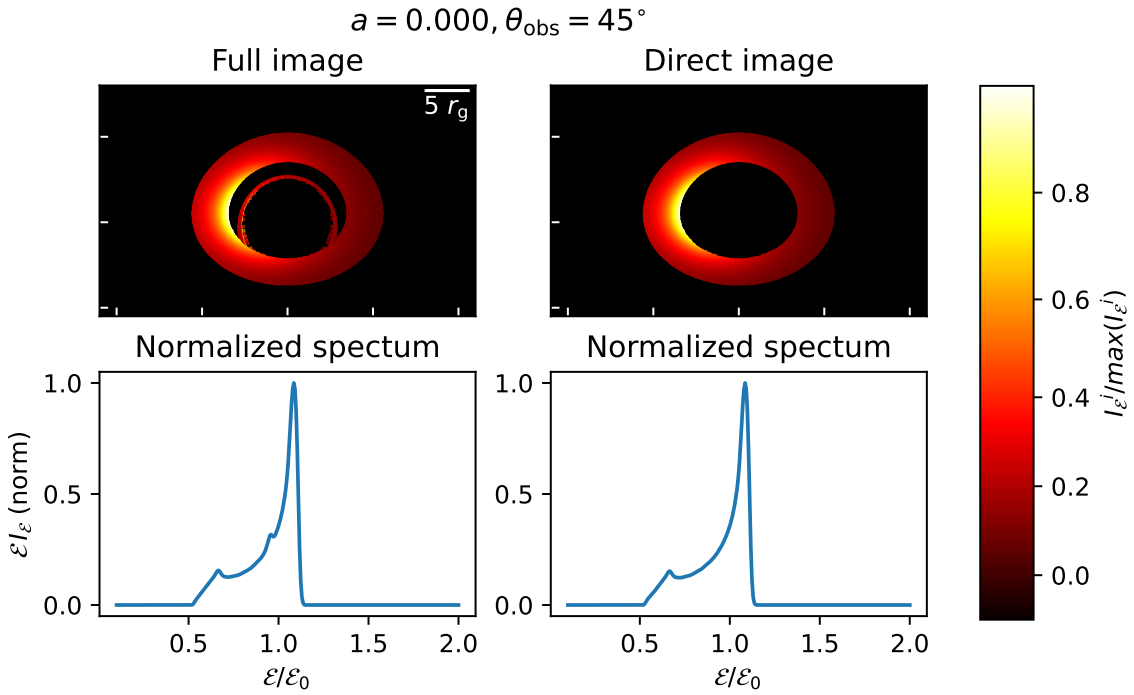

Figure 2.13: Image of a thin disk around a Schwarzschild black hole seen by a distant observer at a viewing angle of 45°. Top: observed image. Bottom: normalized measured SED. Left: including images of all orders. Right: including only the the direct/first order image. The colour coding corresponds to the bolometric intensity at each pixel, $I^{(i)}$. The disk extends from the innermost stable circular orbit ($r_{\rm isco} = 6r_{\rm g}$) up to an outer radius of $10r_{\rm g}$. In the direct image case, the inner circle of the image, caused by rays that orbit the black hole on the way between the disk and the observer, is absent. In order to produce this image, absorption was set to zero everywhere, and the disk considered optically thick (i.e. rays cannot pass through it and reach the observer). The emissivity was set to 0 everywhere other than at the disk surface. On the surface, j was set to decrease with radius as $1/r^3$, as in Fuerst and Wu (2004). In terms of energy dependence, the spectrum was set to a Gaussian centered at an energy $\mathcal{E} = \mathcal{E}_0$ (arbitrary units, corresponds to normalizing by peak energy $\mathcal{E}_0$) and standard deviation equal to $0.01\mathcal{E}_0$. As in figure 2.11, each point on the disk was considered to be moving on Keplerian equatorial orbits of constant r (see section A.1 for the components of the 4-velocity of each segment of the disk as a function of its coordinates.). The key features of the spectrum are as follows: a) the Doppler shift due to the disk's rotation causes the originally Gaussian spectrum to split into two main peaks: one at $\mathcal{E}/\mathcal{E}_0 < 1$ and one at $\mathcal{E}/\mathcal{E}_0 > 1$ (for a comment on the third peak at $\mathcal{E}/\mathcal{E}_0 = 1$ in the full image spectrum, see point c) below). Since $\mathcal{E}I_\mathcal{E} \propto \mathcal{E}^4$, the flux of the blue shifted part of the spectrum increases while that of the red shifted part decreases, which explains the asymmetry in the height of the two peaks. b) In the absence of this effect, the two main peaks would be centered at $\mathcal{E}I_\mathcal{E} = 1$. However, the gravitational redshift causes the whole spectrum to move to lower energies, which explains why the two peaks are not centered around at $\mathcal{E}/\mathcal{E}_0 = 1$, but rather at a lower energy. c) The SED of the full image has an extra peak around $\mathcal{E}/\mathcal{E}_0 = 1$. The explanation for this can be found by looking at figure 2.11: from the images on the top row, it is clear that the rays from higher order images (those forming the inner circles) experience almost no energy shift. This occurs because the gravitational and Doppler shift at these points exactly cancel out, resulting in no net energy shift. This means that, when the full image is considered, there is an excess of photons reaching the observer with $\mathcal{E}/\mathcal{E}_0 \approx 1$, resulting in the third bump observed in this spectrum. Spatial resolution: 122500 pixels; Spectral resolution: 300 energy steps.

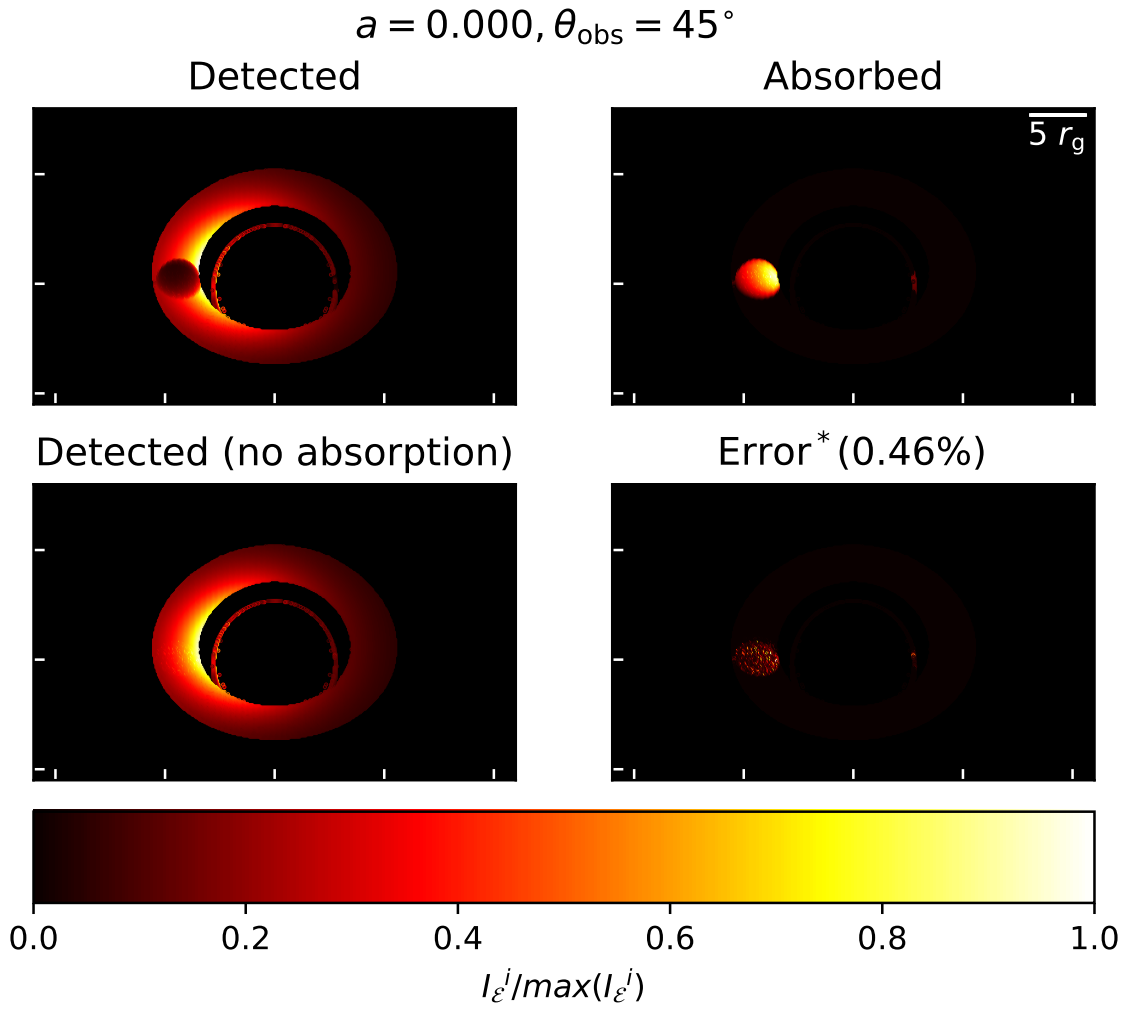

Figure 2.14: Full image of an emitting thin disk as in figure 2.13, but this time with absorption. The material composing this absorber follows Keplerian orbits similar to those of the disk (see section A.1). The top left panel shows the image that would be observed if part of the emission from a geometrically thin and optically thick disk were absorbed by some material on the line of sight. The top right panel shows the absorbed flux. This quantity is very relevant if one wants to study the effect of the emission on local bodies, e.g. the heating of the absorber due to radiation. An interesting feature of this plot is that there is some flux very weakly absorbed on the right region of the figure. This is also visible as a small gap on the right hand side of the secondary image of the detected flux (top left panel). This occurs because the lensing on those secondary rays causes them to go through the absorbing body, which also extends below the disk. The bottom left panel shows the resulting image if one adds the flux that is detected and that which is absorbed by the medium. All working correctly, one should recover the left hand side image from figure 2.13 precisely. There is some small error in this, however, due to the finite step size of the integration, as is visible on the bottom right panel. The fact that the GRRT integration algorithm depends on the step size of the geodesic integration means that the covariant intensity and optical depth will have some error induced by the differences in the step size of the different geodesics when they enter the absorbing body. This is, however, small: the total difference in the flux between the bottom left panel and figure 2.13 is only 0.46% of the total flux across all pixels of figure 2.13. Spatial resolution: 122500 pixels; Spectral resolution: 300 energy steps.

Chapter 3

Massless particles: flares near massive black holes

3.1 Introduction

In section 1.2, we introduced the multi-band observations of flares from Sgr A*. These events are important to improving our understanding of the (astro)physics happening very close to black holes. In an attempt to better understand this phenomenon, Yuan and Wang (2016) performed a statistical study of the light curve profiles of X-ray flares in the $2-8$keV band. They found that the flares generally have asymmetric light curves, with no preference for a fast-rise-slow-decay (FRSD) nor a slow-rise-fast-decay (SRFD) profile. Astrophysical flaring events generally have an intrinsic FRSD profile. As such, this result led the authors to speculate whether the SRFD observed in nearly 50% of the flares could be due to gravitational and relativistic distortions of the emitted light curves. The present chapter addresses this question and asserts whether flares produced by similar mechanisms with some time-dependent emission spectrum can be distorted by gravitational and relativistic effects in such a way that a FRSL emission could be detected as a SLFD flare in several cases. This investigation was performed with the aid of GRRT calculations using the formalism developed in chapter 2.

As mentioned in section 1.2.2, the data on the flares across several energy bands suggests that the emission originates from a compact region orbiting the black hole very close to its event horizon. This is often referred to as the *hotspot model* for the emitting region (Meyer et al., 2006b). Below is a summary of the key properties which justify the adoption of such a model for studying the effects of general and special relativity on the flares, some of which were already mentioned in section 1.2.1:

1. **Flare frequency and duration**
   The period of the detected flares is consistent with the period of objects orbiting the black hole within a few gravitational radii (e.g. Baganoff et al., 2001; Liu and Melia, 2002; Genzel et al., 2003; Eckart et al., 2006b; Yusef-Zadeh et al., 2006; Barrière et al., 2014). The duration of the flares is consistent with a compact emitting region with an

extent smaller than a few gravitational radii (e.g Yusef-Zadeh et al., 2008; Dodds-Eden et al., 2009; Kunneriath et al., 2010; Michail et al., 2021b).

2. **Emitter sky location and IR polarization**
   Using IR observations, it was possible to map the sky location and motion of the centroid of the emission, which appeared to be moving on an orbit. It was also possible to perform polarization measurements of the radiation during several IR flares, which showed a rotation of the Stokes parameters throughout the flare (e.g. GRAVITY Collaboration et al., 2018). Both observations indicate that the emitting body is orbiting the black hole.

3. **Light curve morphology**
   Some of the observed light curves present features resembling those calculated using an orbiting hotspot model (Karssen et al., 2017; GRAVITY Collaboration et al., 2020a).

Given the arguments above, the hotspot model has attracted much attention. The formation mechanism of such hotspots is yet to be precisely established. Nonetheless, the consensus is that it is a consequence of magneto-hydrodynamical processes, potentially in a way akin to the formation of coronal mass ejections and flares in the sun (Yuan et al., 2009), but with the added effects of strong gravity. This has been investigated by several groups using general relativistic magneto-hydrodynamic (GRMHD) simulations (see e.g. Ripperda et al., 2022) and it appears to be physically viable.

In order to understand the causes of these flares, theoretical and computational research groups have modeled different aspects of the emission and propagation of radiation, all of which are essential to form a complete picture of what is happening at the galactic centre. The main focus areas can be split into two:

1. **Plasma and magneto-hydrodynamic (MHD) processes**
   As described in section 1.2.2.i, one of the key focuses of the modeling of flares is the microphysics of the emitting and absorbing processes. The results from these works provide information about the local emissivity and absorption coefficients. MHD simulations are often used to study the formation of the emitting regions (e.g. plasmoids/ hotspots) near the event horizon of Sgr A* and the mechanism through which energy is transferred to the emitting particles. They provide information on the geometry and motion of the emitting regions that may form in black hole environments[1].

2. **Radiation transport**
   Once the mechanisms through which the emitting region forms, the particles are energized and the emission/ absorption occur are understood, it is essential to understand the transport of the emitted radiation towards the observer. This has to take into account the

[1]For references, please refer to section 1.2.2.ii).

strong gravitational field through which the radiation propagates and it allows us to understand any distortions to the emitted radiation caused by relativistic and gravitational effects.

This work investigates relativistic and gravitational effects from a radiation transport perspective. In order do this, it was important to isolate these effects from emission and absorption processes. This is because the emission mechanisms, the effects of GR and the detector properties will all influence the resulting detected light curves. As such, we chose a simple parametric model for the flare emission, absorption and emitting region which is consistent with the current interpretation of observations. Given the wide acceptance of the hotspot model in the community, this was the model adopted in the calculations performed in this chapter.

3.1.1 Relationship of this study with previous work

Multiple groups have published work about radiation transport, with several focusing on the puzzle of flares described in this chapter. In this section we focus on work done using ray tracing and radiation transport within the context of the hotspot model discussed above. None of the works mentioned in this section discuss an intrinsic spectral evolution such as the one we discussed in section 3.3.3, but rather focus mostly on work done along the lines of section 3.3.2. Similarly, non of these works focus on the effect of the energy band at which the observations are performed might have on the observed light curves.

One of the first calculations of an orbiting hotspot was performed by Schnittman and Bertschinger (2004). Their objective was to explain observations of quasi-periodic X-ray emission from accreting binary black hole systems. This was approached by adopting a simplified 2-dimensional hotspot and a fully backward ray tracing calculation. An interesting conclusion from their work was that the results referring to primary images alone were approximately independent of the hotspot's size and shape. As part of their findings, the authors also provided constraints on the timings of flares expected as a function of the ISCO period for different spins.

Later calculations performed by Meyer et al. (2006a,b) focused on a particular IR flare from Sgr A* which presented a large modulation (modeled as disk emission) superposed by smaller flares (modeled as hotspots), and found a weak dependence of the model on the black hole spin. In this study, only primary images were considered. The authors used the "transfer function" method (Cunningham, 1975) for the radiative transfer calculation[2].

[2]In short, this method consists of ray tracing the light rays from the observer to the emitting region and multiplying the emitted radiation by a factor (the transfer function) which incorporates the effects of Doppler shift, gravitational redshift and gravitational lensing at each point in the emitter. The factors depend on the assumed velocity of the emitters, prescribed in Cunningham (1975). The values of the transfer function were calculated and tabulated for several black hole spins and viewing angles in a way that could be used by other researchers.

Broderick and Loeb (2006) performed calculations of the hotspot model to explain the NIR and submm flares from Sgr A*, using a synchrotron emission model. One of the main differences to our work is that the authors used a physically motivated (energy dependent) absorption model. They did not, however consider the case of a time-evolving emission spectrum and how that would affect the results in each energy band.

The work of Hamaus et al. (2009) aimed to explain the observations of IR flares using a methodology similar to the one described in 3.3.2. They considered an opaque sphere on a circular equatorial Keplerian orbit around the black hole and adopt an approach similar to ours, bypassing the direct determination of emissivity, output intensity and fluxes, and instead using a parameterized model. The authors also consider a different emission region, in particular a hotspot followed by an arc extending around the orbit. Their work differs from ours in that no intrinsic spectral evolution is considered nor are the effects of finite energy band passes considered.

Kusunose and Takahara (2011) also calculated the bolometric light curves resulting from a synchrotron emitting plasma blob, this time one ejected from close to the inner accretion of a black hole. Their calculations assumed that the blob was non-relativistic and beaming effects were neglected. The authors focused on using a very accurate model for the intrinsic emissivity and a simplified transport formalism rather than the other way around (which we preferred to use). Their models result in accurate intrinsic emissivity profiles which one could use with our code to perform more realistic predictions.

The geodesic integration and initial conditions used in Li et al. (2014) are similar those used in this chapter. A major difference, however, is that they use a fully backward ray tracing algorithm and consider only what we refer to as instantaneous light curves (which in literature is often referred to as the "fast light approach"), so that (unlike in our case) no time accounting correction is performed. The main results of the paper are observer images (primary and secondary) and spectrograms of constant emissivity flares for Kerr and some non-Kerr BHs viewed from 60 degrees, which are consistent with ours (see appendix B). An interesting result from this paper is that the primary image component of the spectrograms are not very sensitive to the size of the source.

The calculations performed in Younsi and Wu (2015) were again very similar to our constant emissivity calculations, including a similar time accounting algorithm. Their work was used as a validation for our code. Despite the fact that the authors use a more complicated synchrotron-inspired emissivity, note that their bolometric light curves are precisely the same as ours for all viewing angles, with the exception that they appear to be time-reversed[3]. The fact that

[3]After discussions with the authors, it transpired that they performed the calculations of bodies orbiting in the opposite direction from ours.

bolometric light curves do not seem to depend heavily on the injection spectrum is interesting. The work does not consider a spectral evolution of the intrinsic emissivity.

Karssen et al. (2017) performed calculations of an orbiting hotspot in order to estimate the mass of Sgr A* based on the fitting of their models to X-ray observations data. The exact algorithm that they use for the ray tracing and surface finding is not very clear. Again, they use a synchrotron emissivity in an optically thin medium to model the light curves of NIR and X-ray flares, with no calculations of time dependent spectra at different energy bands.

GRAVITY Collaboration et al. (2020b) used the grtrans code (Dexter and Agol, 2009; Dexter, 2016) to predict the motion of the emitter in the observer plane for flares originating from objects in orbits which may not be circular nor in the equatorial plane of the black hole (though their calculations in this paper are in fact for circular orbits) and then compared them to NIR flare observations in order to constraint the orbital radius and inclination of the orbits. They used a more complex emitter location model, but again did not consider the time dependent spectrum or energy band pass effects.

While it is within the capabilities of our code to incorporate complex factors such as intricate injection spectra, orbital motion, and emitter geometry—similar to the referenced work—we have chosen to explore a simplified model. This decision aims to provide a clearer understanding of the interplay between key elements: gravitational and relativistic effects, intrinsic energy drift, and their manifestation in bolometric intensity and across various energy bands. It is noteworthy that the literature lacks a detailed explanation of this nature, and our work serves this purpose precisely. Despite our simplified assumptions, we have successfully demonstrated the significant role played by the strong gravitational and relativistic effects in the distortion of flares, not only for the case of constant emissivity but also for the case of time dependent emission and with a focus on different band-pass observations, which is also absent from the literature.

3.2 Computation model

i) Emitting region

Considering the different limits found by different authors (e.g. $[c]\Delta t \gtrsim 0.5\, r_{\rm g}$ and $[c]\Delta t \lesssim 2.2\, r_{\rm g}$ (Eckart et al., 2012)) we chose an emitting region with a length scale of $\approx 1\, r_{\rm g}$. For simplicity, the emitter was modelled as a spherical region of radius $R_{\rm e} = 0.5\, r_{\rm g}$ orbiting the black hole at $r = 6.5\, r_{\rm g}$ for the case of a Schwarzschild black hole or $r = 2.5\, r_{\rm g}$ for the case of a maximally rotating ($a = 0.998$) Kerr black hole. These values were chosen to be close to the innermost stable circular orbit radius of the black holes, $r_{\rm ISCO}$, for prograde orbits.

Although the code can cope with hotspots with changing radius and moving vertically, the calculations in this section were all performed for emitters of constant size on circular orbits at constant θ. The location of the hotspot at a given time t is given, as per equation (2.78), by

$$\begin{aligned} r^*(t) &= r^*(0) \\ \theta^*(t) &= \theta^*(0) \\ \phi^*(t) &= \phi^*(0) + \frac{2\pi t}{T_{\rm orb}} \end{aligned} \tag{3.1}$$

where $t = 0$ is the time at which the onset of the flare occurs and $T_{\rm orb}$ is the orbital period found by assuming a Keplerian orbit (see A.1 for details on the equations).

ii) Intrinsic emissivity

We used a simplified model for the intrinsic emissivity and absorption. In particular, the emitter was considered to be optically thick and no other absorption sources were considered.

The model of intrinsic emissivity chosen, $j_{0,\mathcal{E}_0}$, can be decomposed into three main components: $j_{\rm S}(\mathcal{E}_0, t)$ represents the time-dependent emission spectrum; $j_{\rm X}(t, \boldsymbol{x})$ encompasses the spatial dependency of $j_{0,\mathcal{E}_0}$ (which is time-dependent in the case of a moving hotspot); $j_{\rm M}(t)$ represents the time-dependent modulation of the flare to capture its explosive nature. Thus:

$$j_{0,\mathcal{E}_0}(x^\mu) \propto j_S(\mathcal{E}_0, t) \times j_{\rm X}(t, \boldsymbol{x}) \times j_{\rm M}(t), \tag{3.2}$$

where t is the coordinate time and $\boldsymbol{x}$ are the spatial coordinates. In particular, the spectrum was chosen to be Gaussian with standard deviation $\sigma_{\mathcal{E}}$ (constant in time) and a time dependent mean $\bar{\mathcal{E}}_0(t)$, i.e.

$$j_S(\mathcal{E}_0, t) = \frac{1}{\sigma_{\mathcal{E}}\sqrt{2\pi}} \exp\left\{ -\frac{\left[\mathcal{E}_0 - \bar{\mathcal{E}}_0(t)\right]^2}{2{\sigma_{\mathcal{E}}}^2} \right\}. \tag{3.3}$$

The spatial dependence of the emission is zero everywhere except on the surface of the hotspot, so that the hotspot is considered optically thick. For the purpose of numerical calculations, (see 2.1.5 for details on the surface finding algorithm), if all points on the surface are symbolically denoted by $\boldsymbol{x}_{\rm surf}$, then

$$j_{\rm X}(t, \boldsymbol{x}) = \begin{cases} 1\,, & |\boldsymbol{x} - \boldsymbol{x}_{\rm surf}(t)| < \epsilon\,, \\ 0\,, & \text{otherwise.} \end{cases} \tag{3.4}$$

where ϵ is some numerical tolerance for the surface finding algorithm (i.e. all points for which $|\boldsymbol{x} - \boldsymbol{x}_{\rm surf}(t)| < \epsilon$ are considered to be on the surface). Finally, the explosive modulation of the emissivity is modeled parametrically as a fast linear increase mimicking an injection period

starting at $t = 0$ and ending at $t = t_{\rm inj}$, followed by a slow exponential decay mimicking a cooling period with timescale $t_{\rm cool}$, with $t_{\rm inj} \ll t_{\rm cool}$, i.e.

$$j_{\rm M}(t) = \begin{cases} 0\,, & t < 0\,, \\ \dfrac{t}{t_{\rm inj}}\,, & 0 \leq t < t_{\rm inj}\,, \\ \exp\left\{-\dfrac{(t - t_{\rm inj})}{t_{\rm cool}}\right\}\,, & t \geq t_{\rm inj}\,. \end{cases} \tag{3.5}$$

Since we chose $t_{\rm inj} \ll t_{\rm cool}$, this gives us a reasonably sharp injection and slow cooling profile. Inspired by solar flares, which exhibit a time-dependent spectrum, we allowed the peak of the emitted spectrum to vary in our calculations[4]. There are several types of solar flares spanning different energy bands and intensities, with different time dependent profiles. Since several types of solar flares exhibit a drift in the emitted energies with time, we chose to incorporate the time dependence of the spectrum as an energy drift. In particular, we chose to adopt an energy drift similar to those of type III radio bursts, which is relatively well understood. Various authors found that several type III radio bursts experience an energy drift of (see Reid and Ratcliffe, 2014, for a review):

$$\mathcal{E}(t) = \mathcal{E}(0)\mathrm{e}^{\mathcal{D}t}. \tag{3.6}$$

We will refer to $\mathcal{D}$ as the *energy drift rate* and, in general, it depends on the energy $\mathcal{E}$. In particular, if we define the drift of the peak energy, in this case the mean of the Gaussian spectrum $\bar{\mathcal{E}}$, as $\bar{\mathcal{D}}$, then the peak energy of the emission will change according to equation (3.6). In particular, the value of $\bar{\mathcal{E}}(t)$ in equation (3.3) is calculated as:

$$\bar{\mathcal{E}}(t) = \begin{cases} \bar{\mathcal{E}}(0)\,, & t < t_{\rm inj}\,, \\ \bar{\mathcal{E}}(0)\, e^{\bar{\mathcal{D}}(t - t_{\rm inj})} & t \geq t_{\rm inj}\,. \end{cases} \tag{3.7}$$

Note that, in the calculations performed here, the width of the spectrum remains constant, which implies that the energy drift rate is not the same for all energies.

Since most type III solar flares have a negative drift rate and given that Yusef-Zadeh et al. (2006) found a justification for the peak emission energy of Sgr A* flares to decrease with time, all the calculations presented here were performed for $\bar{\mathcal{D}} \leq 0$. Nevertheless, our code can equally well deal with positive $\bar{\mathcal{D}}$.

[4] Yusef-Zadeh et al. (2006) show that a model of an adiabatically expanding source is consistent with the peak emission frequency decreasing with time, hence providing a good justification for adopting a solar flare type model with a decrease in the peak intensity.

iii) Light curve calculation algorithm

To calculate light curves, algorithm 2.4 must be executed at multiple times. Particles take time to move between the emitter and the observer and particles moving along different geodesics will take different times to reach the observer, as is evident in figure 2.10. This means that particles reaching the observer simultaneously were not necessarily emitted simultaneously. In a situation where the emitter is stationary and the emissivity and absorption have no time dependence, this is not an issue. However, this is also not a very interesting scenario from the point of view of temporal evolution analysis. The difficulty arises when the emitter (or absorber) is moving and their emissivity (absorption) coefficient is time dependent. In these scenarios, particle bundles reaching the observer simultaneously could have been emitted when the emitter was at different locations and when the local emissivity had different values. This means that their contributions to the light curve will be different. Accounting for these effects correctly is fundamental for all the calculations performed in the present chapter.

There are several ways to deal with this and, after some investigation, we concluded that an algorithm similar to that used in Younsi and Wu (2015) was the most appropriate for our particular setup. The main assumption is that all rays that reach the observer grid were emitted simultaneously. We then use the emission time and the photon travel time to calculate the time at which each photon would be observed. The algorithm is as follows:

1. Set up a grid at a given time (${t_{\rm em}}^j$), defined as the emission frame j.

2. Find the location of the emitter and the emissivity coefficient at that particular time. For the calculations in this chapter, the emitter's location is given by equation (3.1) and its emissivity by equation (3.2). Their values are fixed for the current frame.

3. Backward ray-trace each of the rays in the grid. This is done in parallel using OpenMP, with as many threads as are available in the machine being used, each one dealing with one ray. The initial conditions for the rays are found as per section 2.1.3.

4. Perform the radiation transport calculations along the geodesics as described in section 2.2, using the surface-funding algorithm to check whether the rays intersect the emitter's surface.

5. Record the time taken for each ray i to travel between the emitter and the detector, ${t_{\rm travel}}^i$ and calculate the detection time for each ray as ${t_{\rm det}}^i = {t_{\rm travel}}^i + {t_{\rm em}}^j$. Save the result together with the covariant intensity at each of the sampled energies for that pixel.

6. Set up a similar observer grid at the next emission frame $j + 1$. Repeat the steps above until the full emission time is covered.

7. Order all the rays by arrival time and bin the covariant intensity into equally spaced detection time bins, keeping information of the detection time and the pixel coordinates.

8. Calculate the light curves by summing over the flux or intensity across all particle energies and all pixels in each time bin.

If the emitter is not optically thick, this algorithm is not the best and a full backward ray tracing algorithm would be better. In such algorithms, one would setup a grid at a certain detection time and, at each integration step, would find the emitter's location at that time along the geodesic and perform the surface finding and GRRT calculations. By doing it in this way, one does not need to reorder the pixels by arrival time, as this is automatically done. However, when we experimented with both algorithms we found that, for optically thick emitters, a full backward ray-tracing algorithm missed out on some of the emission. Hence the algorithm presented above is better and was used in these calculations.

In order to show the importance of doing the correct time accounting as described in the algorithm above, some results in this chapter are shown for both the *corrected* and the *instantaneous* algorithms. The instantaneous algorithm does not take into account the photon travel time between observer and emitter and assumes that all photons emitted at the same time reach the observer at the same time. This is often known in literature as the "fast light approach". In practice, it corresponds to replacing step 5 by ${t_{\rm det}}^i = {t_{\rm em}}^j$ and skipping step 7 above.

3.3 Results and discussion

3.3.1 Observer images

When a spherical object orbiting a black hole emits radiation, photons emitted in different directions travel along different paths. Those that reach the observer do so at different times. Figure 3.1 shows the energy shift and the arrival time of photons emitted simultaneously at various locations, as seen by the observer. An energy shift of 1 means that the energy detected is the same as the energy emitted; values < 1 mean that the detected photon's energy was red shifted (i.e. is lower than the emitted energy); values > 1 mean that the detected photon's energy was blue shifted (i.e. is higher than the emitted energy). The energy shifts are calculated by assuming that the emitter is on a Keplerian orbit around the black hole, as described in appendix A. In terms of arrival time, the values plotted are the delay with respect to the first photon that reaches the observer. I.e. a value of 0 means that the photon reached that particular pixel at the same time as the first photon to reach the screen, a value of $20r_{\rm g}/[c]$ means that the photon reached that particular pixel $20r_{\rm g}/[c]$ after the first photon reached the screen, and so on. In this chapter we shall often refer to primary images and secondary or higher order images. Primary images are those formed by photons whose trajectories between

the emitter and observer are bent by an amount less than or equal to $\pi/2$, either in the θ or the ϕ directions. The images are secondary if they orbit the black hole and suffer an angular deflection between $\pi/2$ and $5\pi/4$, and higher order if the angular deflection is greater than $5\pi/4$. Sometimes, we will only distinguish between primary and higher order images, in which case the secondary images are included in the higher order category.

For Schwarzschild spacetime (top panels of figure 3.1), it is very easy to distinguish the primary and secondary images. The primary image corresponds to light that reaches the observer directly from the hotspot. It arrives earlier than the secondary images, which reach the observer after orbiting the black hole (see figure 2.12 for an illustration of the formation of a lensed image of a disk, which follows the same principles as for a hotspot). In figure 3.1, the primary image is coloured more white in the arrival time plots. For $\phi = 0°$, the central blob is the primary image and the thin ring around it, which arrives $\approx 37 r_{\rm g}/[c] \approx 0.36\, T_{\rm orb}$ later, is the secondary image. For $\phi = 180°$, the thick outer ring (which is called an *Einstein ring*) is the primary image and the inner thin ring, which arrives $\approx 35 r_{\rm g}/[c] \approx 0.34\, T_{\rm orb}$ later, is the secondary image. For $\phi = 90°$ and $\phi = 270°$ the larger blobs on the right/left respectively are the primary images and the elongated shapes on the left/right respectively are the secondary images, both of which arrive $\approx 21.5 r_{\rm g}/[c] \approx 0.21\, T_{\rm orb}$ after the primary.

There are also primary and secondary images for the case of Kerr spacetime, but the time difference between the two is not as pronounced. Unlike in the Schwarzschild case, in Kerr spacetimes there is no left-right symmetry in the images. This is due to the frame dragging effect caused by the black hole's rotation. In particular, note how, at $\phi = 180°$, the observer's image appears to be that of a hotspot already moving towards the observer, as if closer to 270°. An Einstein ring similar to that seen in the Schwarzschild case is also present in the Kerr case (see snapshot images in figure 3.3), but it originates when the hotspot has not yet reached 180°. This is also due to the frame dragging effect. The difference in arrival time between the first and last photons to be detected by the observer is much larger in the Kerr than in the Schwarzschild case. The proximity of the orbit to the black hole results in higher order images being able to reach the observer. The photons which give rise to such images orbit the black hole multiple times, reaching the observer as late as $160 r_{\rm g}/[c]$, or $5.2 T_{\rm orb}$ (in the case of $\phi = 90°$) after the first detected photon.

Finally, note that the rings that form the secondary images in both the Schwarzschild and the Kerr cases trace the border of the black hole's shadow (see figure 2.6).

3.3.2 Hotspot with constant emissivity

The first step in the study presented in this chapter was to isolate the general relativistic effects from the intrinsic emissivity. In order to do this, we considered the simplified model of a hotspot

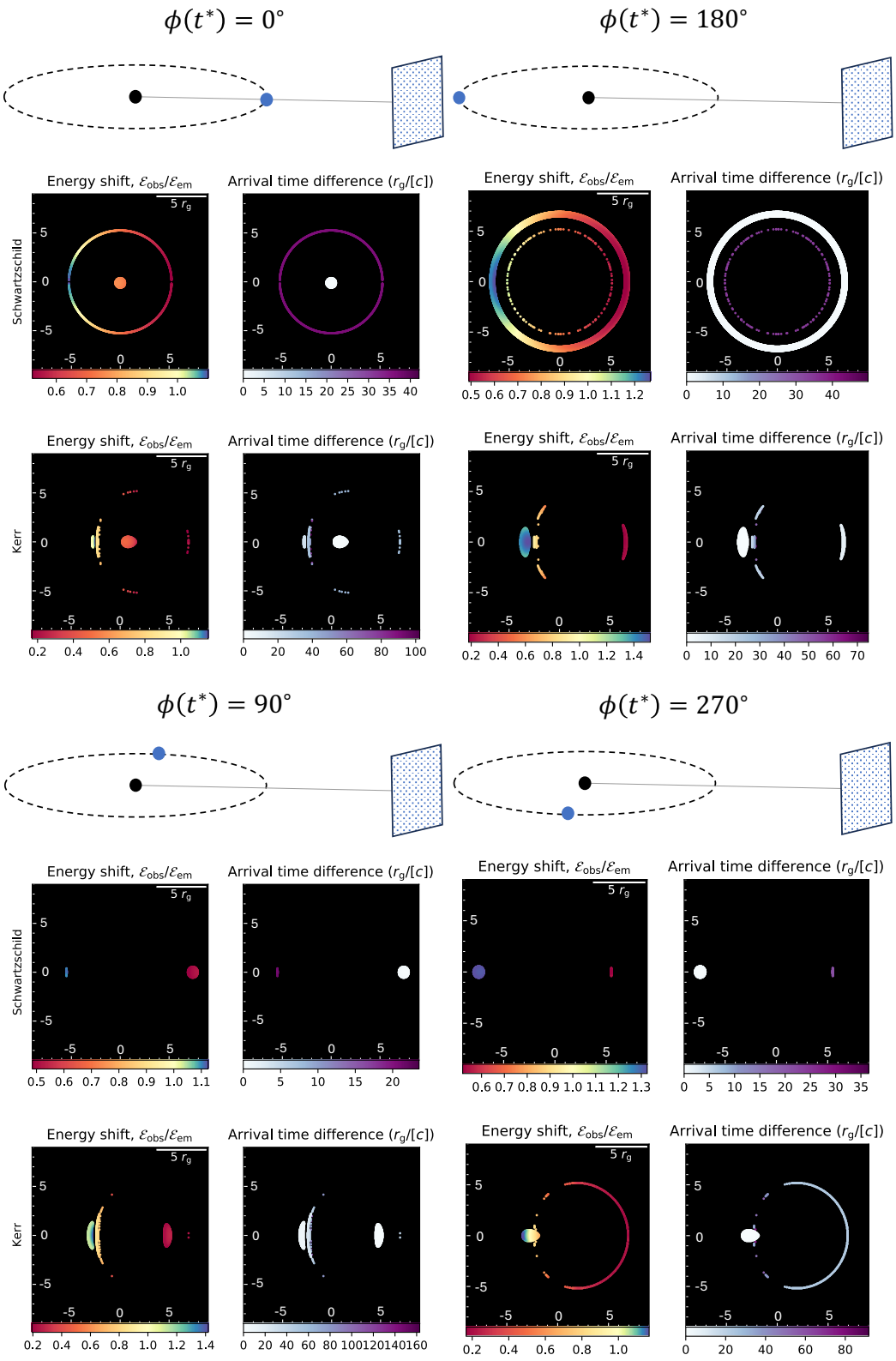

Figure 3.1: The images show the redshift and arrival time of photons on an observer grid of photons emitted by a spherical hotspot instantaneously at position $\phi(t^*)$ during an equatorial orbit. The plasmoid is on an orbit of radius $6.5r_g$ (Schwarzschild) or $2.5r_g$ (Kerr, $a = 0.998$). All images are calculated at an observer viewing angle of 90°. See the main text for a description and explanation of the results. Resolution: 600×600 pixels.

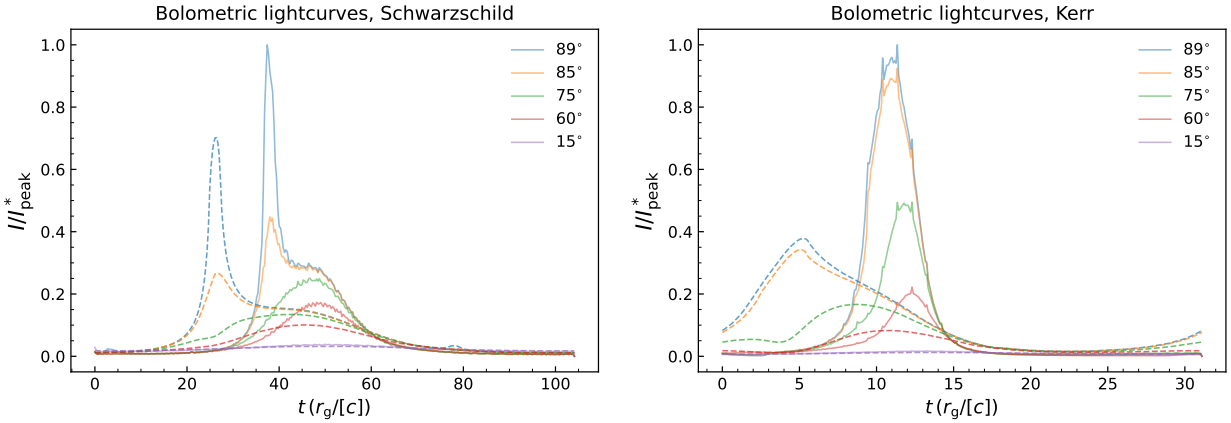

Figure 3.2: Bolometric light curves from an orbiting hotspot at different viewing angles. The quantity plotted is the integrated intensity $I(t) = \sum_i \sum_{\mathcal{E}} I^{(i)}_{\mathcal{E}}(t)$, normalized by $I^*_{\rm peak} = \max(I^*(t))$, where the $*$ denotes the time-corrected light curve for an observer at a viewing angle of 89°. Dashed lines: without travel time correction (assuming instantaneous light travel). Solid lines: with travel time correction (taking into account the light travel time). The x-axis spans one orbital period of the hotspot, with 0 corresponding to the hotspot located at $\phi = 90°$. For Schwarzschild spacetime, the orbital period is $\approx 104 r_{\rm g}$ and for Kerr it is $\approx 31 r_{\rm g}$. Henceforth, all light curves will be plotted with respect to time as fraction of the period rather than in terms of the actual time. These calculations were run on machines with 128 physical cores (AMD epyc processor) and 1Tb of RAM, and each inclination angle calculation took approximately 24 hours.

with constant emissivity orbiting a black hole.

i) Multiple viewing angles

Figure 3.2 shows the bolometric light curves that an observer would see from a hotspot with constant emissivity (i.e. $j_{\rm M}(t) = 1$, $\bar{\mathcal{E}}_0(t) = \bar{\mathcal{E}}_0(t^*) = 1$ and $\sigma_{\mathcal{E}} = 0.01$) on a circular equatorial orbit around a Schwarzschild ($a = 0$) and Kerr ($a = 0.998$) black hole. The results are presented for different observer viewing angles, $\theta_{\rm obs}$. The x-axis spans one orbital period of the hotspot, with 0 corresponding to the hotspot located at $\phi = 90°$. The dashed lines correspond to the instantaneous light curves that would be obtained if light travelled instantaneously between the emitter and the observer (i.e. ignoring the light travel time). The solid lines are the light curves obtained when accounting for the light travel time. The time corrected light curves are more noisy than the uncorrected ones due to sampling: the algorithm used to correct for the travel time results in some detection times being better sampled than others, while all emission times are equally sampled. As the spatial and temporal resolution of the calculation increases, the time corrected light curves become smoother.

Figure 3.2 shows that the peak bolometric intensity is larger the closer the viewing angle is to 90°. This is a combination of more radiation getting lensed towards the observer and of the relativistic beaming effect (see section 2.3.3.i). The latter can be understood as follows: the larger line-of-sight velocity of the emitter when the viewing angle is closer to 90° causes the

emitted radiation to be more blue-shifted when the emitter moves towards the observer. This in turn causes in the intensity of the radiation to increase, resulting in a higher peak bolometric intensity.

Another feature that stands out in figure 3.2 is that the travel time correction affects the light curves by shrinking them into shorter and stronger peaks, which arrive at the observer later than if the light travel time were to be ignored. Finally, as is particularly clear in the Schwarzschild black hole case, for high inclinations there are several peaks in the bolometric light curve. In the next section, we will explore these morphological features by looking at the particular case of a flare observed from a 89° viewing angle. This is because we found that the relativistic effects are more pronounced the closer one is from 90°. We performed the calculations for $\theta_{\rm obs} = 89°$ in order to be able to compare our results with those in literature, which often use 89° instead of 90° since a viewing angle of exactly 90° might be considered unlikely.

ii) Morphology of the light curve at a viewing angle of 89°

Figure 3.3 isolates the light curves seen from a viewing angle of 89° as well as some observer images at some key snapshots. These are helpful to interpret the morphology of the observed light curves and are presented for both the instantaneous and time corrected scenarios.

Although the bolometric light curves provide some insight into the general relativistic effects on detected flares, a better understanding of the processes involved can be obtained by looking at spectrograms, i.e. the light curves at each individual detected energy band (or equivalently, the spectra at each detection time). This is particularly important given that detectors are only sensitive to certain energy bands. As such, detected light curves are rarely bolometric, but rather a cut in the spectrogram. Figure 3.4 shows the spectrogram corresponding to the constant emissivity flares in figure 3.3. The relativistic and gravitational effects are very clear in these plots.

The bolometric light curves in the Schwarzschild case (top panel of top image in figure 3.3) have several interesting features. The peak of the instantaneous light curve happens at $\approx 0.25\,T_{\rm orb}$, when the hotspot is exactly behind the black hole. This corresponds to the observer image at the top of the second column. This shows that the intensity peak in the light curve corresponds to the frame when most rays are lensed towards the observer from behind the black hole. At this point, the observer of the time-corrected light curve still sees the hotspot as if it were traveling away from the detector, between $\phi = 90°$ and $\phi = 180°$ (second column, bottom frame). The peak of the time corrected light curve happens later, just after $\approx 0.35\,T_{\rm orb}$. In the corrected observer image we now see the Einstein ring from when the hotspot was at $\phi = 180°$ (bottom panel, third column), but the fact that the photons have to travel longer to arrive at the detector means that the peak is delayed with respect to the instantaneous one. At this

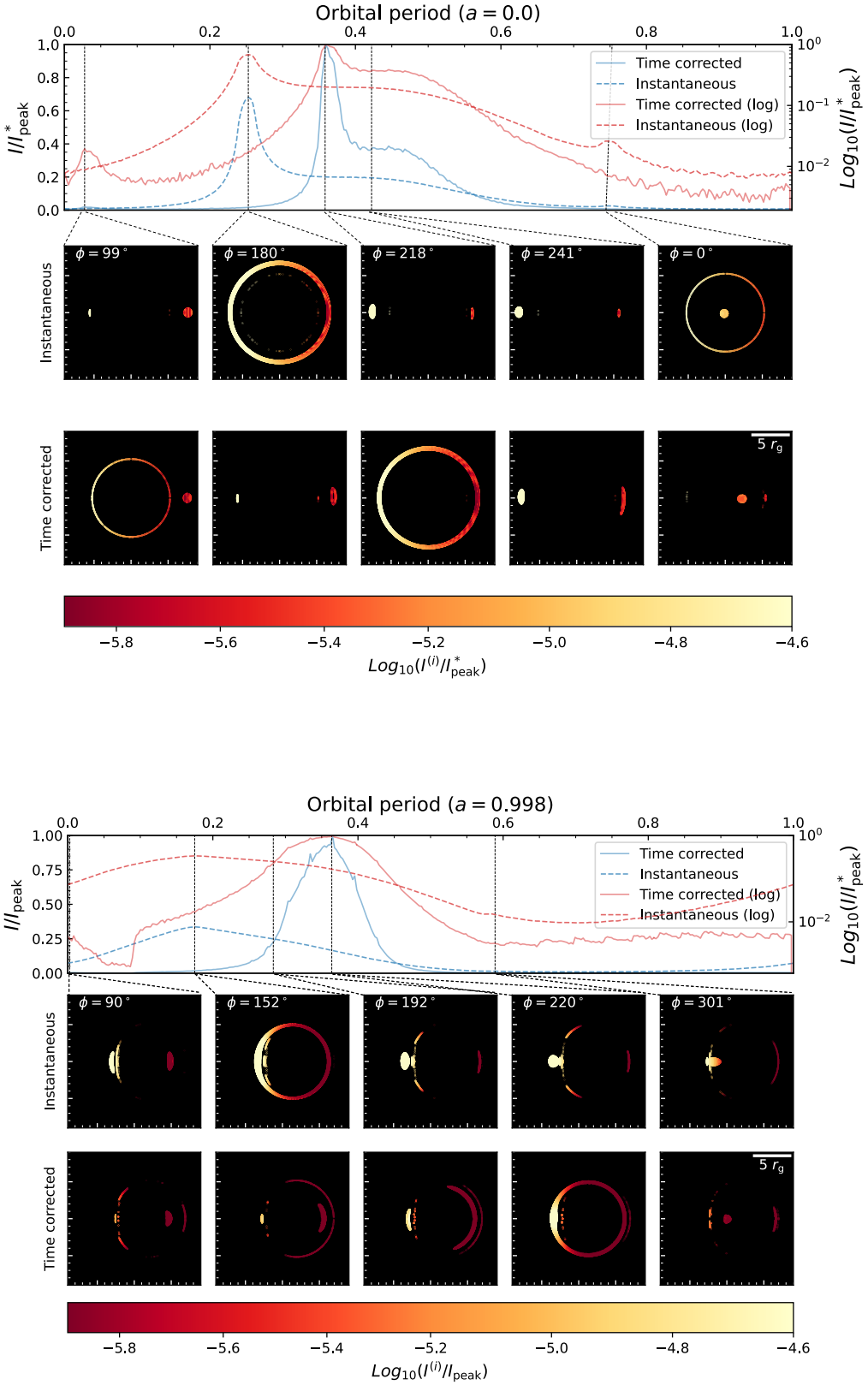

Figure 3.3: Top panel: Bolometric light curves from an orbiting hotspot with constant emissivity for $\theta_{\rm obs} = 89°$ in Schwarzschild (top image) and Kerr (bottom image) spacetime. The light curves are plotted on both linear (blue) and logarithmic (red) scales. Bottom panels: hotspot images. The images are colour coded as the logarithm of the integrated intensity of each pixel ($I^{(i)} = \sum_{\mathcal{E}} I^{(i)}_{\mathcal{E}}$) divided by the peak integrated intensity across all pixels of the time corrected curve ($I^*(t) = \sum_i \sum_{\mathcal{E}} I^{(i)}_{\mathcal{E}}(t)$, where the sum is performed over the time-corrected frames, and $I^*_{\rm peak} = \max(I^*(t))$). The filed of view is the same as in figure 3.1. Resolution: 1000×1000 pixels; 360 time frames; 200 energy bins. The data for these plots comes from the same calculation presented in figure 3.2.

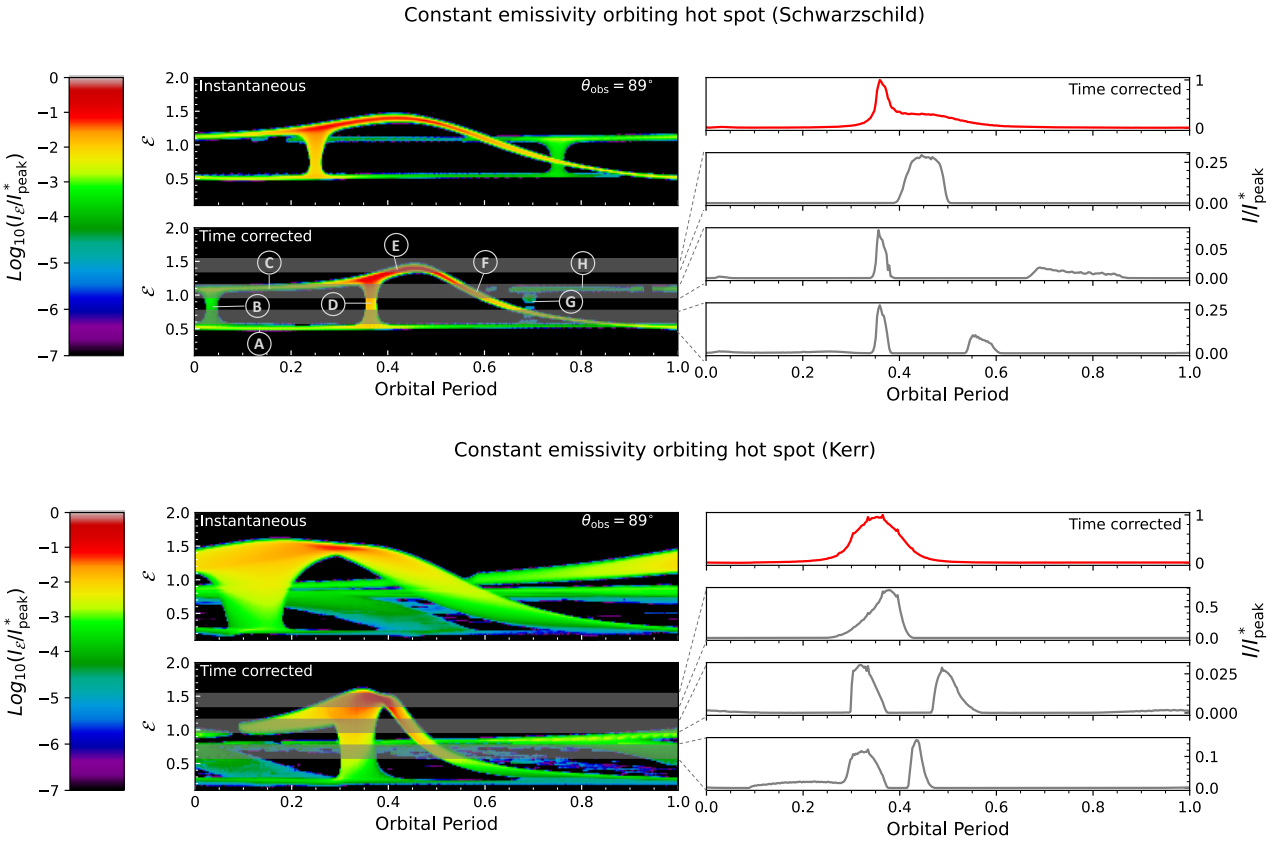

Figure 3.4: Left: Observed spectrograms of an orbiting hotspot in Schwarzschild (top) and Kerr spacetime with $a = 0.998$ (bottom). The x-axis spans one orbital period of the hotspot, starting at a location of $\phi = 90°$ on the instantaneous plots. The time corrected plots start when the first photon emitted at $\phi = 90°$ reaches the observer. The colour code is the specific intensity summed over all pixels at each time frame (i.e. $I_\mathcal{E}(t) = \sum_i I^{(i)}_\mathcal{E}(t)$) normalized by I^*_{peak}, as in figure 3.3. In both calculations the plasmoid starts at $\phi = 90°$. The plasmoid is optically thick with uniform surface emissivity and has a radius of $0.5r_g$. The local emissivity is constant in time and consists of a Gaussian spectrum centered at $\mathcal{E} = 1$ and standard deviation of 0.01 for both cases. Spectrograms for the light curves seen at other viewing angles are presented in appendix B. A summary of the key features is presented in table 3.1. Right: light curves covering the specified energy bands. The data for these plots comes from the same calculation presented in figure 3.2.

point, the hotspot is really already travelling towards the observer (top panel, third column).

In the spectrograms of Schwarzschild spacetime (top of figure 3.4), these two times ($t \approx 0.25\,T_{\rm orb}$ and $t \approx 0.35\,T_{\rm orb}$) correspond to the brightest vertical lines in the instantaneous and the time corrected frames, respectively (feature D). The lines can be explained by looking at the energy shift plot for 180° in figure 3.1, where one sees a wide range of red and blue shifts, resulting in multiple energies being seen in the detected spectrograms.

Feature B on the plots, the fainter (green) vertical line in both the instantaneous and time corrected Schwarzschild spectrograms (at $0.75\,T_{\rm orb}$ and $0.05\,T_{\rm orb}$ respectively) corresponds to the observer images shown in the fifth and first columns of figure 3.3. At $0.75\,T_{\rm orb}$, the hotspot is at $\phi = 0°$ (i.e. in front of the black hole). This is clear since the top image of the fifth column corresponds precisely to the $\phi = 0°$ image in figure 3.1. The ring corresponding to the secondary image, which experiences a wide range of blue and red energy shifts, results in the vertical line seen in the spectrogram. The lensed photons increase the detected intensity causing a small peak in the instantaneous light curve, particularly visible on the logarithmic light curve plot. However, this secondary image will not reach the observer at the same time as the primary image, due to the extra time that it takes for the photons to orbit the black hole and be lensed back towards the detector. Instead, as we saw earlier, it will arrive at the detector $0.35\,T_{\rm orb}$ after the observer sees the hotspot in front of the black hole. Despite the fact that the plasmoid is physically located at $\phi = 0°$ at $0.75\,T_{\rm orb}$, it does not appear to be in this location according to the light curve. The bottom image on the fifth column shows that, at this point, the observer sees the hotspot further along its orbit, between $\phi = 0°$ and $\phi = 90°$. Just like the delay in the appearance of the main peak, this is due to the light travel time and it is a manifestation of the Rømer delay[5]. When the hotspot is in front of the black hole, the time it takes for the direct image to reach the observer will be less than at any other point. This means that, relative to the other rays traveling to the observer, those from this origin will arrive sooner. The apparent location of the hotspot is aligned in the instantaneous and time corrected spectrograms at $\phi = 90°$ (the start of the spectrogram) and $\phi = 270°$ (at $0.5\,T_{\rm orb}$).

The time corrected spectrogram shows a third, very faint vertical line at $t \approx 0.7\,T_{\rm orb}$ (feature G). This is the secondary image from when the hotspot is behind the black hole (thin inner disk at $\phi = 180°$ in figure 3.1). Note that it happens about $0.35\,T_{\rm orb}$ after the main vertical line, as expected from the time delay plots. In the instantaneous spectrogram this secondary ring is assumed to reach the observer at the same time as the primary one, resulting in line G being hidden by line D due to the primary Einstein ring.

[5]If light travelled on a straight line between the hotspot and the observer, the difference in distance travelled between $\phi = 0°$ and $\phi = 180°$ would be $12r_{\rm g}$ for an orbit at $r = 6r_{\rm g}$. This would correspond to an extra travel time of $12r_{\rm g}/[c] \approx 0.12\,T_{\rm orb}$. This is approximately the time difference between the peaks of the corrected and the uncorrected curves in the Schwarzschild spacetime light curve.

There are three other key structures in the Schwarzschild spectrogram: a nearly horizontal line at around $\mathcal{E} = 0.5$ (feature A), a nearly horizontal line at around $\mathcal{E} = 1.1$ (feature C) and a wavy line (features E and F). Before $t \approx 0.35\,T_{\rm orb}$, feature A is produced by the primary image consisting of photons emitted by the plasmoid at locations $\phi \in (0°, 180°)$. These photons are emitted in a direction opposite the plasmoid's direction of motion with respect to the observer and therefore are Doppler red shifted. During this period, feature C (which is a continuation of feature H) is produced by the secondary image also consisting of photons emitted by the plasmoid at locations $\phi \in (0°, 180°)$. Since these photons are emitted in the same direction as the plasmoid's motion relative to the observer, they are Doppler blue shifted (recall blue blob at 90° in figure 3.1).

When the plasmoid is at $\phi = 180°$, around half the emitted photons is Doppler blue shifted and half is Doppler red shifted (recall the range of energy shifts in the Einstein ring at 180° in figure 3.1). This results in the main vertical line visible in the spectrograms, feature D, as discussed above.

After $t \approx 0.35\,T_{\rm orb}$, the primary image is Doppler blue shifted up to a peak at $\phi = 270°$ (feature E), after which it's energy shift decreases until a minimum at $\phi = 90°$ (feature F, joining feature A). All the other portions of the spectrogram correspond to secondary images. Finally, note how the spectrogram is not symmetrical about $\mathcal{E} = 1$, and a much larger portion of the emission is red shifted rather than blue shifted. This is a result of gravitational redshift, which affects all parts of the orbit in a similar way. A summary of the key features of the spectrogram is presented in table 3.1.

These features are also present in the Kerr spacetime case. The presence of a stronger gravitational field due to the closest proximity to the black hole causes the lower range of detected energies to be lower than in the Schwarzschild case and the presence of lensed images of multiple orders results in extra lines and features which make the spectrogram more complicated than its Schwarzschild counterpart.

3.3.3 Hotspot with time dependent emissivity

Next, we explored how these effects influence a flare from an emitter with time dependent emissivity. The time dependency is as described in section 3.2.

i) Calculation parameters

In this section we consider the same emitting region as in the constant emissivity case: an optically thick sphere of radius $R_{\rm e} = 0.5\,r_{\rm g}$ orbiting the black hole at $r = 6.5\,r_{\rm g}$ for Schwarzschild and $r = 2.5\,r_{\rm g}$ maximally rotating ($a = 0.998$) Kerr black holes respectively.

A	Nearly horizontal line at around $\mathcal{E} = 0.5$; primary image consisting of Doppler red-shifted photons emitted by the plasmoid at locations $\phi \in (0°, 180°)$
B	Vertical line at $t \approx 0.75\, T_{\text{orb}}$ (instantaneous) and $t \approx 0.05\, T_{\text{orb}}$ (time corrected); secondary ring visible in observer image in fifth (instantaneous) and first (time corrected) columns of figure 3.3.
C	Nearly horizontal line at around $\mathcal{E} = 1.1$; secondary image consisting of Doppler blue-shifted photons emitted by the plasmoid at locations $\phi \in (0°, 180°)$. Continuation of feature H.
D	Vertical line at $t \approx 0.25\, T_{\text{orb}}$ (instantaneous) and $t \approx 0.35\, T_{\text{orb}}$ (time corrected); due to the Einstein ring that occurs when hot spot is behind the black hole, as seen in the observer images of the second (instantaneous) and third (time corrected) columns of figure 3.3.
E	Highest energies reached in the spectrogram, from $t \approx 0.35\, T_{\text{orb}}$; primary image of the hot spot due to Doppler blue-shifted photons as the hot spot moves towards the observer, peaking at $\phi = 270°$.
F	Continuation of feature E; primary image of the hot spot moving towards the observer with decreasing line-of-sight velocity resulting in decreasing Doppler blue shift.
G	Vertical line at $t \approx 0.7\, T_{\text{orb}}$ (time corrected only); secondary image from when the hotspot is behind the black hole (thin inner disk at $\phi = 180°$ in figure 3.1). Feature hidden behind feature D in instantaneous spectrogram.
H	Nearly horizontal line at around $\mathcal{E} = 1.1$; secondary image consisting of Doppler blue-shifted photons emitted by the plasmoid at locations $\phi \in (0°, 180°)$; effectively corresponds to the same feature as feature C.

Table 3.1: Summary of key features in spectrograms of figure 3.4 (same features as in 3.6).

As mentioned in section 3.2, the emissivity model is not physically motivated by a particular process. It is rather a parameterized model which captures some key characteristics of explosive emissivity in astrophysical systems. As such, the values chosen are in a way arbitrary and could have been different. They were chosen to facilitate the demonstration of the general relativistic effects in the flares.

The calculation was run for a duration of $3\,T_{\rm orb}$ so that the gravitational and relativistic effects on the flare could be fully visible. This corresponded effectively to the flare's emission lasting 3 orbital periods, after which it was switched off. At this point, the emissivity would have decreased significantly due to cooling. However, in our plots this cutoff is still clearly visible.

The mechanism by which the cooling takes place in flares from the vicinity of massive black holes such as Sgr A* is not yet understood, so that it is difficult to make a physically inspired choice of the cooling (or drift) time scales. As such, the value of the cooling timescale used in the calculations presented here was chosen to be comparable with the orbital timescale. It was set to $t_{\rm cool} = 1.5\ T_{\rm orb}$, making it different for flares in Schwarzschild ($t_{\rm cool} = 156.3 r_{\rm g}$) and Kerr ($t_{\rm cool} = 46.8 r_{\rm g}$) spacetimes.

The flare spectrum was initialised as a Gaussian centred at 45 keV with standard deviation 2 keV. The flare injection timescale is effectively instantaneous, with $t_{\rm inj} = 0.03\ T_{\rm orb}$. This results in the sharp initial rise in the bolometric light curve of the intrinsic emissivity.

The frequency drift timescale was also set to a value which would make the visualization of the general and special relativistic effects clearer. In particular, we chose a drift rate such that, at the end of the sampled period, the spectral peak had drifted to 0.1 keV. This corresponds to a drift rate of $\mathcal{D} = \ln(0.1/45)/(3T_{\rm orb})$ or a drift time $t_{\rm drift} \coloneqq -1/\mathcal{D} \approx 0.491\ T_{\rm orb}$.

Figure 3.5 shows what the local emissivity looks like with the parameters used in the long flare calculations performed in this section. The same emissivity parameters in terms of orbital period were used was used for all flares, both in Schwarzschild and Kerr spacetimes. Since the orbital period is different for both flares, however, the numerical values of the parameters are different, though the shape of the intrinsic emissivity is the same.

ii) Spectrograms

Figure 3.6 shows the results for the case of a flare with the intrinsic explosive profile shown in figure 3.5 originating from an object orbiting a Schwarzschild black hole at $r = 6.5 r_{\rm g}$. The figure shows the spectrograms detected by an observer looking at them nearly edge on, at $\theta_{\rm obs} = 89°$ for flares whose onset occurs at four different azimuthal locations. The onsets occur at $\phi = 0°$, i.e. between the observer and the black hole, $\phi = 90°$, $\phi = 180°$, i.e. behind the black hole with respect to the observer, and at $\phi = 270°$. The figure also shows the bolometric

light curves (in red) and the light curves that would be seen in specific energy bands. The first band $2-8\,\mathrm{keV}$ represents the Chandra band and the others were chosen so that they covered different portions of the spectrogram.

Given the long duration of the flares considered, it is expected that, after some initial differences, the overall structure of the spectrogram and bolometric light curve of the flares would look similar for all origins. This is indeed the case. In all four spectrograms is it possible to see three brighter moments. These occur when the emitting hotspot is behind the black hole (equivalent to feature D in the spectrograms of figure 3.4). The effect of the intrinsic peak energy drift is also clearly visible in all four panels. The modulations found in section 3.3.2 are convoluted with the overall energy drift, still being visible but moving down in energy with time, as the flare's intrinsic emissivity changes. In order to capture as much information as possible, the plots in the figure are in logarithmic scale. The bolometric light curves of all four plots closely resemble those shown in logarithmic scale in figure 3.3. The main difference is an overall decrease in the peak intensity over time, as expected due to the intrinsic decrease in emissivity as the flare evolves. A sharp cutoff is also expected around $3T_{\mathrm{orb}}$, the time the intrinsic emissivity is turned off. In the $\phi = 180°$ and $\phi = 270°$ cases, this is precisely what happens, with the remaining intensity being due to the emission from secondary images. In the first cases, $\phi = 0°$ a small cutoff occurs around $3T_{\mathrm{orb}}$, but the main one occurs later due to delays in the arrival of different photons. For $\phi = 90°$, this time delay results in the cutoff happening later, at $\approx 3.2T_{\mathrm{orb}}$

Unlike the continuous emissivity flares, which are assumed to be "turned on" constantly, these flares have a clear onset and cutoff time. This means that the difference in arrival time of photons from primary and secondary images will be clearer. The first panel of figure 3.6 ($\phi = 0°$) shows two solid lines sliding from higher to lower energies, and merging in the red region. The first of them (feature A) is the primary image corresponding to the bottom horizontal line in figure 3.4. The second one (feature C) is the secondary image corresponding to the top horizontal line of figure 3.4. These two sliding lines merge in the large red block: the red vertical line (feature D) corresponds to the vertical line in figure 3.4, when the plasmoid is behind the black hole. Following this are features E and F, produced as the plasmoid moves through $\phi = 270°$ until $\phi = 360°$. The fainter blue-ish sliding lines (feature H) correspond to the fainter horizontal lines in figure 3.4 of similar colour due to secondary images which arrive at the observer while the primary image is sliding down from the peak energy. After this point, the same structures get repeated at lower energies, becoming harder to distinguish by eye due to the smaller spread of detected energies. Similar features are clear in the other plots, especially for $\phi = 90°$. The $\phi = 180°$ spectrogram begins precisely as the Einstein ring forms, with a brief period of Doppler blue shift until the flare reaches its peak energy and starts sliding down to lower energies. The intrinsic energy drift results in an overall decrease in peak energy even at

the start of the flare, when Doppler shift alone would still cause it to increase. The very steep decline which follows in this panel is due to the convolution of both the decrease in relativistic Doppler blue shift and the intrinsic energy drift. The final panel shows very similar behaviour, with the flare beginning already at the point where the decrease in Doppler blue shift would cause it to shift to lower energies even in the absence of an intrinsic emissivity drift.

In figure 3.1 we looked at the delays between the arrival of photons travelling along different paths towards the observer. For the locations sampled in the figure, the shortest and largest time delay between the first and last photon to be detected were respectively $\approx 25 r_{\rm g}/[c]$ for $\phi = 90°$, which corresponds to $\approx 0.24\, T_{\rm orb}$ and $\approx 50 r_{\rm g}/[c]$ for $\phi = 180°$, which corresponds to $\approx 0.48\, T_{\rm orb}$. As such, we would expect there to be some detected radiation until $\approx 0.24\, T_{\rm orb}$ to $\approx 0.48\, T_{\rm orb}$ after the intrinsic emissivity is "turned off", depending on where the cutoff happens. Note that, since the pixel resolution used for the calculation of the spectrograms was higher than that of the observer images, there are some higher order images which are captured here which were not in the panels of figure 3.1, hence explaining why e.g. in the $\phi = 90°$ panel there is some residual radiation detected after $3.25\, T_{\rm orb}$.

Figure 3.7 shows the results for the same flares, now emitted from a body on an orbit at $r = 2.5\, r_{\rm g}$ around a Kerr black hole with $a = 0.998$. Although the local emissivity was the same as for the Schwarzschild case, a striking feature in these plots is the large amount of higher order images present. This should not be a surprise based on the results for Kerr spacetimes presented in section 3.3.2. The proximity to the black hole which orbiting bodies can achieve in fast spinning Kerr spacetimes results in a large amount of high order lensed images. In figure 3.1 we saw that the time delays between the first and last detected photons for the hotspot locations sampled could be as large as $5.2\, T_{\rm orb}$. For a flare cutoff at $t = 3\, T_{\rm orb}$, this means that one would expect to receive emission from secondary images until at least $t \approx 8.2\, T_{\rm orb}$, much later than what was observed in the Schwarzschild case. The detection of very faint radiation close to $t \approx 9\, T_{\rm orb}$ is due to the higher resolution of these calculations relative to those in figure 3.1, which results in even higher order images being detectable at later times.

Just as in the Schwarzschild case, the key features of the constant emissivity spectrogram and bolometric light curve can be identified in the spectrograms and bolometric light curves of figure 3.7, despite with a decreasing intensity. In Kerr spacetime too, horizontal lines become slanted due to the intrinsic emissivity profile, and the emissivity cutoff at around $3\, T_{\rm orb}$ is also visible in some of the spectrograms. In the Schwarzschild case, for $\phi = 0°$ a cutoff is visible at $t = 3\, T_{\rm orb}$. In the Kerr case this cutoff is not clear, likely because at this point it is difficult to distinguish the primary from higher-order images in this spectrogram. Other than in this case, all other Kerr spectrograms show a discontinuity at the same times as in the Schwarzschild case: $t = 3.2\, T_{\rm orb}$ for $\phi = 90°$ and $t = 3\, T_{\rm orb}$ for $\phi = 180°$ and $\phi = 270°$. The cutoff is visible as a discontinuity in the features corresponding to the primary image of the hotspot.

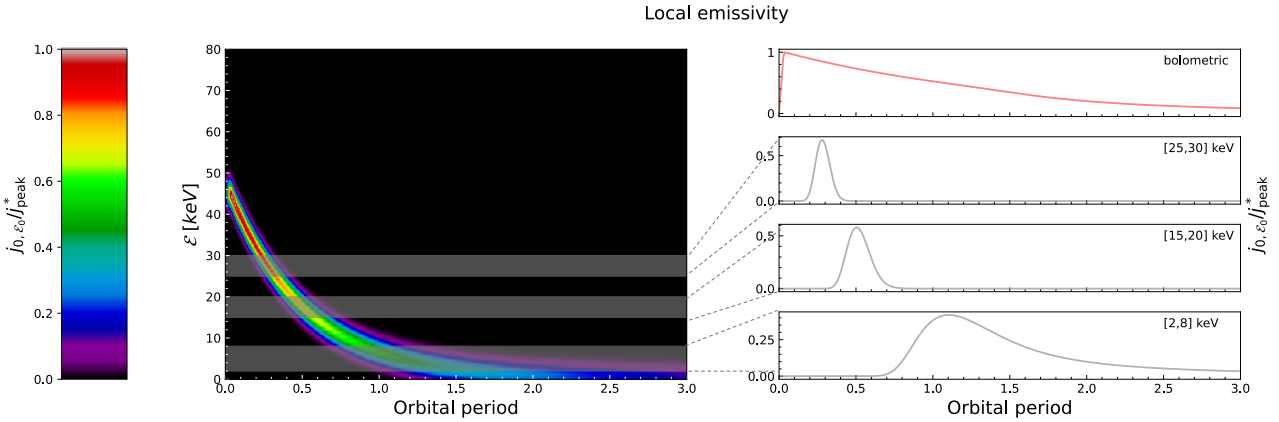

Figure 3.5: Left: Local emissivity spectrogram responsible for the explosive-like flares calculated in this chapter. The same emissivity was used for both Schwarzschild and Kerr spacetimes and for all flare origin locations in terms of orbital period, so the numerical values of the parameters are different in both cases. Right: light curves over the specified energy bands.

A key result from these calculations for both spacetimes is how different the light curves measured at different energy bands are. This was already true in the case of continuous emissivity (section 3.3.2) and it is even more obvious here. In particular, since theses flares intrinsically drift to lower energies, the lower energy band considered (here $2 - 8$ keV) is the band where the detected light curve most resembles the bolometric light curve for most of the flare's duration in each case. If the intrinsic emissivity drifted to higher energies instead, this would be expected for higher energy bands. It is difficult to conclude whether FRSD flares may or may not appear as SRFD flares based on the present calculations: the long duration of the flares and the intrinsic time-dependent emissivity, convoluted with the relativistic effects, gives rise to multiple secondary and higher order images, resulting in complex morphologies of multiple flares from an observer's perspective, which cannot be simply labeled as FRSD nor as SRFD.

3.4 Further remarks

3.4.1 Potential areas for exploration and model improvement

The calculations presented so far were aimed at identifying the effects of general and special relativity, as well as observation band-pass, in the distortion of detected flares. It was therefore desirable to consider a simple emissivity model to avoid the complications which arise due to the convolution of a complicated emissivity profile and the general relativistic effects. As such, a simple parameterized model for the emissivity was chosen (a thin Gaussian spectrum, emitted from the surface of a spherical object on a circular equatorial orbit, without absorption). This is indeed a simplification of the more complex reality. However, it allowed us to separate in part the individual effects at play in each part of the spectrograms and hence provided insights towards the interpretation of real observations. In a realistic situation, one would need to

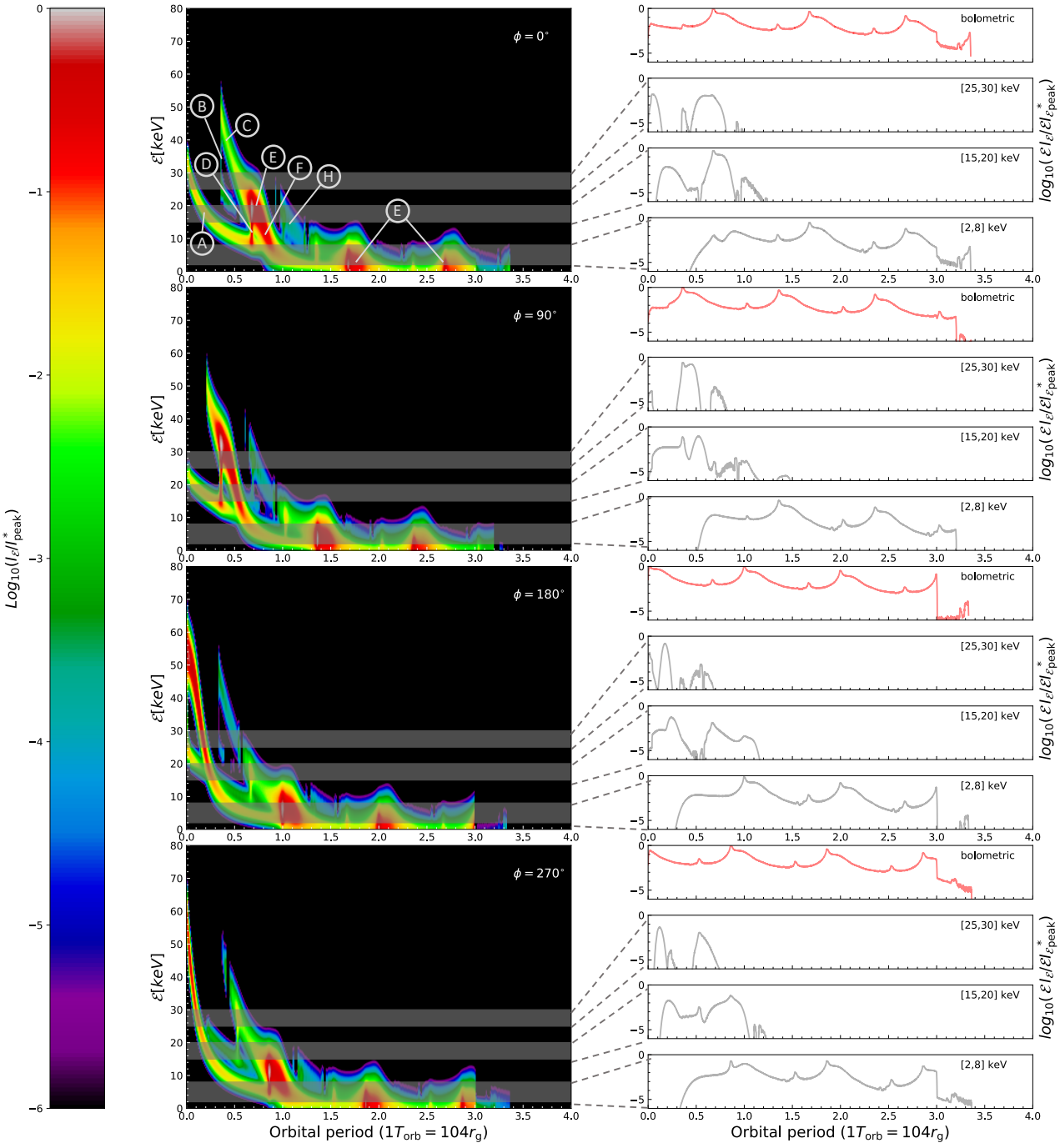

Figure 3.6: Left: Spectrograms of long explosive emissivity flares in Schwarzschild spacetime for different onset locations. The grey bars represent the energy bands at which the band-specific light curves on the right were calculated. A summary of the key features is presented in table 3.1. Right: Bolometric (red) and band-specific light curves (grey) caused by a flare with in local emissivity as in figure 3.5. The features in the top panel are labeled with the same labels as the corresponding features in figure 3.4. Resolution: 1000×1000 pixels; 2160 time frames; 401 energy bins. These calculations were run on machines with 128 physical cores (AMD epyc processor) and 1Tb of RAM, and the calculation took approximately 48 hours for each initial hot-spot location.

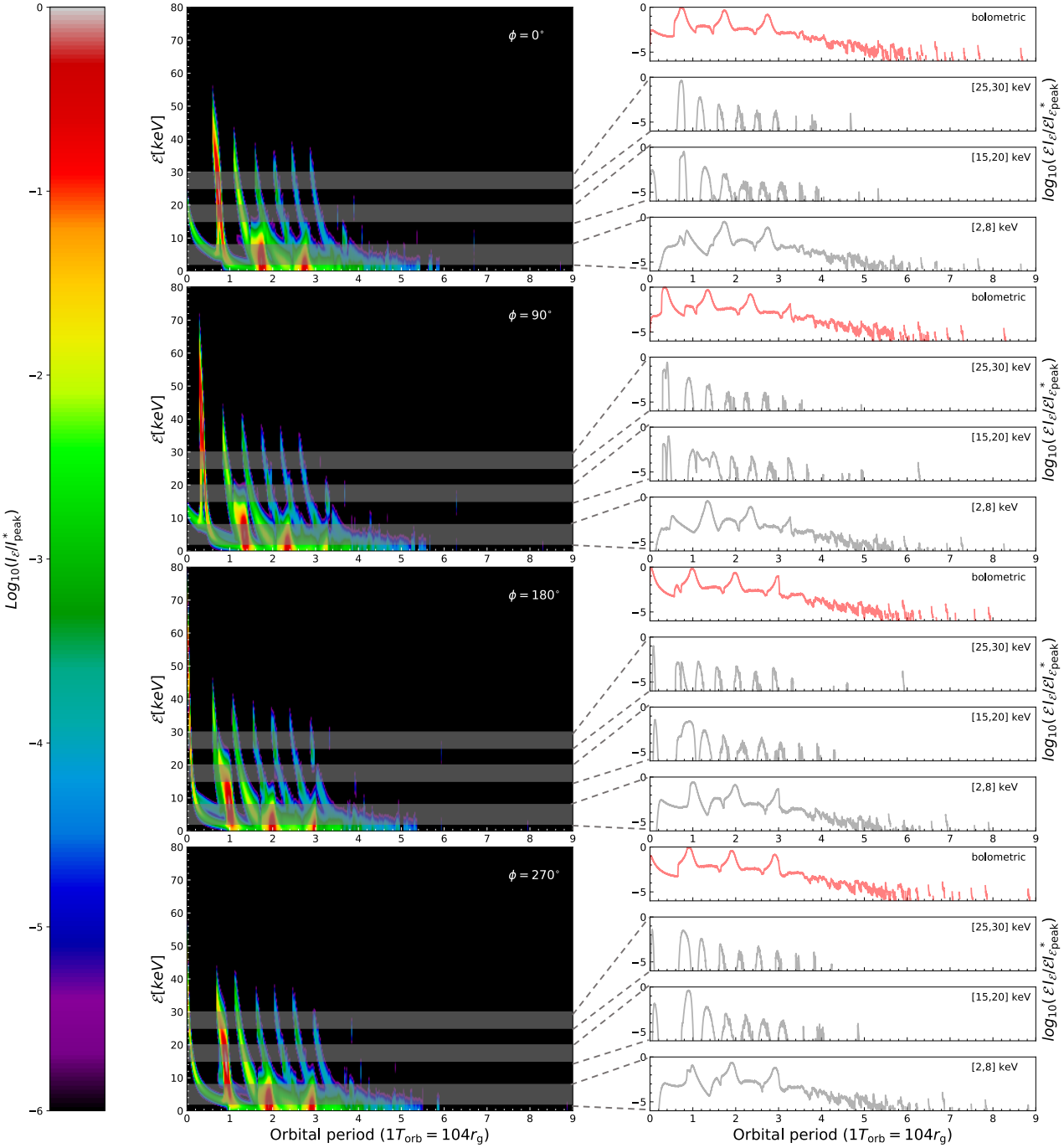

Figure 3.7: Same as figure 3.6, but for a Kerr black hole with spin parameter $a = 0.998$. Resolution: 1000×1000 pixels; 2160 time frames; 401 energy bins. These calculations were run on machines with 128 physical cores (AMD epyc processor) and 1Tb of RAM, and the calculation took approximately 48 hours for each initial hot-spot location.

account for at least the following factors:

- **Emission spectrum:** A more realistic spectrum constructed based on a physical model could be used instead of the simpler parameterised model used here. Although this is not expected to produce large differences in the bolometric light curves (compare e.g. with the light curves from Younsi and Wu (2015), which were calculated using a more complicated synchrotron-inspired spectrum), it will be relevant when assessing full spectrograms or light curves at specific energy bands. Although the final outcome, including the convolution of intrinsic emissivity and GR effects will be different, the GR effects themselves will not change with this.

- **Emission region:** In reality, flares associated with magnetic eruptive events have a complex time evolution and spatial structure, as seen in solar flares and flares form magnetic interactions in other stars (see e.g. Reid, 2020). Furthermore, based on results from GRMHD simulations, it seems unlikely that the emission region is a sphere that retains its shape perfectly over several orbits. Instead, its shape and size are likely to change. Some previous results found that light curves due to the primary image are not highly dependent on the shape or size of the emitting region (Schnittman and Bertschinger, 2004), though the higher order images would cause differences that would likely affect the spectrograms and light curves, both bolometric and at specific energy bands. It's motion is also likely more complicated than an equatorial circular orbit (e.g. GRAVITY Collaboration et al., 2020a). The different relativistic effects at play in a different orbit will cause differences in the emitted light curves.

- **Absorption:** Accurate predictions of the time dependent spectral evolution of flares from magnetic eruption events in the Galactic Centre would require a proper treatment of line of sight absorption. This absorption can occur within the emitter itself (if it is not opaque, both emission and absorption can occur at any point within the emitting region), or outside it. Since absorption is often frequency dependent, it might affect different portions of the same image differently due to Doppler energy shifts. As such, instead of the simplified no-absorption model used in this work, if the aim of such calculations is to make accurate predictions or parameter estimations from the observations, then a self-consistent emission and absorption model will be necessary.

Given the modular structure of the code developed, it is in theory not difficult to adapt it to incorporate any of the above modifications. In order to turn the results in this chapter into more realistic observational predictions, one would be able to use physically motivated emission and absorption models if they were to be provided.

3.5 Conclusions and observational implication

Flaring events across the electromagnetic spectrum are common in several astrophysical scenarios, from the sun and other stellar systems (e.g. Benz, 2017; Hannikainen et al., 2005; García-Alvarez et al., 2003; Retter et al., 2005; Fuhrmeister et al., 2008) to massive black holes in the centre of galaxies such as in the NGC4151 (Lawrence, 1980; Warwick et al., 1996) and 3C111 (Chatterjee et al., 2011; Schulz et al., 2020). Sgr A* also experiences such events. Some of these systems have the benefit of being close to Earth, allowing for intense imaging and studying. For others, on the other hand, accurate imaging becomes much harder and most information must be obtained from light curves and spectral data.

In this work we have shown that, when the systems of interest are associated with black holes, the highly relativistic motion and strong gravitational effects can significantly distort the emitted flares, changing their spectrum, light curve profile and, in some cases making a single flare appear as multiple ones. The closer to the black hole and the faster the emitter moves with respect to the observer, the more pronounced such effects will be. Similarly, most of the distortions are larger in the case of edge-on observations of the emitter's orbit. We considered both the case on continuous, constant emissivity and the case of flaring events with a time-dependent explosive-like emissivity with an intrinsic energy drift and found that both were affected by the gravitational and relativistic effects due to the proximity to the black hole.

Even for the simplified parameterized models used in this work these effects were present and affected different energy bands differently, resulting in different light curve profiles at each band. These calculations exemplify well that, when the events occur very close to a black hole, obtaining light curve data only at specific energy bands may be misleading and, in the absence of multi-wavelength observations and corrections for gravitational effects, may lead to incorrect conclusions about the intrinsic emission properties of the flares. An interesting extension of this work would be to explore the effects on flares with time scales shorter than the orbital time scale. Given their shorter period, they will only cover a small portion of the orbit, so that the general relativistic distortions on it will be less evident, except when the flare happens to cross regions where the spectrogram 3.4 changes significantly in sort periods of time (e.g. around $\phi = 180°$). There will also be multiple flares occurring, this time completely separated in time, due to the late arrival of lensed images. By focusing on the primary image (or alternatively on the strongest one, in the cases when the primary image flare is not the strongest), it would be possible to evaluate the skewness of the corresponding portion of the light curve and evaluate how the profile changed compared to the fast-rise-slow-decay intrinsic emissivity. It would then be interesting to initialize such flares in randomized different locations (r, θ and ϕ) and to perform a statistical analysis of the detected flare properties. Then, it might be possible to establish how likely it is for a certain fast-rise-slow-decay flare to appear as a slow-rise-fast-decay

one.

More realistic calculations of the observations of such flares may be performed by following the proposed areas for future development mentioned in section 3.4.1. By including physically inspired models, it will be possible to use the present code to perform realistic predictions of detections which can be compared to observations. The general relativistic effects observed in the simplified model will be similar, and such realistic calculations may provide a way to correct for such effects in observations, hence aiding in our understanding of the intrinsic mechanisms at play in the vicinity of black holes.

Chapter 4

Massive particles: interactions with the propagation medium

4.1 Introduction

Energetic particles are generally associated with flaring events in the vicinity of black holes such as those discussed in the previous chapter. The particles can carry large amounts of energy and can interact with diffuse media such as accretion disks or tori around the black hole. The deposition of this energy by such particles may unsettle the quasi-equilibrium of such structures, altering their thermal and magneto-hydrodynamic state.

If the particles are emitted at distances from the the black hole comparable to the gravitational radius, the effects of gravitational lensing and relativistic beaming due to the motion of the emitter will cause them to focus in specific regions. The time delays caused by potentially orbiting the black hole multiple times will result in a time-dependent energy injection into the medium. And finally, the effects of gravitational and Doppler energy shifts may result in an injection spectrum significantly different from the original particle spectrum at their emission/acceleration point.

To quantify all these effects, it is necessary to have an appropriate GRRT formulation in the from of a particular code which can account for the effects mentioned above for massive particles. This is a first step into understanding the potential interactions which may take place in the vicinity of black holes due to highly energetic particles, and it is an essential step which must be understood before focusing on the sub-atomic physics and radiative cooling processes through which such interactions actually occur.

This chapter showcases how the the massive particle GRRT formulation developed in chapter 2 can be used to investigate the potential timing and preferred location for these interactions, as well as where the particles are most likely to deposit their energy. Note that the calculations in this chapter are, at the point of writing this thesis, of an exploratory nature, without accurate astrophysical scenarios and models. Despite this, there are clear astrophysical motivations

for considering such a scenario. For example, in order to explain X-ray filaments (Zhang et al., 2014) and certain γ-ray emission (Aharonian et al., 2006) in the Galactic Centre, models have been proposed which invoke the interaction of high energy cosmic rays accelerated in the vicinity of Sgr A* with molecular clouds (Gabici et al., 2009). Such particles (likely protons) would produce secondary particles via these interactions (high energy electrons) which would be responsible for emitting the detected radiation. The calculations in this chapter can shed light into these models.

There is also evidence that tidal disruption events in the vicinity of black holes can lead to the production of neutrinos (Hayasaki, 2021) via hardronic interactions: energetic particles from near the black hole would bombard the debris torus formed by the remnant of the tidally disrupted star and interact with baryons present there. These calculations could be applicable to the study of the particle bombardment and the transport of the resulting particles, which would decay into neutrinos and leptons.

4.2 Computational model

The system considered in this chapter as a case study is that of a torus revolving in a pro-grade direction around a Schwarzschild or Kerr central black hole. The torus is considered to be much less massive than the black hole, so that the spacetime is well described by the black hole metric alone.

Located between the inner surface of the torus and the event horizon of the black hole, on the equatorial plane, is a source of high-energy photons or massive particles. The size of the source D_s is very small compared to the gravitational radius of the black hole (i.e. $D_\mathrm{s} \ll r_\mathrm{g}$), and therefore the source is treated as a point-like object. Given the axisymmetry of both the Schwarzschild and Kerr systems, the ϕ coordinate of emission or acceleration location was set to $\phi = 0$ in all cases and its distance from the black hole, r_em, was varied between $2.5 - 20r_\mathrm{g}$. The geometrical configuration of the system is illustrated in figure 4.1.

The emission was considered to be isotropic in the source's local co-moving frame, and the source is on a Keplerian circular orbit around the black hole. This was modeled by initializing geodesics from the source's location in equally spaced directions, with each geodesic representing a bundle of massive particles or photons. The initial directions were then transformed into the black hole's Boyer Lindquist frame and the initial conditions set as described in section 2.1.4.

The target body was set to be a large torus with a major radius of $700r_\mathrm{g}$ and a minor radius of $300r_\mathrm{g}$. Given the distance between the surface to be found and the black hole, the error tolerance of the surface finding algorithm was set to 1% of the major radius. This is a larger tolerance than that used in chapter 3, where the surfaces to be found were much smaller.

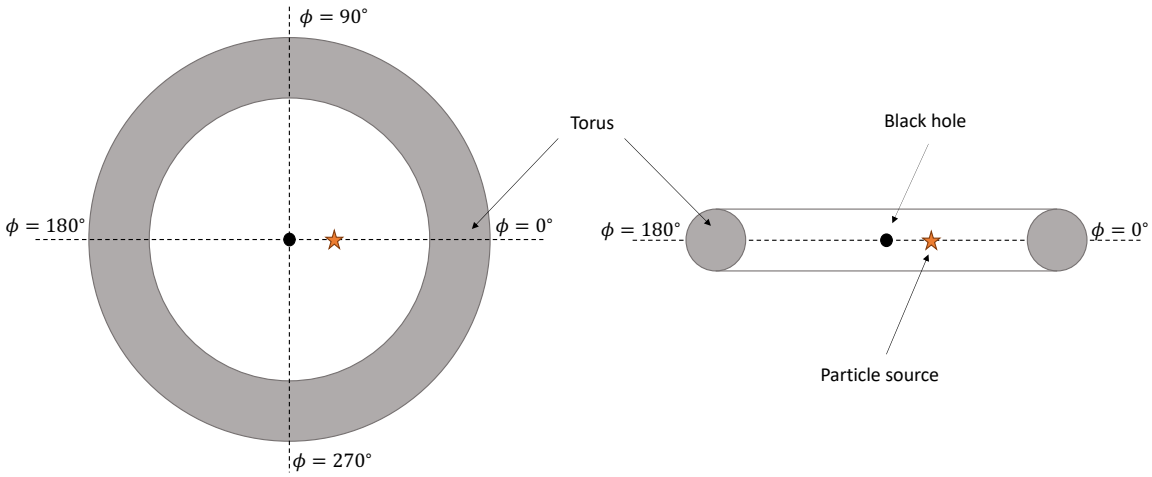

Figure 4.1: A schematic illustration of the geometrical configuration of the model adopted in this study (not to scale); Left: face on (top) view; right: edge on (side) view. The energetic particles are produced in the vicinity of a central black hole, which is surrounded by a geometrically thick accretion torus. The source's size is small compared to the sizes of the black hole and the accretion torus. As such, it is treated as a point source and it is always chosen to be at $\phi = 0°$. The distance between the source and the black hole is much smaller than both the major and minor radii of the torus. The emission of the particles is isotropic in the local rest frame of source.

Importantly, any interactions which would alter the trajectory of the particles (e.g. magnetic fields which would affect charged particles) are neglected.

In this chapter we performed two different calculations. First, we investigated the location and timing of the intersection of the particles with the target surface, without worrying about the processes taking place within the torus. Therefore, the torus was considered optically thick and the geodesic integration terminated as soon as the surface was reached.

Secondly, we investigated whether the energy deposition by the particles as they propagate inside the absorbing body behaved as expected. For these calculations, a particular absorption coefficient was chosen for the torus. The interactions between the particles and the torus material are complicated, each having its own cross section resulting in different probabilities of interaction. An "effective absorption coefficient" could be obtained from a combination of the cross sections of all possible interaction processes that could take place within the torus, which would involve a tricky calculation. In this chapter we do not use such a physically motivated absorption coefficient. Instead, we chose particular values which would better illustrate the capabilities of the GRRT algorithm discussed in this thesis.

Another significant simplification of the code is that we consider absorption coefficients which are constant across all particle energies. This is unlikely to be the case in physical situations and it is not a limitation of the code, which can deal with absorption coefficients of whatever shape one desires, but rather a result of the absence of physical motivation to justify a more complicated energy dependency. In particular, three absorption coefficients were chosen - one

where most particles were absorbed a short distance into the absorbing medium, one where a large percentage of particles escaped the medium and one in between these two. In this way, a wide range of possible physically motivated absorption coefficients is covered by the case study.

4.3 Results and discussion

4.3.1 Time-like geodesics

To perform GRRT of massive particles, the first step is to solve the geodesic equations for massive particles. Unlike for null geodesics in vacuum, there are multiple possible timelike geodesics with the same spatial initial direction which a massive particle may follow, depending on the particle's initial spatial 3-velocity. Specifying an initial mass to energy ratio for the particle determines the unique geodesic the particle will follow for a given initial spatial direction. This is true for both the backward and the forward initial conditions.

Numerical accuracy is a very important factor to establish the validity of the results. Therefore, we start by demonstrating the accuracy and performance of the code for timelike geodesics for different mass to energy ratios. For ease of visualization and comparison, this calculation was performed using backward ray-tracing.

In figure 4.2 we show the paths travelled by particles on timelike geodesics for different mass to energy ratios, where the energy is the energy as measured in the local orthonormal frame comoving with the emitter [1]. As expected, the spatial trajectories followed by massive particles approach those of photons as their Lorentz factor increases (i.e. $m[c^2]/\mathcal{E}$ decreases). In fact, for Lorentz factors greater than $\gamma = 10^2$, the physical trajectories become nearly indistinguishable from those of null geodesics. As shown on the last panel of figure 4.2, the travel times until the vicinity of the black hole is reached also become nearly indistinguishable from the photon travel times as the Lorentz factor of the massive particles increases. Again, this is expected as particles travel closer to the speed of light. As such, in this chapter we only perform calculations for massive particles with $m[c^2]/\mathcal{E} \geq 10^{-4}$.

Let the particle's 4-velocity be given by $k = (\dot{t}_0, \dot{r}_0, \dot{\theta}_0, \dot{\phi}_0) = (\dot{t}_0, \dot{z}_0\hat{\mathbf{n}})$, where $\dot{z}_0$ is the magnitude of the spatial component of the 4-velocity and is given by equation (2.58). Then, as the particle

[1] In special relativity (flat spacetime) the Lorentz factor $\gamma = 1/\sqrt{1-(v/[c])^2}$ and the mass to energy ratio $m[c^2]/\mathcal{E}$ are related by $\gamma = (m[c^2]/\mathcal{E})^{-1}$. In the present chapter it is sometimes useful to talk about the particle's Lorentz factor. Following the special relativity definition, this will be used to refer to a particle's energy to mass ratio as measured by the particle's emitter. I.e. in the present chapter a particle's Lorentz factor is defined $\gamma \coloneqq (m[c^2]/\mathcal{E})^{-1}$ where $\mathcal{E}$ is the particle's energy measured by the emitter. This definition is reasonable since it defines the initial conditions of the particle's spatial velocity in the emitter's frame, which is later transformed into the black hole frame. In order to compare the timelike geodesics with null ones, in this thesis we mostly speak in terms of the mass to energy ratio instead of the Lorentz factor, as it does not make sense to speak of Lorentz factor of light, but for massive particles the terms are used interchangeably.

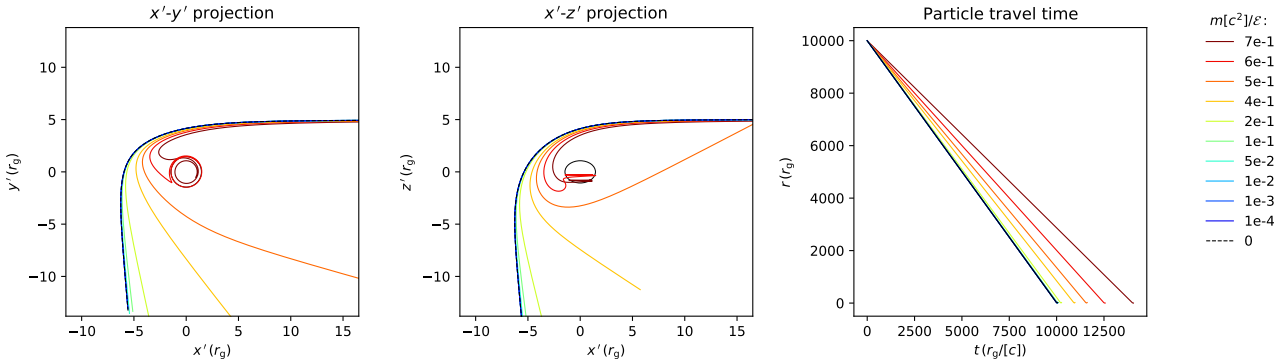

Figure 4.2: Backward ray tracing for particles of different masses in a Kerr spacetime with spin $a = 0.998$. The first two plots show the projections of the spatial trajectory of the particles and the third plot shows the particle's distance from the black hole (which is at $r = 0$) as a function of travel time. All geodesics have the same spatial initial conditions and only differ on their mass to energy ratio. With the exception of the $m = 0$ geodesic (dashed line), which is null, all other geodesics are timelike. Note that both the spatial trajectories and the travel times of timelike geodesics with mass to energy ratios smaller than $m[c^2]/\mathcal{E} = 10^{-2}$ (or Lorentz factor greater than $\gamma = 10^2$) become nearly indistinguishable from those of null geodesics.

becomes more relativistic, the value of $\dot{z}_0$ - and hence also of $\dot{r}_0, \dot{\theta}_0, \dot{\phi}_0$ - becomes increasingly large (see equations (2.51)-(2.53)). $\dot{r}_0, \dot{\theta}_0, \dot{\phi}_0$ are all proportional to $\dot{z}_0$. In order to calculate the value of $\dot{t}_0$ we use equation (2.54), i.e.

$$\dot{t}_0 = \frac{-(2g_{t\phi}\dot{\phi}_0) + \sqrt{(2g_{t\phi}\dot{\phi}_0)^2 - 4g_{tt}(g_{rr}\dot{r}_0^2 + g_{\theta\theta}\dot{\theta}_0^2 + g_{\phi\phi}\dot{\phi}_0^2 - \xi)}}{2g_{tt}}. \tag{4.1}$$

As the particle becomes more relativistic, all but the last term inside the square root increase rapidly as $\dot{z}_0^2$. The ξ term, on the other hand, is always of order 1[2]. This means that, for relativistic particles, the code needs to subtract numbers of very different orders of magnitude from each other, which leads to computational errors.

For example, from equation (2.58) we see that a particle with $m[c^2]/\mathcal{E} = 10^{-5}$ has $\dot{z}_0 \approx 10^5$, so that the first three components of the term $(g_{rr}\dot{r}_0^2 + g_{\theta\theta}\dot{\theta}_0^2 + g_{\phi\phi}\dot{\phi}_0^2 - \xi)$ in equation (4.1) are of order 10^{10}. As such, the code needs to subtract numbers 10 orders of magnitude apart (or more, for more relativistic particles). This results in rounding errors that accumulate as the integration progresses. As a response to this, the code makes use of the adaptive step size in the Runge-Kutta algorithm and decreases it until the integration errors are within an acceptable limit. While this may rectify the issue with the integration error at each step, a much larger number of steps are now required to perform a very similar integration. This leads to two undesirable consequences: firstly, the computational time needed to calculate these geodesics

[2]Although it is usual to use an affine parameter such that $\xi = -1$, one can always re-parameterize the geodesic so that ξ can become any number. However, this will not remove the computational error issue because the terms $\dot{r}_0$, $\dot{\theta}_0$ and $\dot{\phi}_0$ will change similarly with the new parameterization.

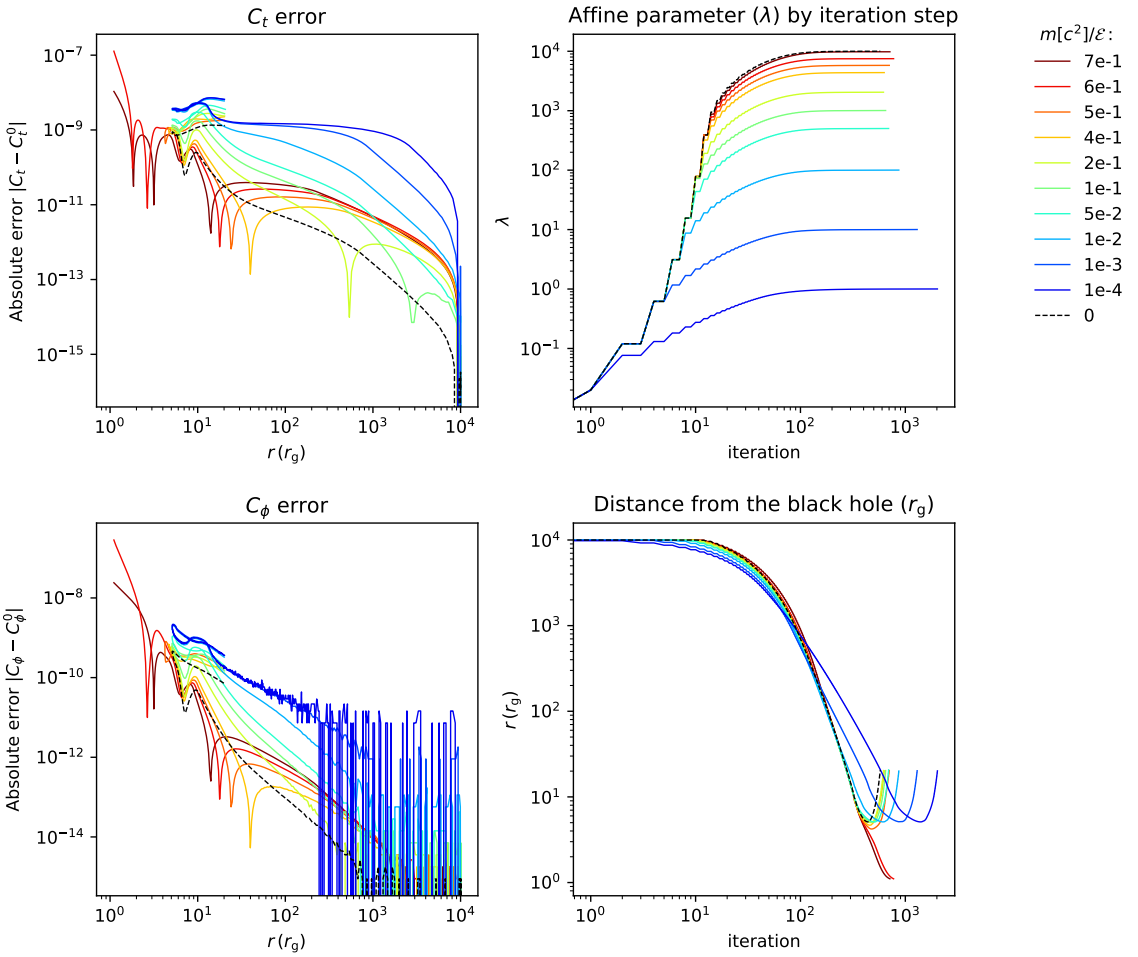

Figure 4.3: Integration errors for the geodesics of particles with different mass to energy ratios. Left: errors in C_t and C_ϕ as a function of radial coordinate along the geodesics of particles with different mass to energy radios. Right: affine parameter λ (top) and radial coordinate r (bottom) as a function of iteration number of the integration calculation.

is much larger than that needed to solve the very similar null geodesics; secondly, it results in an accumulation of rounding errors, making the resulting geodesics less reliable.

Figure 4.3 illustrates this by showing both the errors in C_t and C_ϕ as a function of distance to the black hole for the geodesics plotted in figure 4.2. The two error plots (left) show that the errors for the more relativistic particles increase. Note that the two least relativistic particles, $m[c^2]/\mathcal{E} = 0.7$ and $m[c^2]/\mathcal{E} = 0.6$, have higher errors at very small r. This is due to the fact that these two particles are captured by the black hole. As such, they get much closer to the event horizon - where a coordinate singularity arises and hence errors increase - than any of the other particles in this calculation. However, for comparable r, it is clear that the largest errors occur for the more relativistic particles, namely $\gamma = 10^2$, $\gamma = 10^3$ and $\gamma = 10^4$.

The affine parameter plot (top right of figure 4.3) shows that the more relativistic a particle is, the smaller the size of the integration step taken by the RK algorithm. The integration of

null geodesics and of low velocity particles are the most efficient in terms of integration time and step size. The affine parameter and distance to the black hole plots (right panels) show that, as the initial velocity of the particle increases (i.e. $m[c^2]/\mathcal{E}$ decreases), the total number of iterations required for the particle to reach a similar stage in the integration significantly increases. This results in the code being significantly slower for these particles. Given this, all the calculations in this chapter were performed for particles with Lorentz factors only up to $\gamma = 10^4$, as previously mentioned.

4.3.2 Bombardment of a torus by massive particles

i) Optically thick[3] torus

Figure 4.4 shows a summary of the data calculated across various distances from the black hole for multiple mass to energy ratios. The plot shows a histogram of the azimuth at which the torus is hit by the accelerated particles in each case, followed by a summary of the peak azimuthal location of the hits and the total fraction of the emitted particles which hit the torus. The results provide insightful detail as to the effect of special relativity and gravity in the propagation of particles with different masses emitted close to the event horizon of Schwarzschild and Kerr black holes. The key results we will discuss are the azimuthal location where particles concentrate on the torus (i.e. the *peak* ϕ), the fraction of emitted particles that hit the torus, and the arrival times of the particles to the torus.

Peak ϕ

We begin by looking at the results for large $r_{\rm em}$. As the source's distance from the black hole increases, the differences between Schwarzschild and Kerr histograms decrease. The overall shape of the histograms at large $r_{\rm em}$ has two components: an oscillatory pattern spanning the whole torus and a narrow peak, which in Schwarzschild spacetime is around $\phi = 180°$ and in Kerr changes location with $r_{\rm em}$. This result is a combination of relativistic beaming, which depends on the speed of the source and, hence, indirectly on its location, and gravitational lensing. The interplay between these two effects results in the differences observed between the different particle energies and source locations. Relativistic beaming causes more particles to be emitted in the positive than the negative ϕ direction (see figures 2.4 and 4.6). This results in more hits between $\phi = 0°$ and $\phi = 180°$ than between $\phi = 180°$ and $\phi = 360°$, giving rise to the oscillatory pattern.

The second feature present in the histograms, the thin peak, is a result of gravitational lensing.

[3]Optical thickness is generally used with respect to photonic absorption/ attenuation. In this chapter we use the term *optically thick* to refer to systems where the particle's mean free path is much smaller than the scale of the system, so the system is effectively "opaque" to the particles, and *optically thin* to refer to systems where the particle's mean free path is large compared to the scale of the system, so the system is effectively "translucid" to the particles.

Figures 4.7 and 4.8 show an interesting phenomenon regarding this peak which is also clearly visible on the top and middle panels of figure 4.4: while in Schwarzschild spacetime the peak occurs always around $\phi = 180°$ (with the exception of very high $m[c^2]/\mathcal{E}$ particles at very small $r_{\rm em}$ - see later for comments on these), in Kerr spacetime the peak starts at higher ϕ and moves towards $\phi = 180°$ as the emitter's distance from the black hole increases. This is a result of the frame dragging effect, present only in Kerr spacetime, which competes with the relativistic beaming and lensing effects mentioned above. When the particles travel very close to the black hole, they experience a strong drag in the positive ϕ direction due to the rotation of the spacetime around the black hole, caused by its spin. This means that, while particles would focus at $\phi = 180°$ without spin, the drag causes them to focus further along the torus, at higher ϕ. The frame dragging effect becomes weaker further from the black hole. So, as the source moves away, this effect loses importance and the results become more similar to those of Schwarzschild black holes[4].

For emission locations very close to the black hole, i.e. small $r_{\rm em}$, there are significant differences between histograms of particles of different masses (see also figure 4.5). These differences become less relevant as one progresses to larger radii. As the particle's $m[c^2]/\mathcal{E}$ decreases, the shape of the histograms approaches that of photons, as expected, with little differences between different particle energies for $m[c^2]/\mathcal{E} > 0.1$.

The peak ϕ location for very low energy particles at low $r_{\rm em}$ is more messy than for higher energy particles. These particles are less relativistic and hence are more sensitive to the gravitational lensing from the black hole. The relativistic beaming will also be stronger for these particles. The closer they are to the black hole, the stronger these effects will be. In some cases (e.g. particles with $m[c^2]/\mathcal{E} = 0.7$ emitted at $r < 3r_{\rm g}$ in Schwarzschild spacetime) every emitted particle ends up entering the event horizon, so no particles at all reach the torus. As the particles become more relativistic or their emission radius increases, more of them become able to escape the black hole and be lensed towards the torus. Figure 4.5 illustrates how the patterns produced by such high $m[c^2]/\mathcal{E}$ particles in the torus are complicated, not quite matching those of more relativistic particles or of high $m[c^2]/\mathcal{E}$ particles emitted further from the black hole.

Fraction of hits

The fraction of emitted particles which reach the torus varies both with radius and mass to energy ratio. As shown in figure 4.4 (bottom panel), the fraction of hits is close to 40% in most cases. This is expected for a torus of the given dimensions, which covers a solid angle of around 40% of the total sky plane. Excluding the Schwarzschild cases of $r_{\rm em} = 2.5r_{\rm g}$ and $r_{\rm em} = 3r_{\rm g}$, for which no low energy particles reach the torus[5], the fractions of hits within a certain radius

[4]Recall that the peak of the Kerr light curve in figure 3.3 was also shifted to values of $\phi > 180°$ due to frame dragging. See main text for a further comparison between these histograms and the light curves.

[5]These curves are not shown in the figure because, even for high energy particles the total fraction to reach

as a function of mass to energy ratio follow a similar trend in both Kerr and Schwarzschild spacetimes.

In order to understand these trends we must take into account the different factors which affect whether or not particles reach the torus. These include: capture of the particles by the black hole, gravitational lensing which focuses the particles, and relativistic beaming of the particle's initial directions due to the motion of the source. It is the competition between these different effects that explains the different behaviours in the bottom panel of figure 4.4.

For example, if one considered a stationary source, for a given fixed $r_{\rm em}$, a larger $m[c^2]/\mathcal{E}$ would correspond to a smaller initial particle speed, making it easier for the particles to be captured by the black hole (resulting in less particles hitting the torus); on the other hand, a smaller speed makes it easier for the particles to be focused onto the torus by gravitational lensing (resulting in more particles hitting the torus). For a fixed $m[c^2]/\mathcal{E}$ ratio, a larger $r_{\rm em}$ would result in less particles being captured by the black hole (more torus hits) but it would also result in less particles getting lensed and focused onto the torus (less torus hits).

If one considers also the motion of the source, whose speed increases the closer it is from the black hole, the beaming effect also becomes relevant. For a given fixed $r_{\rm em}$, a larger $m[c^2]/\mathcal{E}$ corresponds to particles with lower initial 3-velocity, which experience a stronger relativistic beaming, and hence a larger amount of particles would be moving closer to the equatorial plane, where they are more likely to hit the torus. On the other hand, similarly to the stationary source case, they are more likely to be captured by the black hole, which would decrease the hit fraction. Finally, for a fixed $m[c^2]/\mathcal{E}$, a source at larger $r_{\rm em}$ will have a lower velocity, resulting in a less intense beaming, so that the particles' initial velocities are more isotropic and hence the fraction that hits the torus decreases[6]. On the other hand, just as in the stationary source case, it also means particles are less easily captured by the black hole, potentially resulting in more hits (but also less lensed, potentially resulting in less hits). Given all these different combinations of factors, understanding how the number of hits changes with changing $r_{\rm em}$ and $m[c^2]/\mathcal{E}$ effectively consists of understanding which of these factors is dominating in each situation.

the torus is also very small compared to higher $r_{\rm g}$. For $r_{\rm g} = 2.5_{\rm g}$, no particles with $m[c^2]/\mathcal{E} \geq 0.4$ reach the torus. At lower mass to energy ratios, the fraction of hits increases until it stabilizes at $\approx 3\%$ for $m[c^2]/\mathcal{E} \leq 0.1$. For $r_{\rm g} = 3r_{\rm g}$, no particles with $m[c^2]/\mathcal{E} = 0.7$ reach the torus. The fraction of hits increases until $m[c^2]/\mathcal{E} = 0.1$, below which it stabilizes at $\approx 15\%$.

[6]This is clear by thinking about the expression for the velocity angle transformations in special relativity. The relative speed of a particle with respect to its emitter will affect how much the angle will change when viewed by a stationary observer (e.g. on the black hole frame). This effect will be smaller if the particle's speed in the emitter's frame is very large compared to the emitter's speed in the black hole frame, and will be more substantial if the particle is less relativistic in the emitter's frame than the emitter in the black hole's frame. So, in the case of small $r_{\rm em}$, where the emitter is more relativistic, the difference in the beaming for low $m[c^2]/\mathcal{E}$ will be more significant than for high $m[c^2]/\mathcal{E}$ and than it will be for higher $r_{\rm em}$.

The bottom panel of figure 4.4 shows three different regimes in terms of the number of hits as a function of particle mass for a given emission radius. We start by considering the hits fraction for each fixed radius as a function of mass to energy ratio.

For large emission radii ($r_{\rm em} \geq 10r_{\rm g}$ for Schwarzschild and $r_{\rm em} \geq 9r_{\rm g}$ for Kerr) the number of hits increases with $m[c^2]/\mathcal{E}$ in both cases. This means that the dominating processes in this regime is likely the stronger beaming that occurs for larger $m[c^2]/\mathcal{E}$, making the particles more focused into the equatorial plane and hence more likely to hit the torus.

For small radii ($4r_{\rm g} \leq r_{\rm em} \leq 5r_{\rm g}$ for Schwarzschild and $r_{\rm em} \leq 5r_{\rm g}$ for Kerr), the fraction remains approximately constant up to a certain value of $m[c^2]/\mathcal{E}$, following which it decreases and increases again. This indicates that there is a balance between the different factors up to a certain mass to energy ratio, which is broken at a certain point. Then, the competition between the different effects results in the drop and increase in the fraction hit. A possible explanation would be that first the higher black hole capture dominates the trend, so that less particles hit the torus as $m[c^2]/\mathcal{E}$ increases, but then the stronger beaming that occurs for larger $m[c^2]/\mathcal{E}$ beings to dominate.

We now look instead at how the hit fraction changes for changing $r_{\rm em}$ given a fixed $m[c^2]/\mathcal{E}$. By looking at one of the more relativistic particles, it is easier to identify a trend for how the fraction of particles reaching the torus changes with source distance to the black hole. For Kerr black holes the trend is obvious: for a fixed $m[c^2]/\mathcal{E}$, the further from the black hole the source is, the lower the fraction of particles that reach the torus. In this sense, the torus hitting fraction in this regime is likely dominated by one of two effects: either gravitational lensing - the further away the source is, the less lensing the particles experience, leading to less focusing onto the torus - or the beaming effect - the larger $r_{\rm em}$ is, the less relativistic the source is, so the less beaming the particles experience and, having a more isotropic emission, the less particles hit the torus.

In the Schwarzschild case, however, the trend is more puzzling. Up to a certain radius, the fraction appears to increase with source distance from the black hole, and after that it starts to decrease. The cutoff point is the ISCO radius, $r_{\rm ISCO} = 6r_{\rm g}$. Figure 4.6 shows the beamed initial conditions of particles with $m[c^2]/\mathcal{E} = 0.6$ for different radii, for both Kerr and Schwarzschild black holes. For radii $r_{\rm em} < 6r_{\rm g}$, the source in Schwarzschild spacetime is within the ISCO, meaning that it cannot have a stable circular orbit (see assumed velocity profile in appendix A). This results in a source velocity with a component in the negative radial direction, which in turn changes the direction of the beamed emission. The component of the source's velocity in the negative radial direction results in more particles being emitted towards the black hole the closer to the black hole the source is. In the extreme case of e.g. $m[c^2]/\mathcal{E} = 0.7$ and $r_{\rm em} < 3r_{\rm g}$, every emitted particle ends up inside the Schwarzschild black hole's event horizon. Particles

with a lower mass to energy ratio will have a larger initial speed, allowing them to escape the gravitational pull of the black hole even with such beamed initial conditions. As the source moves away from the black hole, the beaming in the direction of the black hole becomes less pronounced, and once the source crosses the ISCO, its velocity no longer has an r component, so that the beaming occurs in precisely the same direction as in Kerr spacetime. This explains why, for Schwarzschild black holes, the total hits fraction increases up to a certain radius before it starts decreasing.

Finally, for radii in between these two groups ($6r_{\rm g} \leq r_{\rm em} \leq 11r_{\rm g}$ for Schwarzschild and $6r_{\rm g} \leq r_{\rm em} \leq 10r_{\rm g}$ for Kerr) the behaviour becomes more chaotic, with a trend similar to that of high radii up to a certain point, following which the hit fraction drops in irregular ways. Such behaviour is likely an effect of the competition between the higher Lorentz factor, which allows particles to better escape the gravitational pull of the black hole and the lower Lorentz factor which allows particles to experience a larger gravitational lensing, allowing their trajectories to be bent and hit the torus in situations where more relativistic particles would simply escape.

Similarities with light curves from section 3.3.2

Regardless of how relativistic the source and particles are, the fact that the emission occurs close to a black hole results in gravitational lensing affecting the particle trajectories. In section 3.3.1 we saw that, when a small source orbits around a black hole and the radiation from it is monitored by a far away observer, an intensity peak is detected when the black hole is between the source and the observer. This was due to the formation of an Einstein ring, in which a large amount of the emitted rays was lensed towards the observer forming a ring-like structure.

The peak at $\phi = 180°$ in the histograms of particles emitted in Schwarzschild spacetime is due to a similar effect. This point of the torus is the equivalent to an observer behind the black hole. Though we did not find a perfect Einstein ring around this region of the torus, we found a large over-density around $(z = 0, \phi = 180°)$, indicating that similar lensing effects are at play in this scenario (see figures 4.7 and 4.8). The absence of an actual Einstein ring is also not hard to understand. In the scenario discussed in section 3.3.1, only photons with trajectories normal to the observer plane are allowed to reach the observer. Here, however, particles can reach the torus from any direction, not just directions perpendicular to the torus' surface. Both the Einstein ring and the over-density around $(z = 0, \phi = 180°)$ can be understood by thinking of the particle propagation in terms of wave fronts. By following the particle's geodesics and considering surfaces of constant coordinate time formed by all those geodesics, from a certain time a caustic appears in the $(z = 0, \phi = 180°)$ location. This is a region where, due to the deformation to the wave front caused by the black hole, the wavefront crosses itself. This results in an excess of particles reaching that particular location at all subsequent times. When one considers only particles reaching the target object perpendicularly (as in the case in chapter 3),

one is only sensitive to the portion of the wavefront parallel to it, which happens in a circular region that will correspond to the Einstein ring.

Notice that the systems and treatments presented in the present chapter and in chapter 3 are different in many respects (backward vs forward ray tracing; stationary observer at a specific ϕ vs extensive target; massless vs massive particles; source emitting continuously in its orbit vs single burst of emission etc). However, surprisingly the results seem related: the shape of the histograms in figure 4.4 has a striking similarity to that of the instantaneous bolometric light curves viewed from $\theta_{\rm obs} = 89°$ presented in figure 3.2. This is particularly true for massless particles ($m[c^2]/\mathcal{E} = 0$) emitted from the same distance to the black hole as that in figure 3.2 (i.e. $r_{\rm em} = 2.5r_{\rm g}$ and $r_{\rm em} = 6r_{\rm g}$ for Kerr and Schwarzschild spacetimes respectively - see relevant panels in figure 4.5), except they appear flipped with respect to the x-axis.

In fact, this result can be explained by noting that the systems are not as different as one might think. In both there is a small emitting source orbiting close to the black hole, though here it is a point source and in chapter 3 it had a finite size. In chapter 3, the observer was fixed and the source moved. Here, the source is fixed and each ϕ bin can be considered a different observer location and the number of particle hits in each ϕ bin can be thought of as moving the observer with respect to a stationary source. The distance from the torus to the black hole, $400\,r_{\rm g}$, is significantly larger than both the source size and the emitter's distance from the black hole. As such, the particle trajectories reaching each bin will not be significantly different from those hitting an observer at the same ϕ as far as those in chapter 3.

A key difference between these histograms and the light curves in the previous chapter is that the former measure only the particle count and do not consider their energy, unlike the latter. This means that the shape of the two will not coincide exactly, but the main effects of beaming and gravitational lensing are present in both: the beaming in the direction of travel is responsible for the wavy pattern in the histograms and for the alternate wide increase and decrease in bolometric intensity; in the light curves the gravitational lensing and focusing into an Einstein ring when the source is behind the black hole with respect to the observer (180°) is responsible for the main peak in the light curves, and the same gravitational focusing into a caustic results in the peak seen in the histograms at the equivalent ϕ location.

Particle arrival times

Figures 4.9 and 4.10 show a density plot representing the azimuthal location (x-axis) and arrival time (y-axis) of particles to the torus, with respect to the arrival of the first particle. The figures also show a histogram of the arrival times. Such results would be interesting when considering astrophysical situations when it would be necessary to understand the timings and locations of events occurring far from the black hole due to particles in its vicinity.

The patterns in figures 4.9 and 4.10 may at first appear very different. However, it is possible to see interesting similarities arising. For example, in figure 4.10 the results for $m[c^2]/\mathcal{E} = 0.7$, $r_{\rm em} = 4.5r_{\rm g}$ resemble those of $m[c^2]/\mathcal{E} = 0.5$ $r_{\rm em} = 2.5r_{\rm g}$. Similarly, those of $m[c^2]/\mathcal{E} = 0.7$, $r_{\rm em} = 6r_{\rm g}$ resemble those of $m[c^2]/\mathcal{E} = 0.5$, $r_{\rm em} = 4r_{\rm g}$ and the results from $m[c^2]/\mathcal{E} = 0.5$, $r_{\rm em} = 6r_{\rm g}$ resemble those of $m[c^2]/\mathcal{E} = 0.2$, $r_{\rm em} = 2.5r_{\rm g}$. Similarly, in figure 4.9 there are similarities between the $m[c^2]/\mathcal{E} = 0.6$, $r_{\rm em} = 6r_{\rm g}$ and the $m[c^2]/\mathcal{E} = 0.4$, $r_{\rm em} = 4r_{\rm g}$ cases, as well as the $m[c^2]/\mathcal{E} = 0.4$, $r_{\rm em} = 4.5r_{\rm g}$ and the $m[c^2]/\mathcal{E} = 0.2$ $r_{\rm em} = 3r_{\rm g}$ cases. These similarities support the idea of competing effects affecting high mass particles at small distances. They are also reassuring in the sense that there is a clear evolution pattern as ones moves to higher Lorentz factors and larger $r_{\rm em}$.

An interesting feature in these plots is that the total time span taken by particles to reach the torus from a given $r_{\rm em}$ tends to decrease as $m[c^2]/\mathcal{E}$ decreases. This is a combination of two main effects. First, particles travelling faster will have a shorter arrival time difference between longer and shorter paths than slower particles would for the similar paths. Secondly, a few of the less relativistic particles seem to have significantly longer paths than the rest of the particles, either because they loop around the black hole several times before escaping towards the torus or because they undergo large elliptical-like orbits which eventually hit the torus. Both these effects result in larger arrival time differences for less relativistic particles. A few examples of longer paths are shown in figures 4.11 and 4.12. Only particle paths which reach the torus are plotted, and those which arrive more than $10^3 r_{\rm g}/[c]$ after the first one are plotted in colour instead of in grey.

ii) Optically thin torus

In this section we use the full 3D GRRT capabilities of the code to investigate the energy deposition by massive particles onto a non-opaque torus with varying optical depth. The calculations in this section were performed in Kerr spacetime ($a = 0.998$) for particles with a mass to energy ratio of $m[c^2]/\mathcal{E} = 0.1$ emitted from $r_{\rm em} = 5r_{\rm g}$.

When particles go through dense media such as an accretion torus, they may interact with the particles in that region in several ways. Each of the possible interactions will have a particular cross section which is often energy dependent. As described in section 4.2, we consider a simplified effective absorption coefficient which is independent of particle energy.

Figures 4.13 to 4.15 show the incremental rate of energy deposition into the torus (i.e. the incremental absorbed intensity) as a function of coordinate radius. Classically, from equation (1.10), the bolometric intensity along a geodesic where $j = 0$ and $\alpha =$ constant is $I(s) = I(0)\mathrm{e}^{-\alpha s}$ (where s is some measure of distance along the curve) so that the absorbed intensity is given by $I(s)_{[\rm abs]} = I(0)(1-\mathrm{e}^{-\alpha s})$. At this distance from the black hole the particle's velocity

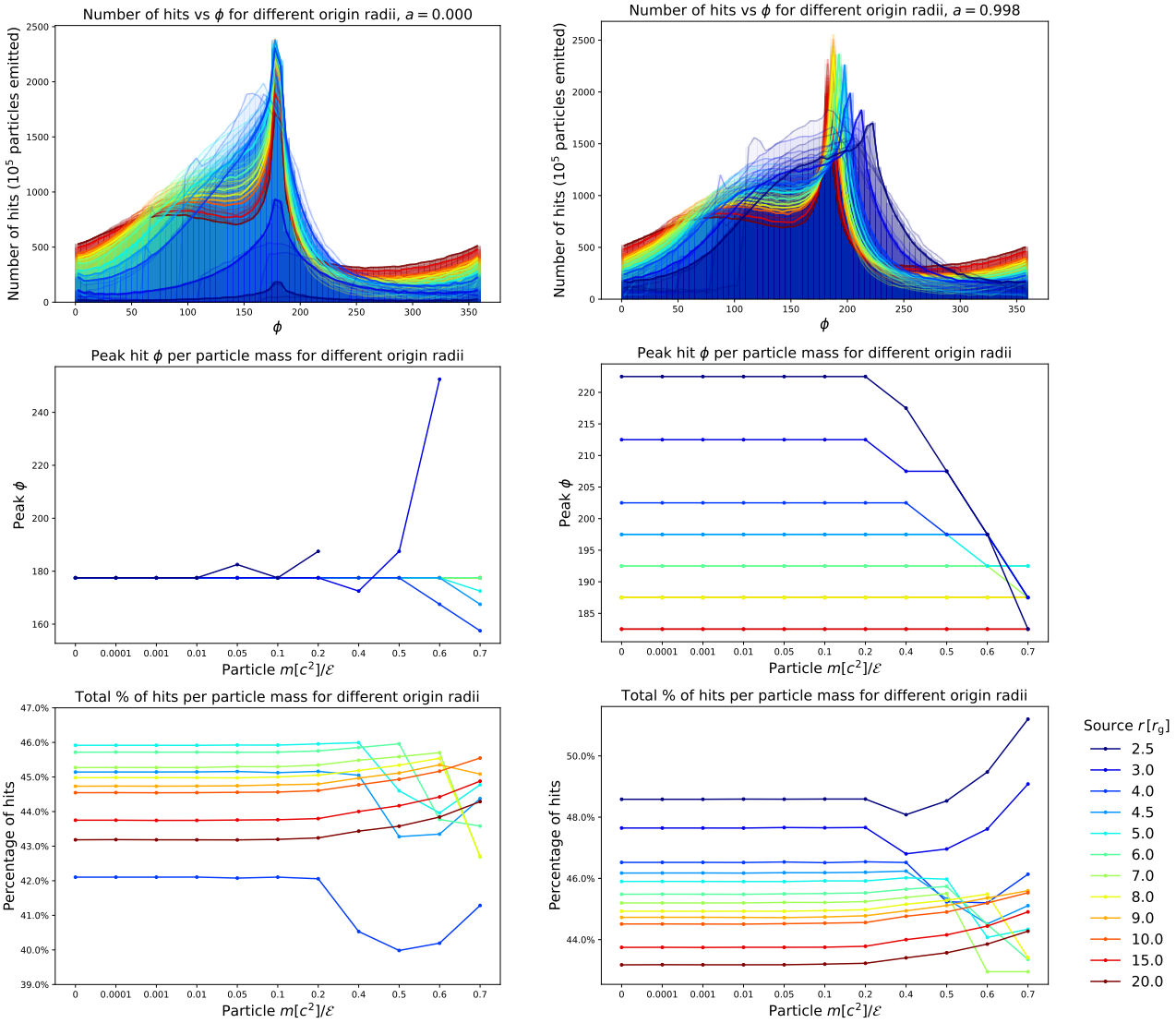

Figure 4.4: Top: histogram showing the number of particles that hit the torus within each ϕ bin. The source is always located at $\phi = 0$. Different colours represent different origin radii r_{em}, with all mass to energy ratios for the same r_{em} plotted in the same colour. Centre: location of the peak ϕ bin for different origin radii and different mass to energy ratios. When no particles reach the torus (e.g. $m[c^2]/\mathcal{E}$ for $r = 3r_{\text{g}}$), no results were plotted. The colours which cannot be seen are hidden under the lines of lower r_{em}, in particular that of $r_{\text{em}} = 6r_{\text{g}}$). Bottom: percentage of the emitted rays which reach the torus. For the Schwarzschild case the $r = 2.5r_{\text{g}}$ and $r = 3r_{\text{g}}$ cases are not shown as the percentages are much lower, reaching a maximum value of 3% and 15% respectively.

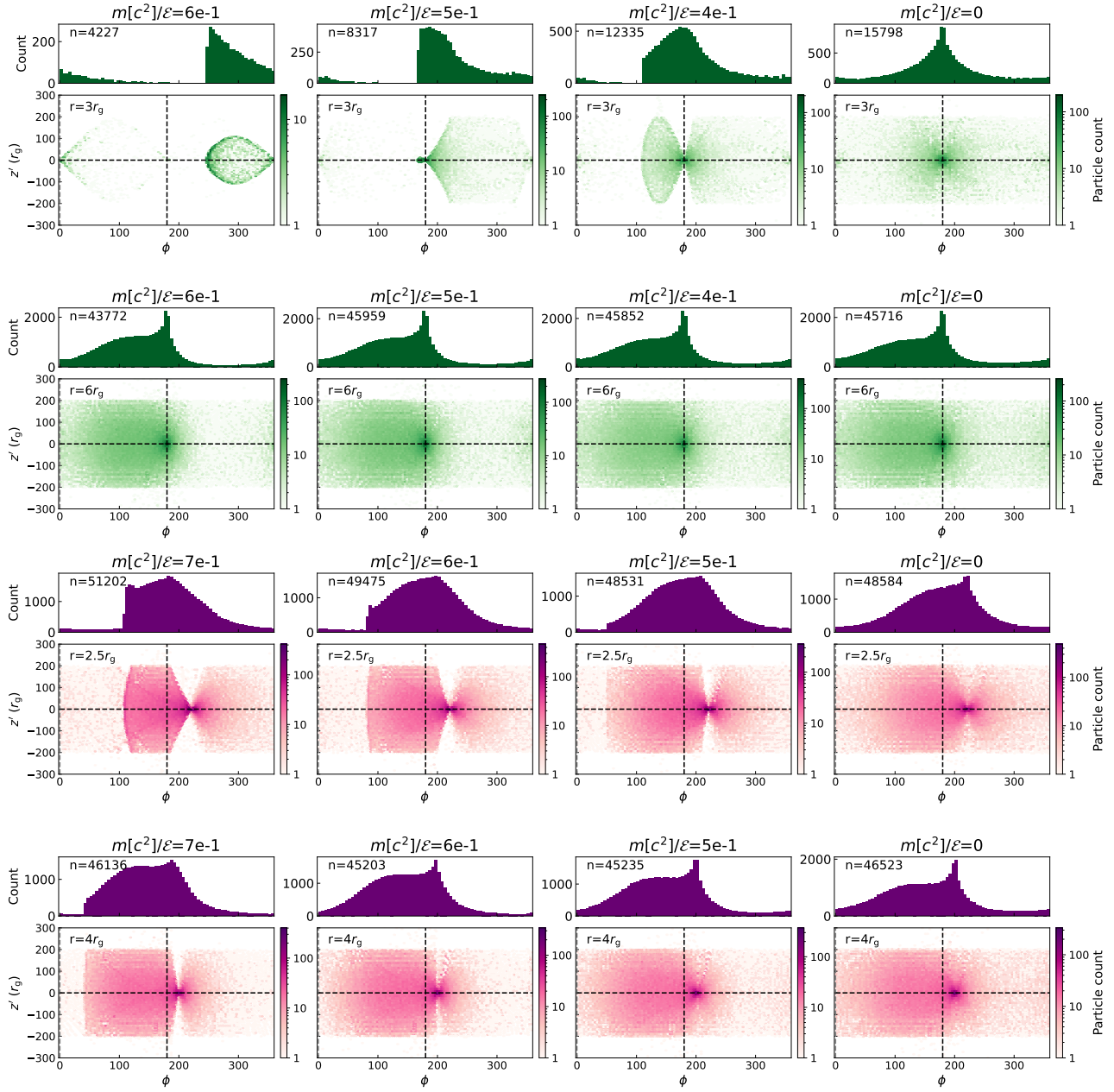

Figure 4.5: Density plots: Arrival locations ($z' - \phi$ plane) of particles emitted from a distance r of a Schwarzschild (green panels) and Kerr (purple panels) black hole for varying $m[c^2]/\mathcal{E}$ (decreasing from left to right) that reach an optically thick torus. The values of $r_{\rm em}$ are indicated on the top left corner of the plots. The colour bar represents the number of particles (summed over all arrival times) in each bin. Histograms: azimuthal locations at which particles hit the torus. The total number of particles that hit the torus, n, is shown on the top left corner of the panel (10^5 particles were emitted).

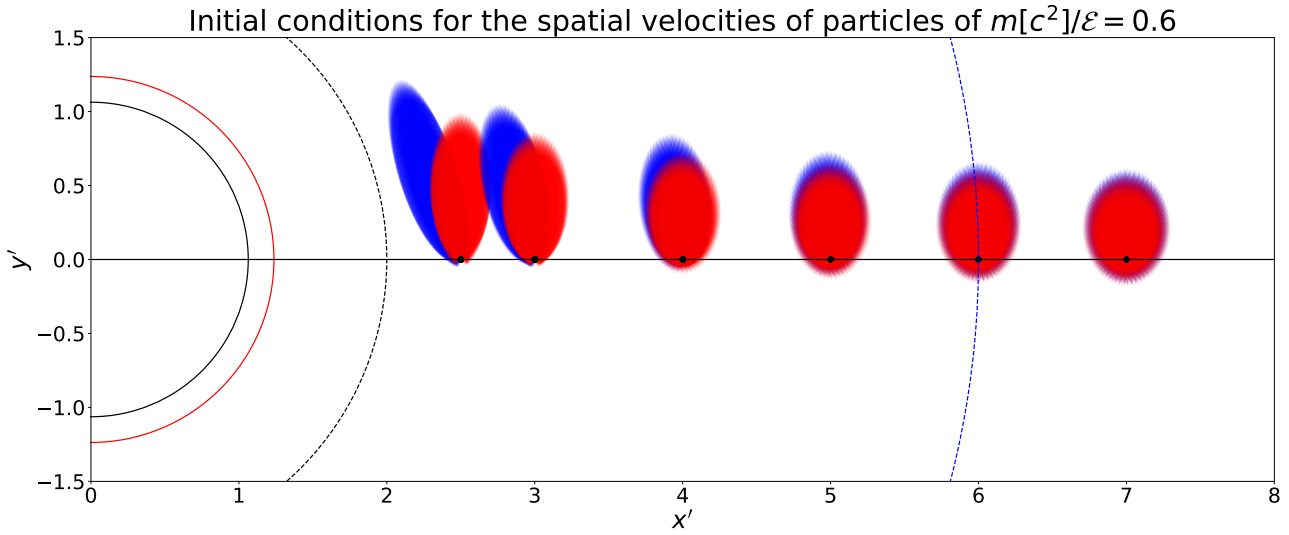

Figure 4.6: Initial conditions of the spatial velocities of particles with $m[c^2]/\mathcal{E} = 0.6$ emitted at different distances from the black hole in both Schwarzschild (blue) and Kerr (red) spacetimes. Each blurred ellipse is composed of 1000 arrows corresponding to the initial conditions of 1000 particles emitted isotropically in the emitter's frame, and projected onto the (x', y') plane. The emitter is a point source with location identified by the black dots along the $y' = 0$ axis and it moves anticlockwise, with a Keplerian velocity given by the equations in appendix A. The filled lines represent the event horizon (black) and ISCO (red) radii for a Kerr spacetime with $a = 0.998$, while the dashed lines represent the event horizon (black) and ISCO (blue) radii for Schwarzschild spacetime.

stays approximately constant, so that we may approximate $\mathrm{d}r/\mathrm{d}\lambda = \mathcal{V}$ for some constant $\mathcal{V}$. This means that we can parameterize the curve using r instead of λ, as we typically would. So we can think of a classical approximation of the expected energy deposition rate as a function of coordinate radius as $\mathrm{d}I_{[\mathrm{abs}]}/\mathrm{d}r \sim \mathrm{e}^{-r\alpha}$.

Over-plotted on the histograms is a curve proportional to $e^{-\alpha r}$, where the proportionality constant is chosen to fit the middle point of the histogram. As expected, for the two largest absorption coefficients, the energy deposition rate matches the expected value as long as the particles remain inside the torus. For the lowest value of α, the mean free path is longer, so that the exponential curve for each particle is truncated as soon as particle leave the torus. Since there are less extended exponential curves being added together (unlike in the cases of higher α and lower mean free path) the results become more noisy which, together with the low number of particles emitted, results in a poor match to the theoretical absorption rate.

The two lower panels in figures 4.13 to 4.15 show the bolometric intensity along each particle path as a fraction of the bolometric intensity at the point of first contact with the torus, I_0. This fraction is a proxy for the probability of a particle not having interacted at that point. As expected, for high absorption coefficients, most of the incoming particle intensity is lost, resulting in a higher rate of energy deposition into the torus, while for low absorption coefficients most of the particle intensity remains unchanged, indicating low probabilities of interactions.

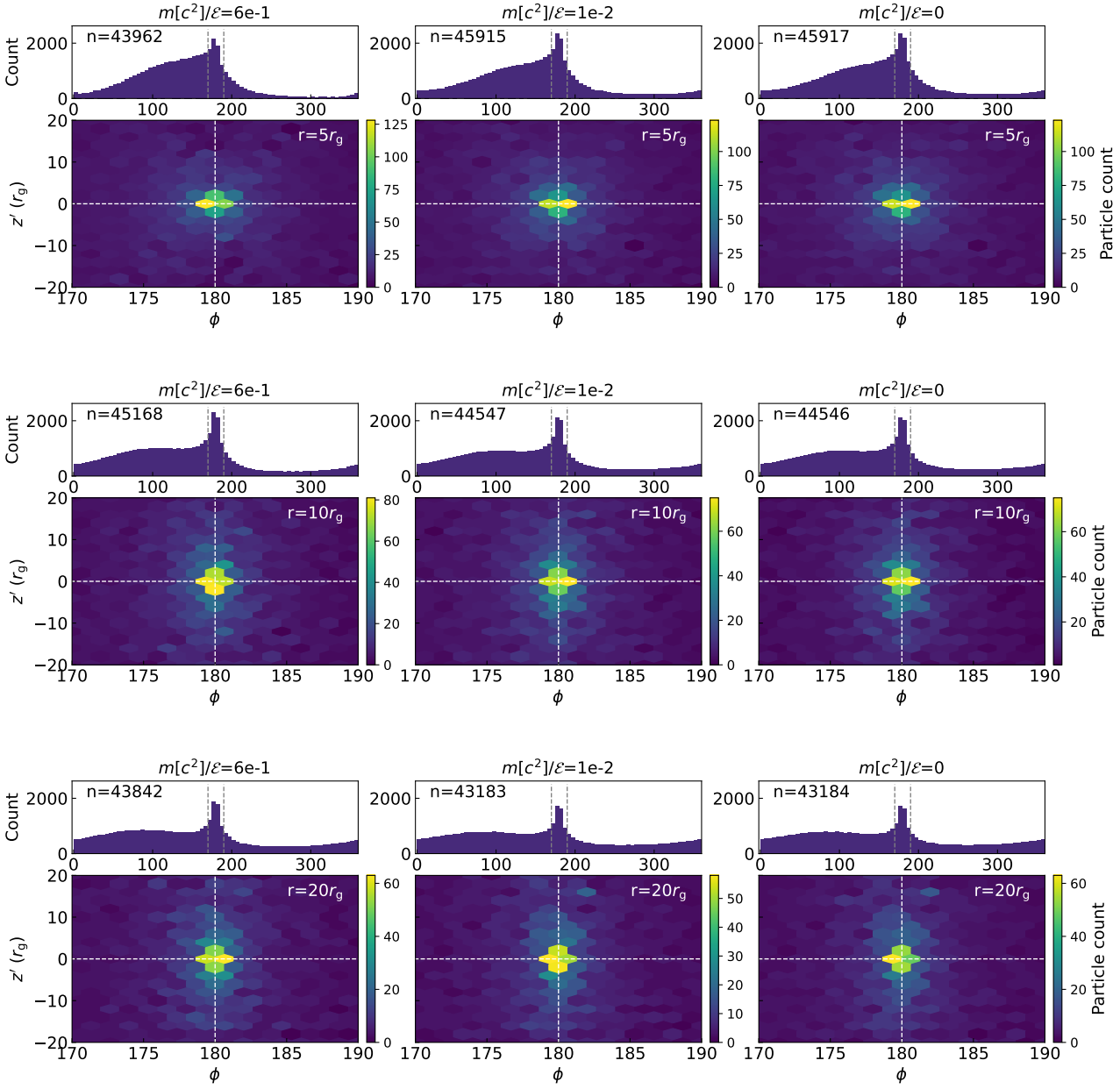

Figure 4.7: Histograms: azimuthal locations at which particles hit the torus in Schwarzschild spacetime (same as figure 4.5). Grey dotted lines show the angular region zoomed into in the bottom panels ($\phi \in [170° - 190°]$). Density plots: Density plot of the central region of the $z' - \phi$ plane.

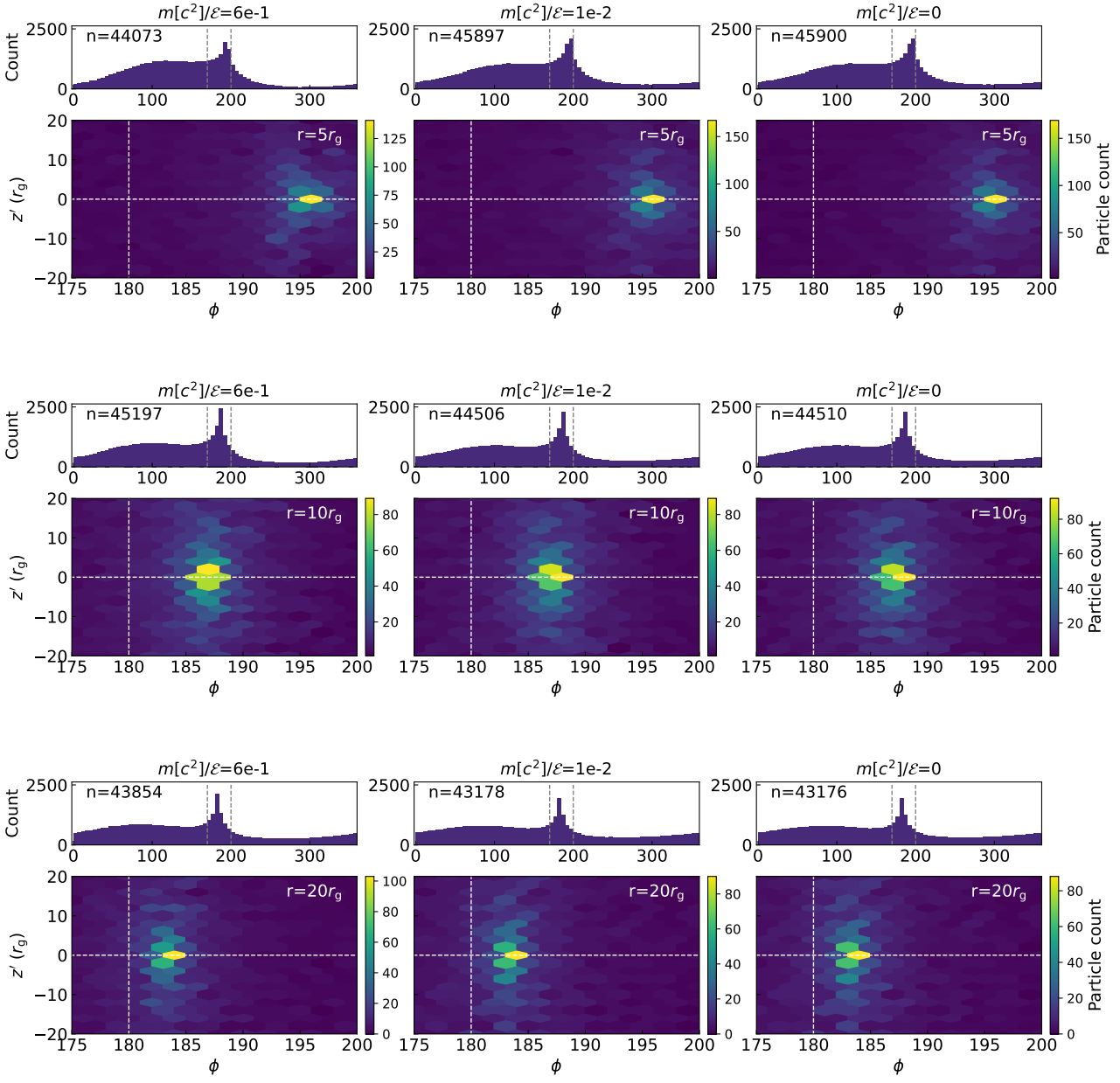

Figure 4.8: Same as for figure 4.7, but for a Kerr black hole with $a = 0.998$. The zoom in the bottom panels is into the region $\phi \in [170° - 200°]$.

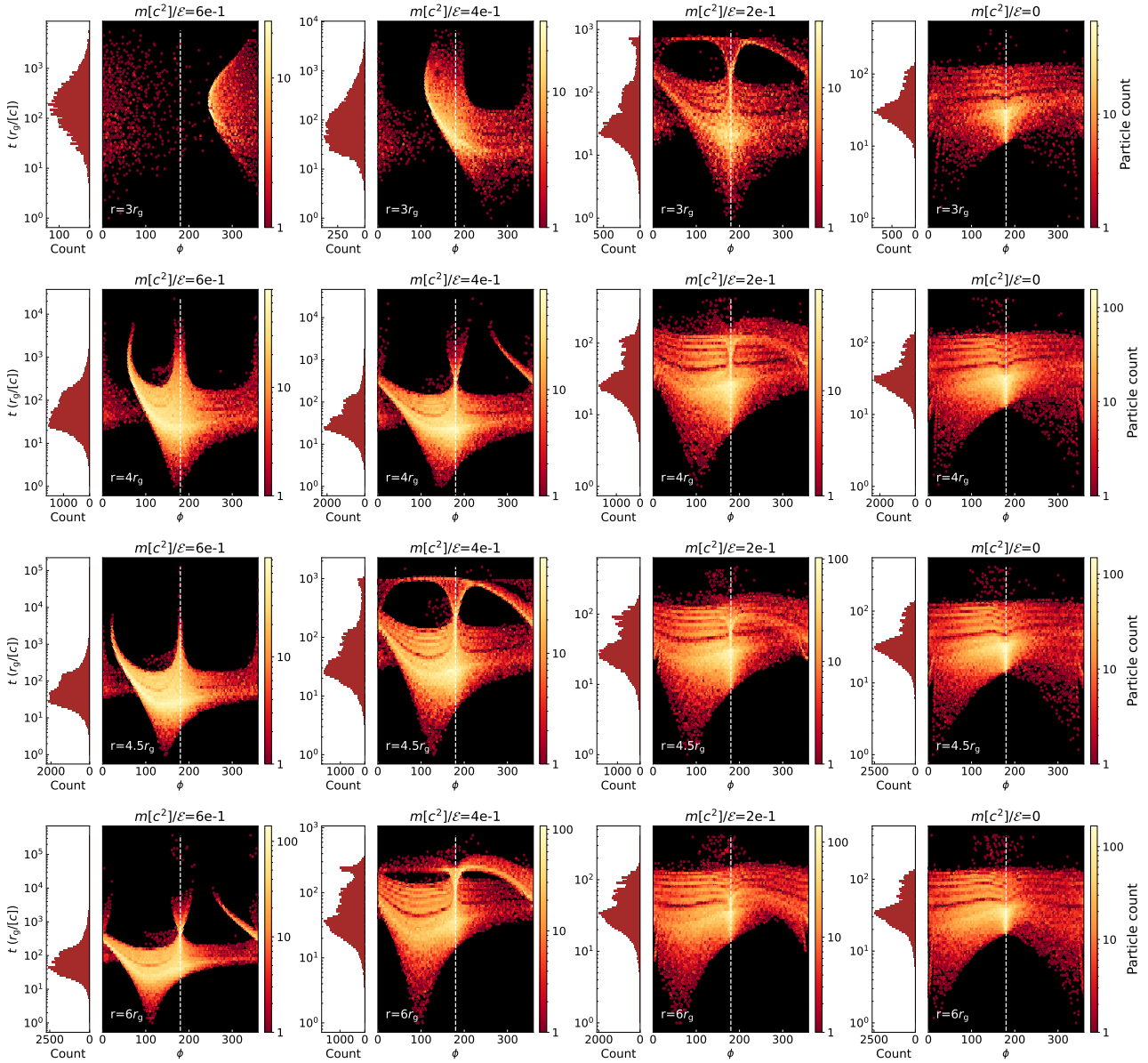

Figure 4.9: Density plots: number of particles reaching the torus as a function of ϕ (x-axis) and time (y-axis). Each column shows results for a given $m[c^2]/\mathcal{E}$ and each row for a given $r_{\rm em}$. Histograms: total number of particles reaching the torus as a function of time since the first hit. These results are for particles emitted in Schwarzschild spacetime.

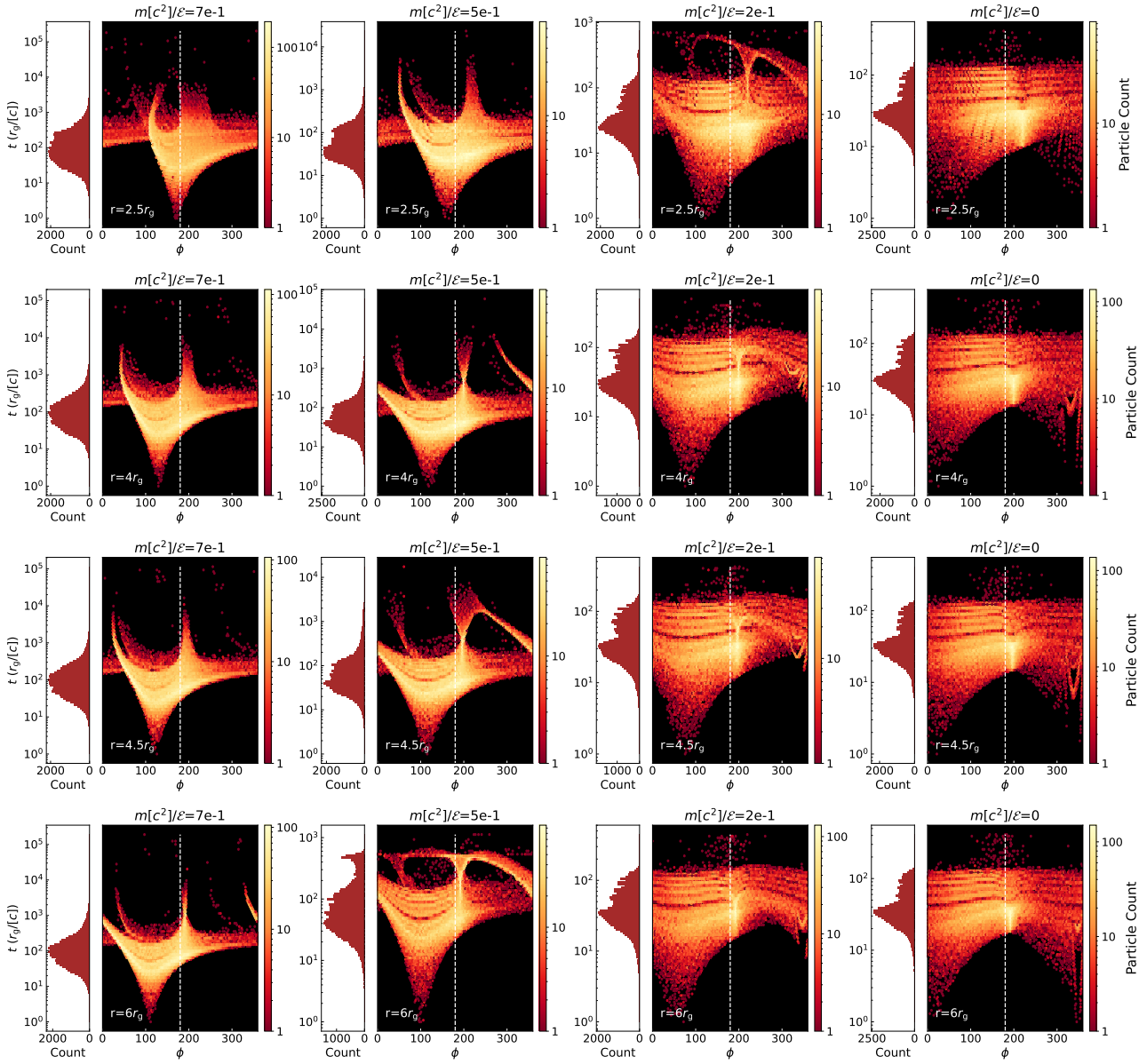

Figure 4.10: Same as for figure 4.9, but for Kerr spacetime with $a = 0.998$.

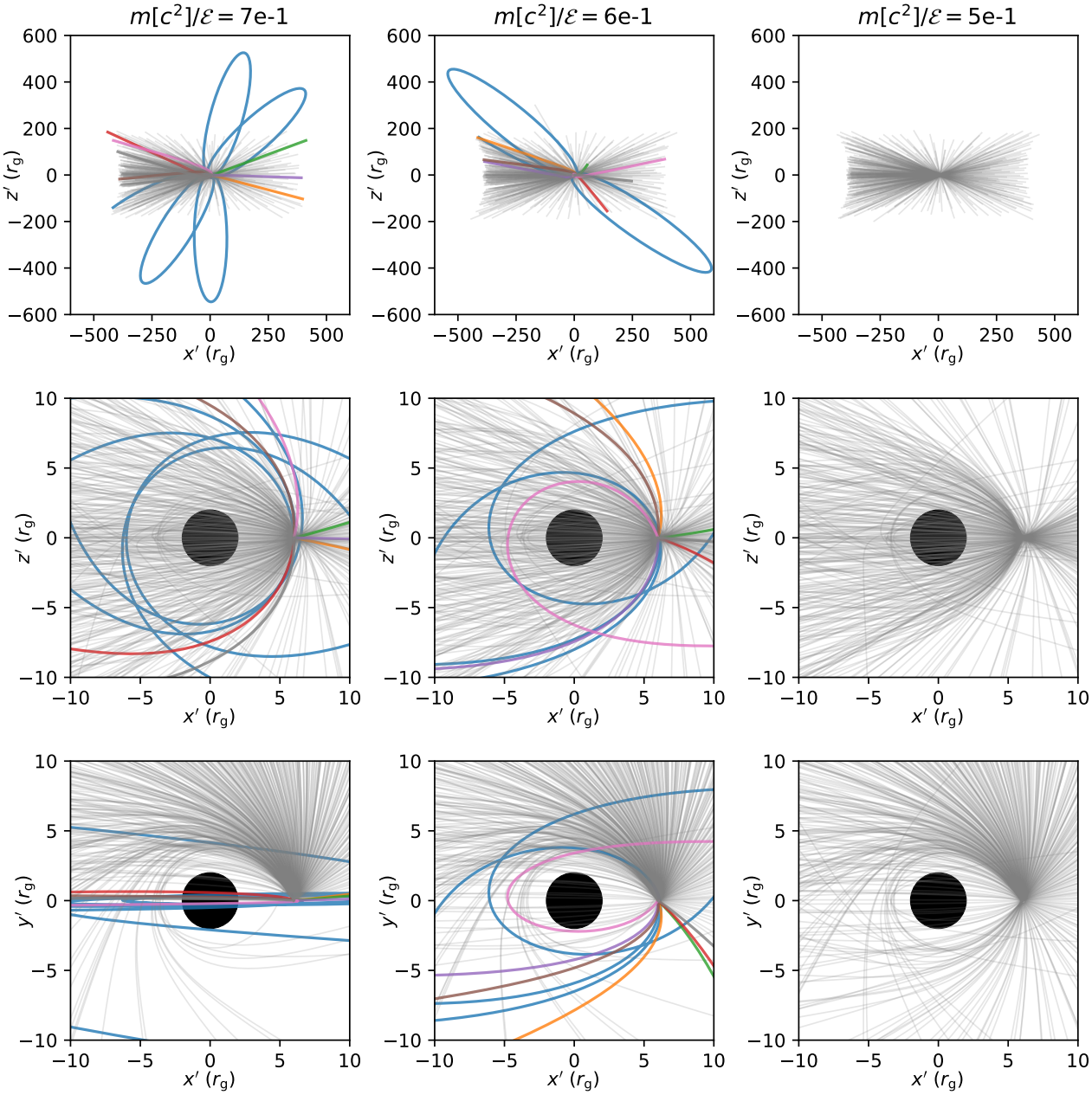

Figure 4.11: Sample particle trajectories for particles with different $m[c^2]/\mathcal{E}$ (one in each column) emitted from $r_{\text{em}} = 6r_{\text{g}}$ around a Schwarzschild black hole. All rays are initialized isotropically in the emitter's rest frame, but end up with different initial conditions after the transformation to the black hole frame depending on the emitter's position and four-velocity. Each row shows a different perspective on the paths. All the paths plotted reach the torus and the ones coloured are those which arrive more than $10^3 r_{\text{g}}/[c]$ after the first particle. The black object on the bottom two rows represents the black hole's event horizon.

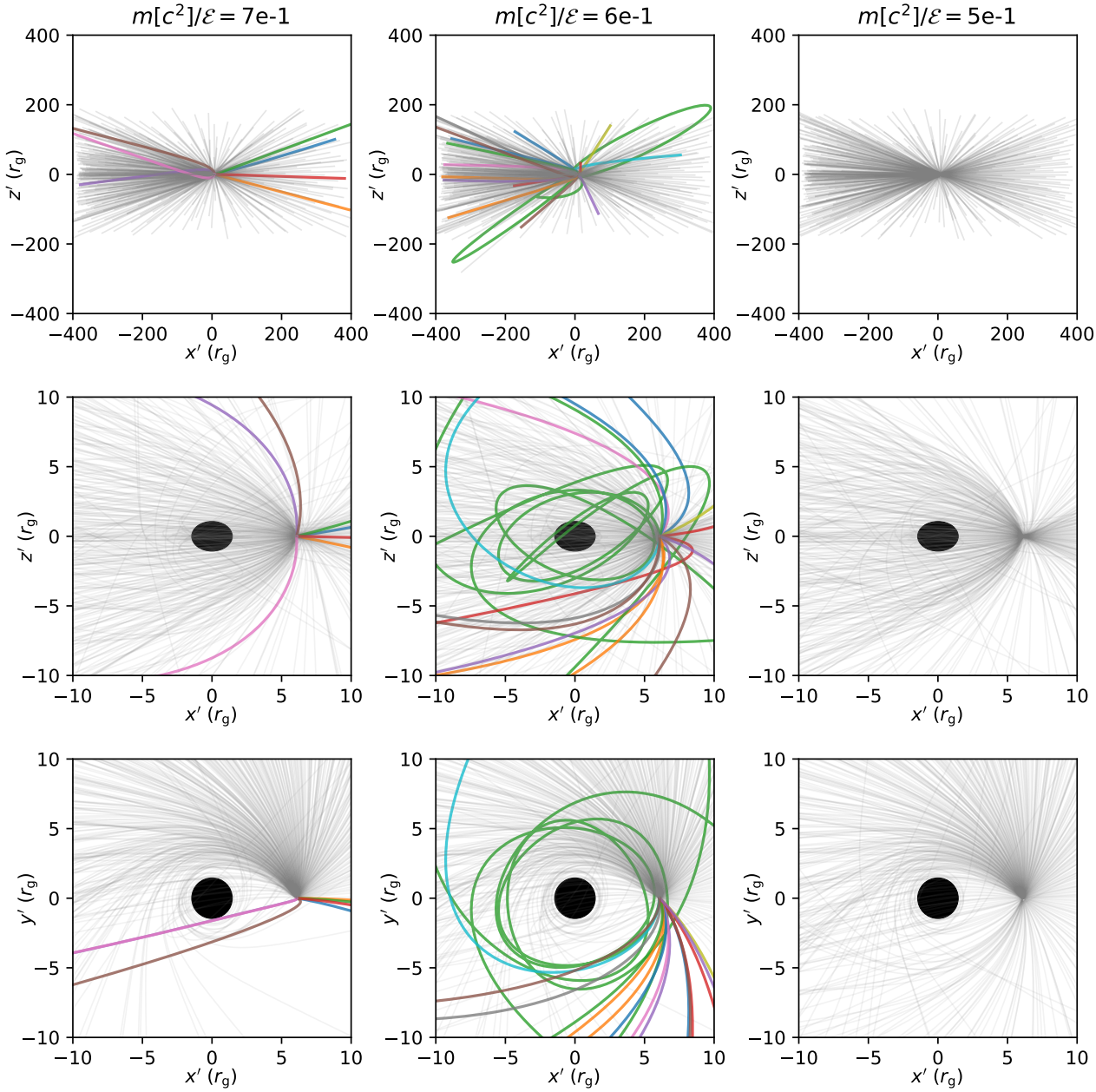

Figure 4.12: Same as in figure 4.11 but for a Kerr black hole with $a = 0.998$.

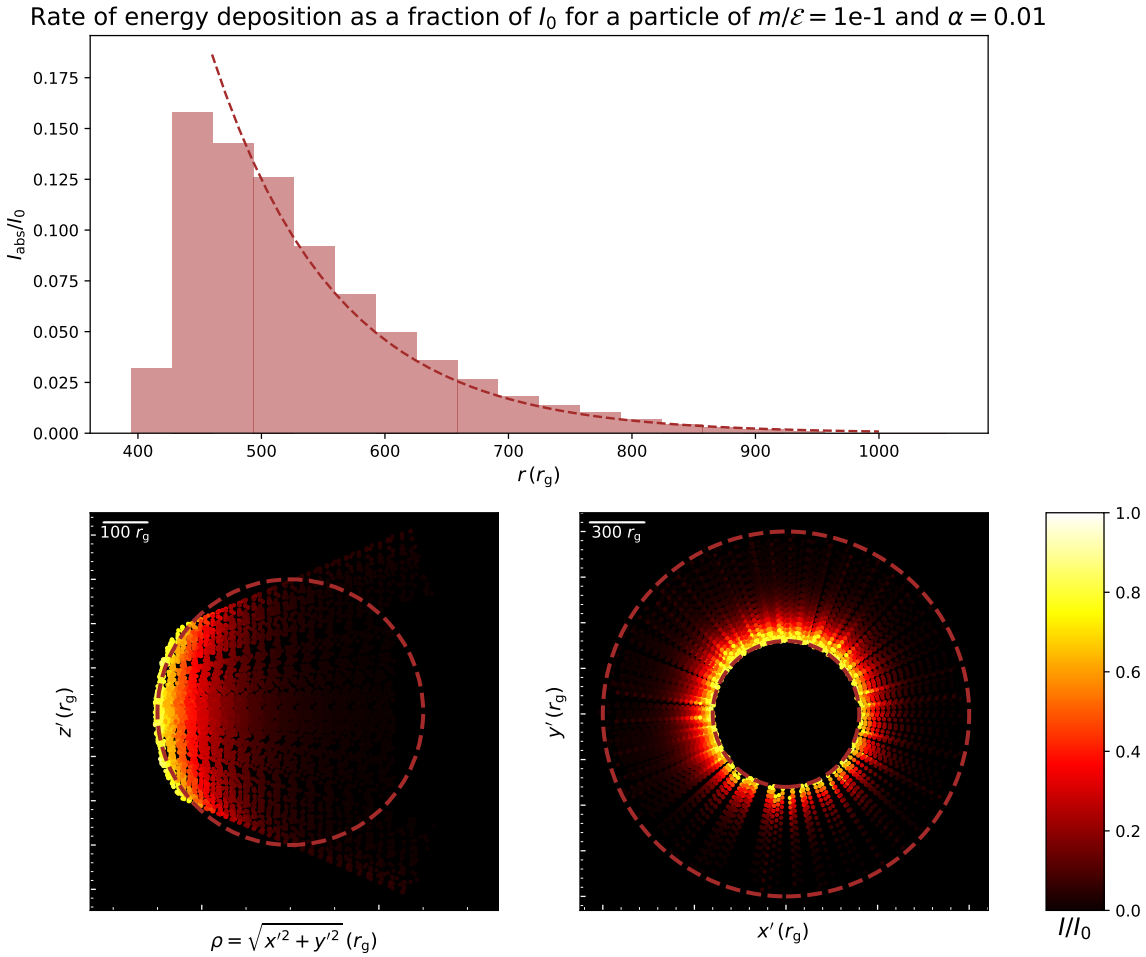

Figure 4.13: Rate of energy deposition on an accretion torus with absorption coefficient $\alpha = 0.01$ by massive particles produced close to a Kerr black hole. The top panel shows the total absorbed intensity (i.e. energy deposition per unit time) as a fraction of the total intensity of the particle bundles that reach the torus, $I_0 = \sum_i I^i{}_0$(i.e. excluding any emitted particles which don't reach the torus), where $I^i{}_0$ is the intensity of the bundle as it reaches the torus. The dotted line is an exponential proportional to $e^{-\alpha r}$. As expected the incremental absorbed intensity follows this trend well. The bottom panels show the bolometric intensity of the particle bundles along the particle trajectories (note that the intensities are calculated from the covariant intensity at each location) as a fraction of $I^i{}_0$. The panel on the left shows a projection of the particle trajectories onto a cross-section of the torus (the red dashed line marks the boundary of the torus' cross section) and the one on the right a projection onto the equatorial plane (the red dashed line marks the boundary of the torus as viewed from above). The error tolerance in the surface finding algorithm results in some points which are still outside the torus to be identified as part of the torus. This explains the yellow dots slightly outside the torus on the bottom left panel and inside the inner circle on the bottom right panel. For a large absorption coefficient, $\alpha = 0.01$, as expected most of the energy is absorbed in the inner part of the disk. Results calculated for 1000 emitted particles.

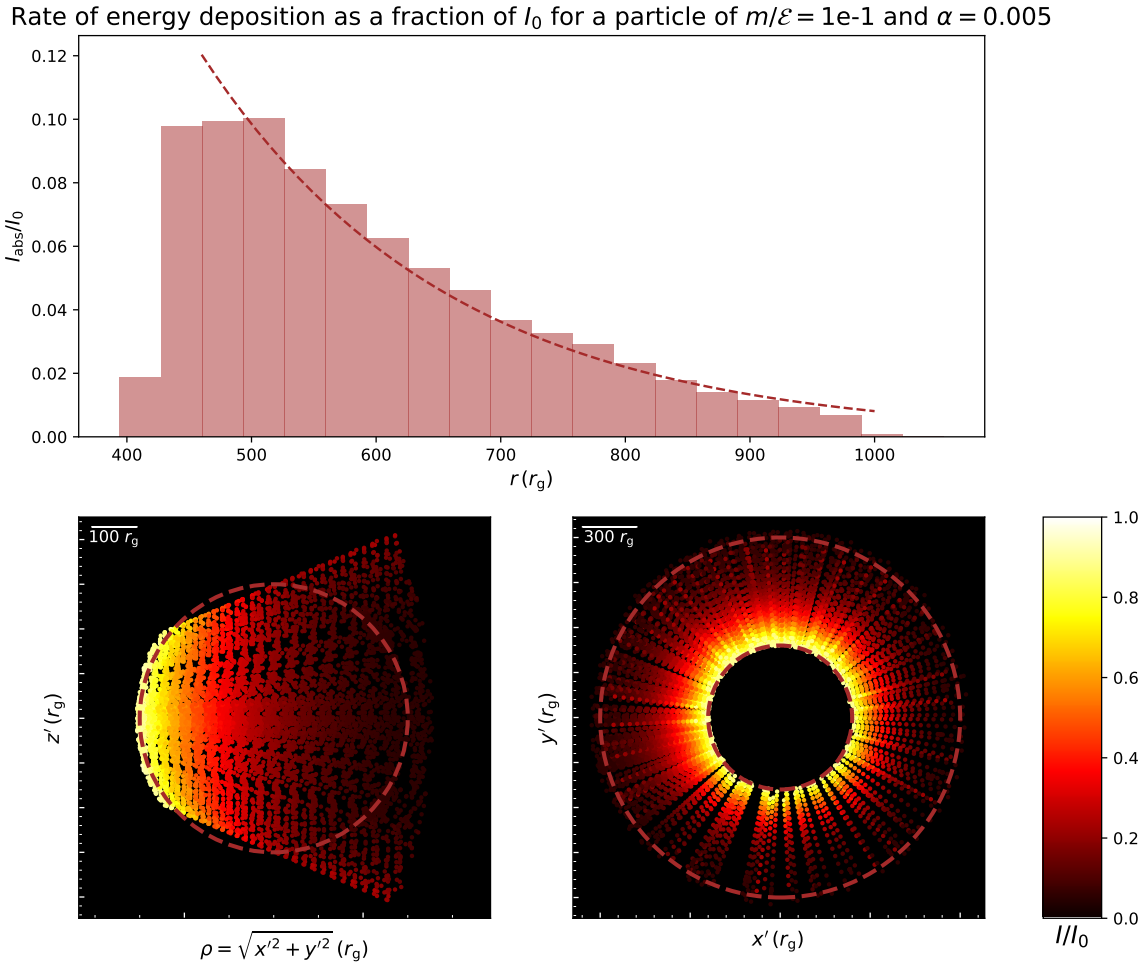

Figure 4.14: Same as figure 4.13 for an accretion torus with absorption coefficient $\alpha = 0.005$. Again the trend followed is, as expected, proportional to $e^{-\alpha r}$.

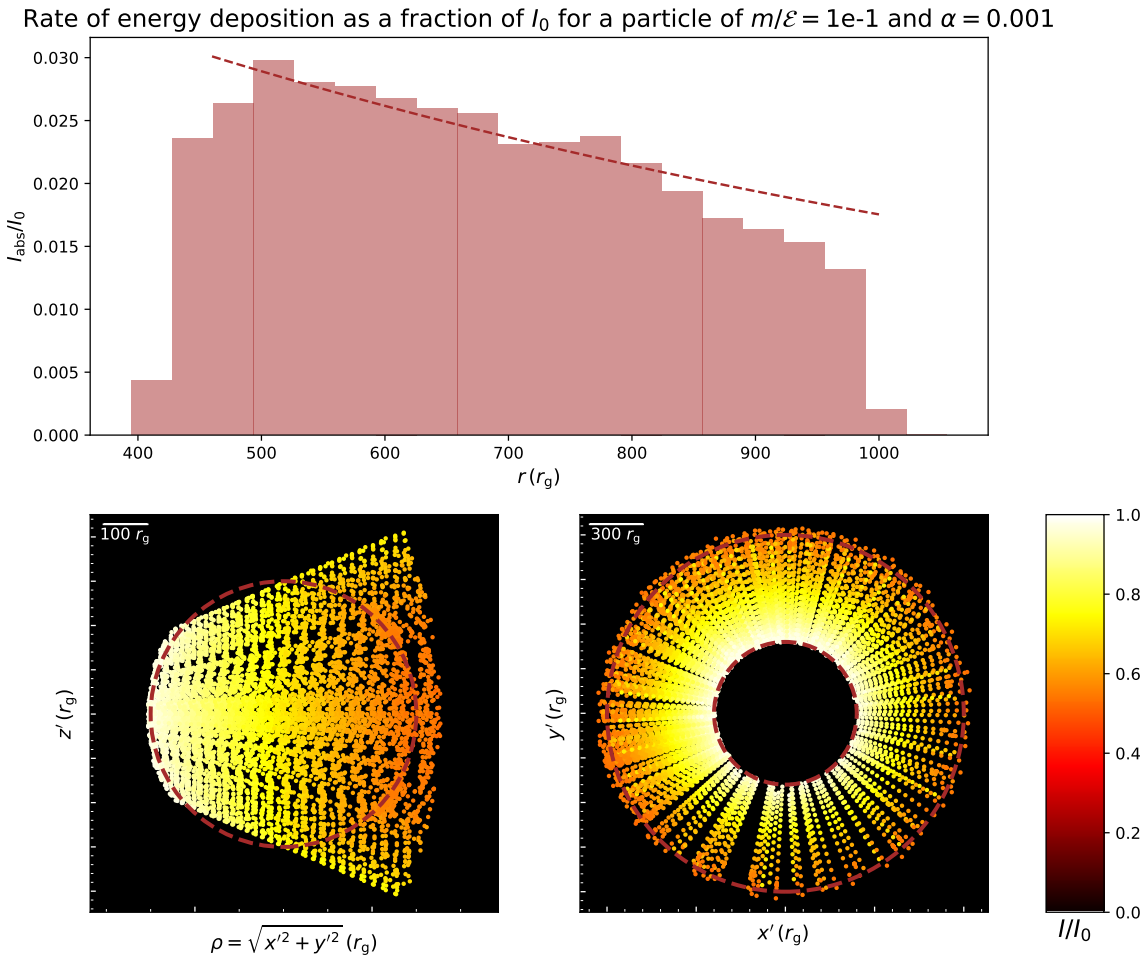

Figure 4.15: Same as figure 4.13 for an accretion torus with absorption coefficient $\alpha = 0.001$. Now the absorption is too low, so the incremental absorbed intensity histogram does not follow closely the expected $e^{-\alpha r}$. An exponential curve would be expected if the rays had a longer journey inside the absorbing torus.

Performing these calculations for different masses, emitter radii and black hole spins would be similar, and these parameters are easy to change in the code. The main differences in the results would be the locations in the torus where the particles would deposit energy (as seen in figures 4.7 and 4.8) and the time when the energy deposition would occur (as seen by the particle arrival times in figures 4.9 and 4.10).

The differences would be even more pronounced if the absorption coefficient had an energy dependency: the different initial energies and energy shifts undergone by the different particles will result is very different absorption patterns.

4.4 Conclusions and future work

In this chapter we have demonstrated how a covariant GRRT formalism with the ability to deal with massive particles provides useful insight into the physics happening close to black holes. Despite the simplified nature of the calculation parameters used, we were able to identify and explain interesting features which are likely to be relevant if similar astrophysical systems are studied.

We demonstrated a sample of the kind of studies which can be performed using the formalism developed in this thesis and opened the door for potentially interesting astrophysical studies.

Massive and massless particles emitted in the vicinity of a black hole will propagate and interact with the material, while subject to the effects of gravity. If they eventually reach us, the flux and arrival timing of these particles will depend on the difference in their paths and the material through which they propagated. If they do not reach us directly, secondary particles resulting from their interaction with the material would carry such information. As such, regardless of whether it is the primary or secondary particles that reach us, they may provide a way to determine the location of their acceleration region in the vicinity of the black holes.

This work also provides a word of caution when interpreting observations from radiation or particles produced by interactions close to black holes. The convergence of our results for Kerr and Schwarzschild black holes as the emission region moves away from the black hole suggest that there is a degeneracy between the black hole spin and other parameters. Similarly, our results uncovered a degeneracy in the hits pattern in terms of azimuth and arrival time between the particle's Lorentz factor and its acceleration location $r_{\rm em}$. That fact that the patterns are not unique makes it more challenging to understand the exact acceleration mechanisms and locations by looking at this data alone. Understanding the interacting medium and the type of interactions which would take place, together with using such a solid GRRT framework, is essential to forming a complete picture of the physical processes involved.

A potential future direction that seems particularly interesting would be to improve the numerical accuracy of the code to be able to distinguish subtle differences between the trajectories of highly relativistic particles with only slightly different masses. In section 4.3.1 we showed how timelike geodesics of particles with mass to energy ratios $m[c^2]/\mathcal{E} < 10^{-3}$ were effectively indistinguishable from each other and from null geodesics. If one is interested in investigating highly relativistic particles such as cosmic rays or neutrinos and take their mass into account, it is necessary to have a significantly better numerical accuracy. If this were the case, it might be possible to identify subtle differences for instance in arrival times of the three neutrino mass eigenstates emitted or transiting very close to a black hole in a way that would allow us to calculate the corresponding interference between mass eigenstates and predict the shape of the "light curve" of neutrinos arriving at the earth. This might provide interesting insights into the nature of the neutrino mass hierarchy.

Overall, in this chapter we demonstrated the validity of the massive particle GRRT by showing the convergence to the massless particle case for highly relativistic particles and demonstrated the potentialities of such a formalism to the study of physics and astrophysics in the strong gravity regions around black holes of different spins.

Chapter 5

Conclusion

5.1 Summary of key outcomes

The first major outcome of this work is an algorithm able to perform general relativistic transport calculations of both particles with and without mass in a self-consistent manner. In chapter 2 we described in detail the formalism and the construction of the computational algorithm that is able to do this. We have demonstrated the validity of the code by evaluating the computational errors of individual geodesics and comparing some radiative transport calculation results with others presented in literature. We also explored the physical meaning of different components of the formalism. We found, for instance, that there is a relationship between a massive particle's Lorentz factor, a massless particle's redshift and the constants of motion along a geodesic.

Once the GRRT algorithm software was built, we used it to investigate different astrophysical scenarios. In chapter 3 we showed that the highly relativistic motion and strong gravitational effects that are associated with black hole systems can significantly distort the observational features of the flares emitted in their vicinity, changing their spectrum, light curve profile and, in some cases, making a single flare appear as multiple ones. We explained in detail the effects of each of these components and when each was important. In particular, we saw how the competition between gravitational redshift, Doppler shift and gravitational lensing affected the spectrograms of these flares. We saw this for the case of a hot spot both with constant and with time-dependent intrinsic emissivity. We found that, for flares of long duration compared to the orbital time scale, the detected flares are significantly different from the intrinsic emissivity profile, with a single flare appearing as multiple flares in both Schwarzschild and Kerr spacetimes. In Kerr spacetime, flares resulting from higher order images of the emitting hot spot were detected for more than double the flare duration time. These results provide initial insights towards understanding the observed flare statistics.

In chapter 4 we evaluated the behaviour and accuracy of our code for particles of different mass to energy ratios. We showed that the results tend to those of photons as the mass to energy ratio decreases, as expected. We investigated the timings and positions where particles of

different masses would interact with material along their path. These interactions may produce secondary photons or other particles which could be detectable on earth. Performing GRRT calculations of both the primary and secondary particles may provide a way to determine the location of the primary acceleration region in the vicinity of the black holes. However, we also identified certain degeneracies in the hits pattern in terms of azimuth and arrival time between the particle's Lorentz factor and its acceleration location, which might make it challenging to determine the acceleration location and understand its mechanism by looking at this data alone. A particularly interesting result was the similarity between the particle hit location histograms calculated in chapter 4 and the light curves from a hot spot with constant emissivity calculated in chapter 3. Although in hindsight the similarities are reasonable, as we started these calculations we did not expect such an interesting connection between the two cases. This also helped us better understand the nature of the Einstein ring and when it is and is not manifest in the observer's plane.

5.2 Open avenues for future developments

The work presented in this thesis is far from closed. There are several potential avenues for further developments and investigations in each of the fields we mentioned. Below are some ideas.

5.2.1 GRRT algorithm

The algorithm build as part of this PhD and presented in chapter 2 is modular in nature. This makes it easy to add new features to it and to adapt the existing ones. Something that would be interesting to add to the code which might be useful for the further explorations mentioned in 5.2.2 would be polarization transport. This would allow us not only to calculate changes in the intensity of radiation but also its polarization, which would provide another source of information regarding the systems being studied. Some examples would include a better understanding of the emission and the structure of the magnetic field along the line of sight.

Another interesting development would be to consider how the medium through which the radiation propagates may affect its propagation from a geodesic's perspective. As shown in Kimpson et al. (2019), when traveling through a plasma, light rays experience dispersion so that photons of different energies travel along different (non-null) geodesics. Similarly, charged particles travelling in media with magnetic fields will experience changes in their trajectories with respect to the geodesic motion considered so far. Including these effects in the code might result in interesting insights for both massless and massive particle propagation in ways that might affect our interpretation of the observations. This is likely to impact further work in

both fields 5.2.2 and 5.2.3.

5.2.2 Flares from massive black holes

The puzzle of the formation of flares in the Galactic Centre and in similar systems (discussed in chapter 3) is still far from being resolved. In this work, we contributed to a better understanding of how the strong gravity environment affects the morphology of these flares as seen by an observer. A potential next step would be to incorporate physically motivated emission and absorption models into our GRRT code. These would make it possible to use the present code to perform realistic predictions of observables which could be compared to detections.

Another avenue for potential extension of this work would be to explore the effects on flares with time scales significantly shorter than the orbital time scale. If the flares are indeed caused by magnetic reconnection events, it is likely that their duration is shorter than what was considered in chapter 3. It is also unlikely that the emission region would last such a long time without being disrupted. These factors make the study of shorter flares an interesting extension of the work. Their short duration would result in the individual gravitational and relativistic effects being harder to identify, as only a portion of the spectrogram 3.4 would be covered by them. However, having already understood the individual effects at play at each location, it is now easier to spot them in shorter flares. Magnetic reconnection events which may give rise to these flares in the dynamical environment that likely surrounds Sgr A* may occur in any location around the black hole. As seen in the previous chapter, initializing a flare in different azimuthal locations produces different observed light curve profiles. As such, it would be interesting to initialize such flares in randomized different locations and to perform a statistical analysis of the resulting observed flare properties. The insights gained from such a study would offer us a handle to interpret the observational data for a better understanding of the statistics, allowing us to better conclude whether the different morphologies of light curves could be distortions to similar flares at their origin or whether they indicate different formation mechanisms.

5.2.3 Massive particles GRRT

Chapter 4 is arguably the one with the most potential for further developments. Since this chapter was mostly a showcase of some of the features of the code, there could be multiple physical systems to which it would be worth applying it. Some examples mentioned in section 4.1 include the interactions of cosmic rays accelerated in the vicinity of black holes with molecular clouds, resulting in secondary electrons which would be responsible for the emission of X-ray filaments in the Galactic Centre. Another system would include the bombardment of highly energetic particles associated with tidal disruption events into the disrupted star's debris, which would result in the production of particles that would decay into neutrinos.

Another potential future direction that seems particularly interesting would be to use the results from chapter 4 regarding the differences in the geodesics and arrival time of particles of different masses to study the mass hierarchy of neutrinos. Our formalism has the capability to deal with this, since it includes the subtle effects of mass, and our code had the potential to calculate them. The main challenge to this is that, at the moment, the numerical errors associated with our code do not allow us to distinguish particles with $m[c^2]/\mathcal{E} < 10^{-3}$ from one another. As such, the next step would be to improve the numerical accuracy of the code to be able to distinguish subtle differences between the trajectories of highly relativistic particles with only slightly different masses. It might then be possible to identify subtle differences for instance in arrival times of the three neutrino mass eigenstates emitted very close to a black hole in a way that would allow us to predict the shape of the "light curve" of neutrino flux arriving at the earth based on the interference between those mass eigenstates. This might provide interesting insights into the nature of neutrino masses (e.g. whether the mass hierarchy is normal or inverted).

5.3 Final remarks

Black holes are interesting objects from the point of view of several research areas, from Mathematics to Physics and Astrophysics. Within Physics one of the things that makes them interesting is the apparent incompatibilities associated with them that arise between the quantum mechanical and general relativistic theories. From an Astrophysics point of view, their ability to power extremely energetic phenomena and the process by which supermassive black holes form are some of their major interests.

In recent years, GRRT calculations have allowed scientists in the Event Horizon Telescope to produce the first images of black holes and their surrounding environment (Event Horizon Telescope Collaboration et al., 2019). These and subsequent results have shown than the environment surrounding black holes can be rather complicated, with the effects of strong gravity making them even harder to study and understand. Given this, it is clear that being able to disentangle the gravitational effects from other physical processes taking place in these regions is very important. The work presented in this thesis contributes to understanding this interplay.

As such, while this thesis does not directly address the specific issues of the formation of supermassive black holes, the black hole's ability to power extremely energetic events or the interplay between general relativity and quantum mechanics, it developed ideas which contributed to improving our understanding of some general relativistic phenomena; it also built tools that allow researchers to make better sense of observations from these extreme regions of the universe, hence contributing another piece to the puzzle of black holes.

Appendix A

Fluid velocity model

A.1 Keplerian fluid velocity

The code used for the calculations in this thesis uses the same flow velocities as in Pu et al. (2016a). The code can support Keplerian (K), sub-Keplerian and free-fall flows, though all calculations presented in this thesis were performed for a Keplerian flow. The exact expressions used are:

$$u^r_{\rm K}(r) = \begin{cases} 0 & r > r_{\rm isco}\,, \\ -\left[2/\left(3r_{\rm isco}\right)\right]^{1/2}\left[\left(r_{\rm isco}/r\right)-1\right]^{3/2} & r \le r_{\rm isco} \end{cases} \tag{A.1}$$

$$\Omega_{\rm K}(r) = \begin{cases} \left(r^{3/2}+a\right)^{-1} & r > r_{\rm isco}\,, \\ \left(\lambda + aH\right)\left[r^2+2r(1+H)\right]^{-1} & r \le r_{\rm isco} \end{cases} \tag{A.2}$$

where a is the spin of the black hole and

$$\Omega \coloneqq u^\phi/u^t, \tag{A.3}$$

$$\lambda \coloneqq \left(r^2_{\rm isco} - 2a\sqrt{r_{\rm isco}} + a^2\right) / \left(\sqrt{r^3_{\rm isco}} - 2\sqrt{r_{\rm isco}} + a\right), \tag{A.4}$$

$$H \coloneqq (2r - a\lambda)/\Delta \tag{A.5}$$

for the Keplerian flow. For the other flow types, please refer to Pu et al. (2016a).

Appendix B

Constant emissivity hot spot spectrograms at various angles

For completeness, here we present the spectrograms corresponding to a constant emissivity hot spot on an equatorial as viewed by observers at different viewing angles, θ_{obs}. These complement the bolometric light curves presented and discussed in figure 3.2.

By comparing the results side by side it is easy to identify similar features appearing the both the Schwarzschild and the Kerr cases, despite the more complicated structures in Kerr spacetime. The main structures discussed in chapter 3 for $\theta_{\text{obs}} = 89°$ are still visible in these plots, especially for higher inclinations. As the inclination angle decreases and the observation happens more face on, the features become less well distinguished. This is especially the case for $\theta_{\text{obs}} = 15°$, where the Doppler blue and red shift becomes so small that the features caused by it (the wavy pattern) becomes nearly imperceptible. As the viewing angle decreases, the vertical line associated with the Einstein ring (feature D in figure 3.4) disappears and becomes part of the oscillatory pattern due to the change between the Doppler red shifted and Doppler blue shifted portions of the orbit.

The absence of this feature, which corresponds to the disappearance of the Einstein ring, makes the distinction between the contribution of the primary and higher order images more clear, especially in the Schwarzschild cases: the primary image corresponds to the trajectory in the spectrogram that goes through the highest intensity peak (features E and F in figure 3.4). The other lines in the spectrogram are produced by higher order images.

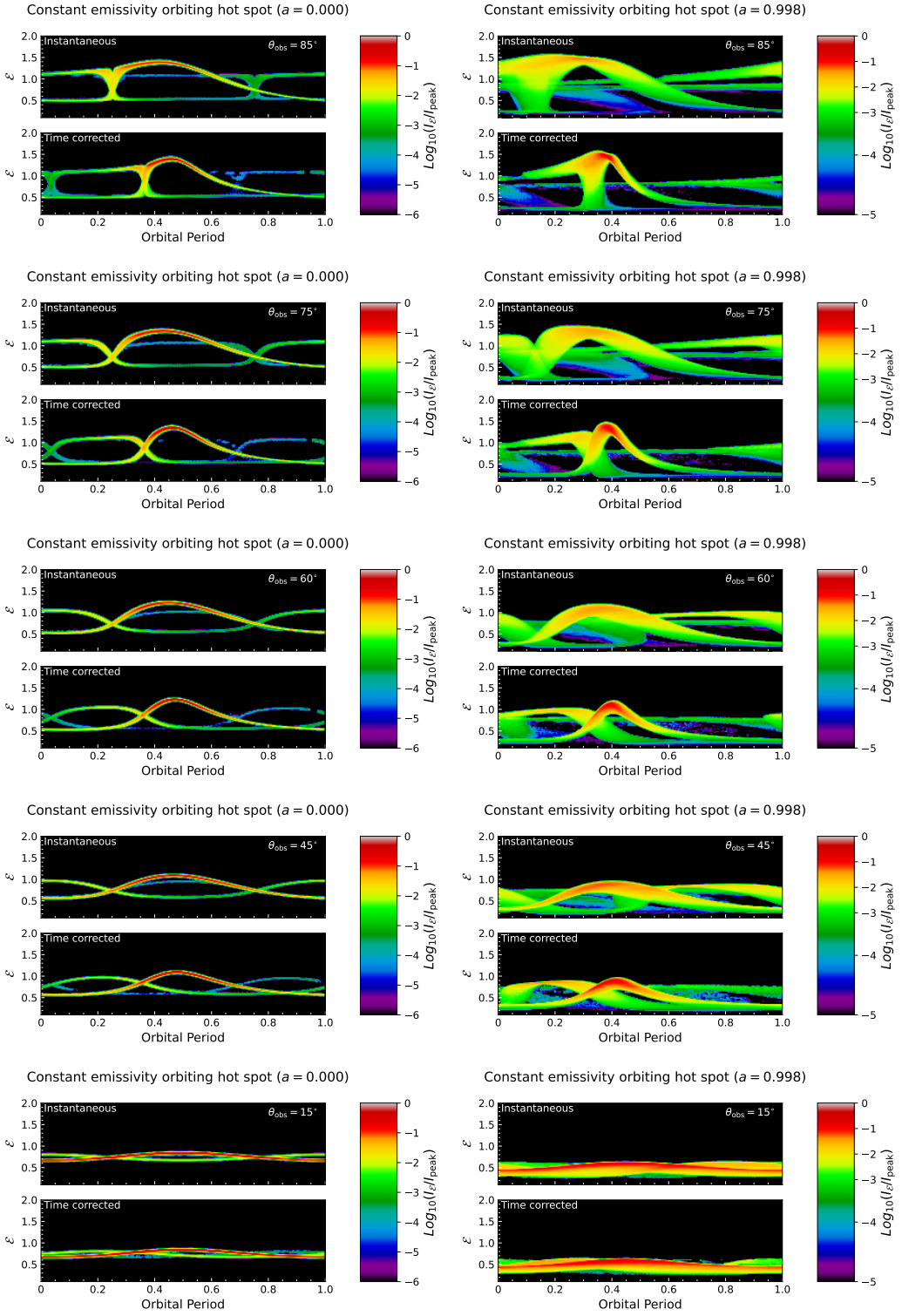

Figure B.1: Spectrograms of hot spots with constant emissivity for different $\theta_{\rm obs}$ in Schwarzschild (left) and Kerr ($a = 0.998$, right) spacetime. The Schwarzschild spectrogram viewed from 60° is precisely consistent with the spectrogram in figure 3 of Li et al. (2014), which includes the primary and secondary image, while our spectrogram includes an extra order of lensed images (faint blue line). If one considers the fist order images only, it is also consistent with the spectrograms in figure 4 of Schnittman and Bertschinger (2004) and figure 7 of Pu et al. (2016b).

References

Aharonian, F., Akhperjanian, A. G., Bazer-Bachi, A. R., et al. (2006). Discovery of very-high-energy γ-rays from the Galactic Centre ridge. *Nature*, 439(7077):695–698.

Baganoff, F. K., Bautz, M. W., Brandt, W. N., et al. (2001). Rapid x-ray flaring from the direction of the supermassive black hole at the galactic centre. *Nature*, 413(6851):45–48.

Barrière, N. M., Tomsick, J. A., Baganoff, F. K., et al. (2014). NuSTAR Detection of High-energy X-Ray Emission and Rapid Variability from Sagittarius A$*$ Flares. *ApJ*, 786(1):46.

Bélanger, G., Goldwurm, A., Melia, F., et al. (2005). Repeated X-Ray Flaring Activity in Sagittarius A*. *ApJ*, 635(2):1095–1102.

Benz, A. O. (2017). Flare Observations. *Living Reviews in Solar Physics*, 14(1):2.

Boyce, H., Haggard, D., Witzel, G., et al. (2022). Multiwavelength Variability of Sagittarius A* in 2019 July. *The Astrophysical Journal*, 931(1):7.

Boyce, H., Haggard, D., Witzel, G., et al. (2019). Simultaneous X-Ray and Infrared Observations of Sagittarius A*'s Variability. *The Astrophysical Journal*, 871(2):161.

Broderick, A. E. and Loeb, A. (2006). Imaging optically-thin hotspots near the black hole horizon of Sgr A* at radio and near-infrared wavelengths. *MNRAS*, 367(3):905–916.

Bronzwaer, T., Davelaar, J., Younsi, Z., et al. (2018). RAPTOR. I. Time-dependent radiative transfer in arbitrary spacetimes. *Astronomy & Astrophysics*, 613:A2.

Brown, R. L. and Lo, K. Y. (1982). Variability of the compact radio source at the Galactic Center. *ApJ*, 253:108–114.

Capellupo, D. M., Haggard, D., Choux, N., et al. (2017). Simultaneous Monitoring of X-Ray and Radio Variability in Sagittarius A*. *ApJ*, 845(1):35.

Carter, B. (1968). Global Structure of the Kerr Family of Gravitational Fields. *Physical Review*, 174(5):1559–1571.

Chael, A., Rowan, M., Narayan, R., et al. (2018). The role of electron heating physics in images and variability of the Galactic Centre black hole Sagittarius A*. *MNRAS*, 478(4):5209–5229.

Chan, C.-k., Liu, S., Fryer, C. L., et al. (2009). MHD Simulations of Accretion onto Sgr A*: Quiescent Fluctuations, Outbursts, and Quasiperiodicity. *ApJ*, 701(1):521–534.

Chan, C.-k., Psaltis, D., and Özel, F. (2013). GRay: A Massively Parallel GPU-based Code for Ray Tracing in Relativistic Spacetimes. *The Astrophysical Journal*, 777(1):13.

Chatterjee, K., Markoff, S., Neilsen, J., et al. (2021). General relativistic MHD simulations of non-thermal flaring in Sagittarius A*. *Monthly Notices of the Royal Astronomical Society*, 507(4):5281–5302.

Chatterjee, R., Marscher, A. P., Jorstad, S. G., et al. (2011). Connection Between the Accretion Disk and Jet in the Radio Galaxy 3C 111. *The Astrophysical Journal*, 734(1):43.

Cunningham, C. T. (1975). The effects of redshifts and focusing on the spectrum of an accretion disk around a Kerr black hole. *APJ*, 202:788–802.

de Felice, F. and Preti, G. (1999). On the meaning of the separation constant in the Kerr metric. *Classical and Quantum Gravity*, 16(9):2929–2935.

Dexter, J. (2016). A public code for general relativistic, polarised radiative transfer around spinning black holes. *MNRAS*, 462(1):115–136.

Dexter, J. and Agol, E. (2009). A Fast New Public Code for Computing Photon Orbits in a Kerr Spacetime. *The Astrophysical Journal*, 696(2):1616–1629.

Dexter, J., Tchekhovskoy, A., Jiménez-Rosales, A., et al. (2020). Sgr A* near-infrared flares from reconnection events in a magnetically arrested disc. *Monthly Notices of the Royal Astronomical Society*, 497(4):4999–5007.

Dodds-Eden, K., Porquet, D., Trap, G., et al. (2009). Evidence for X-Ray Synchrotron Emission from Simultaneous Mid-Infrared to X-Ray Observations of a Strong Sgr A* Flare. *The Astrophysical Journal*, 698(1):676–692.

Dodds-Eden, K., Sharma, P., Quataert, E., et al. (2010). Time-Dependent Models of Flares from Sagittarius A*. *ApJ*, 725(1):450–465.

Eckart, A., Baganoff, F. K., Morris, M., et al. (2004). First simultaneous NIR/X-ray detection of a flare from Sgr A*. *A&A*, 427:1–11.

Eckart, A., Baganoff, F. K., Morris, M., et al. (2006a). The flare activity of Sagittarius A*. New coordinated mm to X-ray observations. *Astronomy and Astrophysics*, 450(2):535–555.

Eckart, A., García-Marín, M., Vogel, S. N., et al. (2012). Millimeter to X-ray flares from Sagittarius A*. *A&A*, 537:A52.

Eckart, A., Schödel, R., García-Marín, M., et al. (2008). Simultaneous NIR/sub-mm observation of flare emission from Sagittarius A*. *A&A*, 492(2):337–344.

Eckart, A., Schödel, R., Meyer, L., et al. (2006b). Polarimetry of near-infrared flares from Sagittarius A*. *Astronomy and Astrophysics*, 455(1):1–10.

Einstein, A. (1916). The foundation of the general theory of relativity. In *Volume 6: The Berlin Years: Writings, 1914-1917 (English translation supplement)*, The collected papers of Albert Eisntein, page 147–200. Princeton University Press.

Event Horizon Telescope Collaboration, Akiyama, K., Alberdi, A., et al. (2022). First Sagittarius A* Event Horizon Telescope Results. V. Testing Astrophysical Models of the Galactic Center Black Hole. *The Astrophysical Journal*, 930(2):L16.

Event Horizon Telescope Collaboration, Akiyama, K., Alberdi, A., et al. (2019). First M87 Event Horizon Telescope Results. I. The Shadow of the Supermassive Black Hole. *The Astrophysical Journal*, 875(1):L1.

Fazio, G. G., Hora, J. L., Witzel, G., et al. (2018). Multiwavelength Light Curves of Two Remarkable Sagittarius A* Flares. *The Astrophysical Journal*, 864(1):58.

Fuerst, S. V. and Wu, K. (2004). Radiation transfer of emission lines in curved space-time. *Astronomy and Astrophysics*, 424:733–746.

Fuhrmeister, B., Liefke, C., Schmitt, J. H. M. M., and Reiners, A. (2008). Multiwavelength observations of a giant flare on CN Leonis. I. The chromosphere as seen in the optical spectra. *Astronomy and Astrophysics*, 487(1):293–306.

Gabici, S., Aharonian, F. A., and Casanova, S. (2009). Broad-band non-thermal emission from molecular clouds illuminated by cosmic rays from nearby supernova remnants. *"MNRAS"*, 396(3):1629–1639.

García-Alvarez, D., Foing, B. H., Montes, D., et al. (2003). Simultaneous optical and X-ray observations of flares and rotational modulation on the RS CVn binary HR 1099 (V711 Tau) from the MUSICOS 1998 campaign. *Astronomy and Astrophysics*, 397:285–303.

Genzel, R., Schödel, R., Ott, T., et al. (2003). Near-infrared flares from accreting gas around the supermassive black hole at the Galactic Centre. *Nature*, 425(6961):934–937.

Ghez, A. M., Duchêne, G., Matthews, K., et al. (2003). The First Measurement of Spectral Lines in a Short-Period Star Bound to the Galaxy's Central Black Hole: A Paradox of Youth. *The Astrophysical Journal*, 586(2):L127–L131.

Ghez, A. M., Salim, S., Weinberg, N. N., et al. (2008). Measuring Distance and Properties of the Milky Way's Central Supermassive Black Hole with Stellar Orbits. *The Astrophysical Journal*, 689(2):1044–1062.

Ghez, A. M., Wright, S. A., Matthews, K., et al. (2004). Variable Infrared Emission from the Supermassive Black Hole at the Center of the Milky Way. *The Astrophysical Journal*, 601(2):L159–L162.

Gillessen, S., Eisenhauer, F., Fritz, T. K., et al. (2009). The Orbit of the Star S2 Around SGR A* from Very Large Telescope and Keck Data. *The Astrophysical Journal*, 707(2):L114–L117.

Goldston, J. E., Quataert, E., and Igumenshchev, I. V. (2005). Synchrotron Radiation from Radiatively Inefficient Accretion Flow Simulations: Applications to Sagittarius A*. *ApJ*, 621(2):785–792.

Goldwurm, A., Brion, E., Goldoni, P., et al. (2003). A New X-Ray Flare from the Galactic Nucleus Detected with the XMM-Newton Photon Imaging Cameras. *ApJ*, 584(2):751–757.

Grant, A. (2020). *Angular Momentum in General Relativity*. PhD thesis, Cornell University.

GRAVITY Collaboration, Abuter, R., Aimar, N., et al. (2022). Mass distribution in the Galactic Center based on interferometric astrometry of multiple stellar orbits. *Astronomy & Astrophysics*, 657:L12.

GRAVITY Collaboration, Abuter, R., Amorim, A., et al. (2018). Detection of orbital motions near the last stable circular orbit of the massive black hole SgrA*. *A&A*, 618:L10.

GRAVITY Collaboration, Bauböck, M., Dexter, J., et al. (2020a). Modeling the orbital motion of Sgr A*'s near-infrared flares. *A&A*, 635:A143.

GRAVITY Collaboration, Jiménez-Rosales, A., Dexter, J., et al. (2020b). Dynamically important magnetic fields near the event horizon of Sgr A*. *Astronomy & Astrophysics*, 643:A56.

Hamaus, N., Paumard, T., Müller, T., et al. (2009). Prospects for Testing the Nature of Sgr A*'s Near-Infrared Flares on the Basis of Current Very Large Telescope—and Future Very Large Telescope Interferometer—Observations. *The Astrophysical Journal*, 692(1):902–916.

Hannikainen, D. C., Rodriguez, J., Vilhu, O., et al. (2005). Characterizing a new class of variability in GRS 1915+105 with simultaneous INTEGRAL/RXTE observations. *Astronomy and Astrophysics*, 435(3):995–1004.

Hayasaki, K. (2021). Neutrinos from tidal disruption events. *Nature Astronomy*, 5:436–437.

Hull, C. (2020). Lecture notes in differential geometry.

JaJa, J. (2000). A perspective on quicksort. *Computing in Science & Engineering*, 2(1):43–49.

Karssen, G. D., Bursa, M., Eckart, A., et al. (2017). Bright X-ray flares from Sgr A*. *Monthly Notices of the Royal Astronomical Society*, 472(4):4422–4433.

Kerr, R. P. (1963). Gravitational Field of a Spinning Mass as an Example of Algebraically Special Metrics. *PRL*, 11(5):237–238.

Kimpson, T., Wu, K., and Zane, S. (2019). Spatial dispersion of light rays propagating through a plasma in Kerr space-time. *"MNRAS"*, 484(2):2411–2419.

Koutsantoniou, L. E. (2022). Algorithms and radiation dynamics for the vicinity of black holes. I. Methods and codes. *Astronomy & Astrophysics*, 657:A32.

Kunneriath, D., Witzel, G., Eckart, A., et al. (2010). Coordinated NIR/mm observations of flare emission from Sagittarius A*. *A&A*, 517:A46.

Kusunose, M. and Takahara, F. (2011). Synchrotron Blob Model of Infrared and X-ray Flares from Sagittarius A*. *The Astrophysical Journal*, 726(1):54.

Laplace, P. S. (1799). Translation of 'allgemeine geographische ephemeriden herausgegeben von f. von z'. In *The Large Scale Structure of Space-Time*, Cambridge Monographs on Mathematical Physics, page 365–368. Cambridge University Press.

Lawrence, A. (1980). Repeated X-ray flaring in NGC 4151. *Monthly Notices of the Royal Astronomical Society*, 192:83–94.

Li, Y.-P., Yuan, F., and Wang, Q. D. (2017). A magnetohydrodynamic model for multiwavelength flares from Sagittarius A* (I): model and the near-infrared and X-ray flares. *MNRAS*, 468(3):2552–2568.

Li, Z., Kong, L., and Bambi, C. (2014). Testing the Nature of the Supermassive Black Hole Candidate in SgrA* with Light Curves and Images of Hot Spots. *The Astrophysical Journal*, 787(2):152.

Lindquist, R. W. (1966). Relativistic transport theory. *Annals of Physics*, 37(3):487–518.

Liu, S. and Melia, F. (2002). An Accretion-induced X-Ray Flare in Sagittarius A*. *The Astrophysical Journal*, 566(2):L77–L80.

Liu, S., Petrosian, V., and Melia, F. (2004). Electron Acceleration around the Supermassive Black Hole at the Galactic Center. *ApJ L.*, 611(2):L101–L104.

Liu, S., Petrosian, V., Melia, F., and Fryer, C. L. (2006). A Testable Stochastic Acceleration Model for Flares in Sagittarius A*. *The Astrophysical Journal*, 648(2):1020–1025.

Lynden-Bell, D. and Rees, M. J. (1971). On quasars, dust and the galactic centre. *MNRAS*, 152:461.

Markoff, S., Falcke, H., Yuan, F., and Biermann, P. L. (2001). The Nature of the 10 kilosecond X-ray flare in Sgr A*. *A&A*, 379:L13–L16.

Marrone, D. P., Baganoff, F. K., Morris, M. R., et al. (2008). An X-Ray, Infrared, and Submillimeter Flare of Sagittarius A*. *The Astrophysical Journal*, 682(1):373–383.

Masada, Y., Nagataki, S., Shibata, K., and Terasawa, T. (2010). Solar-Type Magnetic Reconnection Model for Magnetar Giant Flares. *PASJ*, 62:1093.

Meyer, L., Eckart, A., Schödel, R., et al. (2006a). Near-infrared polarimetry setting constraints on the orbiting spot model for Sgr A* flares. *Astronomy and Astrophysics*, 460(1):15–21.

Meyer, L., Schödel, R., Eckart, A., et al. (2006b). K-band polarimetry of an Sgr A* flare with a clear sub-flare structure. *Astronomy and Astrophysics*, 458(2):L25–L28.

Michail, J. M., Wardle, M., Yusef-Zadeh, F., and Kunneriath, D. (2021a). Multiwavelength Observations of Sgr A*. I. 2019 July 18. *ApJ*, 923(1):54.

Michail, J. M., Yusef-Zadeh, F., and Wardle, M. (2021b). Detection of a 20-min time lag observed from Sgr A* between 8 and 10 GHz with the VLA. *MNRAS*, 505(3):3616–3623.

Michell, J. (1784). On the Means of Discovering the Distance, Magnitude, &c. of the Fixed Stars, in Consequence of the Diminution of the Velocity of Their Light, in Case Such a Diminution Should be Found to Take Place in any of Them, and Such Other Data Should be Procured from Observations, as Would be Farther Necessary for That Purpose. By the Rev. John Michell, B. D. F. R. S. In a Letter to Henry Cavendish, Esq. F. R. S. and A. S. *Philosophical Transactions of the Royal Society of London Series I*, 74:35–57.

Misner, C. W., Thorne, K. S., and Wheeler, J. A. (1973). *Gravitation*. W. H. Freeman, San Francisco.

Miyazaki, A., Tsutsumi, T., and Tsuboi, M. (1999). A search for short-term variability of Sagittarius A* at millimeter wavelengths. *Advances in Space Research*, 23(5-6):977–980.

Miyazaki, A., Tsutsumi, T., and Tsuboi, M. (2004). Intraday Variation of Sagittarius A* at Short Millimeter Wavelengths. *ApJ L.*, 611(2):L97–L100.

Miyoshi, M., Moran, J., Herrnstein, J., et al. (1995). Evidence for a black hole from high rotation velocities in a sub-parsec region of NGC4258. *Nature,*, 373(6510):127–129.

Murchikova, L. and Witzel, G. (2021). Second-scale Submillimeter Variability of Sagittarius A* during Flaring Activity of 2019: On the Origin of Bright Near-infrared Flares. *ApJ L.*, 920(1):L7.

Nathanail, A., Mpisketzis, V., Porth, O., et al. (2022). Magnetic reconnection and plasmoid formation in three-dimensional accretion flows around black holes. *Monthly Notices of the Royal Astronomical Society*, 513(3):4267–4277.

Nishiyama, S., Tamura, M., Hatano, H., et al. (2009). Near-Infrared Polarimetry of Flares from Sgr A* with Subaru/CIAO. *ApJ L.*, 702(1):L56–L60.

Nowak, M. A., Neilsen, J., Markoff, S. B., et al. (2012). Chandra/HETGS Observations of the Brightest Flare Seen from Sgr A*. *ApJ*, 759(2):95.

Oppenheimer, J. R. and Snyder, H. (1939). On Continued Gravitational Contraction. *Physical Review*, 56(5):455–459.

Penrose, R. (1965). Gravitational Collapse and Space-Time Singularities. *Physical Review Letters*, 14(3):57–59.

Porquet, D., Grosso, N., Predehl, P., et al. (2008). X-ray hiccups from Sagittarius A* observed by XMM-Newton. The second brightest flare and three moderate flares caught in half a day. *A&A*, 488(2):549–557.

Porquet, D., Predehl, P., Aschenbach, B., et al. (2003). XMM-Newton observation of the brightest X-ray flare detected so far from Sgr A*. *A&A*, 407:L17–L20.

Pu, H.-Y., Akiyama, K., and Asada, K. (2016a). The Effects of Accretion Flow Dynamics on the Black Hole Shadow of Sagittarius A*. *The Astrophysical Journal*, 831(1):4.

Pu, H.-Y., Yun, K., Younsi, Z., and Yoon, S.-J. (2016b). Odyssey: A Public GPU-based Code for General Relativistic Radiative Transfer in Kerr Spacetime. *The Astrophysical Journal*, 820(2):105.

Reid, H. A. S. (2020). A review of recent type III imaging spectroscopy. *Frontiers in Astronomy and Space Sciences*, 7:56.

Reid, H. A. S. and Ratcliffe, H. (2014). A review of solar type III radio bursts. *Research in Astronomy and Astrophysics*, 14(7):773–804.

Retter, A., Richards, M. T., and Wu, K. (2005). Evidence for Superhumps in the Radio Light Curve of Algol and a New Model for Magnetic Activity in Algol Systems. *The Astrophysical Journal*, 621(1):417–424.

Ripperda, B., Bacchini, F., and Philippov, A. A. (2020). Magnetic Reconnection and Hot Spot Formation in Black Hole Accretion Disks. *ApJ*, 900(2):100.

Ripperda, B., Liska, M., Chatterjee, K., et al. (2022). Black Hole Flares: Ejection of Accreted Magnetic Flux through 3D Plasmoid-mediated Reconnection. *The Astrophysical Journal*, 924(2):L32.

Roberts, M. (2020). How to evenly distribute points on a sphere more effectively than the canonical fibonacci lattice. Accessed in April 2023.

Rosquist, K., Bylund, T., and Samuelsson, L. (2009). Carter's Constant Revealed. *International Journal of Modern Physics D*, 18(3):429–434.

Rybicki, G. B. and Lightman, A. P. (1979). *Radiative processes in astrophysics*. John Wiley and Sons, New York.

Schnittman, J. D. and Bertschinger, E. (2004). The Harmonic Structure of High-Frequency Quasi-periodic Oscillations in Accreting Black Holes. *ApJ*, 606(2):1098–1111.

Schödel, R., Ott, T., Genzel, R., et al. (2002). A star in a 15.2-year orbit around the supermassive black hole at the centre of the Milky Way. *Nature,*, 419(6908):694–696.

Schulz, R., Kadler, M., Ros, E., et al. (2020). Sub-milliarcsecond imaging of a bright flare and ejection event in the extragalactic jet 3C 111. *Astronomy and Astrophysics*, 644:A85.

Schwarzschild, K. (1916). On the gravitational field of a mass point according to Einstein's theory. *arXiv e-prints*, page physics/9905030. *translated by* Antoci S. and Loinger A. [1999].

Semerák, O. (1993). Stationary frames in the Kerr field. *General Relativity and Gravitation*, 25(10):1041–1077.

Takahashi, R. (2007). Equations of general relativistic radiation hydrodynamics in Kerr spacetime. *MNRAS*, 382(3):1041–1049.

The Nobel Comittee for Physics (2020). Theoretical foundation for black holes and the supermassive compact object at the galactic centre. *Nobel Prize Outreach Advanced information.*

Thorne, K. S. and Blandford, R. D. (2017). *Modern classical physics : optics, fluids, plasmas, elasticity, relativity, and statistical physics*. Princeton University Press.

Trap, G., Goldwurm, A., Dodds-Eden, K., et al. (2011). Concurrent X-ray, near-infrared, submillimeter, and GeV gamma-ray observations of Sagittarius A*. *Astronomy & Astrophysics*, 528:A140.

Trippe, S., Paumard, T., Ott, T., et al. (2007). A polarized infrared flare from Sagittarius A* and the signatures of orbiting plasma hotspots. *Monthly Notices of the Royal Astronomical Society*, 375(3):764–772.

Uzdensky, D. A. (2011). Magnetic Reconnection in Extreme Astrophysical Environments. *Space Sci Rev*, 160(1-4):45–71.

Wald, R. M. (1984). *General Relativity*. The University of Chicago Press.

Warwick, R. S., Smith, D. A., Yaqoob, T., et al. (1996). Multiwavelength Observations of Short-Timescale Variability in NGC 4151. III. X-Ray and Gamma-Ray Observations. *The Astrophysical Journal*, 470:349.

Wielgus, M., Marchili, N., Martí-Vidal, I., et al. (2022). Millimeter Light Curves of Sagittarius A* Observed during the 2017 Event Horizon Telescope Campaign. *ApJ L.*, 930(2):L19.

Wu, K., Fuerst, S. V., Lee, K.-G., and Branduardi-Raymont, G. (2006). General Relativistic Radiative Transfer: Emission from Accreting Black Holes in AGN. *Chinese Journal of Astronomy and Astrophysics Supplement*, 6(S1):205–220.

Younsi, Z. (2013). *General Relativistic Radiative Transfer in Black Hole Systems*. PhD thesis, University College London.

Younsi, Z. and Wu, K. (2015). Variations in emission from episodic plasmoid ejecta around black holes. *Monthly Notices of the Royal Astronomical Society*, 454(3):3283–3298.

Younsi, Z., Wu, K., and Fuerst, S. V. (2012). General relativistic radiative transfer: formulation and emission from structured tori around black holes. *Astronomy and Astrophysics*, 545:A13.

Yuan, F., Lin, J., Wu, K., and Ho, L. C. (2009). A magnetohydrodynamical model for the formation of episodic jets. *Monthly Notices of the Royal Astronomical Society*, 395(4):2183–2188.

Yuan, F., Quataert, E., and Narayan, R. (2003). Nonthermal Electrons in Radiatively Inefficient Accretion Flow Models of Sagittarius A*. *ApJ*, 598(1):301–312.

Yuan, F., Quataert, E., and Narayan, R. (2004). On the Nature of the Variable Infrared Emission from Sagittarius A*. *ApJ*, 606(2):894–899.

Yuan, Q. and Wang, Q. D. (2016). A systematic Chandra study of Sgr A* - I. X-ray flare detection. *Monthly Notices of the Royal Astronomical Society*, 456(2):1438–1450.

Yusef-Zadeh, F., Bushouse, H., Wardle, M., et al. (2009). Simultaneous Multi-Wavelength Observations of Sgr A* During 2007 April 1-11. *ApJ*, 706(1):348–375.

Yusef-Zadeh, F., Roberts, D., Wardle, M., et al. (2006). Flaring Activity of Sagittarius A* at 43 and 22 GHz: Evidence for Expanding Hot Plasma. *ApJ*, 650(1):189–194.

Yusef-Zadeh, F., Wardle, M., Cotton, W. D., et al. (2007). The Variability of Polarized Radiation from Sagittarius A*. *ApJ L.*, 668(1):L47–L50.

Yusef-Zadeh, F., Wardle, M., Heinke, C., et al. (2008). Simultaneous Chandra, CSO, and VLA Observations of Sgr A*: The Nature of Flaring Activity. *The Astrophysical Journal*, 682(1):361–372.

Zhang, S., Baganoff, F. K., Ponti, G., et al. (2017). Sagittarius A* High-energy X-Ray Flare Properties during NuSTAR Monitoring of the Galactic Center from 2012 to 2015. *The Astrophysical Journal*, 843(2):96.

Zhang, S., Hailey, C. J., Baganoff, F. K., et al. (2014). High-energy X-Ray Detection of G359.89-0.08 (Sgr A-E): Magnetic Flux Tube Emission Powered by Cosmic Rays? *The Astrophysical Journal*, 784(1):6.